Wrocław University of Science and Technology

Faculty of Electrical Engineering

PhD Thesis

MSc. Roberto Eduardo Quintal Palomo

Operation and faults analysis of energy-saving permanent magnet synchronous generator for small wind turbine

Supervisor
Mateusz Dybkowski, Ph.D., D.Sc.,WrUST Prof.
Co-supervisor
Maciej Gwoździewicz, Ph.D.

Wroclaw, 2019

Streszczenie

W pracy przedstawiono analizę teoretyczną, symulacyjną oraz weryfikację eksperymentalną nowego generatora synchronicznego z magnesami trwałymi (PMSG) dedykowanego dla małych turbin wiatrowych (ang. SWT). Maszyna z wewnętrznymi magnesami trwałymi (ang. IPM) została zaprojektowana w oparciu o seryjny silnik indukcyjny (ang. IM). W konstrukcji wirnika wykorzystano efekt indukowania biegunów. Przeprowadzono optymalizację parametrów w celu uzyskania najwyższego poziomu siły elektromotorycznej EMF przy jak najmniejszym zniekształceniu prądu przez wyższe harmoniczne. W rezultacie opracowano generator PMSG o dwukrotnie większej gęstości mocy niż pierwotna maszyna indukcyjna. W kolejnej części pracy analizowano działanie generatora PMSG z prostownikiem pasywnym i z dwupoziomowym przemiennikiem częstotliwości sterowanym przy wykorzystaniu metody polowo - zorientowanej (ang. FOC). Oba układy (pasywne i aktywne) były sterowane przy wykorzystaniu algorytmu OTC (optymalne sterowanie momentem), w celu uzyskania maksymalnej mocy z turbiny wiatrowej o trzech łopatach i poziomej osi obrotu. Działanie generatora PMSG analizowano również pod kątem symetrycznego i asymetrycznego zwarcia w celu analizy jego częściowego rozmagnesowania. Następnie przeanalizowano działanie generatora PMSG z częściowym rozmagnesowaniem. Podano wnioski dotyczące rozmagnesowania takich magnesów podczas normalnej pracy. W pracy zaprezentowano wyniki badań symulacyjnych, co-symulacyjnych oraz badania eksperymentalne wykonane na prototypie generatora i karcie DS1103.

Słowa kluczowe: *PMSG, IPM, SWT, demagnetyzacja, FOC, OTC, MPPT.*

Abstract

In this thesis the design, theoretical analysis, experimental validation and operation of a novel Permanent Magnet Synchronous Generator (PMSG) for Small Wind Turbines (SWT) is presented. An Interior Permanent Magnet (IPM) machine was designed on the basis of a series produced induction motor (IM). An approach called consequent pole (sometimes induced pole) was applied in the rotor design. A sweep parameter optimisation was done in order to obtain the highest back EMF with low total harmonic distortion. The result is a PMSG with almost double the power density of the IM on which is based. Then the operation of the PMSG with a passive rectifier and with a two level voltage source converter is analysed. This last topology was controlled with the Field Oriented Control (FOC). Both topologies (passive and active) where operated with an optimal torque control strategy, for obtaining the maximum power point of operation with the three blade horizontal axis turbine model. The operation of the PMSG was also analysed for symmetrical and asymmetrical short circuit in order to obtain partial demagnetization. Then the operation of the PMSG with partial demagnetization was analysed and conclusions, about the possibility of demagnetizing such interior permanent magnets in normal operation, are presented. The paper presents the results of simulation and co-simulation tests as well as experimental tests carried out on the built prototype of the generator and DS1103 card.

Keywords: *PMSG, IPM, SWT, demagnetization, FOC, OTC, MPPT.*

Contents

1. Introduction

1.1. Motivation

Global warming and climate change, has driven countries to act on the reduction of carbon dioxide emissions, a main contributor of these man-made pollution effects. A main part of these emissions come from the electric power generation, therefore an improvement in the efficiency and the development of new technologies for exploitation of renewable energy sources has been and will continue to be an intensive research topic.

Until some decades ago, wind energy and the technologies associated with it were stagnated. After the surge in 1970's of the world oil prices and the lack of gas, coal or oil in certain countries the development of the wind turbine technologies revived.

Nowadays, the main focus in the development of these technologies is the reliability [1]. The Cost-Of-Energy (COE) for the onshore wind turbines has come to a level where it is competitive with fossil fuel technologies even without any subsidies, see Fig. 1.1. As shown in Eq.1.1 the COE comprises the Capital cost (CAPEX), the Operation and maintenance cost (OPEX) and the Annual Energy Production (AEP). Therefore, higher reliability and effective maintenance lowers the downtime. Lower OPEX and higher AEP lowers COE.

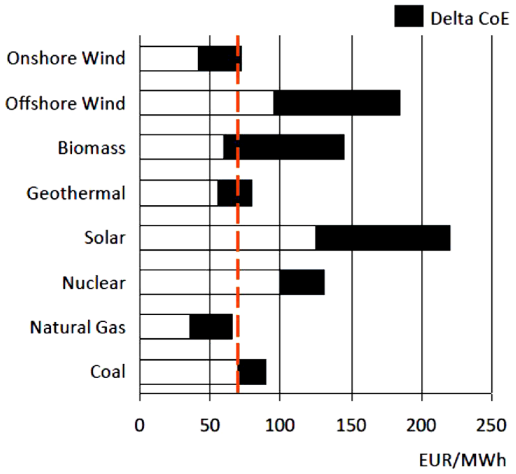

Note: NG prices = USD 4.00-6.75/MMBTU, Coal = USD 1.60-1.70.MMBTU, onshore wind capacity factor = 30% no CO2 costs for fossil technology, EUR = 1.45 USD.

Fig. 1.1. Wind competitive with fossil fuels [2]

$$COE = \frac{CAPEX + OPEX}{AEP} \tag{1.1}$$

Different studies [3, 4, 5] have shown that for megawatt-large wind turbines the generator's assembly has the third largest contribution to overall failure rate in percentage, just after blade's pitch control system and the frequency converter (power electronics) as shown in Fig.1.2.

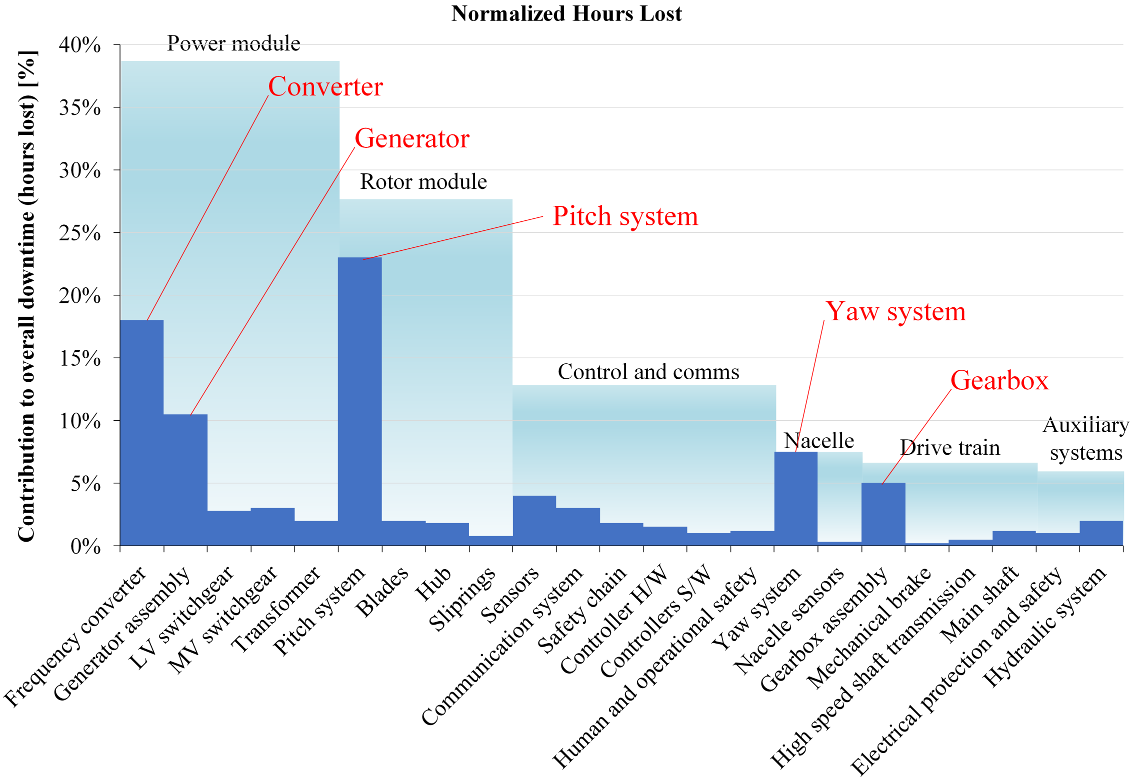

Fig. 1.2. Percentage contribution to overall failure rate (data from [3]). Normalised hours lost

Also its important to notice that the top three contributors indicated by most of these databases are: power module, drive train module, and rotor module, among which drive train and rotor modules are typically more expensive to repair due to the on-site crane costs.

Industry standards demand a design target lifetime of 20 years or 120,000 hours. For the wind turbines to be able to minimise the time to the Return On Investment (ROI) and minimise COE as explained before, the *availability* is the factor of most importance due to the intermittent nature of the energy source.

Another important motivator for reliability design is the reduction of costs from repeating sketches, drawings and specs with all the engineering costs, the lost market share, the lost production and the warranty and recall of parts. The earlier the reliability is introduced in the design the better, as shown in Fig. 1.3.

From these motivators for the improvement of the wind turbine reliability, this works focuses on the design of a Permanent Magnet Synchronous Generator (PMSG) and the fault analysis for Small Wind Turbines (SWT).

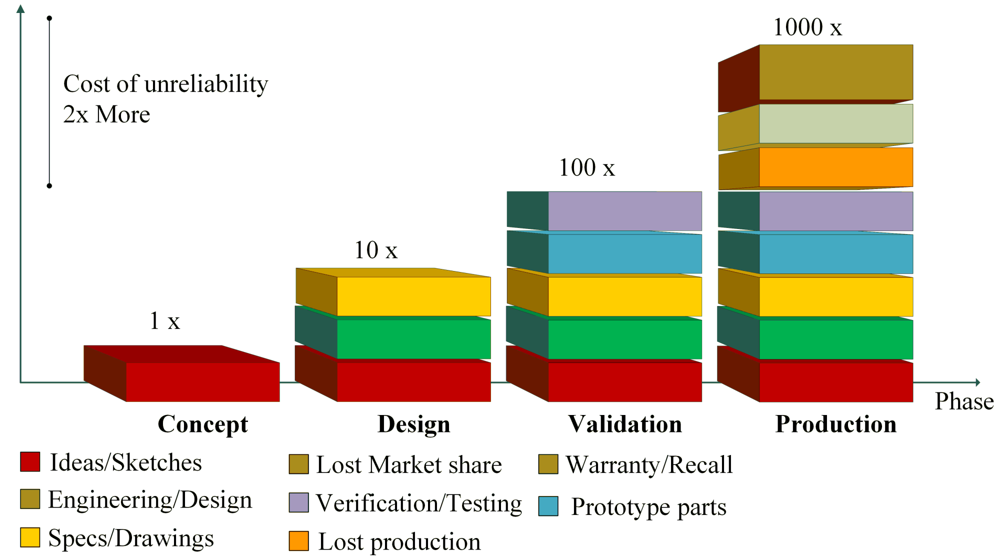

Fig. 1.3. Reduction of costs by improving reliability upfront (data from [6])

The PMSG was chosen due to the volume and mass vs power characteristics of these kind of machines, shown in Fig. 1.4.

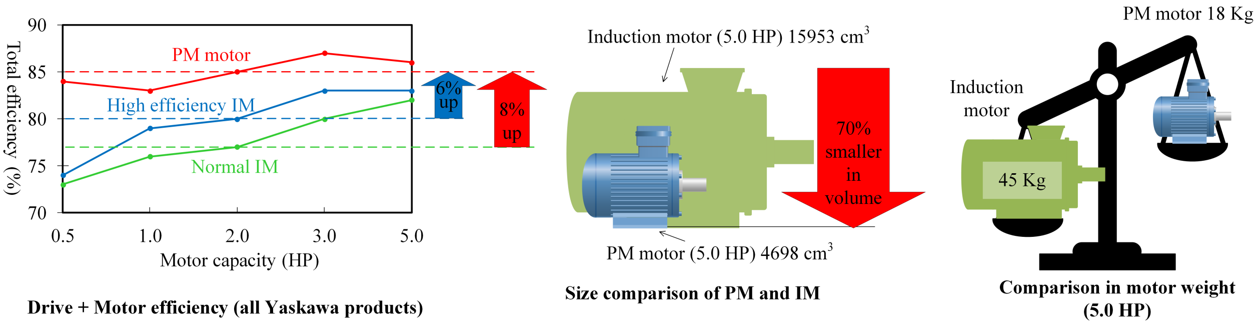

Drive + Motor efficiency (all Yaskawa products)

Size comparison of PM and IM

Comparison in motor weight (5.0 HP)

Fig. 1.4. Advantage of PM motors vs. induction motors (data from [7])

Due to the application, a small horizontal axis wind turbine (HAWT), the weight of the electrical machine plays an important role in the design due to the structural stresses on the tower and the on-site assembly over the tower.

1.2. State of the art - modelling and simulation of PMSG

Since the 1970's oil crisis, improvements in the wind turbine design have been reported in the literature [8] including the historical development of these technologies. In parallel, the material science focus on high energy density magnetic materials during the 1980's and 1990's made the PMSG a suitable solution for the energy conversion in the wind turbine systems.

In the papers [9] and [10] a detailed analysis of the evolution of the maximum energy product for different materials was analysed. In Fig.1.5 the author's results of these analysis are presented.

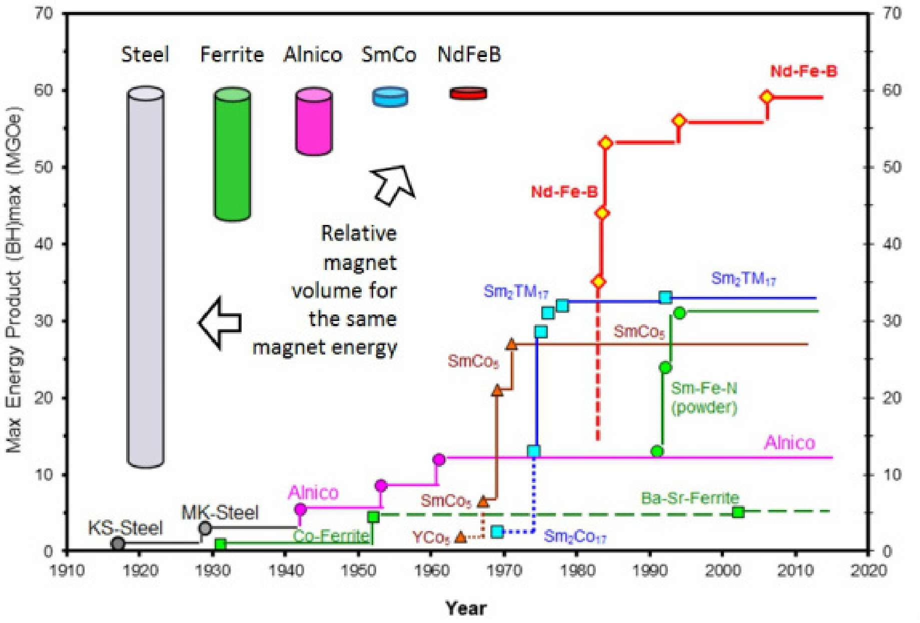

Fig. 1.5. Maximum energy product (BH_{max}) for different ferromagnetic materials. Modified from [10]

These situations launched the development of better designs for the PMSG. New designs with axial and transverse flux have been developed as early as 1992 in the case of [11] to more recent work (2017) in [12], as consequence. Work done specifically for small wind turbines SWTs can be found in [13] and [14]. A good compendium of the theory and design rules behind the PMSG can be found in [15].

When designing a PMSG, the design goals are: to optimise the magnetic flux density (**B**) by the proper selection of materials, to maximise the interaction between magnetic flux density and the stator windings by optimising the geometry, and to minimise losses such as eddy-current, hysteresis, frictional losses and cogging torque. Work as early as 2002 [16] showed that this could be done to the surface permanent magnets SPM by changing the rectangular shape of the magnets to a rounded and radially magnetised one. Further work optimising the stator tooth geometry can be found in [17] and using the third harmonic in the magnet shape in [18].

For interior permanent magnets IPM machines some work in cogging torque reduction was done in [19] and [20] which are based on the previous work done for SPM in [21].
More recent work shown in [22] included total harmonic distortion THD vs geometry maps in the optimisation and showed the mature capabilities of rotor manufacturing laminations and in [23] a methodology is proposed, based on discrete steps for geometry modification, for the IPM rotor shape optimisation.

Other techniques for cogging torque minimisation specifically for SWTs are mentioned in [24] which refer to the previous work done in [25] by the same authors.

All the mentioned literature has the common methodology of calculating by finite element analysis FEA the transient behaviour of the rotating machine under different conditions, for that reason a further improvement in this transient simulations is presented in Fig. 1.6.

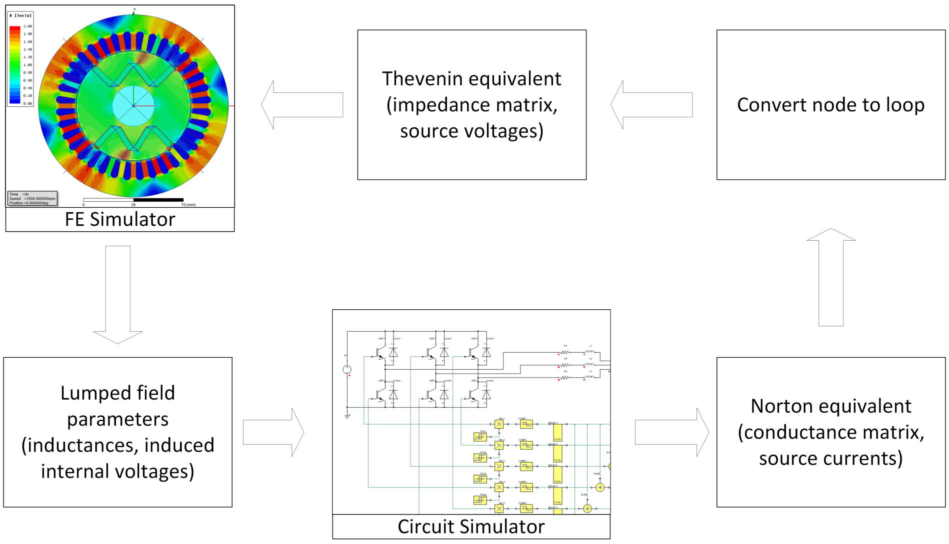

Fig. 1.6. Coupled Field-Circuit Co-simulation Mechanism.

The co-simulation mechanism allows to calculate many different parameters that are dependent on the interaction between the rotating machine and the voltages and currents fed to it. This approach is useful, for example, for new methods of cogging torque reduction which employ new modulation techniques as in [26].

The co-simulation principles have been applied already since the beginning of 2000's, for example in [27] a co-simulation between control, circuit analysis and FEA was done in order to asses electromagnetic compatibility (EMC) of the whole electric drive system. It was until recently that the advances in computational capabilities of common personal computers (PC) allowed the widespread adoption of the co-simulation. Further development in the libraries of components available for the co-simulation have increased its adoption and minimised the development time of complex systems as shown in [28].

1.3. The co-simulation approach

The approach used in this research is called the coupled field-circuit co-simulation. In the literature the co-simulation approach normally refers to the simulation of a system using two or more software packages, e.g. Mathworks Simulink and PSIM like in [29] and [30]. A similar approach with different software can be found in [31] and [32] where the analytical model of the machine is given in LabVIEW's mathematical equations and the power electronics circuit is simulated with another Simulation Program with Integrated Circuit Emphasis (SPICE) e.g. Multisim. However all those co-simulation examples use an analytical model of the electrical machine, sometimes with an additional modelled saturation (hysteresis) for taking into account some nonlinearities of the machine like in [33].

Other authors in the literature use a combination of software and hardware when referring to co-simulation but again, the electrical machine is modelled as first order differential equations (no nonlinearities take into account) then the analytical model is discretized and embedded in the hardware´s real-time platform as in [34], [35] and [36].

The method used in this PhD thesis was first described in [37], here the electric machine's 2D geometry layout for FEA is connected to the power electronics' model in a SPICE software. It is important to mention previous efforts from [38] where the co-simulation is described but the results of the FEA are extracted as a multi-dimensional lookup table with a technology called Equivalent Circuit Extraction (ECE). Also, some efforts from other authors were reported in [39] although, this was still not implemented as a tool for commercial FEA software (proprietary software of Helsinki University of Technology called FCSMEK) and was based on the previous work from the same authors [40]. As mentioned before the Finite Element Analysis has become the standard for modelling, simulating, and designing electric machines as stated in the seminal work from Prof. Arkkio [41] and Prof. Salon [42], also in more recent work like [43], [44], and [45]. However, most of the research in this area has focused only on the electrical machine like in [46]. Only until very recently ($\sim$ 2018) it has been recognised the importance of the simulation of the interconnected systems in the design phase as mentioned in the book [47].

Here is important to differentiate the coupled field-circuit simulation and the co-simulation. In [48], [49], and [50], the authors used the coupled field-circuit method to analyse different behaviours of the machine e.g. losses due to switching frequency. The coupled field-circuit approach allows one software (e.g. ANSYS Maxwell) simulate the switching behaviour during transient analysis through the conversion of the FEA results as a nodal form for the circuit equations and the circuit simulator (e.g. ANSYS Simplorer) results to get converted into a loop form for the FEA as shown in [51].

For analysis of interconnected systems and complex machines the coupled field-circuit co-simulation offers advantages over the coupled field-circuit-only approach because different specialised software can be used to simulate different parts of the system. Also, since the electrical machine might be unconventional and/or difficult to manufacture, the coupled field-circuit co-simulation allows to analyse different types of faults without risk of damage to the machine, as shown for example with a doubly salient permanent magnet (DSPM) motor in [52] or for a five-phase dual-rotor permanent magnet [53]. Also in [54], the coupled field-circuit co-simulation was used to analyse faults two phase short-circuit and one transistor short circuit in induction motors in [55] the coupled field-circuit co-simulation method was used to analyse open diode and shorted diode in the field rectifier and single line to ground faults in a Wound Field Synchronous Machine (WFSM). In [56], the authors used the coupled field-circuit co-simulation to analyse the design of a 4kW hydro generator. In [57], the authors used the same method for analysis and comparison with experimental results of a 1kW direct drive wind turbine. A similar coupled field-circuit co-simulation was done but with different FEA software, in [58] authors used Flux2D to model a surface permanent magnet (SPM) connected to the converter modelled in Simulink. Also, in [59] the authors used the FEA software Mentor MagNet connected to Simulink to analyse the back electromotive force (BEMF) of a PMSG. In a similar manner, the author in [60] used a coupled field-circuit co-simulation to analyse a 12 pole 16kW and 20kVA wound field hydro generator connecting FEA software Maxwell and SPICE software Simplorer. The author of [61] used the Maxwell-Simplorer-Simulink co-simulation to analyse a 32 pole 120 kW PMSG. These proved the usefulness of the co-simulation method to analyse big machines too.

The research presented so far does not take into account the exact generator model and is usually based on simple linear models. Therefore, it is necessary to perform detailed tests of a small wind turbine using the coupled-field co-simulation method. In addition, there is no analysis of the behaviour of the wind turbine during demagnetization states.

1.4. Scope and thesis

The goal of the thesis is to design energy-saving permanent magnet synchronous generator for small wind turbines and analyse its properties in opened and closed control structure for various work conditions.

Additional aims of this work: is fault diagnostic and analysis during normal operation of a small wind turbine with permanent magnet generator, allowing for continuous operation of the turbine and converter, post-fault.

Thesis:

First: It is possible to design an energy-saving permanent magnet synchronous generator for small wind turbines working stable in opened and closed control structure. Application of a voltage source converter, with vector control methods, in the small wind turbine with PMSG provides a more efficient operation and lower distortion of the stator current than open control system.

Second: It is possible to achieve stable operation of an energy-saving permanent magnet synchronous generator for small wind turbine during permanent magnets faults in open and closed system.

2. Designing of energy-saving permanent magnet synchronous generator for small wind turbines

2.1. The Permanent Magnet Synchronous Generator

Even though there are many topologies for the PMSG e.g. Axial-Flux, Transverse-Flux, Radial-Flux, etc. This thesis will focus on the radial flux PMSG due to the use of an off-the-shelf stator and housing from a commercial Induction Motor (IM), the Sh90L-4 from the Celma-Indukta manufacturer [62]. The designed was based on the stator and housing of a three phase 4 pole IM. The frame, stator and winding connections were used from the IM.
A common classification of the radial PMSG, from here on referred only as PMSG, is shown in Fig. 2.1 and Fig. 2.2.

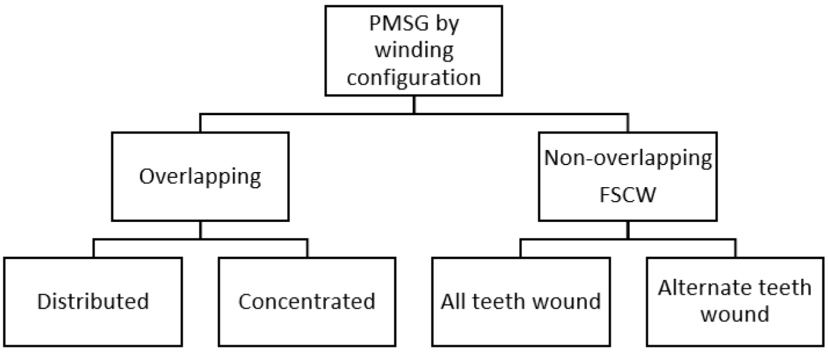

Fig. 2.1. PMSG stator topologies [63]

In this thesis the overlapping distributed stator winding is analysed using the circumferential Interior Permanent Magnet (IPM) configuration.

Relevant literature [65, 66, 67, 68, 69] shows that for slow-speed direct drive wind turbine applications a higher number of poles is desirable. This is mainly due to the fact that for low wind speed the rotor of the PMSG will also rotate slowly. For a slow mechanical speed (ω) the electrical frequency (f) is directly proportional to the number of pole pairs (p):

$$f = p\omega \tag{2.1}$$

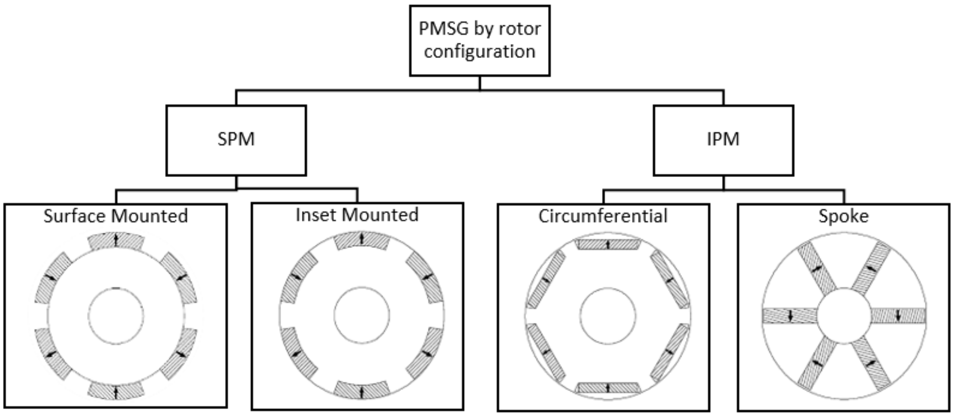

Fig. 2.2. PMSG rotor topologies [64]

Therefore, in order to acquire more energy from the wind, a slower cut-in speed is desirable, and can be obtained by having more poles on the rotor. Also, the inclusion of a gearbox to multiply the mechanical speed adds losses which lower the overall system efficiency [68]. Nevertheless, advances in gearbox technology e.g. Continuous Variable Transmission (CVT), Infinitely Variable Transmission (IVT) and magnetic gears [70, 71, 72, 73, 74], may return focus to machines with a small number of poles for wind turbine applications.

On the other hand, an additional advantage of using an IM as a basis of the PMSG is the high reliability of these type of machines due to standard manufacturing processes and mass-production.

In comparison, non-standard manufacturing processes have shown to be a source of faults (low reliability) in high power wind turbines [75] and in low power SWTs [76], with new designs of direct drive multiple-poles generators.

2.2. Rotor design

For the design of the PMSG some geometric constraints are given by the stator and housing of the IM used as basis for the project. As stated before, a Sh90L-4 IM stator and housing were used for the PMSG. The parameters of the IM are presented in Table 2.1.

The air gap of the PMSG is 0.5 mm and therefore the rotor has 81 mm diameter with the same 30 mm diameter shaft. The Sh90L-4 IM has a 0.3 mm air gap, but is common for the permanent magnet machines to have bigger air gap [15].

Previous works [77, 78, 79, 80] have shown that the W shape as pattern for the rotor magnets has high back EMF magnitude and low total harmonic distortion (THD) of back EMF.

During the last 3 decades, permanent magnet (PM) machines have gained popularity due to advances in high energy density product (BH_{max}) rare-earth PM materials, like neodymium-iron-boron (Nd-Fe-B) and samarium-cobalt (Sm-Co) [81, 82, 83, 84]. For the

Table 2.1. Sh90L-4 IM parameters. Data from [62]

Phases	3
Nominal power	1.5 kW
Nominal speed	1410 rpm
Nominal frequency	50 Hz
Nominal current	3.5 A
Nominal torque	10.16 Nm
Number of poles	4
Stator Slots	36
Shaft diameter	30 mm

design exploration, 18 mm by 4 mm by 30 mm rectangular cuboid N38SH Neodymium magnets were available for the project.

Due to the space constraints and the price of neodymium magnets the Honsinger's approach [85] was applied to minimise the use of permanent magnets. In this configuration, called *induced pole* in [77], the flux is focused towards the air gap in the adjacent poles, to obtain a heteropolar structure, this eliminates the need of more magnets in the adjacent region. So that the 2 pole pair machine (4 poles total), only two poles located in alternate positions would require magnets, because the flux re-distribution automatically generates the other two poles, this decidedly reduces the total number of magnets needed. This is effect is better shown in Fig. 2.3, the magnetic field intensity **H** closes itself over the sides of the rotor generating 4 poles (2 pole pairs).

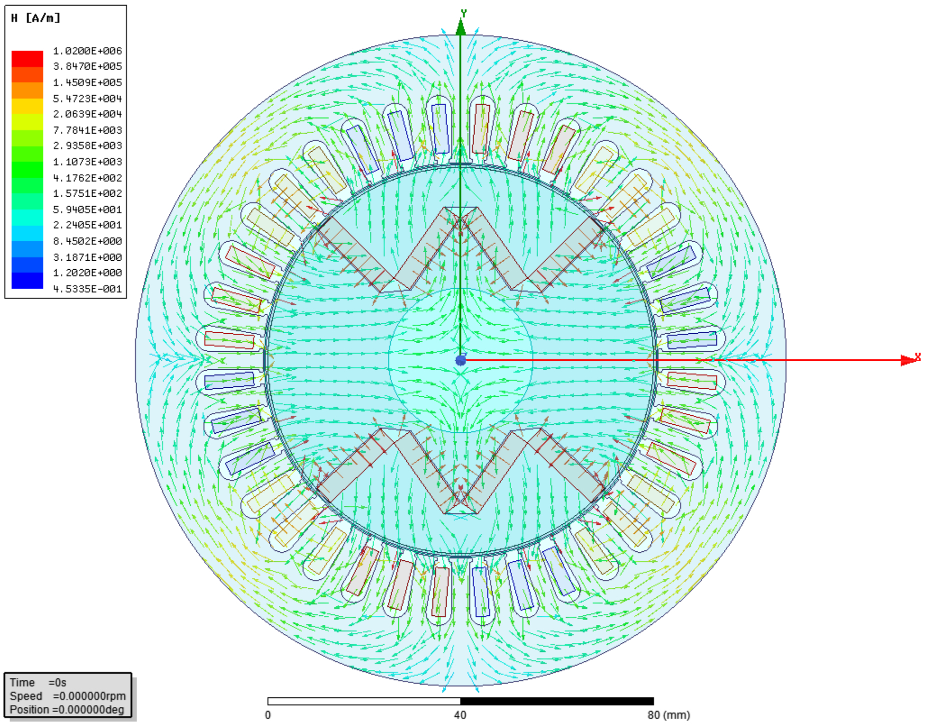

Fig. 2.3. Magnetic field intensity vector **H** distribution over the induced pole rotor

2.2.1. Parametrization

In Fig. 2.4 the rotor is presented with the design space delimited by the shaft (inner circle) and the dotted line. This limit is given by the rotor diameter of 81 mm (outer circle) minus a *bridge* or small part of the steel sheet lamination that will hold the magnets inside the rotor. The minimum size for this bridge is given by the mechanical strength of the steel sheet from which the rotor laminations are cut, also from the saturation due to the magnetic flux density since the flux should go through the stator and not through the bridge.

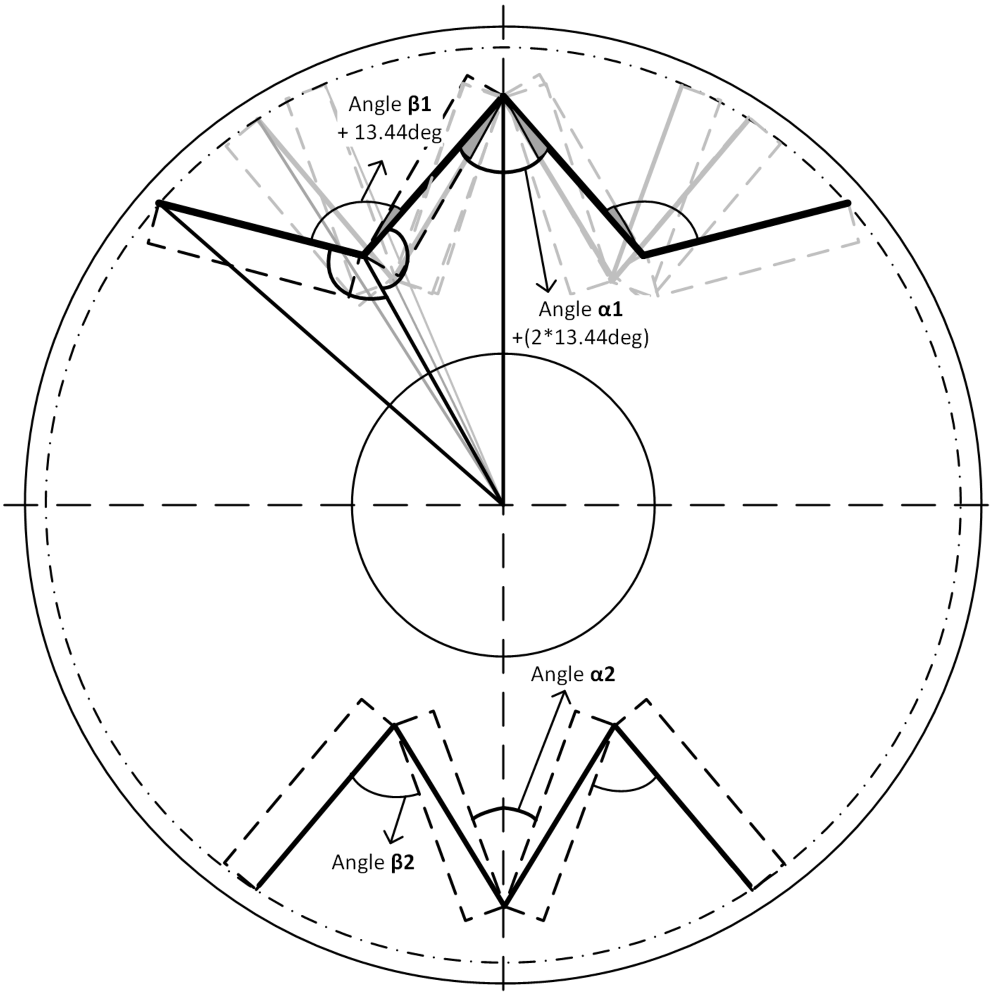

Fig. 2.4. Angle variations for the W shape in the rotor

For this project a 0.5mm bridge was chosen as constraint for the design space, also because the rotor laminations were cut by laser on a computer numerical controlled (CNC) machine whose precision is about ±0.1mm. This distance is later analysed by stress calculation in FEA software to ensure a proper safety factor.

Also in Fig. 2.4, a relation between angle α and angle β is shown. These are angles between the magnets which form the W shape. In order to obtain the maximum flux density through the stator the tip of the outer magnets in the W shape should be coincident with the dotted line.

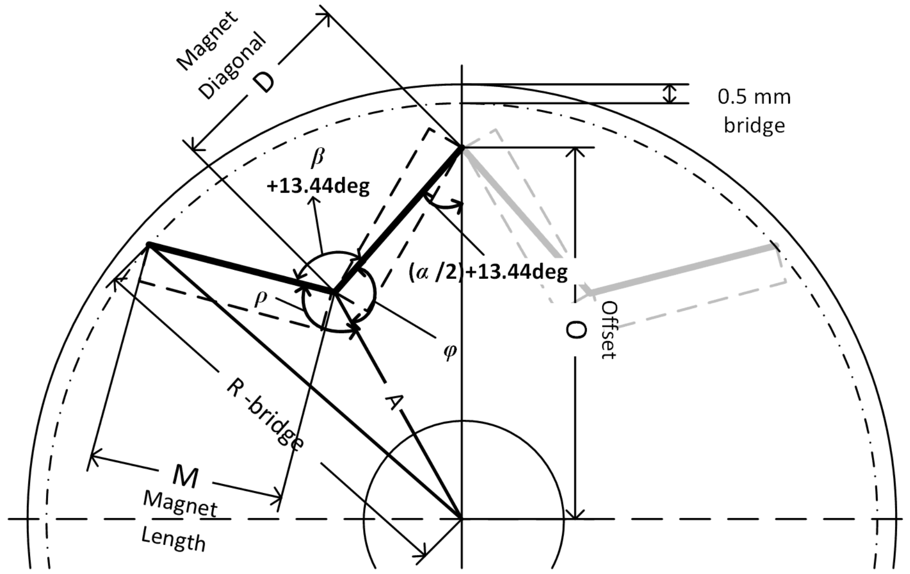

Fig. 2.5. Parametrization of the W shape

From figures 2.4 and 2.5, a relation between angle $\boldsymbol{\alpha}$ and $\boldsymbol{\beta}$ can be found. Notice in Fig. 2.5 that the magnet length and magnet diagonal are fixed by the available cuboid magnet's size.

Therefore, to find the angle $\boldsymbol{\beta}$ that assures the coincidence between the outer magnet tip to the dotted line, given angle $\boldsymbol{\alpha}$, first it has to be calculated:

$$A = \sqrt{D^2 + O^2 - 2(D)(O)\cos\left(\frac{\boldsymbol{\alpha}}{2} + 13.44\,\mathrm{deg}\right)} \tag{2.2}$$

Where A is the distance from the centre to the vertex of the two magnets, D is the magnet diagonal length, O is the offset or distance from the rotor centre to the centre of the W as shown in Fig. 2.5. In Eq. 2.2 only angle $\boldsymbol{\alpha}$ and the offset O are subject to optimisation. Once A is obtained, the angle $\boldsymbol{\phi}$ is calculated as:

$$\boldsymbol{\phi} = \cos^{-1}\left(\frac{D^2 + A^2 - O^2}{2DA}\right) \tag{2.3}$$

And the angle $\boldsymbol{\rho}$ as:

$$\boldsymbol{\rho} = \cos^{-1}\left(\frac{M^2 + A^2 - (R - bridge)^2}{2MA}\right) \tag{2.4}$$

Where M is the magnet length, R is the rotor radius and $bridge$ is the aforementioned amount of lamination necessary to hold the magnets inside. Finally the angle $\boldsymbol{\beta}$ is obtained as:

$$\boldsymbol{\beta} = 360\,\mathrm{deg} - 13.44\,\mathrm{deg} - \boldsymbol{\phi} - \boldsymbol{\rho} \tag{2.5}$$

From equations 2.2 to 2.5 it can be found that $\boldsymbol{\beta}$ only depends on the offset O and angle $\boldsymbol{\alpha}$, since all the other lengths are fixed.

2.3. Symmetric vs Asymmetric rotor magnet's configuration

In Fig. 2.6 two rotor geometries are shown depicting the difference between the symmetric and the asymmetric geometries. Notice that for the asymmetric case the lower half of the rotor stays the same and the upper half is varied according to the sweep analysis, explained in the next section.

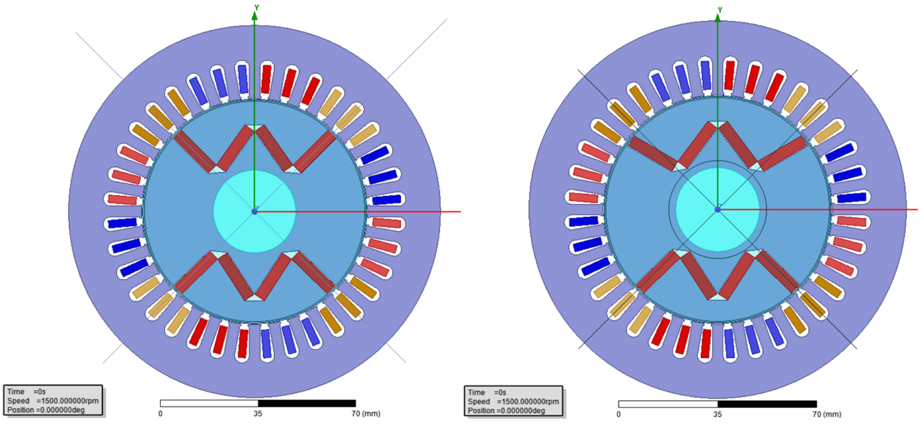

(a)

(b)

Fig. 2.6. Comparison of the a) symmetric geometry, b) asymmetric geometry

The end effect of this difference between the symmetric and asymmetric cases can be observed in Fig. 2.7, here even though some teeth seem to be saturated by the magnetic flux density, the distribution over all the phase's teeth is still appropriate.

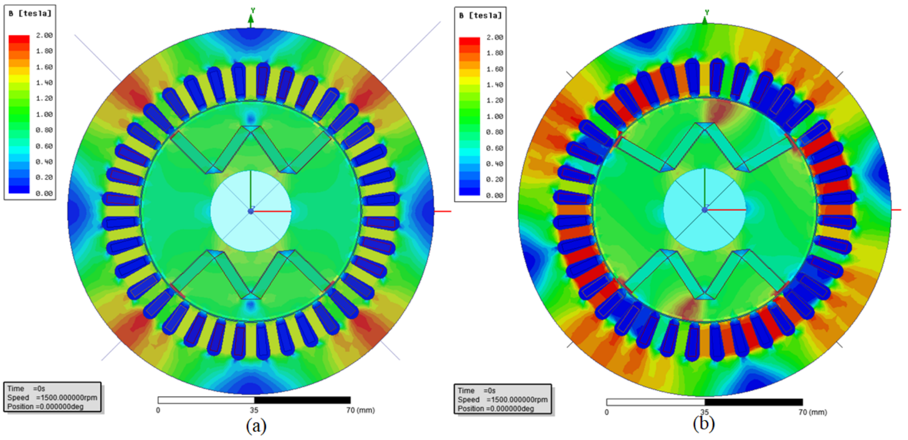

(a)

(b)

Fig. 2.7. Comparison of the magnetic flux density B in a) symmetric geometry, b) asymmetric geometry

2.4. Finite Element Analysis

To find the maximum induced voltage (back EMF) with the W shape with the given geometric constraints a sweep analysis was performed using the finite element method (FEM) for electromagnetic fields. In Fig. 2.8 the results of the sweep analysis are shown.

It is noticeable that with 66 degrees in α the back EMF is the highest. Therefore, an asymmetrical study was also performed. In the asymmetrical sweep one W had the α angle fixed at 66 degrees while the other W (the lower one in Fig. 2.6a) was modified. For both cases an offset of 30 mm was used.

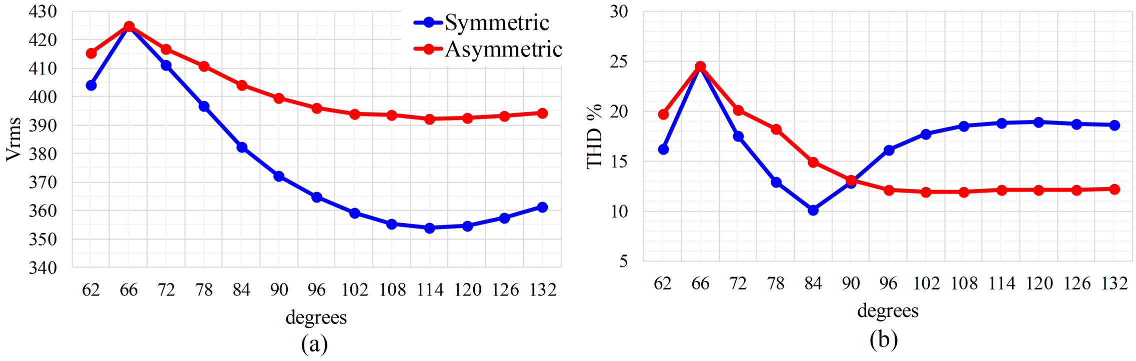

Fig. 2.8. Sweep analysis of angle α with 1500 rpm: a) Line voltage at no load (back EMF), b) THD in percentage of the fundamental frequency (50 Hz)

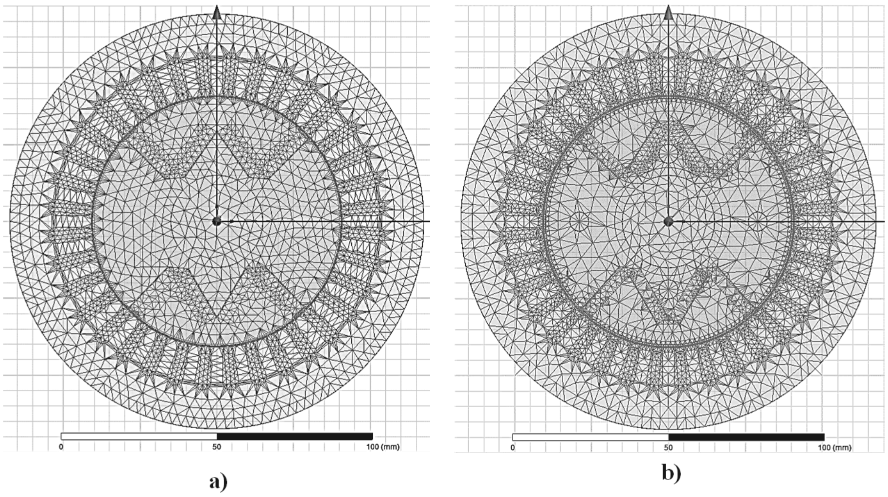

Fig. 2.9. Mesh for the 2D FEA models: a) reduced detail (7 644 elements) b) full detail (10 052 elements)

In Fig. 2.9 the mesh for the 2D FEA model is shown. Notice that due to the symmetrical and asymmetrical analysis, a full rotor and stator model was used in the calculations.

This model was run in transient analysis at 1500 rpm without load (open circuit), in order to analyse the Fast Fourier Transform (FFT) of the back electromotive force (EMF). The obtained FFT of the back EMF was then used for the THD calculation shown in Fig. 2.8 b.

A comparison of the THD for the symmetric and asymmetric can be done with Fig. 2.10 and Fig. 2.11 . Notice that in the symmetric geometry case (Fig. 2.10) the 17th harmonic tends to have higher magnitude than in the asymmetric geometry. Also, in the asymmetric geometry case (Fig. 2.11) the 3th harmonic is the highest in every variation.

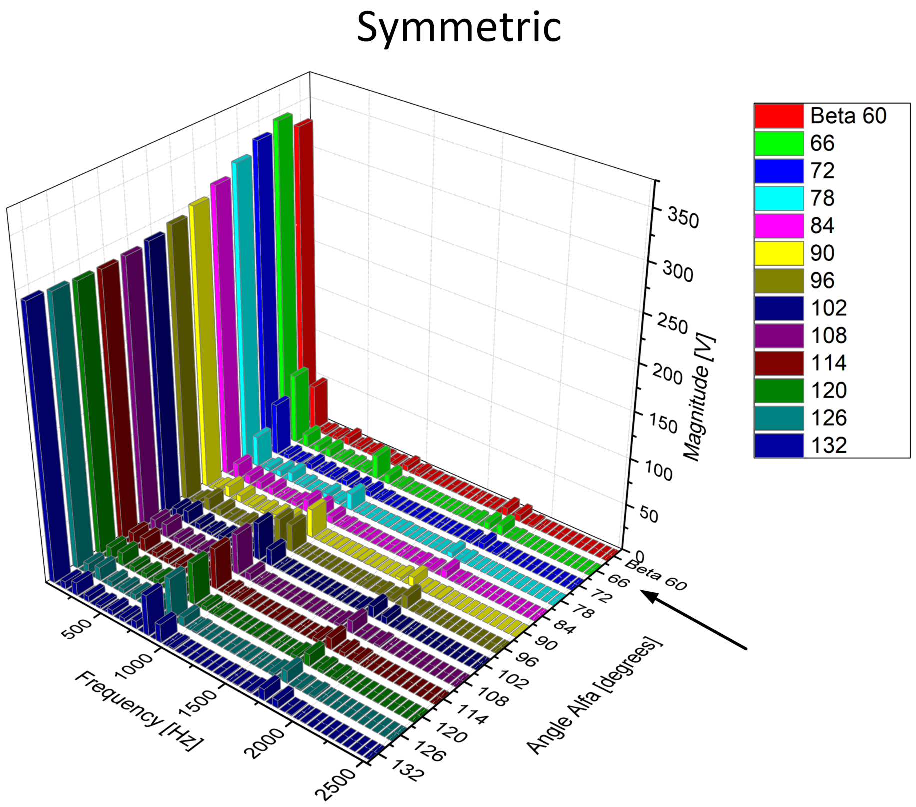

Fig. 2.10. Harmonic content comparison for the symmetric geometry. Arrow indicates the highest V_{rms}

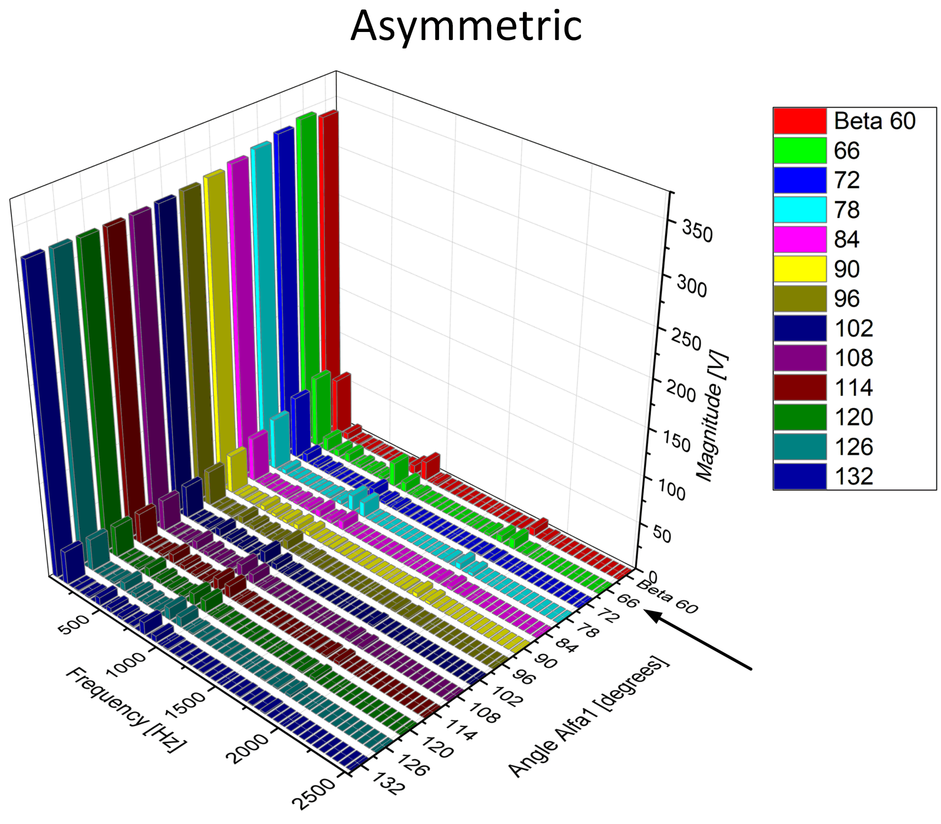

Fig. 2.11. Harmonic content comparison for the asymmetric geometry. Arrow show the highest V_{rms}

In Fig. 2.12 the comparison between the FEA calculated Back EMF and the open circuit measurements is shown. Very good agreement between measurements and FEA results were obtained. Also in Fig. 2.13 a loaded case is shown. Also here good agreement was found between measurements and FEA calculations.

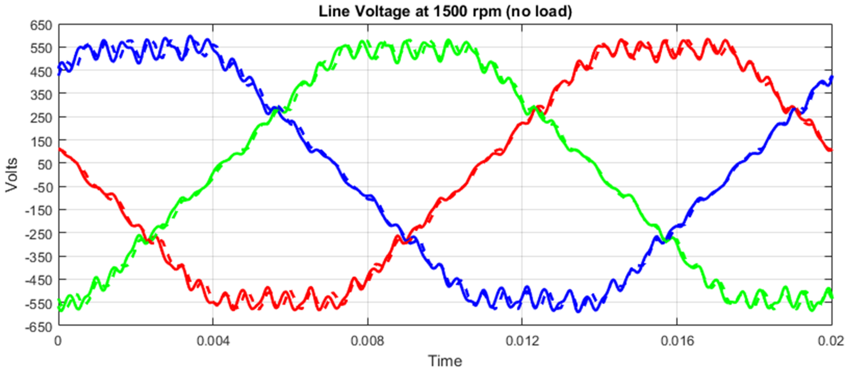

Fig. 2.12. Back electromotive force BEMF. Solid lines are from open circuit measurements and dashed lines are from transient analysis in FEA

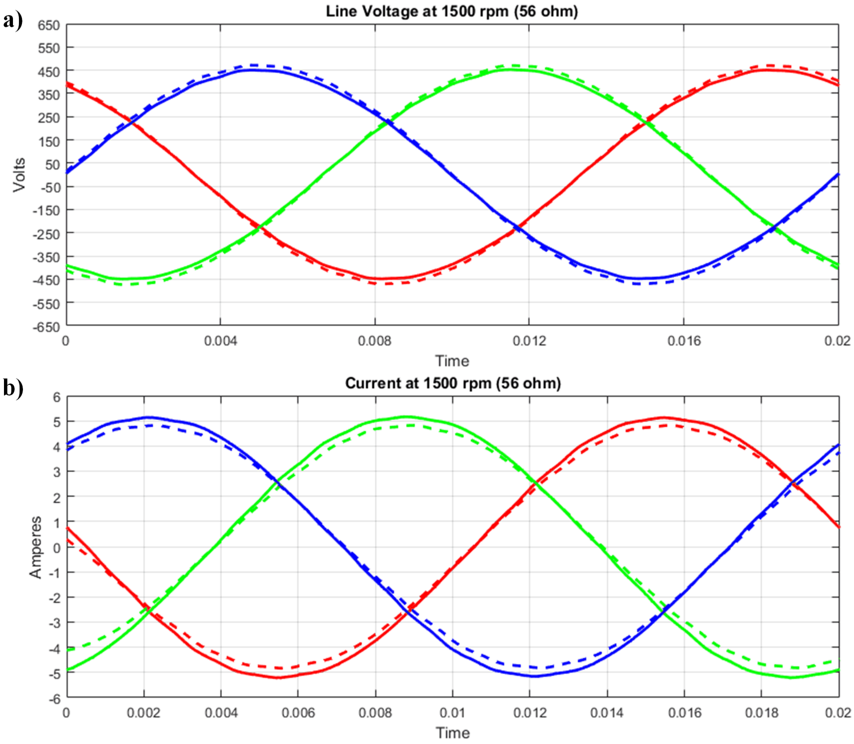

Fig. 2.13. Comparison between FEA results and measurements with 56 ohm load for a) line voltages and b) currents. Solid lines are measurements and dashed lines are from FEA

2.5. Mechanical design considerations

In Fig.2.14 the isometric view of the rotor is shown. Notice that it uses 4 threaded rods with hex nuts at both ends. Two of these rods are for holding the steel sheets together, the other two are for holding the end plates at each end of the rotor stack.

Fig. 2.14. Isometric view of the built rotor without magnets

As mentioned in section 2.2 the space between the tip of the outer magnets and the air gap is determined by two factors. The first one, is the precision of the laser cutter with which the prototype was manufactured. The second is the mechanical strength at high speed rotation at which the generator may operate (1.2 times the maximum speed of 3000 rpm according to norm IEC 60034 part 1). The stress on that space of the steel lamination, called bridge, must be calculated to ensure a proper safety factor.

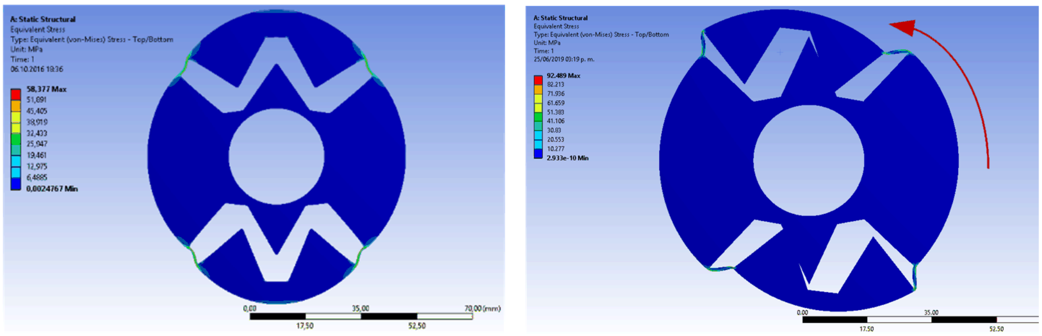

(a) (b)

Fig. 2.15. Results of the mechanical FEA, with rotor spinning at 3600 rpm (a) and with a 15 Nm tangential torque (b)

In Fig. 2.15 the results of the rotor spinning at 3600 rpm is shown. No area was over 70 MPa. An additional analysis with a tangential moment of 15 Nm and fixed shaft gave as a result a 92.5 MPa. The maximum yield strength of the M400-50A steel is 325 MPa [86]. With a safety factor equal to 2 allows a maximum strength of 162.5 MPa. This clearly demonstrates that the bridge will withstand the centrifugal forces of the generator spinning inside the nominal speed range and even in the flux weakening region.

2.6. Generator validation

As shown in the previous sections the generator measurements have very good agreement with the FEA calculations. In Fig. 2.16 the test bench for the machine validation is shown.

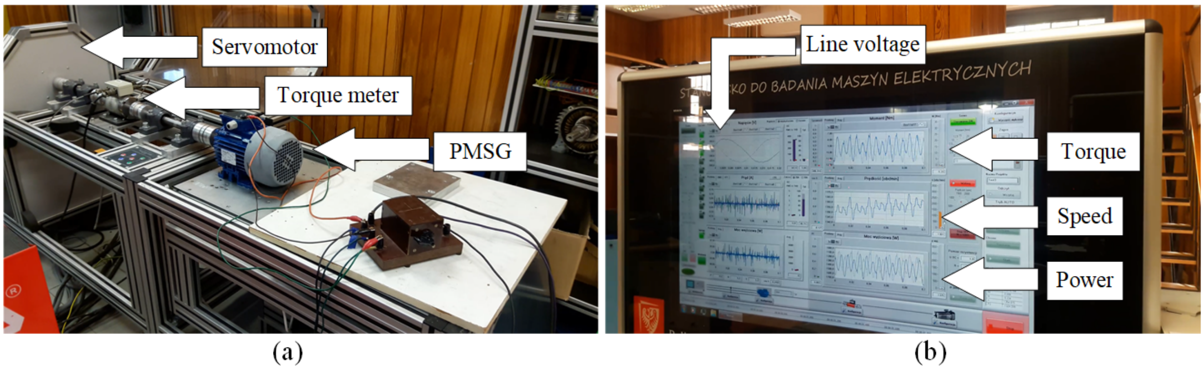

Fig. 2.16. Test bench with servomotor and torque transducer (a), and data acquisition panel (b)

From Fig. 2.17 and Fig. 2.18 a comparison between the harmonics from the FEA calculations and harmonics of the back EMF measurements can be done.

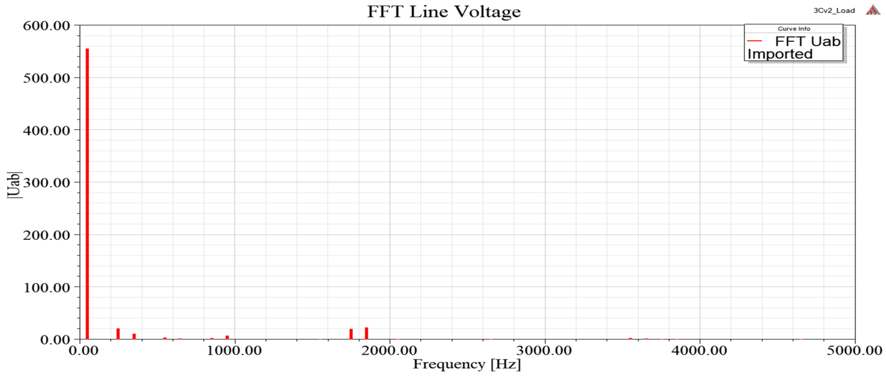

Fig. 2.17. ANSYS Maxwell FFT of the FEA line voltages at 1500 rpm with no load

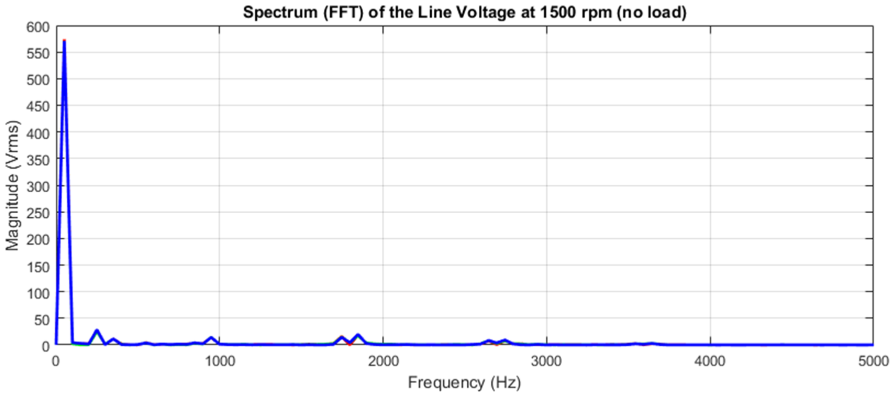

Fig. 2.18. FFT of the line voltages measured at 1500 rpm with no load

Notice in Fig. 2.17 and 2.18 the similitude with the chosen configuration in Fig. 2.11, the selected geometry configuration has a THD of 25% (see Fig. 2.8b) but also a high back EMF.

In Fig. 2.19 the calculated efficiency map of the generator is shown. Notice that the calculated maximum efficiency is about 90%. This was corroborated by laboratory measurements also shown in Table 2.2. These measurements were done only with a 3 phase resistor (56 ohm).

Table 2.2. Results of the W generator at 1500 rpm and 56 ohm load

	P_{mech} [W]	Line Voltage [V$_{rms}$]	Current per phase [A$_{rms}$]	$P_{electrical}$ [W]	Efficiency [%]
FEA	2530	320	3.603	2275	89.0
Measurements	2530	316	3.661	2250	88.9

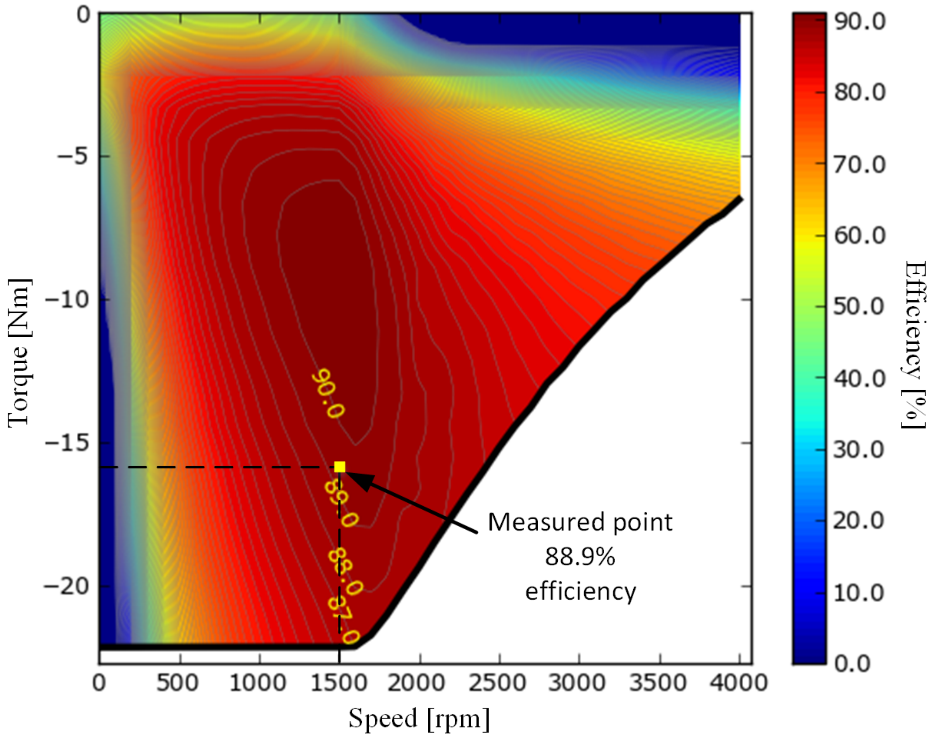

Fig. 2.19. FEA calculated efficiency map for the W generator

Notice that Fig. 2.19 was calculated using the Maximum Torque Per Ampere (MTPA) strategy, which, in the generator case, is obtaining the maximum current at each given torque. The calculations were done also for speeds higher than the nominal (flux weakening region).

In Fig. 2.20 the measurements of efficiency at constant 1500 rpm are shown. Notice that the input power goes from 200 to 2390 W, this roughly corresponds to the torque from 2.5 to 15 Nm, in other words a straight line at 1500rpm in Fig. 2.19. Also notice that the efficiency curve goes well with the straight vertical line over 1500 rpm in Fig. 2.19.

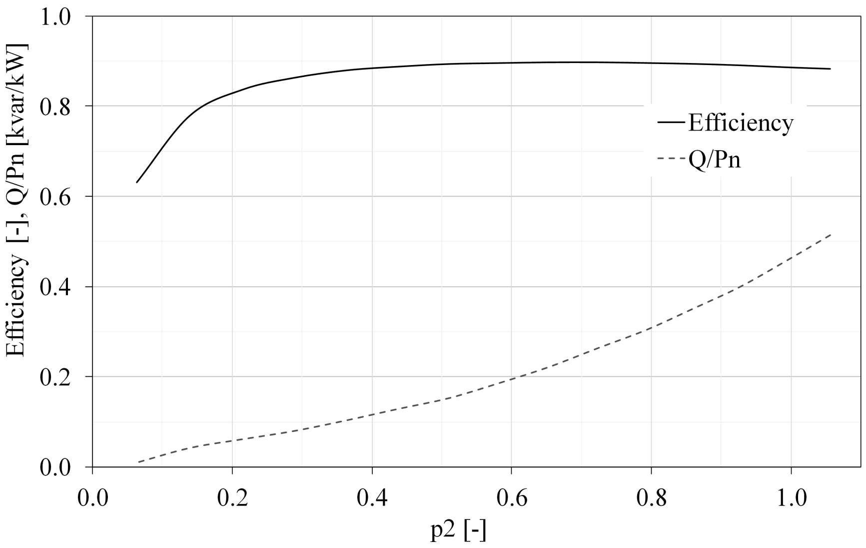

Fig. 2.20. Efficiency curve at nominal speed (1500 rpm) and reactive to active power ratio with input power from 200 to 2390 W

In Fig. 2.21 the output power calculated by FEA is shown. Notice that according to Fig. 2.21 the generator should be able to provide even 3 kW of electricity in high wind conditions.

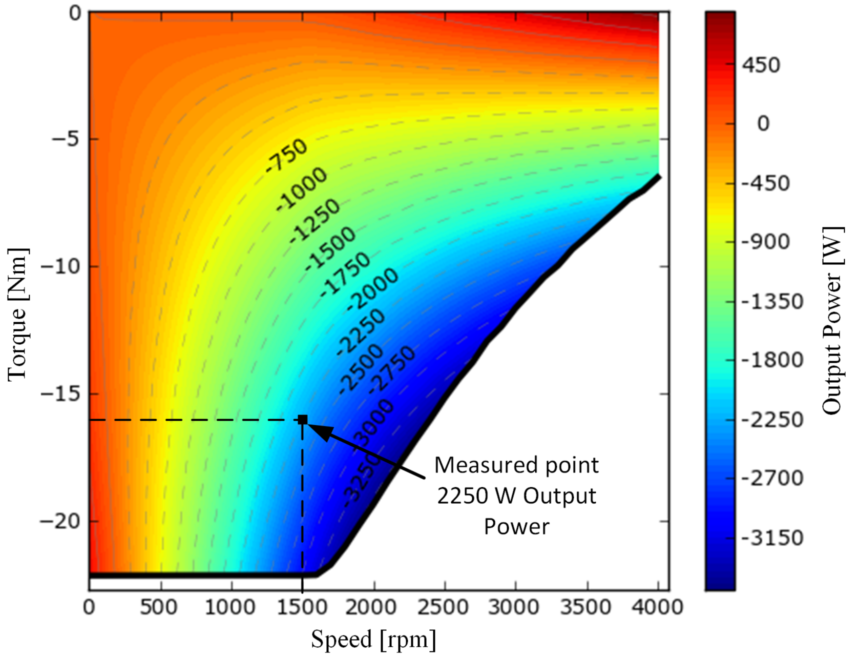

Fig. 2.21. Output power for the FEA calculation of the efficiency map

Also, in Fig.2.22 the current obtained from the generator, using the maximum current per torque optimisation, show that the maximum current that can be obtained from the generator is less than 5 amperes. This is particularly useful because the stator wingdings are designed to withstand continuous current of 6 amperes maximum.

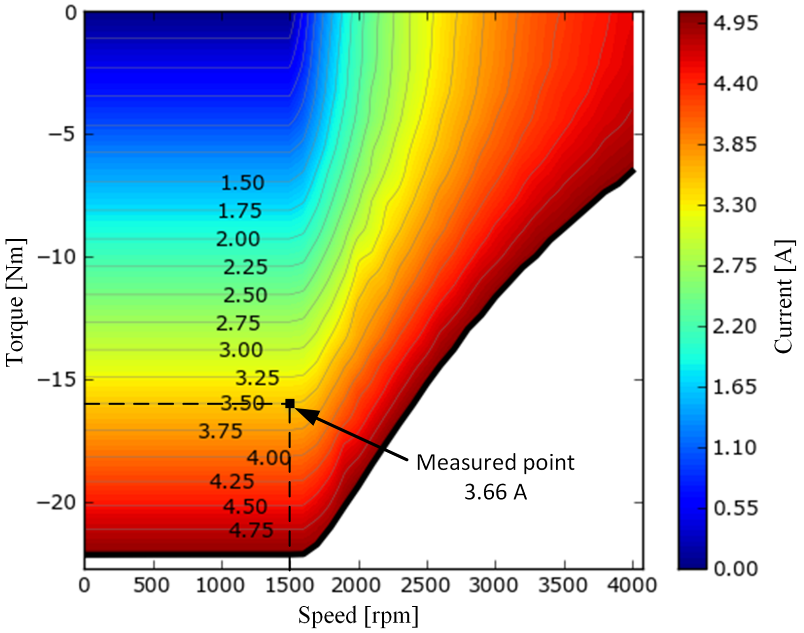

Fig. 2.22. Currents obtained from the generator using MTPA

Lastly in Fig. 2.23 the torque ripple at different operating points is shown. Notice that for the measured operating point the torque ripple should be around 2.6 Nm, taking into account that the generator is operating with 16 Nm of torque this ripple corresponds to 16.2% of the input torque. Further analysis were done in order to corroborate this parameter.

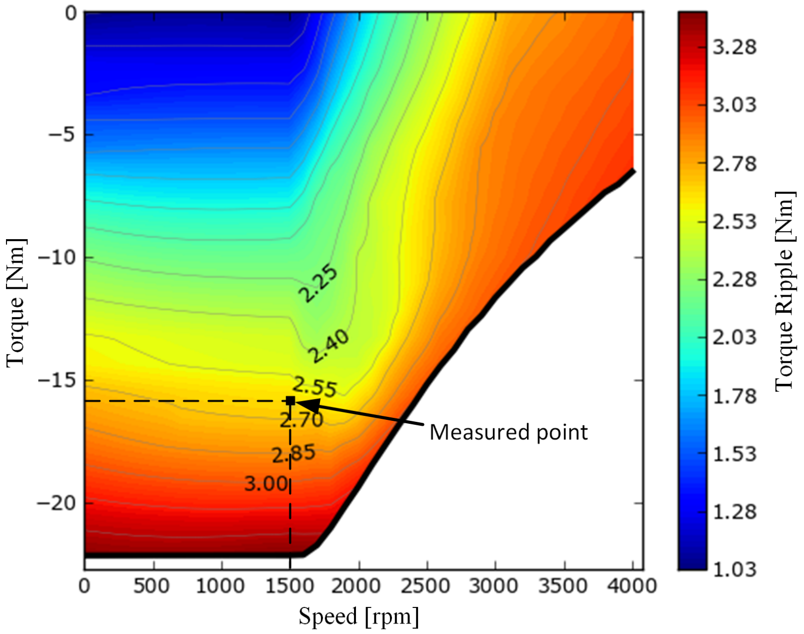

Fig. 2.23. Torque ripple map obtained from FEA

In Fig. 2.24a measured torque of the generator at 1500 rpm and 3.7 Arms shows a bigger ripple torque than in Fig. 2.24b the transient FEA for 1500 rpm is shown.

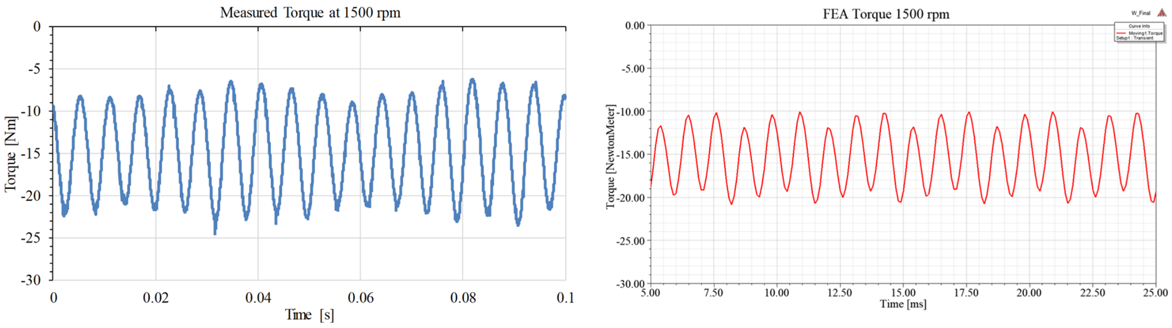

(a) (b)

Fig. 2.24. Torque ripples at 1500 rpm with 56 ohm load per phase, measured (a), and from FEA (b)

It is important to mention that the torque pulsations shown in Figures 2.24a and 2.24b are a combination of the cogging torque (torque due to the magnets alignment with the stator teeth) and load dependent torque (due to stator tooth geometry and winding currents). Therefore the discrepancies between FEA and measurement could be linked to the difference in load resistance i.e. contact resistance, and also to the torque pulsations of the driving machine.

In Figures 2.25, 2.26, 2.27, 2.28 and 2.29 the line voltages and phase currents for the PMSG connected to a linear load (resistor) and being rotated at different speeds, are presented. Notice in Fig. 2.25a the similitude between the measurements and FEA results. In Fig. 2.25b the currents show some discrepancy between measurements and FEA results but the shape of the waveform is still very similar to the measured one. Note that almost in all cases the currents showed a bigger discrepancy than the voltages.

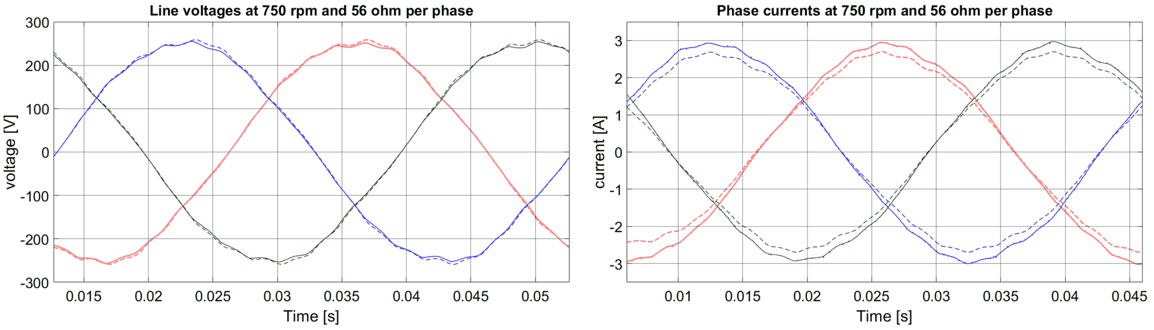

(a) (b)

Fig. 2.25. Pure resistive load at 750 rpm Line voltages 178 V_{rms} (a), and Phase currents 2.05 A_{rms} (b) the measured output power is 708 W. Solid line measurements, dashed line FEA results

In Fig. 2.26,´again, some discrepancy between the FEA results and measurements is visible but in general the waveforms are similar. Also notice that Fig. 2.26 is very similar to Fig. 2.13 shown in section 2.4.

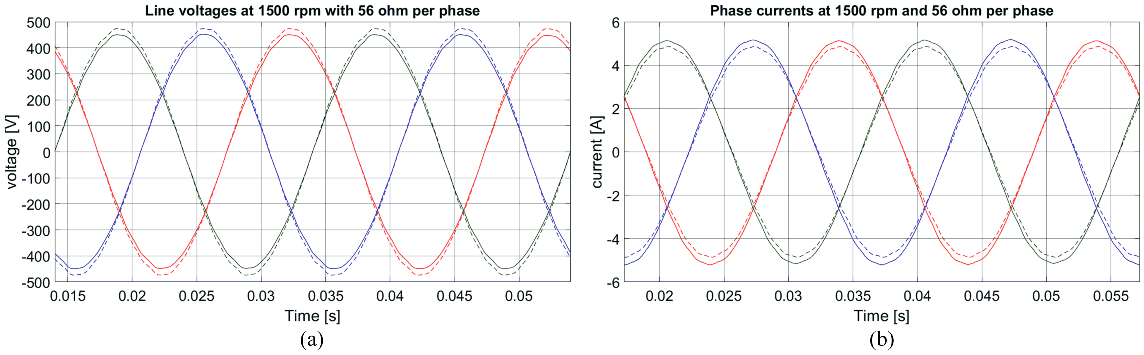

(a) (b)

Fig. 2.26. Pure resistive load at 1500 rpm Line voltages 316 V$_{rms}$ (a), and Phase currents 3.66 A$_{rms}$ (b) the measured output power is 2250 W. Solid line measurements, dashed line FEA results

Figure 2.27 also was measured with three 56 ohm resistors at a lower speed. The currents in Fig. 2.27b show bigger discrepancy than the voltages.

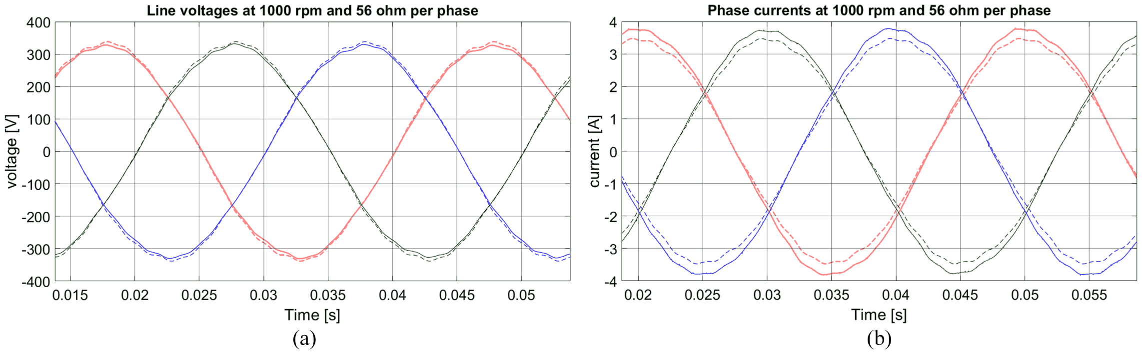

(a) (b)

Fig. 2.27. Pure resistive load at 1000 rpm Line voltages 239 V$_{rms}$ (a), and Phase currents 2.7 A$_{rms}$ (b) the measured output power is 1248 W. Solid line measurements, dashed line FEA results

For a very slow rotational speed (250 rpm) Fig. 2.28 shows that the voltages are very similar between measurements and FEA and the currents have almost the same waveform.

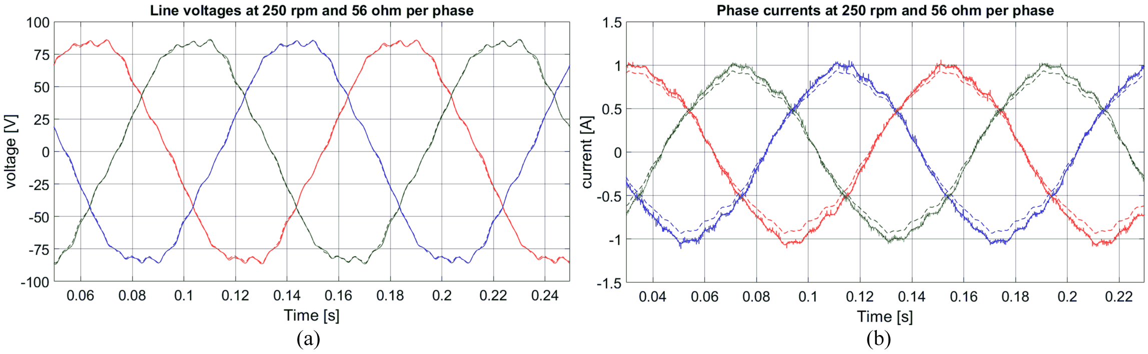

(a) (b)

Fig. 2.28. Pure resistive load at 250 rpm Line voltages 63 V$_{rms}$ (a), and Phase currents 0.721 A$_{rms}$ (b) the measured output power is 80 W. Solid line measurements, dashed line FEA results

The results presented in Fig. 2.29 demonstrate that the PMSG has the possibility to be operated in powers close to 2500 W with currents over 4 A$_{rms}$. As it was shown in [87] a similar machine (also based on the Sh90-L4) reached 75°C at the rotor and 64°C at stator windings operating with 3.4 A and 1900 W. Taking into account that the stator is the same and the machine analysed in [87] has a copper cage in the rotor (bigger rotor losses), then the temperatures in steady state (after 1.5 hours) should be around the same values (∼80°C).

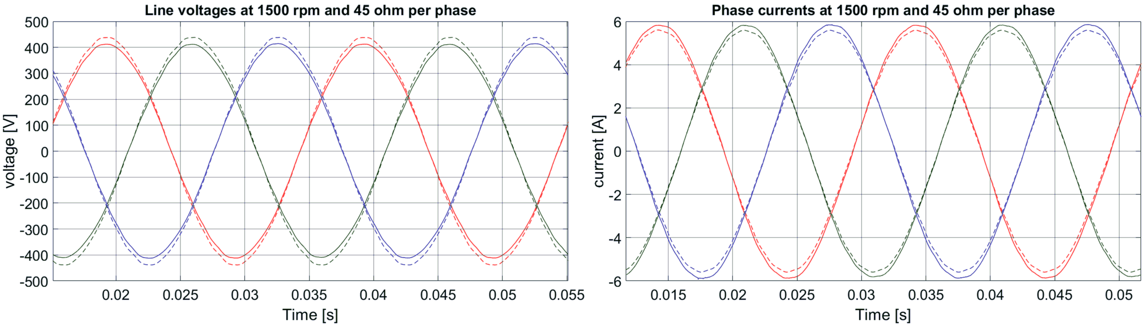

(a) (b)

Fig. 2.29. Pure resistive load (45 ohm per phase) at 1500 rpm Line voltages 291 V$_{rms}$ (a), and Phase currents 4.16 A$_{rms}$ (b) the measured output power is 2352 W. Solid line measurements, dashed line FEA results

From the results shown in this section and further results that will be presented in Chapter 6, it can be said that the FEM for analysing the behaviour of the PMSG under different operating conditions deliver very similar results as the measurements from the real constructed machine.

3. Demagnetization

Permanent magnet synchronous machines have been gaining importance in the last two decades due to the advancements in material science related to the maximum energy density (BH_{max}) of hard magnetic materials with linear magnetisation B-H curve [88], this characteristics allowed the machines to have higher efficiency and to be more compact [89]. On the other hand, rare earth magnets with the highest energy density (Nd-Fe-B) also have temperature dependent magnetisation curves with knee points at lower coercivity than other materials [15], this means that Nd-Fe-B magnets can suffer irreversible demagnetization or partial demagnetization at temperatures higher than ambient temperature (higher than 40°C). Early attempts to include such demagnetization effects in the analysis of electrical machines can be found in [90] where the authors included a d-q axis (rotating reference frame) inductance computation loop additional to the finite element analysis (FEA), in [91] the authors included one B-H curve for the 2D finite element analysis (FEA) of a single phase line-start permanent magnet synchronous machine (LSPMM). A B-H curve is presented in Fig. 3.1, notice that demagnetization occurs in the 2nd and 3rd quadrant.

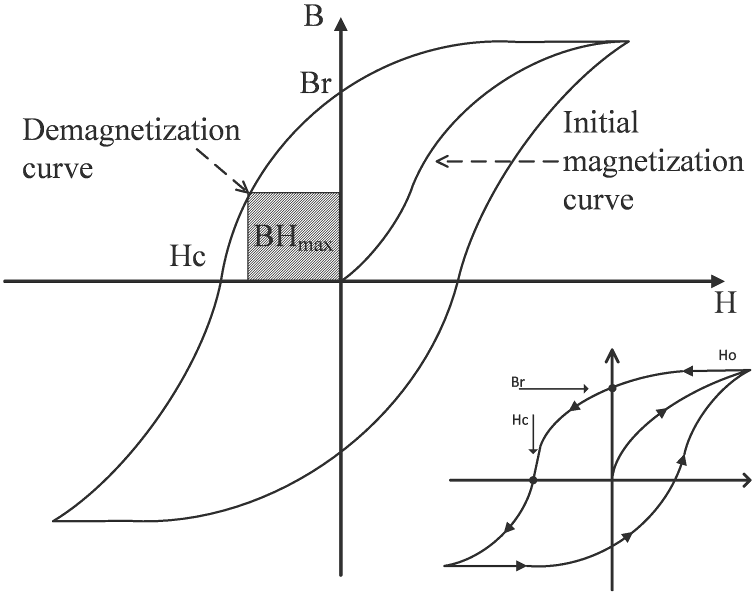

Fig. 3.1. Hysteresis loop with initial magnetization B-H curve. In the second quadrant coercivity Hc and remanence Br

In [92] the authors make a comparison between the demagnetization models implemented in FEA with one B-H curve measurements, in [93] the authors explain the interdependence of demagnetization, load, and temperature rise in a permanent magnet synchronous machine (PMSM) with two B-H curves for 20°C and 190°C in a special FEA software developed in the Helsinki University of Technology. In [94] the authors demonstrated an algorithm to implement the nonlinear characteristic using only the normal B-H curve as an input of the time-stepping field-circuit coupled FEA (dynamic computation of the B-H curve for the operating point). The first time the temperature-dependent demagnetization model was implemented inside of a commercial FEA software is reported in [95] by the software company ANSYS, here the authors included the effects on the electromagnetic torque with no demagnetization model, including a demagnetization model, and including a temperature dependent demagnetization model in a 3D transient FEA of a 50kW IPM motor. The same company (formerly known as Ansoft) included the interaction between the field-circuit coupled time stepping simulation and a Simulation Program with Integrated Circuit Emphasis (SPICE) for the paper from [37] the SPICE software was Simplorer.

In the literature, some early analysis done with the FEA demagnetization model can be found in [96] where the authors analysed three different IPM rotor configurations with same volume of PM per pole, the demagnetization model was analysed at 150°C but the model was not temperature dynamic (only one B-H curve). In [97] the authors used a self-developed model that is dynamically-temperature-dependent (the B-H curve is calculated at each iteration), this was done inside the Ansys software environment but was not general or commercially available in the software. In [98] the authors applied a nonlinear anhysteretic approximation of the soft magnetic material behaviour, called the Marroco equation. There, the recoil line is calculated with the parameters determined by fitting procedure of the original B-H curve. In Fig. 3.2 many B-H curves (different temperature) are shown for the N38 and N38SH magnets. Notice that N38SH has more dysprosium therefore is much more expensive.

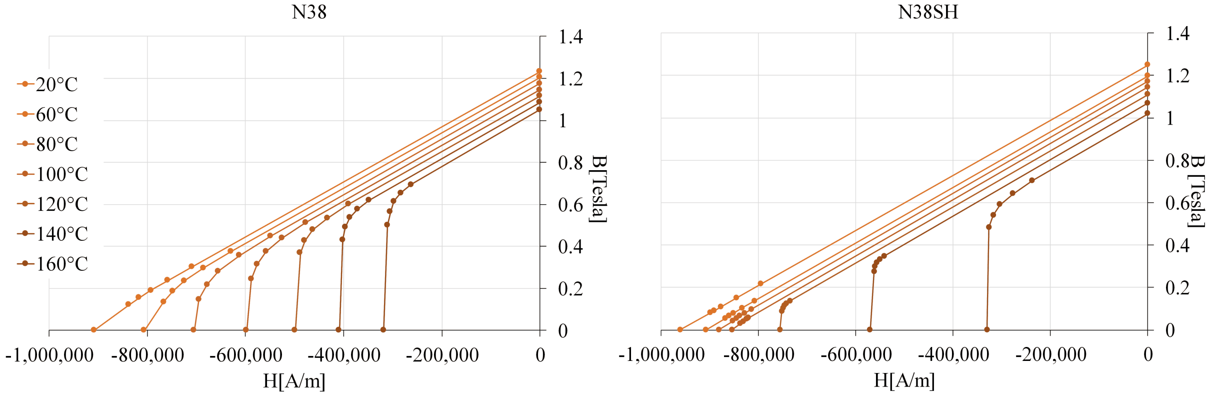

(a)

(b)

Fig. 3.2. Second quadrant B-H curve for Nd-Fe-B magnets N38 (a), and N38SH (b) data from [99]

3.1. Validation of the models

In [100] the authors tested the FEA demagnetization model with a self-made fixture, namely a laminated iron core with 423 turn coil of 6 mm^2 copper cable. The steel was characterised in an Epstein frame and its hysteresis curve included in the simulation, the tested magnets were Samarium Cobalt (SM30L) with remanence (Br) of 1.1 Tesla and a BH_{max} of 235 kJ/m^3. The magnets were demagnetized with a 30 A current pulse (12690 A-turns) at 20°C for comparison purposes with very good accordance between the experiment and 2D FEA software (COMSOL).

Another test fixture was done in [101] for demagnetizing N48H Nd-Fe-B magnets, these have a remanence of Br=1.38 Tesla. The magnets were demagnetized applying a 0.6 second current pulse on the windings of the laminated C core at 20°C room temperature. The fixture was rated to generate a demagnetizing magneto motive force (MMF) of 10800 A-turns with a 20 AWG (53.47 mm^2) cable. Good accordance was obtained between experiments and 3D FEA software (JMAG).

Even before these validations were published some authors used the FEA demagnetization model to assess the PM machine performance after partial demagnetization. The first reported FEA with demagnetization was [102] where authors analysed a 6 pole IPM machine with inter-turn short circuit fault at 150°C, the authors employed a temperature chamber in order to verify the FEA results. In [103] the authors analysed different geometries of the IPM with distributed winding and fractional slot concentrated winding (FSCW) a constant operating temperature (180°C) is assumed and a demagnetizing MMF of 1090 A-turns is used in the JMAG FEA software. In [104] the post-fault performance of a 6 phase 8 pole FSCW IPM is compared to experimental validation, the estimated magnet temperature of the 16 magnets (N35EH) was 194.8°C. Finally, in [105] the authors analyse the demagnetization through FEA model of a hybrid vehicle with 8 poles single layer distributed winding with inter-turn short circuit fault at 150°C operating temperature.

In [106] the authors make a comparison of the linear and exponential demagnetization models against temperature controlled measurements.

3.2. Operating point

In Fig. 3.3 three operating points over the 80°C curve are shown. The difference between these depend on the magnet shape. Notice the that the slope of the line crossing the BH curve (load line) is calculated as:

$$\mu_L = \frac{B_d}{\left(H_d - \frac{NI}{l_{PM}}\right)} = P_{sys}\frac{l_{PM}}{a_{PM}} \tag{3.1}$$

where μ_L is the permeance coefficient, B_d is the operating-point's magnetic flux density, H_d is the permanent-magnet's field intensity, N is the number of turns in the coil, I is the current in amperes, l_{PM} is the length of the permanent magnet, P_{sys} is the system's permeance, and a_{PM} is the permanent-magnet's area transverse to the magnetic flux. These are important figures of merit when designing a permanent magnet machine since as explained before the volume (mass) of rare earth's PM impacts directly on the machine cost.

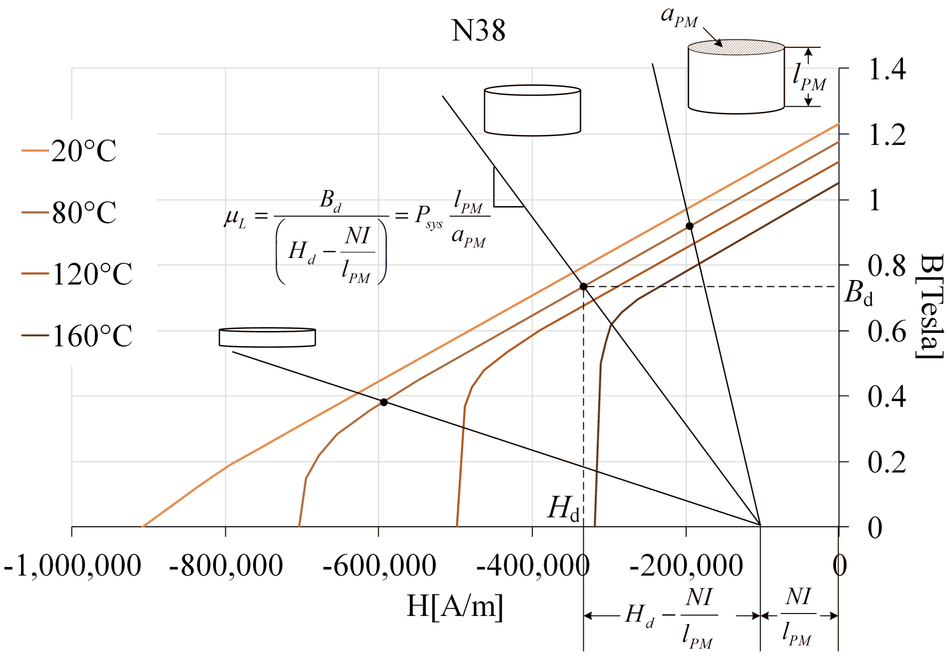

Fig. 3.3. Three operating points for three different permeance coefficients

In Fig. 3.4 a simplified magnetic circuit C_1 is shown. Note that the slope of the load line when the current I=0 depends on the geometry of the magnet (a_{PM}, l_{PM}) and the geometry of the air gap (a_g, l_g). This is a very important relation since the operating point should not lie close to the B-H curve's knee, this would mean that the magnet is in demagnetization risk because as shown in Fig. 3.3 the load line will move to the left as response to the armature reactance, in other words, the opposing magnetic field produced by the machine coils will move the operating point further to the left perhaps after the knee point causing demagnetization.

3.3. Recoil line

The phenomena described before (demagnetization by opposing magnetic field) can be explained better with the Fig. 3.5. There the *recoil line* is shown in red. First the magnet is at the operating point A, then a demagnetizing current moves the operating point to B, notice that the load line moved parallel to the original but further to the left thanks to the armature reactance (NI/l_{PM}). Now the operating point is below the knee of the B-H curve for 80°C.

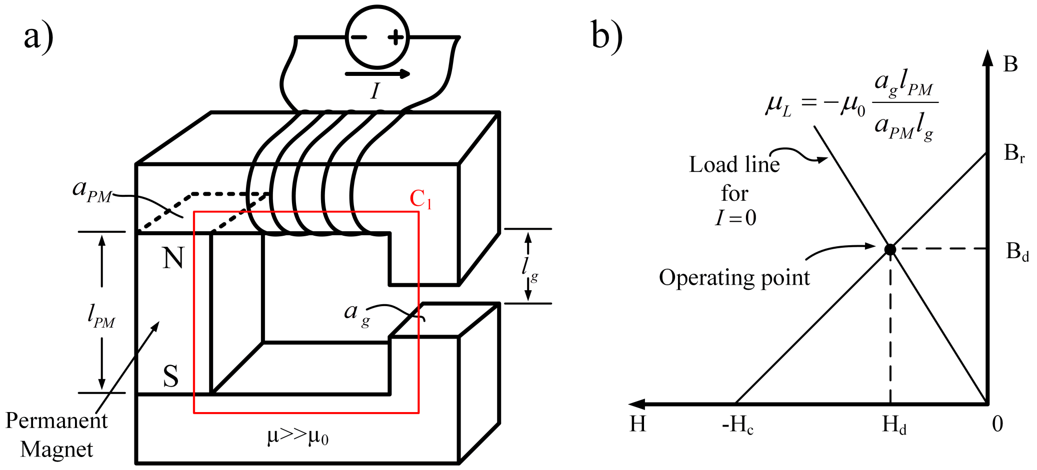

Fig. 3.4. C-core (a) and load line when I=0 A (b)

When the opposing magnetic field is turned off, the magnet's operating point returns to C. This means that the magnet has lost its original BH_{max}. Note that the recoil line is parallel to the linear part of the B-H curves.

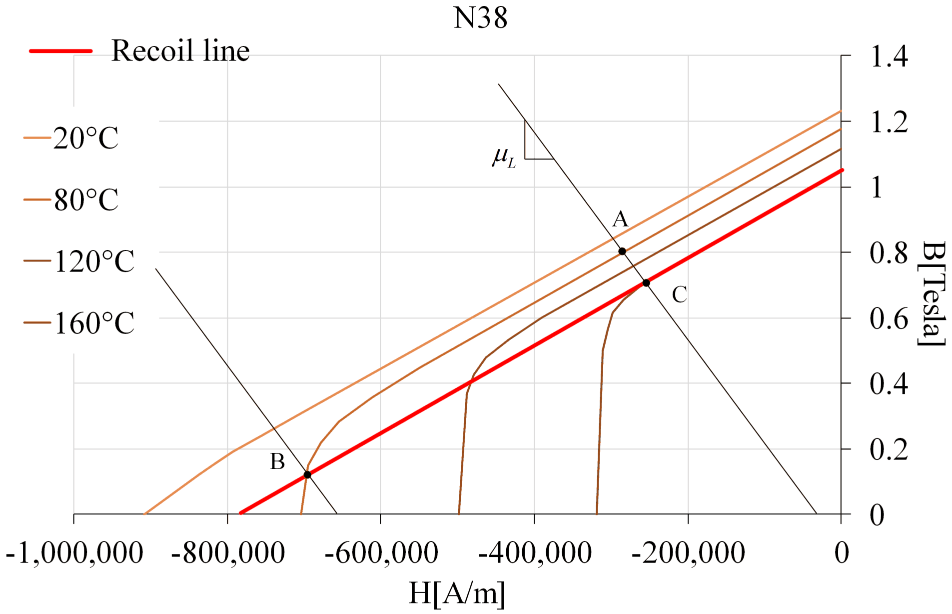

Fig. 3.5. Recoil line of the N38 magnet at 80°C

Another *failure mechanism* that will obtain the same results (operating point C) is to augment the temperature from the 80°C to 160°C. This is clear in Fig. 3.5 because the operating point C coincides with the 160°C B-H curve.

In Fig. 3.6 a qualitative depiction of the hysteresis curves (B-H curves) for two different temperatures are shown. Notice the change in the remanence Br and coercivity Hc when the temperature rises. In the magnet's data sheet [107], this rate of change (Reversible Temperature Coefficients) are expressed as ΔBr and ΔHc both expressed in %/°C. These figures of merit are useful for the non-linear model of the magnetic material in FEA, since they are used to calculate the new B-H curve when the temperature changes.

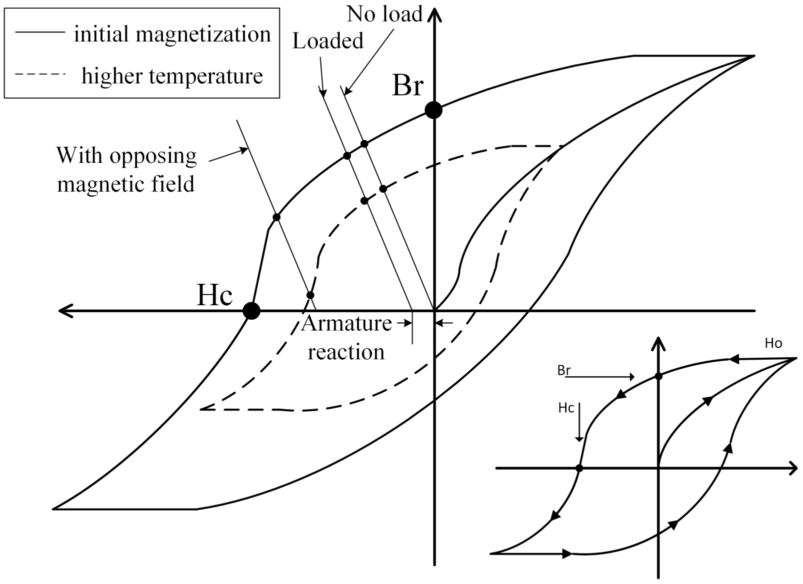

Fig. 3.6. Qualitative depiction of the B-H curves under different temperatures

3.4. Initial analysis of the PMSG demagnetization

In this section the results of the initial analysis of the PMSG demagnetization are shown. The first test was an open circuit then a 3 phase short circuit is maintained for about 200 ms and then the fault is cleared to open circuit again. For this analysis no co-simulation was used, namely only the FEM coupled with a simple circuit shown in Fig. 3.7 was used. The red square shows the three phase short circuit location. LUphase, LVphase and LWphase are the link to the FEM, Rstator and Lstator are the stator winding resistance and the leakage inductance.

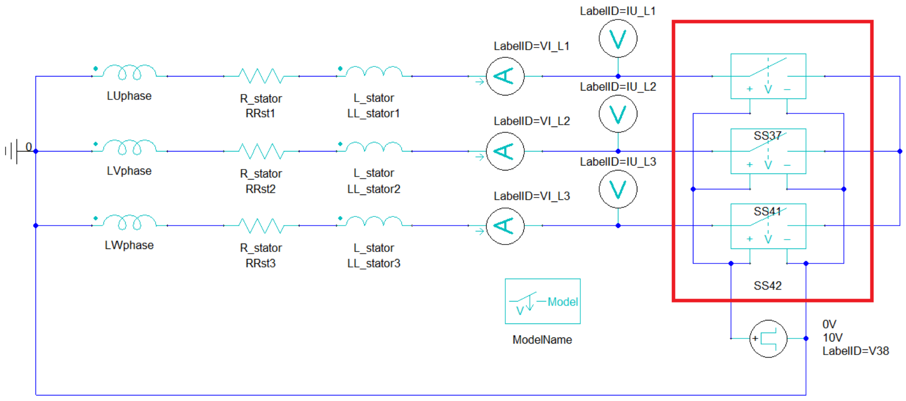

Fig. 3.7. Maxwell's circuit editor used for the demagnetization back EMF analysis.

First the PMSG was tested for nominal speed (1500 rpm) and "low" operating temperature of the magnets (60°C), in other words, an operating temperature lower than the measured one by Lipinski et. al. in [108, 109, 87] with a similar machine also based on the Sh90L-4 IM. In those publications, the author compares Computational Fluid Dynamics (CFD) calculations to laboratory measurements and concludes that the magnets in the LSPMSM rotor achieve a steady state temperature of $\sim$72°C. after about 1.5 hours, under nominal speed and nominal torque (10.15 Nm).

In Fig. 3.8 the results of the first test at 60°C are shown. Note that the tests were made with constant speed input, this means that before the short circuit, during the short circuit and after the short circuit, the speed is kept constant at 1500 rpm. In Fig. 3.8b the torque at the shaft is presented, the PMSG behaves as an electromagnetic brake during the 3 phase to ground fault, opposing the input torque with $\sim$5 Nm average.

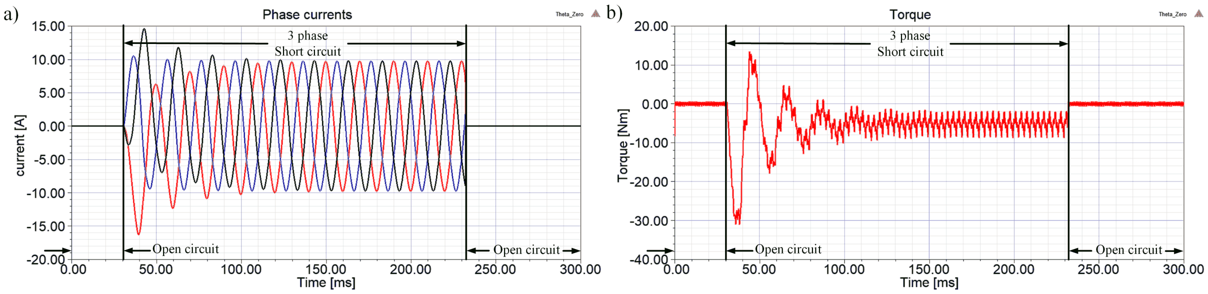

Fig. 3.8. Open circuit-Short circuit-Open circuit test at 60°C, currents (a) and torque(b)

In Fig. 3.9 the results of the same test (open circuit-short circuit-open circuit) for a higher temperature of 150°C are presented. Here the opposing torque is only of about $\sim$2 Nm in the steady state (between 150 to 230 ms).

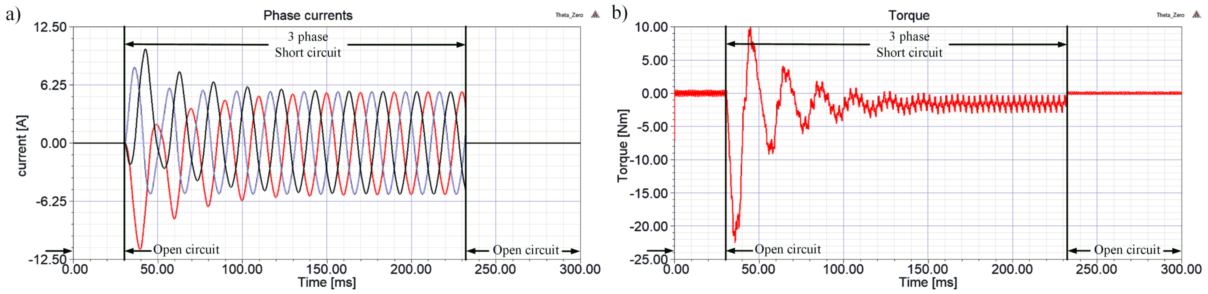

Fig. 3.9. Open circuit-Short circuit-Open circuit test at 150°C, currents (a) and torque(b)

In Fig. 3.10 the back EMF for the tests presented before are shown. Notice the difference between the initial (before the fault) and the final back EMF in Fig. 3.10b.

What Fig. 3.10 is showing, is the effect of a strong opposing field over the magnets when they are operating at high temperature. The fact that the PMSG has a lower Back EMF after the

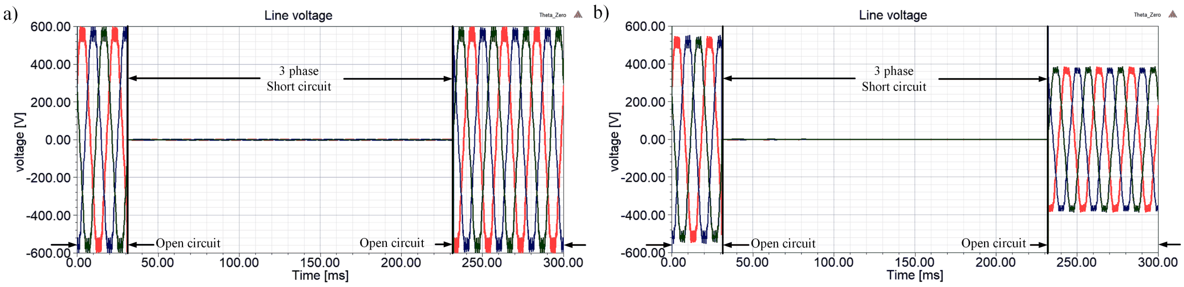

Fig. 3.10. Back EMF before, during and after the 3 phase short circuit for 60°C (a) and 150°C (b)

short circuit is evident in Fig. 3.10b. Also by comparing Fig. 3.8b and Fig. 3.9b the ability to work as an electromagnetic brake is lost with higher temperature.

In Fig. 3.11 the magnetic flux density distribution through the transverse cut (2D geometry) of the PMSG, before and after the short circuit, is presented for a magnet temperature of 150°C.

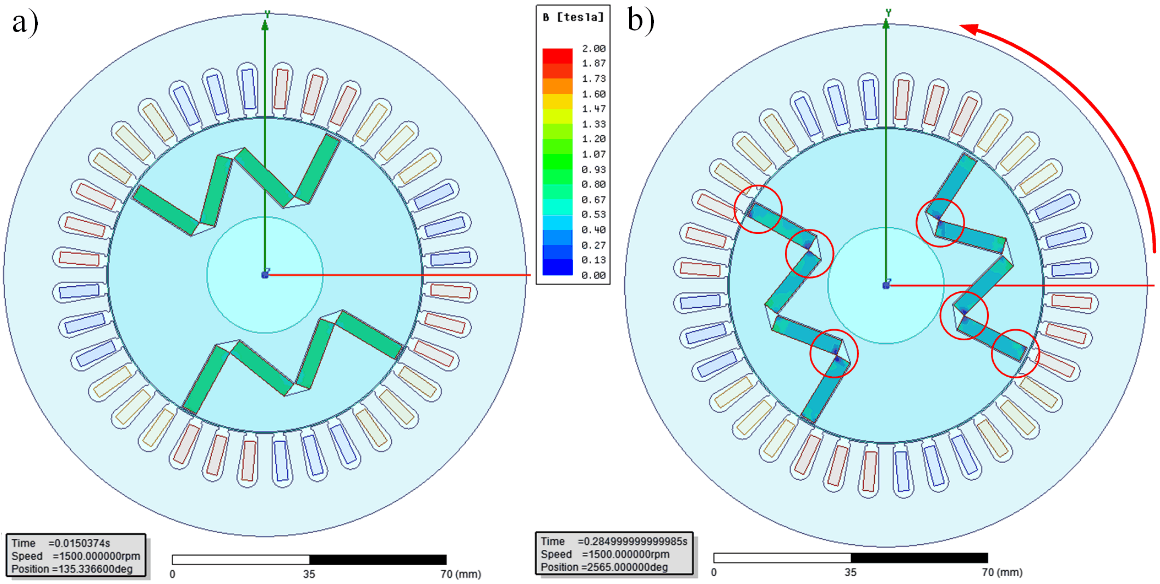

Fig. 3.11. Magnetic flux density distribution at 150°C before short circuit (a) and after short circuit (b)

From Fig. 3.11b is visible that the inner corners of the W shape are where the magnets are demagnetized more. Also the trailing magnet's upper corner present high demagnetization. The trailing magnet is the last magnet in the W shape taking into account that the rotation is counter clockwise as indicated by the red arrow. In Fig. 3.11b the highest demagnetized places are indicated with red circles. In general, all the magnets in Fig. 3.11b have suffered partial demagnetization.

In Table 3.1 the Back EMF voltage at 1500 rpm before and after the three phase short circuit is presented. notice that at 90°C even before the 3 phase short circuit the Back EMF is already 10 V$_{rms}$ lower than the designed goal of 420 V$_{rms}$. Note that the difference between

Table 3.1. Back EMF at 1500 rpm before and after 3 phase short circuit

Magnets Temperature	Before	After
60°C	416 V_{rms}	415 V_{rms}
70°C	413 V_{rms}	412 V_{rms}
80°C	410 V_{rms}	408 V_{rms}
90°C	407 V_{rms}	404 V_{rms}
100°C	403 V_{rms}	399 V_{rms}
110°C	400 V_{rms}	392 V_{rms}
120°C	396 V_{rms}	382 V_{rms}
130°C	392 V_{rms}	367 V_{rms}
140°C	387 V_{rms}	329 V_{rms}
150°C	382 V_{rms}	272 V_{rms}
160°C	376 V_{rms}	206 V_{rms}

the initial Back EMF and the Back EMF after the fault becomes bigger the higher the magnets' temperature was before the fault occurred. This means that, if the fault occurred during an over load condition (hot rotor), it is more likely to demagnetize at least partially the PMSG.

In Fig. 3.12 the difference between column 2 and column 3 of Table 3.1 is plotted as the solid line. Notice how after 130°C the difference of the Back EMF before and after the short circuit becomes bigger than 50 V_{rms}, all the way to 170 V_{rms} at 160°C. This indicates a very high demagnetization rate.

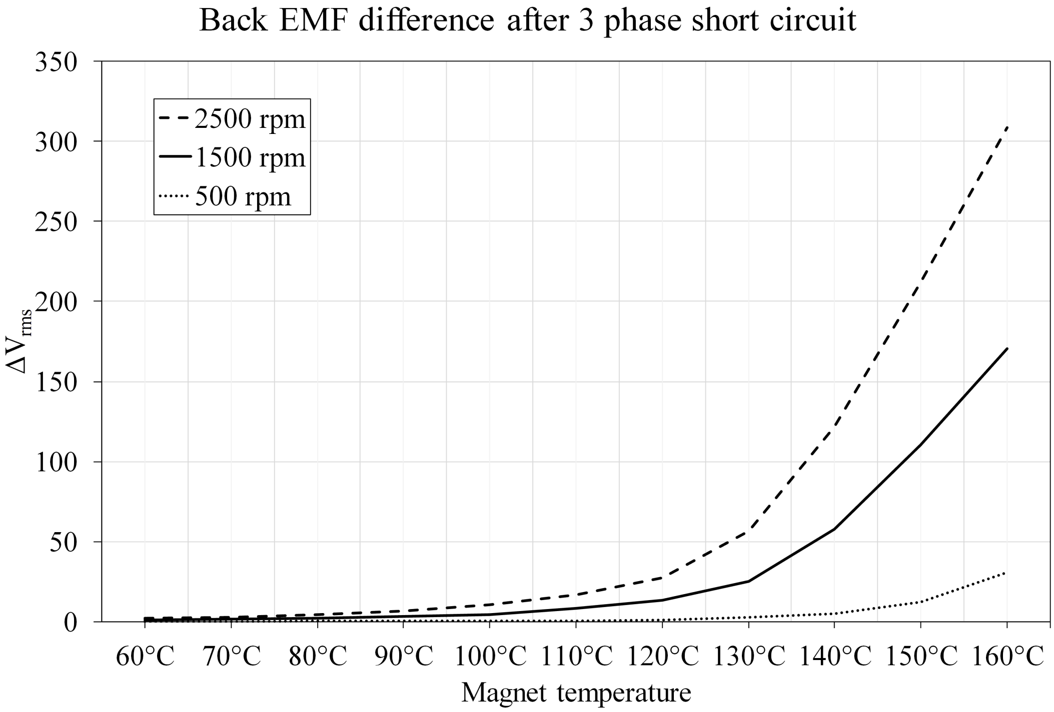

Fig. 3.12. Back EMF difference before and after the three phase short circuit at different temperatures and at 2500 rpm (dashed line), 1500 rpm (solid line) and 500 rpm (dotted line)

Also in Fig. 3.12 the other lines corresponding to the same analysis but for different constant speed indicates that the speed of operation of the PMSG, before and during the fault, also has an impact on the level of demagnetization that the IPM machine will get. Bigger ΔV$_{rms}$ is worst. From Fig. 3.12 it can be concluded that the PMSG can be operated up to 120°C without risk of high demagnetization in case of a fault, or even at higher temperatures but at low speed. Keep in mind that all the tests shown in this section were done at constant speed, namely no acceleration occurs during the fault.

4. Wind turbine Generator

4.1. Wind turbine technology

The technologies applied in the wind turbine's industry have evolved remarkably in the last 4 decades. At the beginning of the wind turbine expansion, about 1970's, the technology chosen for the generators was the very well-known induction machine. As is known, the induction generator works in super-synchronous speed but close to the electrical synchronous speed (2-3%), see Fig.4.1a. Some early manufacturers made some modifications to the IM for the purpose of obtaining a wider speed range in which the turbine could operate, namely, they added a second winding in the same stator with a different pitch factor (coil span), see Fig.4.1b. This obviously increased the cost of the machine but allowed the wind turbine to work over a wider range of wind speeds and without a power converter.

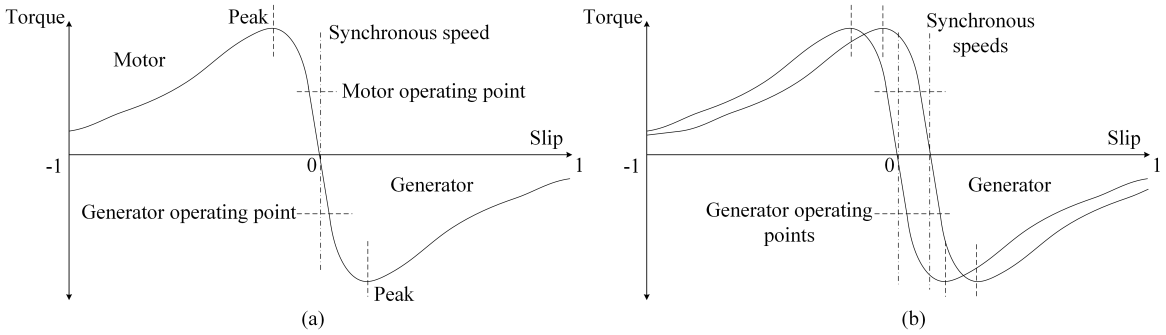

Fig. 4.1. Operation regions of the induction machine (a), and double stator IM (b)

Also at the beginning (1960s to 1970s), due to the limited switching frequency (<1kHz) of the available power transistors (thyristor and gate turn-off thryristor GTO), the cost per device and the negative effects of driving the electrical machine at low switching frequencies (e.g. augmented ohmic losses, non-symmetrical B-H loops, torque pulsations) made the wind turbine industry search for alternatives to the use of variable frequency drives (VFD). With the development of the insulated gate bipolar transistors (IGBT) during the 1980s, with switching frequencies higher than 1kHz, the wind turbine manufacturers started adopting the VFD in the Wind Energy Conversion System (WECS). The limit on the IGBT voltage and current rating, and also its initial cost, made the wind industry adopt a lower rating converter for the wind turbines. This launched the adoption and development of the doubly fed induction generator (DFIG) for WTs, which is a wound rotor induction machine which thanks to the frequency converter acting on the rotor windings is able to work as a synchronous generator over a wider speed range than the IM. The power generated by the WT is directly fed through the stator windings directly connected to the grid. Since the rotor currents have to control the frequency of the injected power to the grid (50 Hz in Europe) this kind of generator also operates around the synchronous speed (±25%). The power electronics needed for the DFIG have to withstand only 30% of the nominal power of the generator, this made it suitable for the recently developed IGBTs during the 1990s and 2000s [110].

From the explanation done before, is clear that these machines, IM and DFIG, need to operate at high speeds to feed the grid with voltage and currents at the base frequency (50 Hz). Taking into account that the rotational speed of a 100 m diameter wind turbine is up to 25 rpm, it is immediately clear that the IM and DFIG need a multiplier gearbox to spin the machine shaft around the 1500 rpm in order for the control/converter to achieve 50 Hz synchronous operation. A schematic of the IM and DFIG with gearbox are shown in Fig.4.2 a and b respectively.

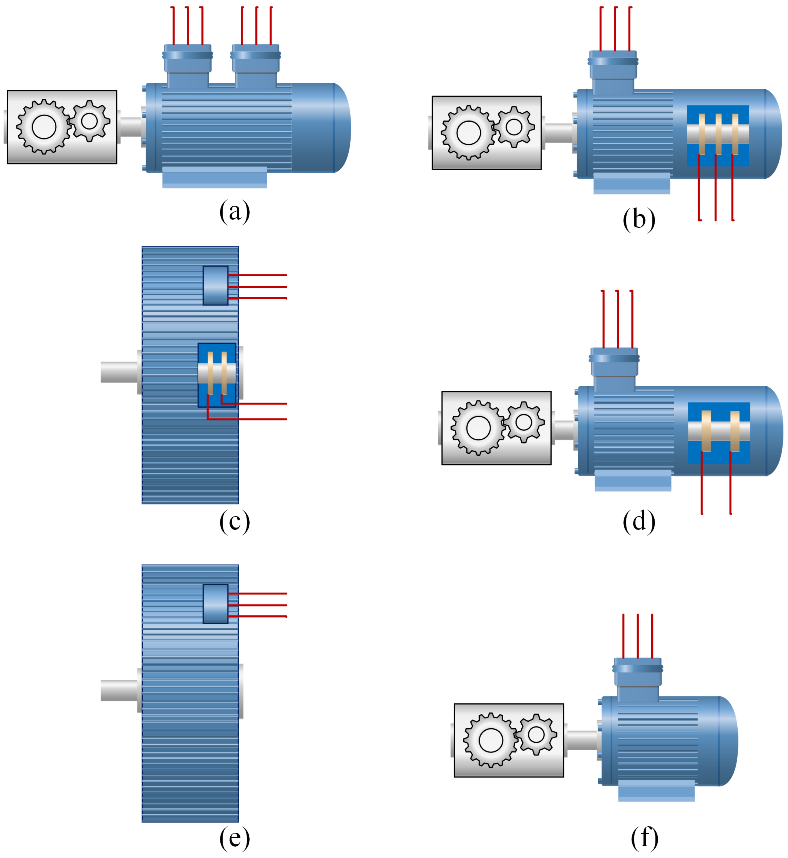

Fig. 4.2. Generator technologies for WTs, Squirrel-Cage two speed induction generator (a), Doubly-fed induction generator (b), direct-drive wound rotor SG (c), wound rotor SG with gearbox (d), direct-drive PMSG (e), PMSG with gearbox (f)

Another technology widely used first in the hydroelectric generators is the wound rotor synchronous machine (WRSM) also called electrically excited synchronous generator (EESG). Again, a multiplier gearbox is needed when the machine has only 4 or 6 poles (see Fig.4.2d), but for the hydroelectric power plants there are no gearboxes because the natural speeds of hydro-turbines are higher than the speeds of wind turbines. For some applications, including slow hydro-turbines and big wind turbines, the construction of the machine allows for a larger diameter and therefore a larger number of poles, this partially compensates for the difference between the rotational speed of the WT and the base frequency of the grid. Although, a full size converter (with generator's nominal power) is still needed due to the operation with variable speed of the wind. A schematic of this EESG is shown in Fig.4.2c and the main manufacturer of this kind of generator is the German company Enercon. Notice that for both wound rotor synchronous generators (Fig.4.2 c and d) an automatic voltage regulator (AVR) is needed between the DC voltage source and the rotor windings.

Finally, due to the advancements done in material science with the permanent magnets (see section 1.2), in the last 2 decades, the adoption of permanent magnet machines for different applications have taken place. Of course, with the increase in the demand for rare-earth materials, the market prices soar and in the large WT industry, delayed the adoption of such technologies. The Table 4.1 is taken from a review [111] of the different technologies for WECS. Nevertheless, as the Table 4.1 summarises, there are still many benefits of using the permanent magnet technology, which is why lately (2013-2018) the PMSG adoption has gained traction and manufacturers like GE Renewable Energy (formerly Alstom) are introducing a 6 MW direct-drive PMSG for off-shore wind farms in USA [112] and other producers like Lagerwey and Novawind (part of Rosatom) started a joint venture for on-shore wind farms in Rusia with 2.5 MW direct-drive PMSG [113]. In Fig.4.3 a schematic diagram of the recently developed direct-drive PMSG technology is shown. Notice that in order to generate voltages and currents with frequencies in the order of tens of hertz many magnetic poles have to cross the stator windings every single turn, thus a larger diameter is needed.

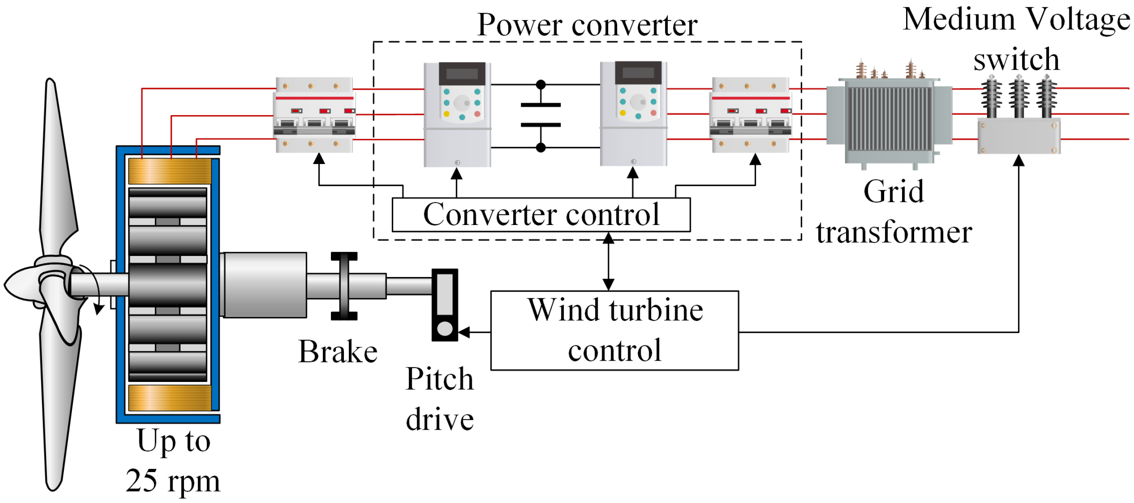

Fig. 4.3. Direct-Drive PMSG technology adopted for large WTs

4.2. Wind turbine control concepts

In Fig. 4.4 the somewhat older concepts for WT control are shown. As explained before, they are mostly based on the classical IM without power electronics converter. The concept shown in Fig. 4.4a is commonly referred in the literature as the "Danish concept", although is based on the very robust squirrel-cage induction generator (SCIG), it needs a soft starter and a capacitor bank for reactive power compensation, this means that no reactive power could be injected to the grid in case of a grid fault. This disadvantage was overcome with the addition of full converter as shown in Fig. 4.4b still the disadvantages of the SCIG (need for a multiplier gearbox) and the losses of gearbox, squirrel-cage and full converter, deliver lower efficiency.

In Fig. 4.4c the wound rotor induction generator (WRIG) with variable rotor resistor is shown. This is very similar to the SCIG without converter but the rotor of the machine is windings instead of the squirrel-cage. This concept was used by the manufacturer Vestas during the 1990s and they avoided the need for slip rings and brushes to connect the resistors to the rotor windings by incorporating the variable resistors onto the rotor and the control signal was transmitted optically [114].

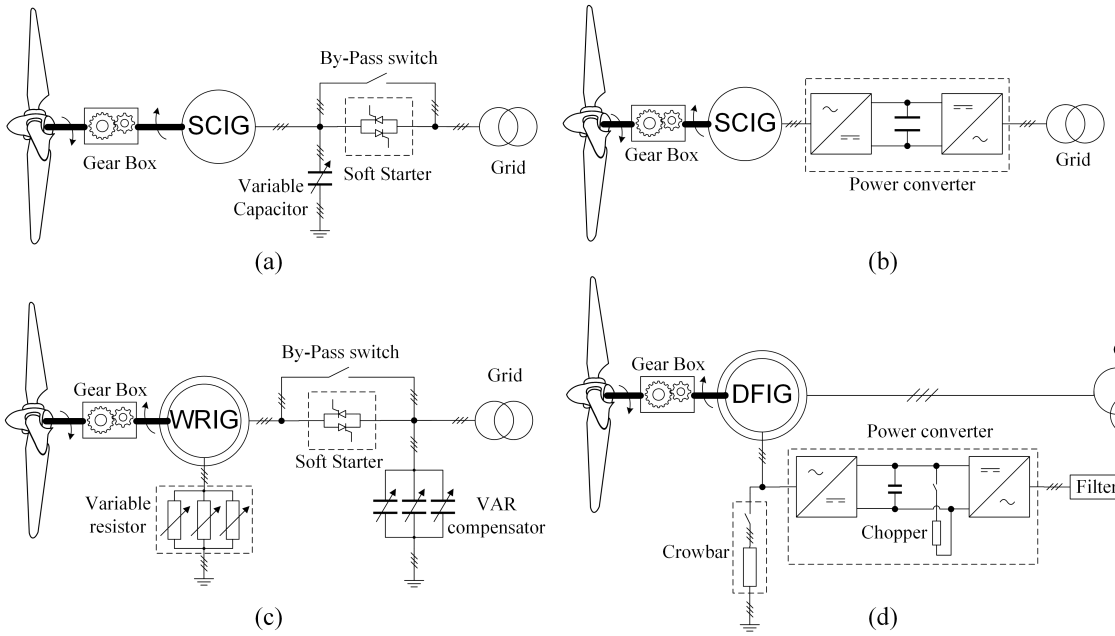

Fig. 4.4. Earlier WT concepts, squirrel-cage induction generator without converter (a), squirrel-cage induction generator with full converter (b), wound rotor induction generator with variable rotor resistor (c), and the doubly-fed induction generator with lower power converter (d)

In Fig. 4.4d the doubly-fed induction generator (DFIG) concept is shown. Notice the need for a break resistor (crowbar) as the stator windings are directly connected to the grid.

Table 4.1. Comparison of various generator technologies for wind turbines. Data from [111]

Generator	Advantages	Disadvantages
Squirrel-Cage single-speed or two-speed induction generator (2p=4 or 6)	— simple construction — simple maintenance — attenuated pulsations of turbine torque — low cost — direct connection to the power grid	— requires reactive power — requires soft start device for initial connection to the grid — applicable only for fixed turbine speed — requires a gearbox — cannot be used for large number of poles (>20)
Doubly-fed induction generator	— significantly reduced power rating and cost of the converter — possible speed regulation for optimal utilisation of energy (typically ±20-25%) — reactive power for magnetisation of the machine is provided by the power converter — sub-synchronous and super-synchronous operation is possible	— slip rings and brushes, wear and tear maintenance — complex control of the entire unit — direct connection to the grid is somewhat difficult
Synchronous generator with rotor excitation winding	— simple control of reactive power — wide range of speeds — simple control	— requires power converter of the same power rating as the machine — requires an excitation system — slip rings and brushes, wear and tear maintenance
Direct-Drive	— no gearbox — higher efficiency	— large dimensions and weight, problems with construction, transportation and installation
With Gearbox	— small dimensions and weight — standard construction can be used	— high cost, losses (2-3%) — problematic maintenance of the gearbox
Synchronous permanent magnet generator	— simple rotor with no parts prone to wear and tear — very low rotor losses	— high cost of permanent magnets — possibility of demagnetisation — insufficient experience in construction and installation
Direct-Drive	— no gearbox — higher efficiency — simple maintenance	— large dimensions and weight, problems with construction, transportation and installation
With Gearbox	— small dimensions and weight — standard construction can be used	— high cost, losses (2-3%) — problematic maintenance of the gearbox

In case of a grid fault (i.e. short circuit somewhere in the grid) the rotor voltages would exceed the power electronic converter ratings, therefore a resistor is needed to dissipate this power. Also a chopper circuit in the DC bus avoids overvoltage that may damage the converters.

The DFIG configuration was popularised by many manufacturers e.g. Senvion (formerly REpower), Nordex, Gamesa, Vestas during the 2000s because its lower cost converter, reactive power compensation capabilities and changes in the european regulations about reactive power compensation during grid faults (grid code).

A newer concept of DFIG used to avoid the slip rings and brushes is shown in Fig. 4.5 a, here the machine has a second stator winding which is used to induce currents in the rotor windings, this second stator winding is known as the "control winding" while the normal stator winding is known as the "power winding". Notice that the pole pitch (relation to the poles in the rotor) of the control and power windings have to be different in order to avoid direct magnetic coupling.

An earlier concept revisited with the development of power converters is the direct-driven electrically excited synchronous generator (EESG), shown in Fig. 4.5, this is the traditional wound rotor synchronous generator only that due to the rotor diameter, some manufacturers (e.g. Enercon) decided to put the automatic voltage regulator (AVR) to control the field inside the rotor. This concept attracted a lot of attention during the rare earths price peak [115] at the beginning of the 2010s (China export ban) due to the lack of permanent magnets and the possibility to work at low speeds (multi-pole).

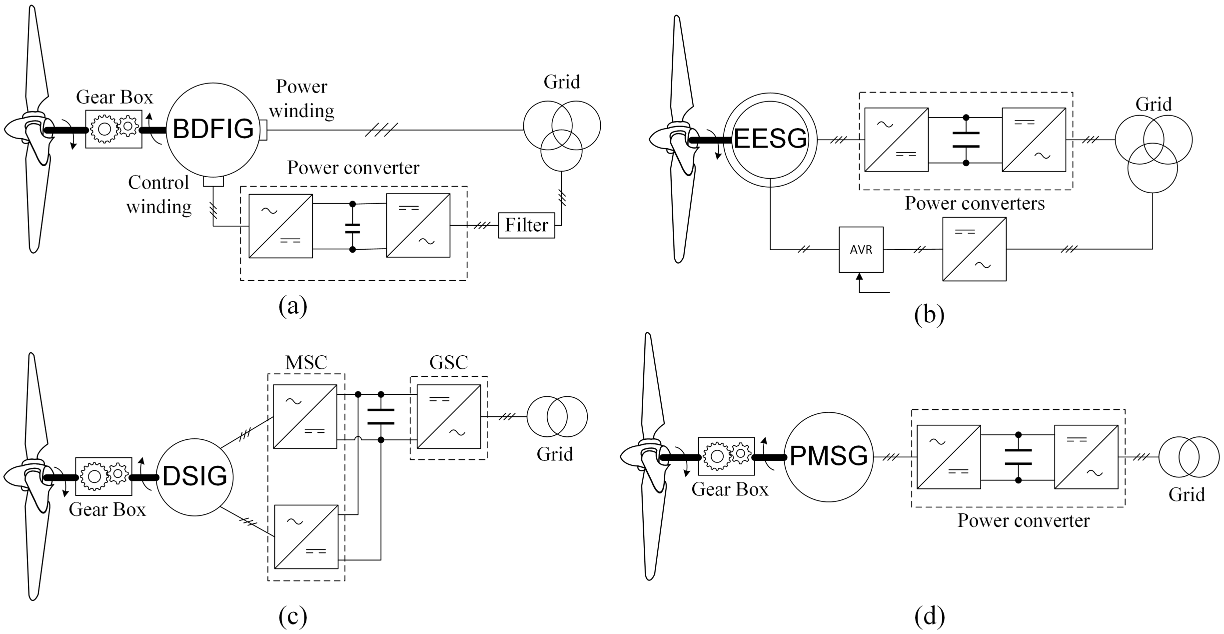

(a) (b)

(c) (d)

Fig. 4.5. Newer WT concepts, brushless doubly-fed induction generator (BDFIG) (a), electrically excited synchronous generator (EESG) (b), double stator induction generator (DSIG) with mutlicell converter (c), and the high speed PMSG with full converter (d)

A concept that seems to have fallen into oblivion is the multiple stator-winding machine with multicell converters, shown in Fig. 4.5 c, here each machine side converter (MSC) connects to a 3 phase winding inside the same stator, so that each converter rating has to be only a fraction of the machine's nominal power. This concept was used by the Spanish manufacturer Gamesa (now Siemens-Gamesa) with a permanent magnet rotor [116]. The multicell converter was abandoned because they result in reduced reliability as if one cell fails the whole system starts malfunctioning.

The decreasing cost of power electronics (roughly a factor of 10 over the past 10 years) and the absence of slip rings and brushes have made the PMSG concepts more attractive. In Fig. 4.5 d the PMSG with multiplier gearbox is shown. This is a good concept when a compact machine is needed (small nacelle), obviously the inclusion of a gearbox increases maintenance costs and decreases reliability and efficiency, but, it allows the generator to be built by well-known standard manufacturing procedures which actually increases the generator reliability. Special machines in non-standard form factors are prone to mechanical loads and eccentricities [75].

To summarise, the wind generator classification tree shown in Fig. 4.6 shows in red the chosen configuration for this thesis. Notice some other advanced concepts mentioned in the classification, that have not been mentioned like high temperature superconductor (HTS) technology mostly because it is still not commercially available and the cooling systems represent a big loss in overall efficiency [117]. Also the PMSG with axial flux (disc machine) or the transverse flux are only commercially available in small wind turbines. Lastly, the planetary gearbox with multiple shaft output was abandoned by Siemens when they bought Areva-Multibrid in 2017 [118]. This was a gearbox with four output shafts where 4 generators were connected, this allowed the generators to be rated to a fraction of the WT nominal power.

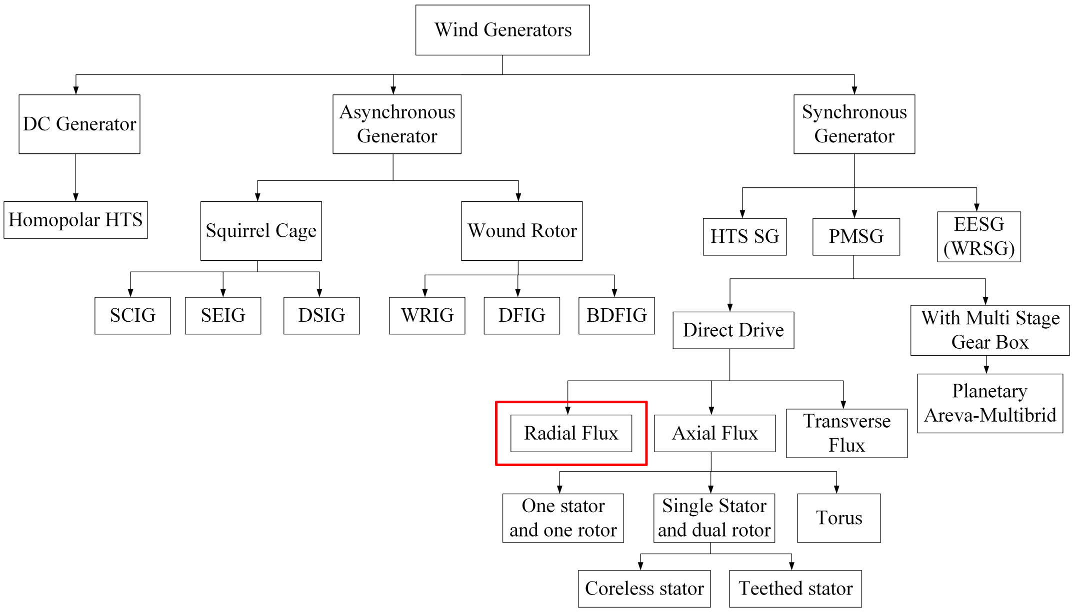

Fig. 4.6. Classification of wind turbines by generator type, data from [119]

Another classification found in the literature is shown in Fig.4.7. Here again, some technologies are still not adopted in the WT are shown. Some emerging permanent magnet machines like the hybrid-excited (permanent magnets and rotor windings) have advantages that matter mostly for motor applications [120], e.g. lower efficiency as a generator than the simple PMSG. Some other technologies have not been fully adopted in the WT, like the switched reluctance machine (SRM) mainly because of lower efficiency and other unsolved problems like higher cogging torque and open loop instability [121].

Notice the special new machines, here another new technology is mentioned, the electrostatic machine [122], which is a concept that uses the duality between magnetic and electric fields, this is often overlooked in electromechanical energy conversion. This means, the electric fields may also create force/torque to perform work. A major disadvantage is that the machine has to be filled with dielectric liquid or gases providing insulation in the order of 10 kV. Finally a new technology being applied to the machines is the wireless power transfer to feed the stator of isolated machines [123]. This is the same technology applied in wireless chargers for cellphones, cars, etc.

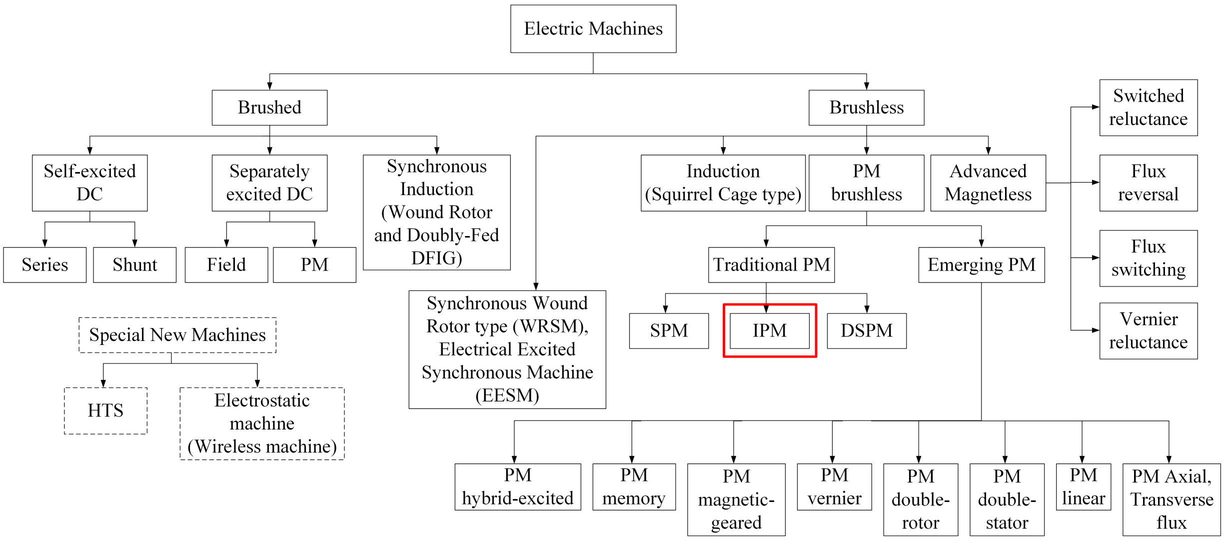

Fig. 4.7. Classification of emerging electric machines, data from [124]

4.3. Wind Turbine with Permanent Magnet Synchronous Generator

From the thorough investigation done in this chapter about the state of the art in wind turbine technology, it is safe to say that the permanent magnet technology will continue to develop in the wind turbine industry. Furthermore, emerging PM technologies make the research on this area very useful in future developments. New modelling techniques to take into account the intricacies of the new designs will be needed. Also, the modelling and analysis of the different effects that affect this type of machines, namely, partial demagnetisation, temperature effects, and materials (electrical steel, magnets) nonlinearities.

From the industrial point of view, recent plans of expansion of on-shore wind farms in Rusia will use the direct-drive PMSG concept [113], also, off-shore wind farms expansion in USA are using the PMSG concept [125], moreover, General Electric is already manufacturing the largest off-shore wind turbines, the Haliade X with 12 MW nominal power based on the ´PMSG technology [112]. These all demonstrates that the bid for PMSG in WTs will continue, and therefore the interest in related research.

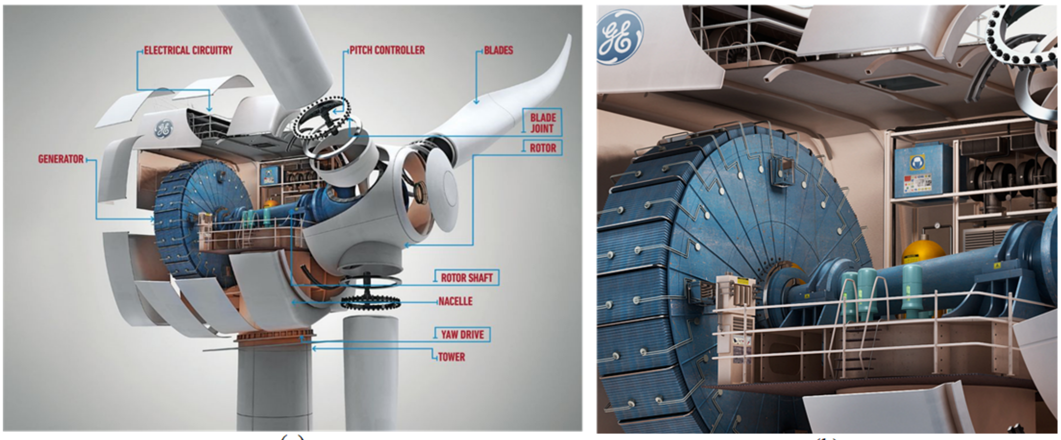

(a) (b)

Fig. 4.8. Haliade X concept (a), world largest commercially available PMSG (b) [126]

4.4. The case for Small Wind Turbines

As stated in Chapter 1, this thesis is focused on the wind energy conversion systems, specifically the small wind turbine. The small wind turbine share many of the same characteristics of its bigger counterparts. Some of the earlier work found in the literature with the small wind turbines is related to the application in which they stand-out the most, this means, isolated (off-grid) hybrid power systems. In [127] the author describe a battery back-up system for a remote telecommunications site with difficult access to which the WT was delivered to the site by helicopter. In [128] the authors describe a hybrid power system where the solar panels and diesel generator are integrated into a shipping container for ease of transportation, the SWT should be installed aside near the container on a guyed tower. Here is important to notice that in both these publications even as early as 1980's the focus was already put in reliability and lifetime. On this matter, some reports show cases of outstanding SWTs in harsh environmental conditions, that have survived more than 27 years with only routine maintenance. In [129] the report describe a micro grid consisting of four 3kW SWTs, a 7.8 kW photo-voltaic array and a 1.2 kW closed cycle vapour turbine. According to that report (published in 2001) the SWTs have been operating in the Black Island in Antarctica since 1985 with documented wind speeds of 317 km/h and temperatures as low as -57°C. In [130] an anecdote about this same system (Black Island, Antarctica) is recount, there a SWT operated for 12 hours in furled position during an Antarctic storm, the radio station turned off when the smoke-shaft for the backup generator was blown away. After the worst part of the storm had passed, the SWT dropped back into running position and recharged the system batteries bringing the radio on again. All these make a very good case for SWTs in isolated operation.

Here is important to note one of the main differences of the SWT in comparison to its bigger counterparts, as it was just mentioned, the SWTs have some different mechanical systems when it comes to the over-speed protection (yaw system). For example, it was declared that the SWT survived a storm through furling mechanism, this means that the SWT has a mechanical system that will allow the turbine to fold in order to deflect the excess of wind. In the bigger WTs an ancilliary system has to rotate the hub so that the blades direction stay out of the wind (yaw control). In Fig. 4.9 the mechanism that allows this movement (furling) in SWTs is shown. Notice that the tail of the SWT stays pointing at the wind while the rotor is deflected.

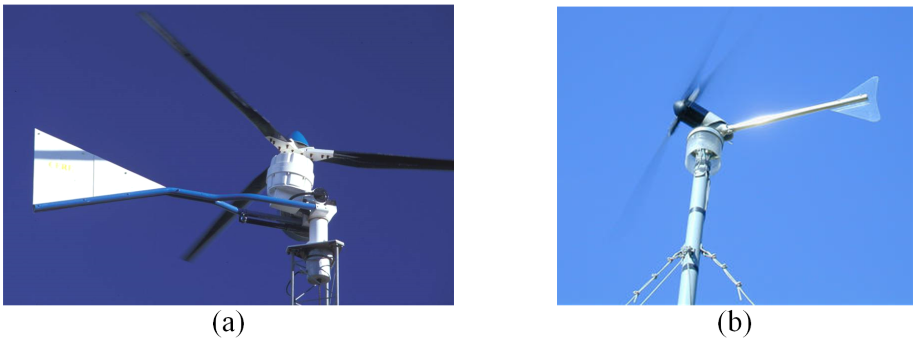

(a) (b)

Fig. 4.9. Two furling methods for SWTs (a) vertical, (b) horizontal [130]

Also in Fig. 4.9, note that for SWTs in general no blade pitch control is used (fixed blades), this is mainly as a result of the lack of space in the hub for an additional mechanism that would spin the blades into the desired angle β. This is important because it simplifies the aerodynamic model of the wind turbine described in Appendix A making in equation A.12 that β=0.

5. Wind Turbine Control

In this Chapter the different strategies for WT control are described in detail. The first one is the simple system with passive rectifier, second one is system with additional boost converter. Advantages and disadvantages of those systems are analysed. Additionally the more complicated vector control system for WT is presented. In the section 5.3 the strategies for obtaining the Maximum Power Point Tracking (MPPT) are described.

5.1. Power electronics in Small Wind Turbines

In Fig. 5.1 four different options used for SWT's converters are shown. Notice that Fig. 5.1b and Fig. 5.1c are quite similar but Fig. 5.1c allows for extended power regulation since it can work as a chopper, limiting the power the generator transfers to the DC bus. This operating mode (chopper) can be seen in Fig. 5.2 region B.

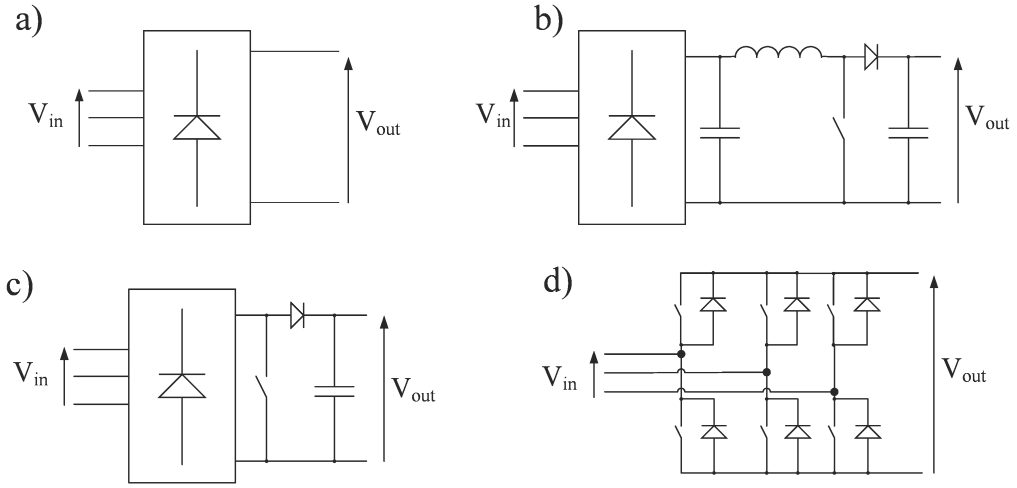

Fig. 5.1. Converter options, (a) passive rectifier, (b) rectifier and boost converter, (c) switched-mode rectifier, (d) full converter

In Table 5.1 a comparison of the 4 topologies presented in Fig. 5.1 is done. Note that only the full converter is operate in all the regions of Fig. 5.2. A deeper analysis of these topologies can be found in [131], their findings were also corroborated in [132] there an additional topology similar to the full converter, namely Half Bridge Switch Mode Rectifier (HBSMR) is also analysed, this consist of the same arrangement as the full converter only without the three upper switches. As stated in that paper, the HBSMR does not offer any advantage in comparison to the topologies presented in Fig. 5.1. Also, in [132] another characteristic not shown in Table 5.1 is analysed, the Total Harmonic Distortion (THD) of the generator currents. There, the full converter is the only topology able to provide a THD below 10%. The THD is also important for the analysis of current signals for fault diagnosis, namely Motor Current Signature Analysis (MCSA).

Table 5.1. Comparison of small wind turbine converters, data from [131]

Topology	**Diode count**	**Switch count**	**Control**	**Region in Fig. 5.2**	**Cost**
Passive Rectifier	6	0	None	Dashed line	Low
Boost	7	1	Simple	A	Medium
SMR	7	1	Simple	A and B	Low-Medium
Full converter	6	6	Complex	A, B and C	High

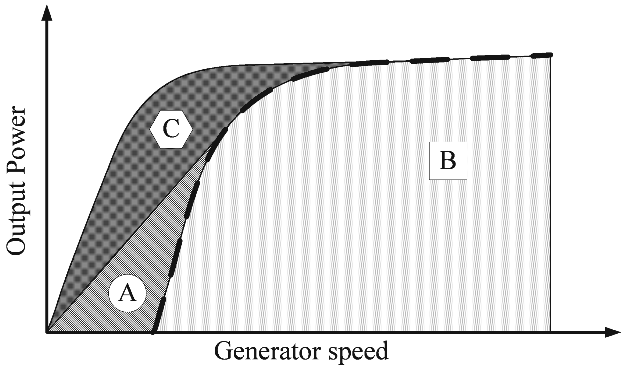

Fig. 5.2. Converter's operating regions, data from [131]

In this thesis, the topologies shown in Fig. 5.1a rectifier, Fig. 5.1b rectifier with boost converter and Fig.5.1d full converter are applied for the analysis of the operation with the PMSG. As mentioned before, the main difference between the passive rectifier with boost converter, and the switched-mode rectifier (SMR) is that the SMR can lower the power output to the DC bus by short-circuiting the rectifier output. This is regularly undesirable since the focus is in the extraction of the maximum power from the available resources. Note in Fig. 5.2 that for the uncontrolled rectifier (passive rectifier) the operating region is reduced to a curve (dashed line).

5.2. Control strategies with full converter for Wind Turbines

To summarise the benefits of using the full converter in the WECS, it can be listed:
— higher power output even at low wind speeds (see Fig. 5.2),
— lower THD on the 3-phase current signals (sinusoidal),

— lower losses even at high temperature operation (see [132]).

— possibility to apply fault tolerant control

About this last item, in the lower part of Fig. 5.3 we can see the different schemes to apply a control algorithm which can be used as a fault tolerant system.

Also in Fig. 5.3 notice that the chosen control strategy for the 2 level converter (2LC) used in this thesis is the Field Oriented Control (FOC), specifically the i_d=0 strategy. This mainly follows that for the PMSG there is no need to provide reactive power.

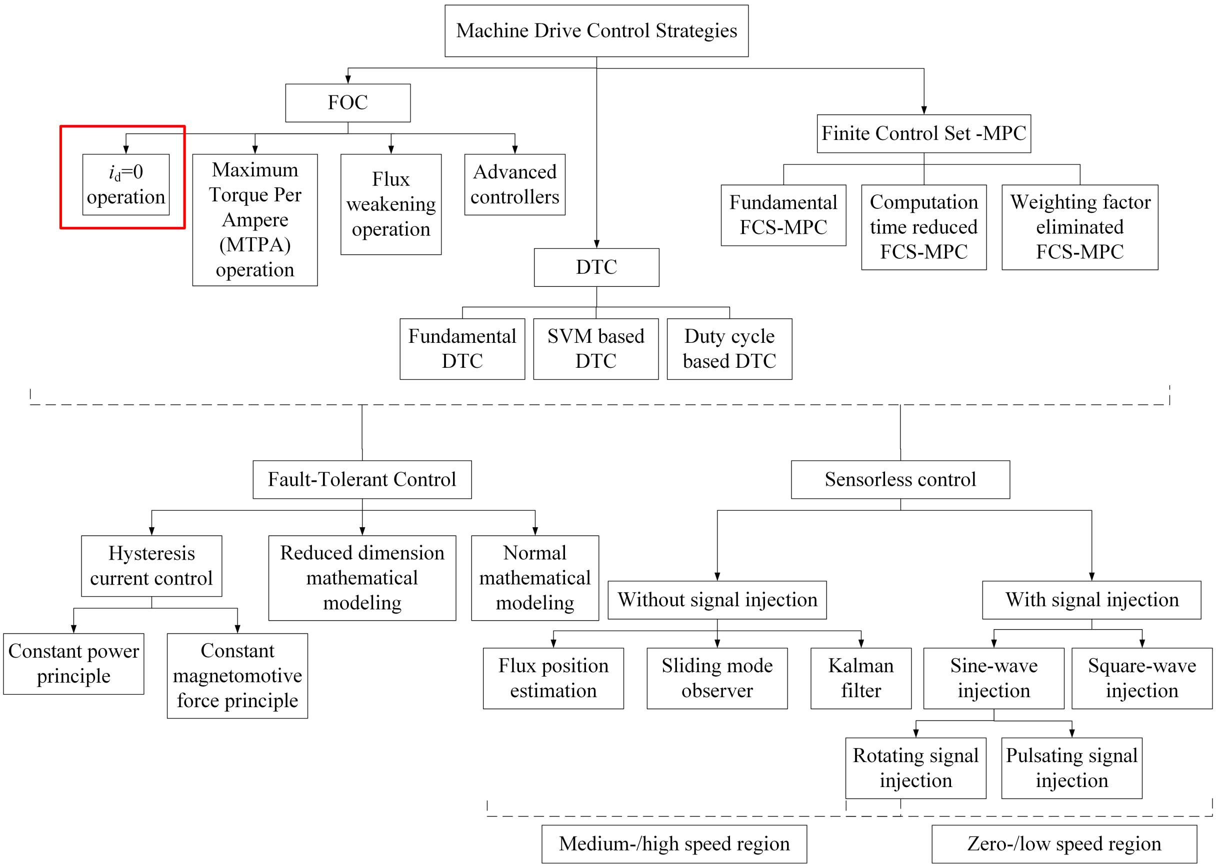

Fig. 5.3. Classification of the control strategies for electric machines. Data from [124]

Notice in Fig. 5.3 that other control strategies are available, namely the Direct Torque Control (DTC) and the Model Predictive Control (MPC). Although some research has been published using the DTC strategy [133, 134] and MPC [135, 136], the FOC method is preferred for WTs because of lower THD and higher efficiency as demonstrated in [137]. Also, the i_d=0 is preferred over the Flux weakening because it procures lower losses (core losses and winding losses present at higher speed) consequently the WECS is designed to rotate close or below the generator's nominal speed (aerodynamics, gearbox, etc.).

In Fig. 5.4 three schematics of the main control strategies are shown. In the next section the explanation of the maximum power point tracking (MPPT block) is done, but here is important to show that as a general rule the MPPT algorithm requires some feedback from the rotational speed. As shown in the classification given in Fig. 5.3 (lower right) there is also the possibility of doing without the encoder (sensorless mode). Notice that the DTC diagram (Fig. 5.4b) uses an estimation of the rotor position θ_s since this is common in the flux estimation. In general, for the transformation of the electrical variables to the rotating reference frame (Park tranform) and also to transform back this signals to the three phase system (inverse Park transform) the rotor position is needed. A common procedure to obtain this angle is to count the number of pulses that have come out of the encoder (incremental encoder in Fig. 5.4) in a certain amount of time (microcontroller interruption).

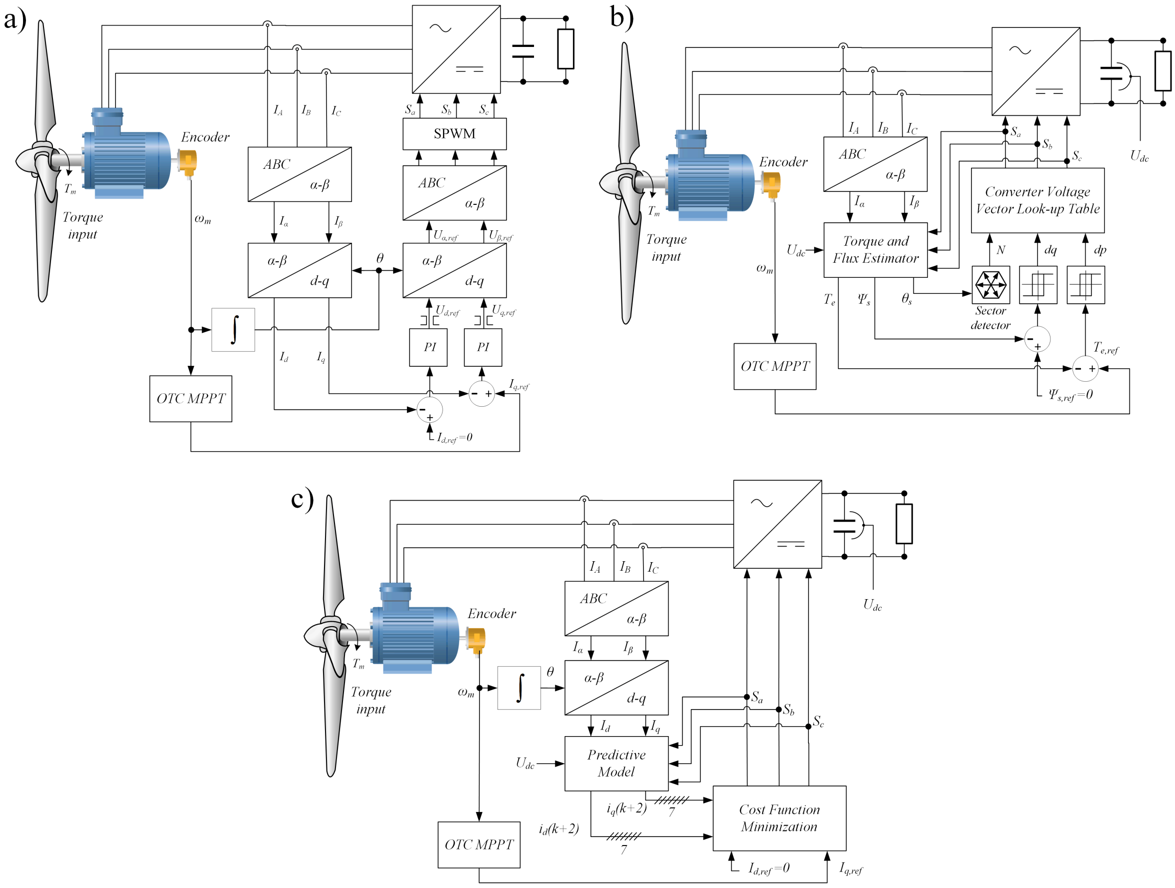

Fig. 5.4. Schematic diagram of the three main control strategies, FOC (a), DTC (b) and MPC (c)

Notice in Fig. 5.4 only the FOC diagram has a fixed switching frequency (SPWM block), although DTC and MPC also have a way to fix the switching frequency by Sinusoidal Pulse Width Modulation (SPWM) or Space Vector Modulation (SVM) e.g. DTC-SVM, the fundamental DTC and FCS-MPC can only offer an average switching frequency and a bell-shaped curve as shown in [135]. Furthermore, FCS-MPC shows bigger steady state error than FOC and high THD at low load currents also shown in [135].

5.3. Maximum Power Point Tracking

As it can be seen in Appendix A the WT has a rotating speed at which it will extract the maximum power from the wind at each wind speed. Note that this is not the same control strategy as the one shown in Fig. 5.3 as Maximum Torque Per Ampere (MTPA), this is because the MTPA tries to obtain the maximum torque from the electrical machine (motor) and the MPPT tries to extract the maximum power from the prime mover (wind). In Fig. 5.5 some output curves from the aerodynamic model described in Appendix A are shown. Notice that for this rotor blades the nominal mechanical power (torque) is reached at a wind speed of 12 m/s. Also notice that for lower (and higher) wind speeds the maximum power attainable is achieved at a different generator speed. In Fig. 5.5 this is represented by the dotted curve. Thus, for the MPPT algorithm to extract correctly the maximum power at each wind speed it should drive the generator to rotate at the reference speed given by the dotted line from Fig. 5.5.

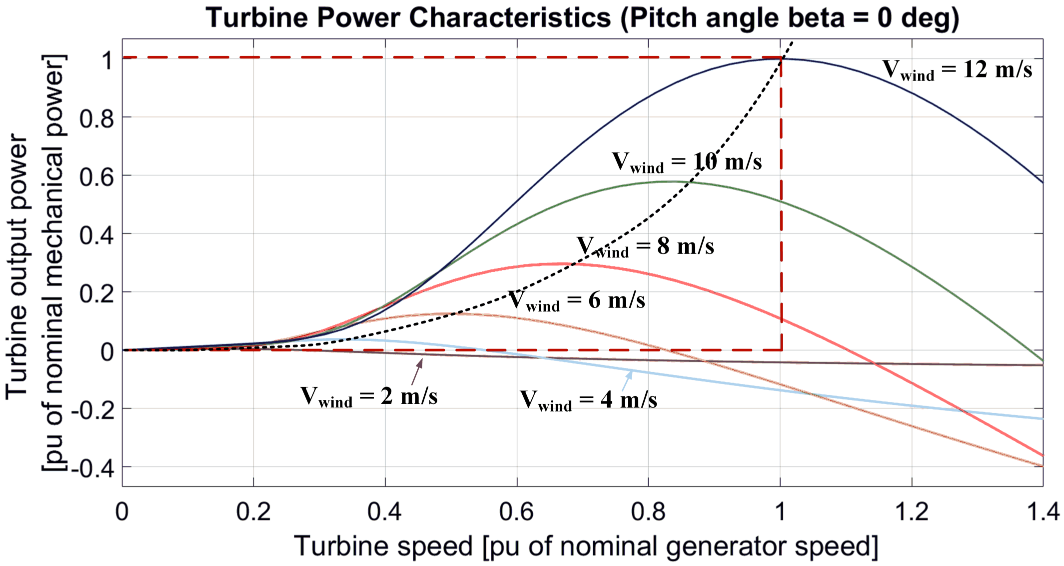

Fig. 5.5. Aerodynamic-model's output with Maximum Power Point curve (dotted line)

In Fig. 5.6 the different options for the MPPT algorithm are shown. In this thesis the Optimal Torque Control (OTC) algorithm is used. This is as a result of the analysis presented in [138] where the authors compare the Tip Speed Ratio (TSR) method, the Power Signal Feedback (PSF) method and the Perturb and Observe (P&O) method with the OTC. From that reference is clear that the OTC has better dynamics (faster recovery time) and achieves the highest efficiency. The disadvantages of the OTC are that it requires *a priori* knowledge of the turbine characteristics, namely radius and tip speed ratio (λ) at the maximum power C_{p_max}. The tip speed ratio λ is given as:

$$\lambda = \frac{Tip\ speed\ of\ the\ blade}{Wind\ speed} = \frac{\omega R}{V} \tag{5.1}$$

where ω is the rotational speed of the turbine's shaft, R is the turbine radius and V is the wind speed in m/s. The C_{p_max} is the maximum value the power coefficient C_p that can be obtained for a given λ.

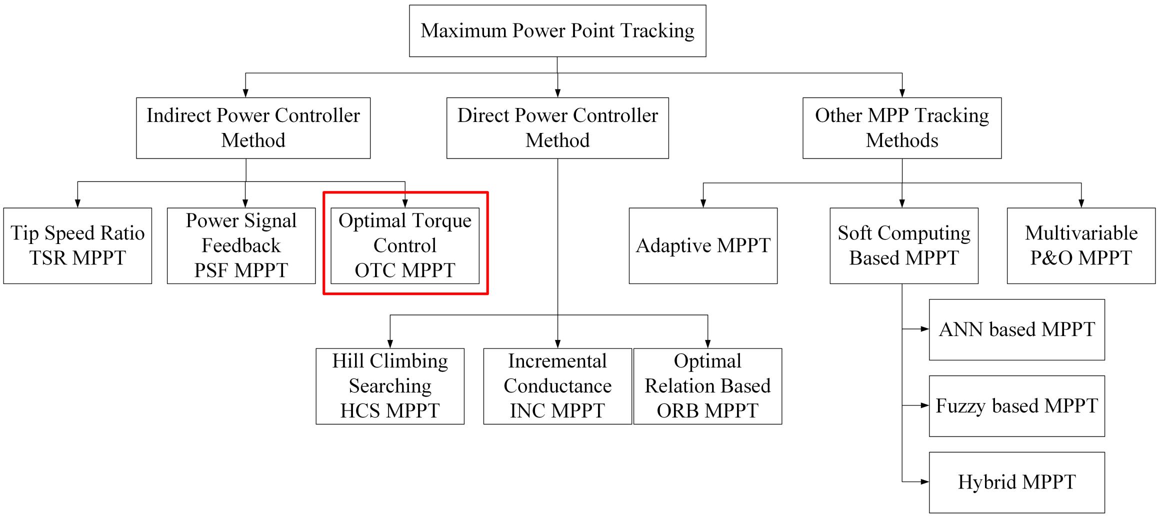

Fig. 5.6. Classification of the MPPT strategies for wind turbines. Data from [119]

From the Appendix A it is known that C_p for a fixed pitch angle (β=0) is:

$$C_p(\lambda) = c1 \cdot \left(\frac{c2}{\lambda_i} - c4\right) \cdot e^{-\frac{c5}{\lambda_i}} + c6 \cdot \lambda \tag{5.2}$$

where the aerodynamic constants are c1=0.5176, c2=116, c3=0.4, c4=5, c5=21, c6=0.0068. Notice that equation 5.2 only depends on λ, namely on shaft speed ω and wind speed V.
For the OTC used in this thesis the optimal torque is calculated as:

$$T_{opt} = \frac{0.5\pi\rho C_{p\_max} R^5}{{\lambda_{opt}}^3} \cdot \omega^2 = K_{opt} \cdot \omega^2 \tag{5.3}$$

where C_{p_max}=0.48 at the optimal tip speed ratio λ_{opt}=8.1, the air density ρ=1.13 kg/m^3, rotor radius R is 0.8 m, and ω is the feedback of the rotational speed. From equation 5.3 the current reference is calculated as:

$$I_{ref} = \frac{P_{max}}{v_{dc}} = \frac{T_{opt} \cdot \omega}{v_{dc}} = \frac{K_{opt} \cdot \omega^3}{v_{dc}} \tag{5.4}$$

where P_{max} is the theoretical maximum power obtained from the turbine, v_{dc} is the DC bus voltage at the output of the passive rectifier, and T_{opt} is calculated from equation 5.3. Note that in equation 5.3 the constant K_{opt} is calculated as:

$$K_{opt} = \frac{0.5\pi\rho C_{p\_max} R^5}{{\lambda_{opt}}^3} \tag{5.5}$$

From equations 5.4 and 5.5 is important to notice that the two variables that have the biggest influence in the power output are the turbine radius R which is raised to the power of 5 and the rotational speed ω raised to the power of 3.

In Fig. 5.7 four of the most used MPPT methods are shown using the FOC. Note that Fig. 5.7c is the same as Fig. 5.4a, this is the OTC MPPT with FOC. Here is important to mention that all the other MPPT methods (TSR, PSF and P&O) require additional sensors apart from the encoder. For example, in Fig. 5.7a the wind speed for the TSR (λ) calculation comes from an anemometer close to the turbine (normally on the same tower). In Fig. 5.7b the Power signal comes from a voltage and a current sensor on the DC bus. In Fig. 5.7d the power signal also comes from two additional sensors (voltage and current on the DC bus). From the reliability point of view having more sensors makes the WECS prone to failure, therefore the OTC with FOC combination (Fig. 5.7c) is the most reliable.

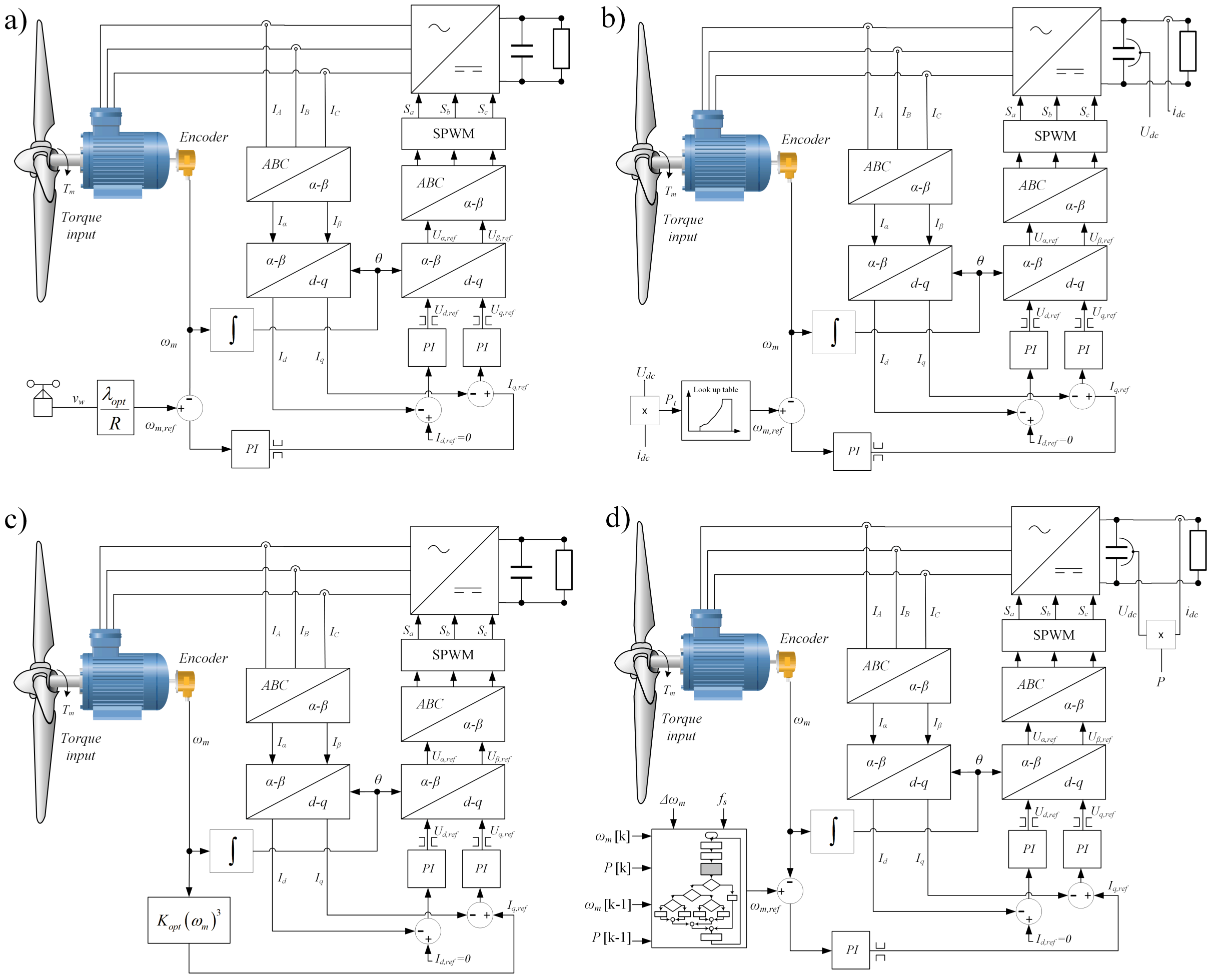

Fig. 5.7. Four MPPT strategies, TSR (a), PSF (b), OTC (c), and P&O (d)

6. Simulation and co-simulation of a PMSG with Passive Rectifier and Boost Converter

In this Chapter some results of the first analyses made with the designed PMSG are presented. First, as a validation for the co-simulation approach described in Chapter 1 section 1.3, a passive rectifier with a simple capacitor and resistor is presented. Then, the same arrangement is analysed including a boost converter as one of the topologies presented at the beginning of Chapter 5, finally some concluding remarks about the obtained results are discussed.

6.1. Idea of the Co-simulation vs simulation

As it was described in Chapter 1 section 1.3, the co-simulation is the interaction between different software programs to simulate the behaviour of a complex interconnected system. In other words, each specific software simulates the subsystem in which they are specialised e.g. electromagnetic transient, control, fluid dynamics, heat transfer, etc and these software programs share data (results) in *real-time*.

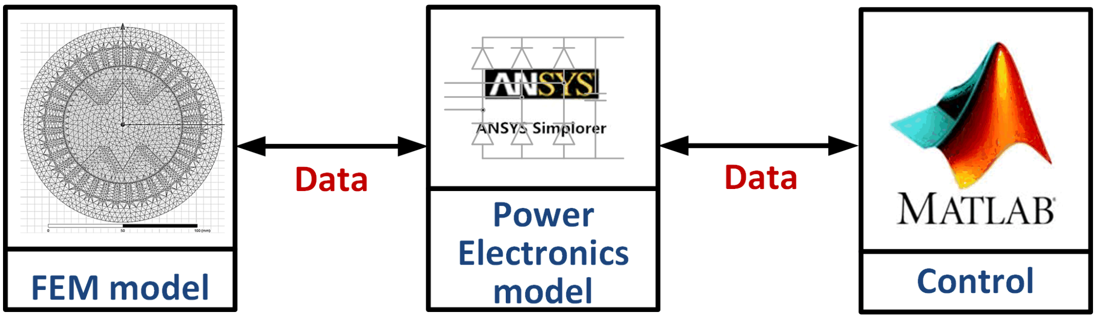

Fig. 6.1. Idea of the Co-simulation with more than two software programs

In Fig. 6.1 the interaction between the software for the approach used in this thesis is shown. Note that in this thesis the communication is regulated by the software in the middle (ANSYS Simplorer), which in this case acts as the *master*, while the FEA software (ANSYS Maxwell) and the control simulation software (Matlab Simulink) are the *slaves*. Put differently, ANSYS Simplorer has a fixed time step of $50\mu s$ in this case, therefore the other software would have to make calculations at this same time step to feedback the results *on time* to the master.

In comparison, for the simulation, the mathematical model for the PMSG on the rotating reference frame can be found in the literature [15, 139, 140] as:

$$\frac{d}{dt} i_d = \frac{1}{L_d} V_d - \frac{R}{L_d} i_d + \frac{L_q}{L_d} p\omega i_q \tag{6.1a}$$

$$\frac{d}{dt} i_q = \frac{1}{L_q} V_q - \frac{R}{L_q} i_q - \frac{L_d}{L_q} p\omega i_d - \frac{p\omega \Phi_{PM}}{L_q} \tag{6.1b}$$

$$T_e = \frac{3}{2} p \left[\Phi_{PM} i_q + (L_d - L_q)\, i_d i_q\right] \tag{6.1c}$$

where: L_d and L_q are the d and q axis inductances, R is the resistance of the stator windings, i_d and i_q are the d and q axis currents respectively, V_d and V_q are the d and q axis voltages, ω is the angular velocity of the rotor in radians per second, Φ_{PM} is the amplitude of the flux induced by the permanent magnets of the rotor into the stator phases, p is the number of pole pairs, and T_e is the electromagnetic torque. L_d and L_q inductances represent the relation between the phase inductance and the rotor position due to the saliency of the rotor. For example, the inductance measured between phase a and phase b when phase c is left open is given by:

$$L_{ab} = L_d + L_q + (L_q - L_d)\, cos\left(2\theta_e + \frac{\pi}{3}\right) \tag{6.2}$$

where: θ_e is the electrical angle. For a round rotor (no saliency) the phase inductance is:

$$L_d = L_q = \frac{L_{ab}}{2} \tag{6.3}$$

In Fig. 6.2 the values for L_{ab} depending on θ_e are shown. Note that since the inductance is sinusoidal and the input and output of the model use the Park and inverse Park transformation respectively, the model always give a sinusoidal output.

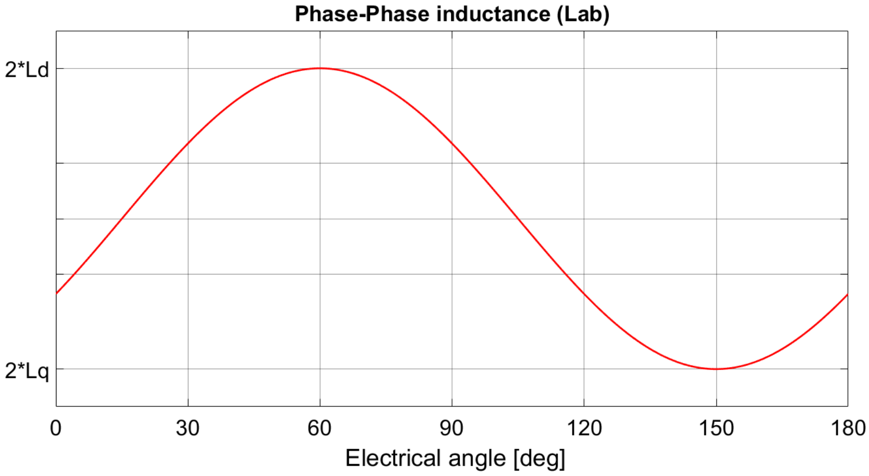

Fig. 6.2. Phase to phase inductance measured when third phase is left open.

The mechanical part of the model is given by:

$$\frac{d}{dt}\omega = \frac{1}{J}\left(T_e - T_m\right) \tag{6.4}$$

where ω is the rotational speed, J is the system inertia, T_e is the electromagnetic torque, and T_m is the mechanical torque produced by the prime mover.

The complete model in the rotating reference frame is shown in Fig. 6.3 . This is the same model used in Simulink's SimPower system toolbox and other well-known simulation software, e.g. PSIM, PLECS, etc. Due to the sinusoidal behaviour of the model's output, this model is also known as the *sinusoidal model*.

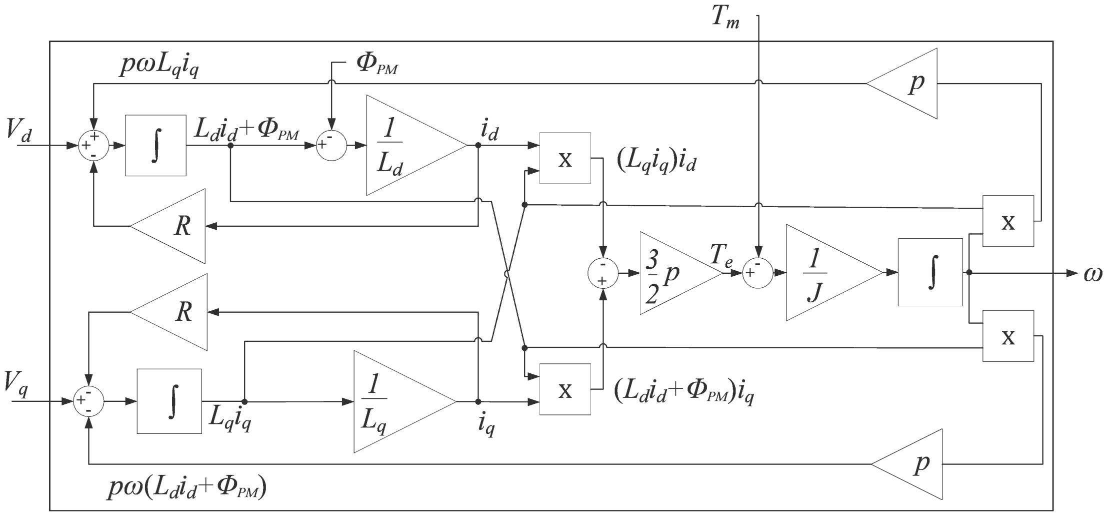

Fig. 6.3. Simplified model of the PMSG in the rotating reference frame.

Another model slightly more complex and widely used in the simulation software [140] is:

$$\frac{d}{dt}i_a = \frac{1}{3L_s}\left(2v_{ab} + v_{bc} - 3R_s i_a + p\omega\Phi_{PM}\left(-2\Phi'_a + \Phi'_b + \Phi'_c\right)\right) \tag{6.5a}$$

$$\frac{d}{dt}i_b = \frac{1}{3L_s}\left(-v_{ab} + v_{bc} - 3R_s i_b + p\omega\Phi_{PM}\left(\Phi'_a - 2\Phi'_b + \Phi'_c\right)\right) \tag{6.5b}$$

$$\frac{d}{dt}i_c = -\left(\frac{d}{dt}i_a + \frac{d}{dt}i_b\right) \tag{6.5c}$$

$$T_e = p\Phi_{PM}\left(\Phi'_a \cdot i_a + \Phi'_b \cdot i_b + \Phi'_c \cdot i_c\right) \tag{6.5d}$$

where L_s is the inductance of the stator windings, i_a, i_b and i_c are the a, b and c phase currents, v_{ab} v_{bc} are the ab and bc phase to phase voltages, Φ'_a, Φ'_b and Φ'_c are the a, b and c phase's electromotive forces in per unit value to the amplitude of the flux Φ_{PM} represented in Fig. 6.4. Due to the trapezoidal nature of the model's output this is also known as the *trapezoidal model*.

From equations 6.1a to 6.1c and 6.5a to 6.5d is visible that although the mathematical model is able to model the dynamics three-phase PMSG, the first order differential equations fail to model any of the nonlinearities of the magnetic circuit, this means it models no saturation of the stator and rotor iron nor the permanent magnet B-H curve.

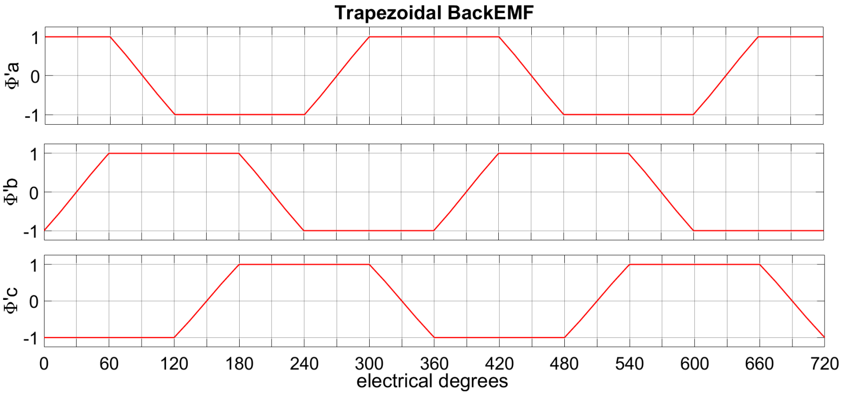

Fig. 6.4. Electromotive force Φ for the SimPower systems' trapezoidal model

6.2. Comparative analysis of classical simulation and co-simulation of the PMSG with passive rectifier

The first analysis done with the PMSG was the validation of the co-simulation method by comparison with the classical models very popular in the automatic control and digital signal processing software, e.g. Matlab Simulink. These results are compared against laboratory measurements done with the built PMSG (with W shape magnets).

In Fig. 6.5 the schematic diagram of the system with PMSG and passive rectifier is shown. Notice that an IM is used as torque source for the experiment.

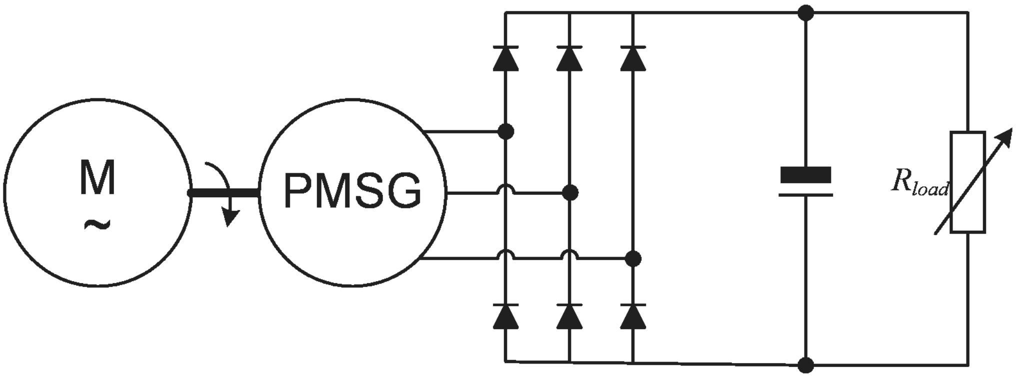

Fig. 6.5. Schematic diagram of the test with passive rectifier

Here the comparison was made between two different mathematical models of the PMSG available in the popular Simulink software for Model-Based Design (MBD), specifically in the SimPower system's library of this software.

In Fig. 6.6 the schematics of both methods, classical (mathematical) modelling and co-simulation (with FEA) are shown. Notice that in Fig. 6.6b the symbol of the PMSG machine with the W shape magnets is a link to the FEA software.

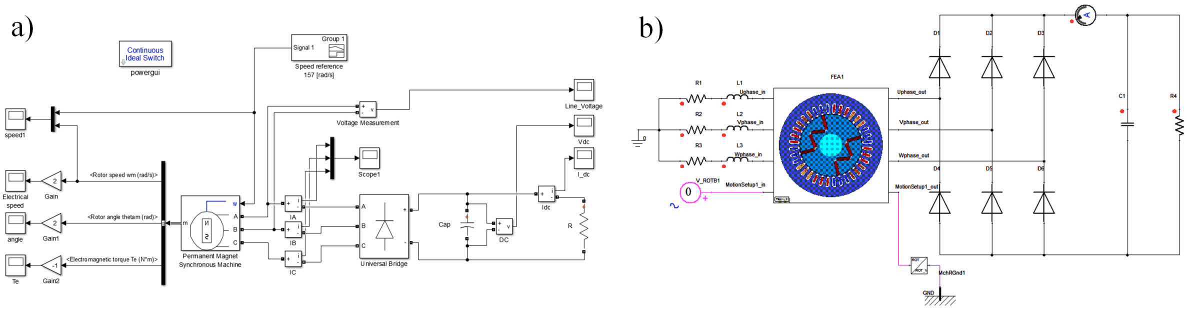

Fig. 6.6. Schematic diagram of the simulation (a), and co-simulation (b) models

In Fig. 6.7 the phase currents of both mathematical models (sinusoidal and trapezoidal) of the PMSG are shown. Notice that the shape of the currents is different but the action of the diode rectifier is the same. In this test the system includes the machine and the non-linear circuit elements namely the diodes.

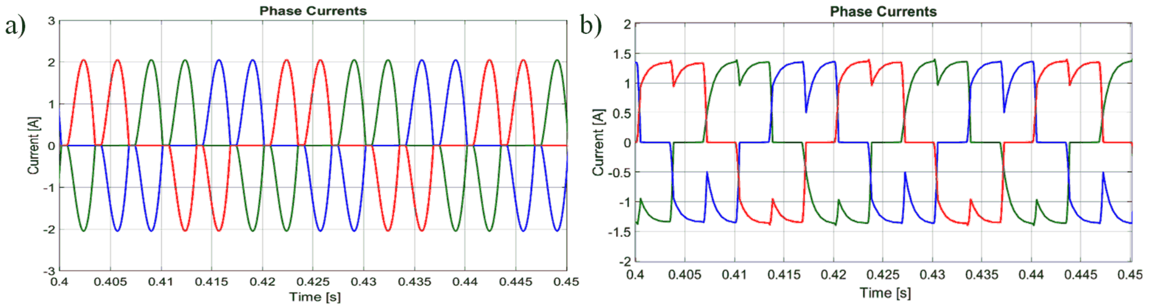

Fig. 6.7. Phase currents with passive rectifier for sinusoidal model (a), and trapezoidal model (b)

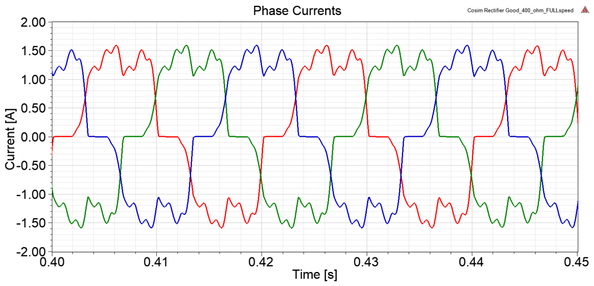

Fig. 6.8. Phase currents with passive rectifier for co-simulation

In Fig. 6.8 the phase currents for the co-simulation are shown. Here also the action of the non-linear elements (diodes) is visible. The shape of the currents is more similar to the trapezoidal model of Fig. 6.7b, this means that the PMSG with the W shape magnets is similar to a trapezoidal flux machine i.e. a Brushless DC Machine (BLDCM). However, notice that the co-simulation results give more details around the peaks of the current, these contain information about the machine and its geometry.

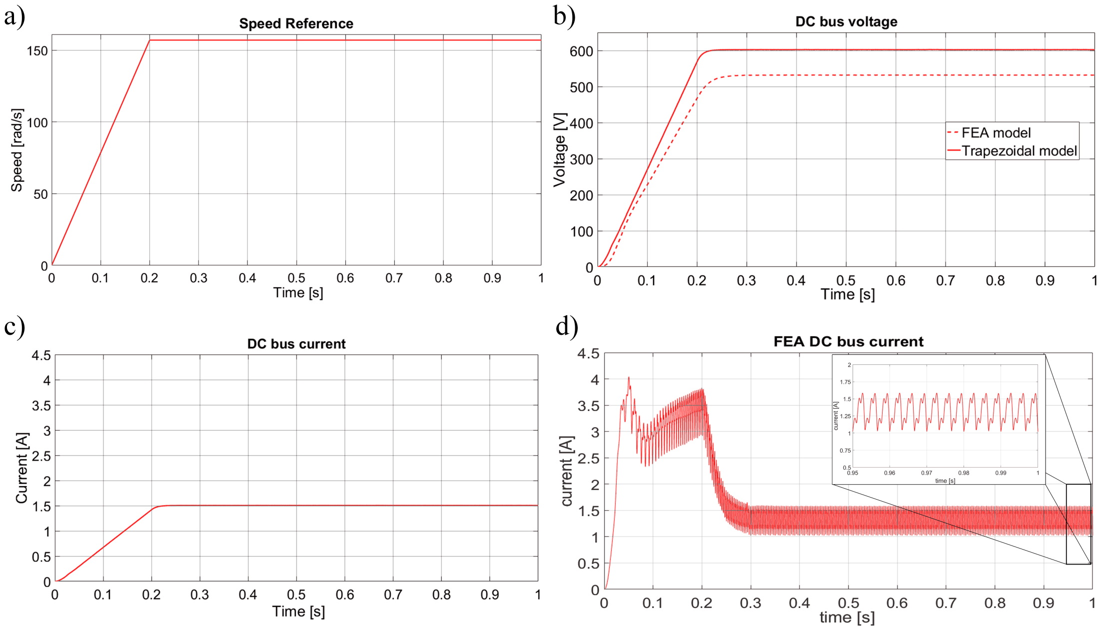

Fig. 6.9. Speed reference for simulation and co-simulation (a), DC bus voltage from simulation and co-simulation (b), DC bus current from simulation (c) and DC bus current from co-simulation (d) all with a 400 ohm load

In Fig. 6.9 the results for the simulation with trapezoidal model and co-simulation are shown. The capacitor and load where the same for both, namely 1000 μF and 400 ohm. From Fig. 6.9b, 6.9c and 6.9d the differences in the model's output are clear. Note that the co-simulation DC bus current correctly predicts an initial transient peak current while the Simulink's trapezoidal model shows no transient. Also note in Fig. 6.9d the DC bus current shows a ripple not visible in the Simulink simulation. The parameters of the Simulink model can be seen in Appendix B.

6.3. Comparison with measurements

In order to asses correctly the accuracy or level of detail that the co-simulation can offer, some experimental tests were done and compared with the simulation and co-simulation results. In Fig. 6.10 two test results are shown. In Fig. 6.10a and b the results for a 0.5 second speed ramp from 0 to nominal speed (1500 rpm). In Fig. 6.10c and d the results for 0.5 second speed ramp from 0 to half nominal (750 rpm).

With the results shown in Fig. 6.10a is clear that the co-simulation provide better results since the trapezoidal model overestimates the DC bus voltage ($\sim$ 40 V more) in steady state.

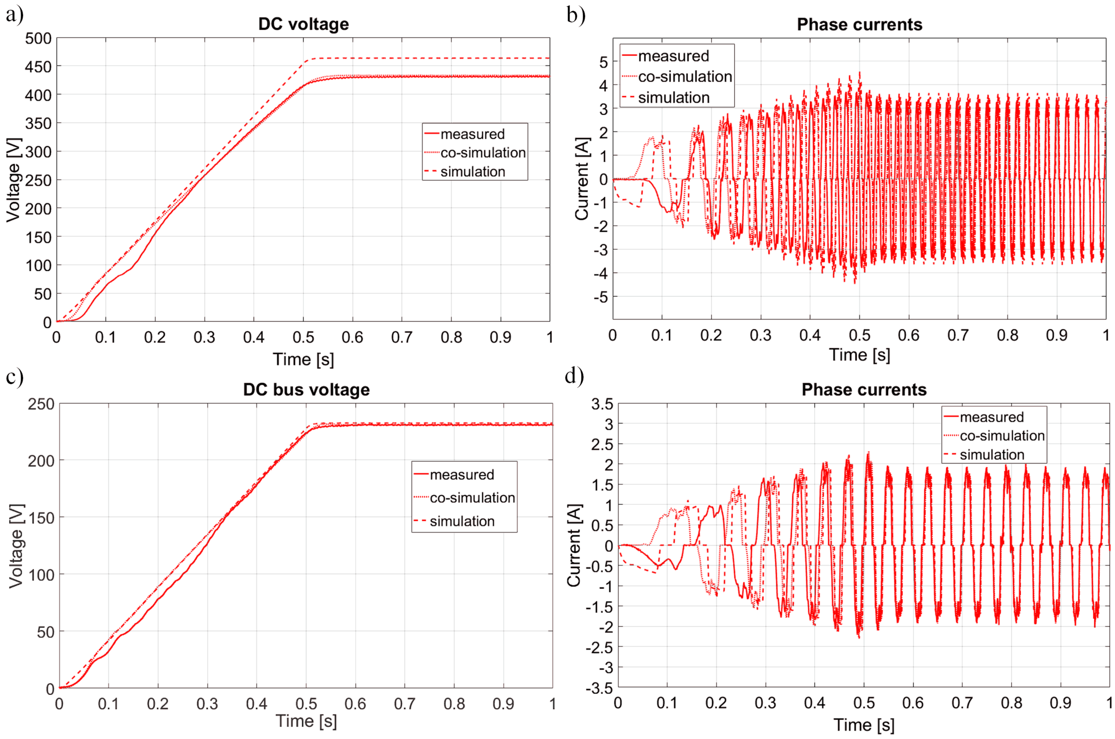

Fig. 6.10. Transient comparison with a 140 ohm load from 0 to 1500 rpm, DC bus voltage (a), phase currents (only one phase shown for clarity) (b), and from 0 to 750 rpm DC bus voltage (c) and phase currents (d)

Although the results at half the nominal speed are similar for the two methods (simulation and co-simulation), the co-simulation method offers superior resemblance to the measured currents as it can be seen in Fig. 6.11. Further results were published in [141].

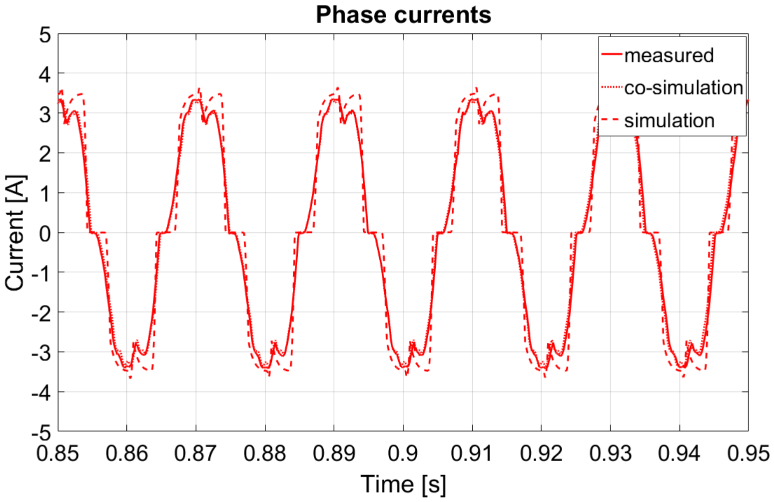

Fig. 6.11. Phase current comparison: simulation, co-simulation and measurements at nominal speed with 140 ohm load, only one phase is shown for clarity

6.4. Comparative analysis of classical simulation and co-simulation of the PMSG with passive rectifier and boost converter

With the co-simulation validated, further experiments were co-simulated. In Fig. 6.12 the schematic of the simulated WECS with boost converter is shown.

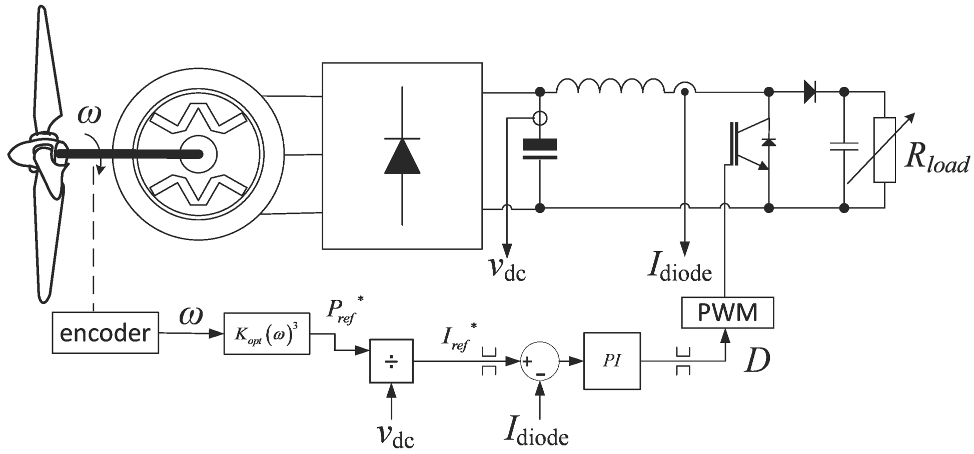

Fig. 6.12. WECS schematic with passive rectifier and boost converter for MPPT

Here the model of the aerodynamics of a three-blade WT rotor (0.8 m radius) described in Appendix A.1 was used as well as a boost converter in order to obtain the maximum power from the wind. Also, notice from Fig. 6.12 that the MPPT method is the OTC described before (Chapter 5). In Fig. 6.13 the diagram of the Simulink SimPower system simulation is presented.

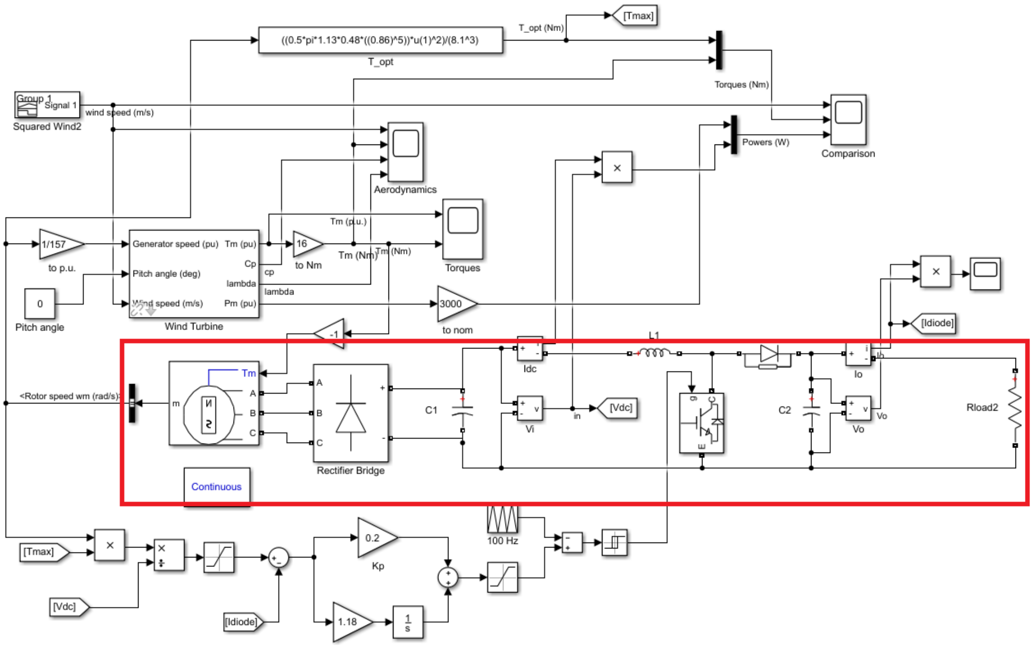

Fig. 6.13. Simulink SimPower system diagram with the trapezoidal model of the PMSG

Notice in Fig. 6.13 that all the components inside the red rectangle are replaced by their equivalent model in the co-simulation. In Fig. 6.14 the co-simulation diagram of the WECS with the boost converter is shown. Notice that is similar to Fig. 6.6b since it also has the nonlinear components (diodes) but the control for MPPT is done with a transistor. Also, in comparison to 6.6b the input of the system is not a rotational speed but a torque given by the WT model's output.

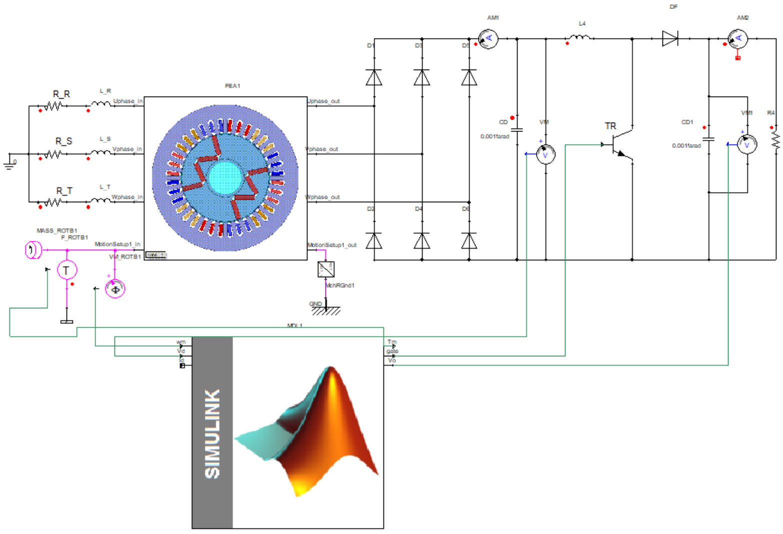

Fig. 6.14. Co-simulation diagram with boost converter

The control diagram of the co-simulation is shown in Fig. 6.15.

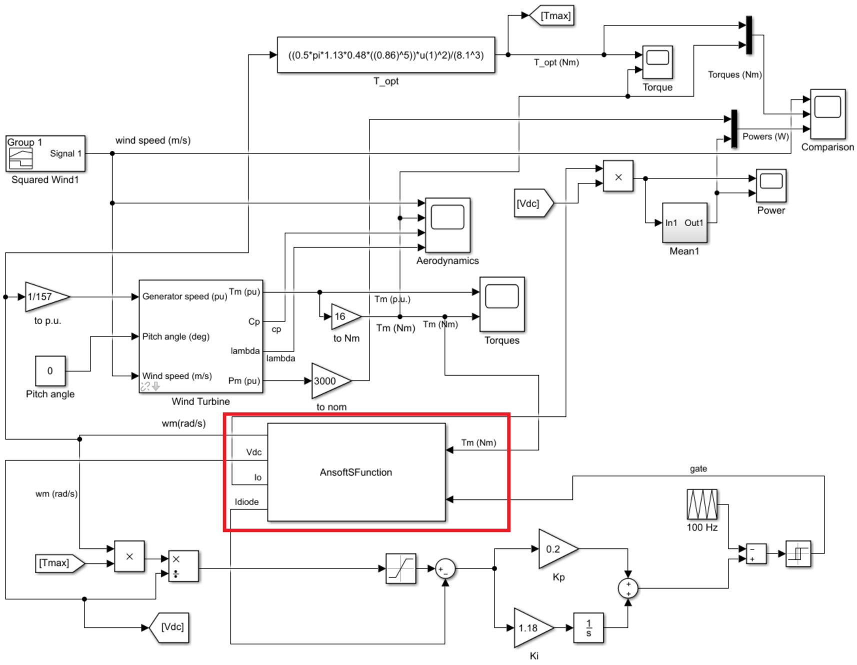

Fig. 6.15. Simulink system diagram with link (red rectangle) to the Simplorer co-simulation

In Fig. 6.16 the input signal to the WECS simulation and co-simulation is presented. Note that the wind speed is given by a staircase signal type, this is done in order to assess the system's response to the MPPT strategy. In Fig. 6.17 some results of the simulation (a, b, c) are compared to the co-simulation (d, e, f).

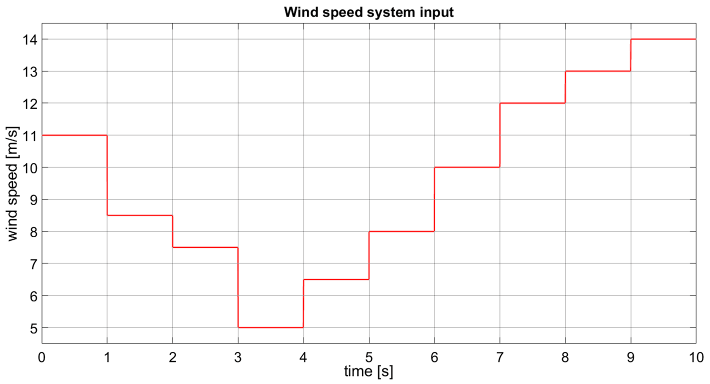

Fig. 6.16. Input signal for both simulation and co-simulation

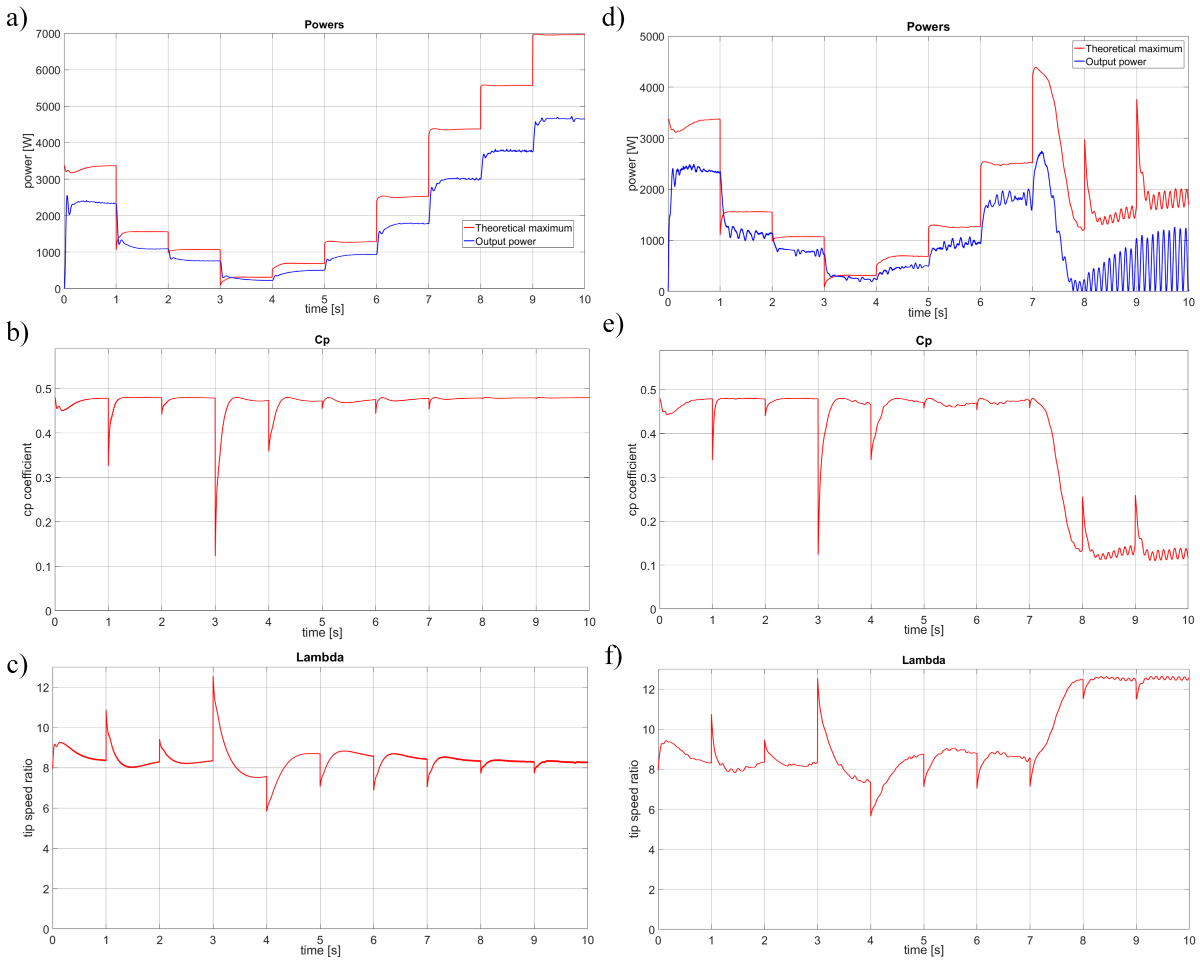

Fig. 6.17. Comparison of the results for the simulation, power (a), C_p (b) tip speed ratio (c) and co-simulation power (d), C_p (e) tip speed ratio (f)

Observe that in the co-simulation (Fig. 6.17d) the PMSG is unable to produce the 3 kW of power that the turbine could produce with a wind speed of 12 m/s at time 7 s. Since the PMSG cannot produce that power the WT stalls and the power coefficient C_p drops to almost 10% (0.1) and the tip speed ratio λ deviate from the optimal (λ_{opt}=8.1). This can be explained by observing Fig. 6.18, there the phase currents for the simulation and co-simulation are presented.

Note that in Fig. 6.18b the co-simulation phase currents reach up to 10 A amplitude and saturate the PMSG.

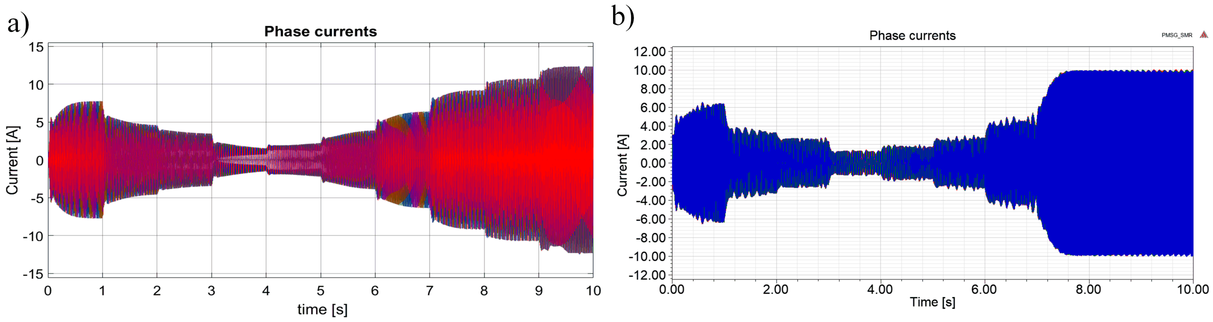

Fig. 6.18. Phase currents for simulation (a), and co-simulation (b)

In Fig. 6.19 the DC bus voltage is compared and in Fig. 6.20 the rotational speed in radians per second for simulation and co-simulation is presented.

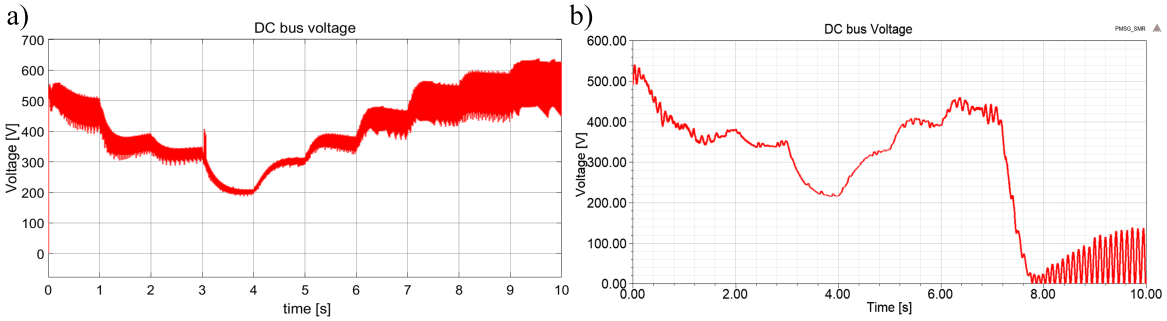

Fig. 6.19. DC bus voltage for simulation (a), and co-simulation (b)

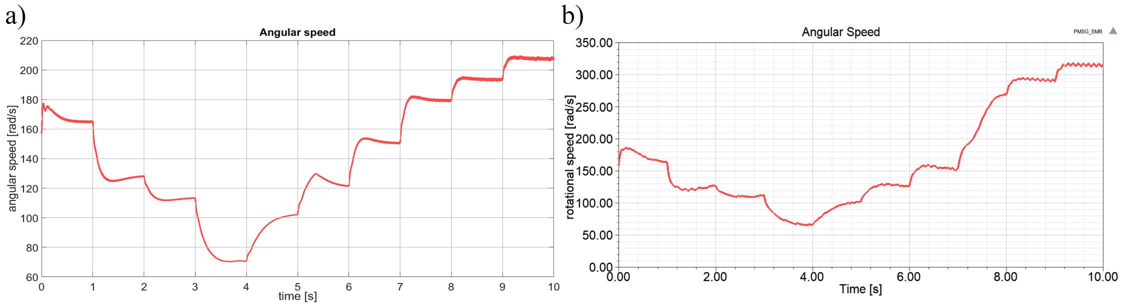

Fig. 6.20. Angular speed in radians per second for simulation (a), and co-simulation (b)

From Fig. 6.20b it can be observed that the PMSG is still rotating after t=7 s, but the DC bus voltage collapses to 0 V with a ripple (see 6.19b) since the machine is over its nominal speed (157 rad/s). In Fig. 6.21 the results for another simulation (a, b, c, d) and co-simulation (e, f, g, h) with longer blades (0.86 m radius) and feedback amplification are presented. The input wind speed is the same as Fig. 6.16.

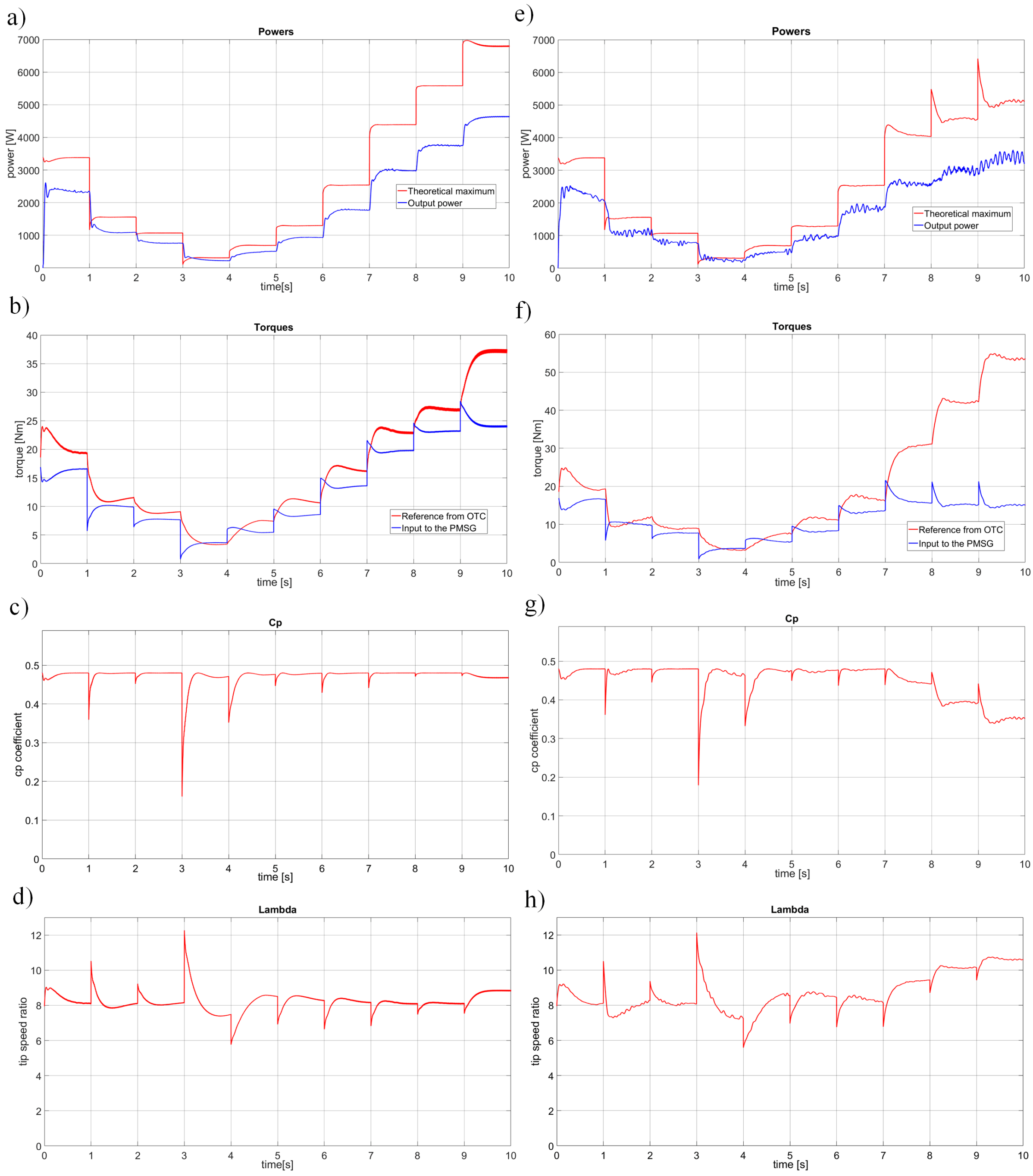

Fig. 6.21. Results with 0.86 m blades for simulation power (a), torque (b), C_p (c), tip speed ratio (d) and co-simulation power (e), torque (f), C_p (g), tip speed ratio (h)

Also in this scenario (longer blades and feedback amplification) the explanation of the behaviour of the PMSG is related to the phase currents. In Fig. 6.22 the phase currents for the scenario with longer blades are presented. Notice in Fig. 6.22b that the phase current amplitude does not reach 10 A, therefore the WECS is able to track the maximum power point closer even at high wind speeds.

Notice in Fig. 6.21g and 6.21h that the C_p and λ deviate from the optimal at high wind speeds (after 7 s). Apart from these deviations, Fig. 6.21e shows that the PMSG is able to generate over 3 kW of power at those wind speeds in this configuration (longer blades). A deeper discussion about the results shown in this section was published in [142].

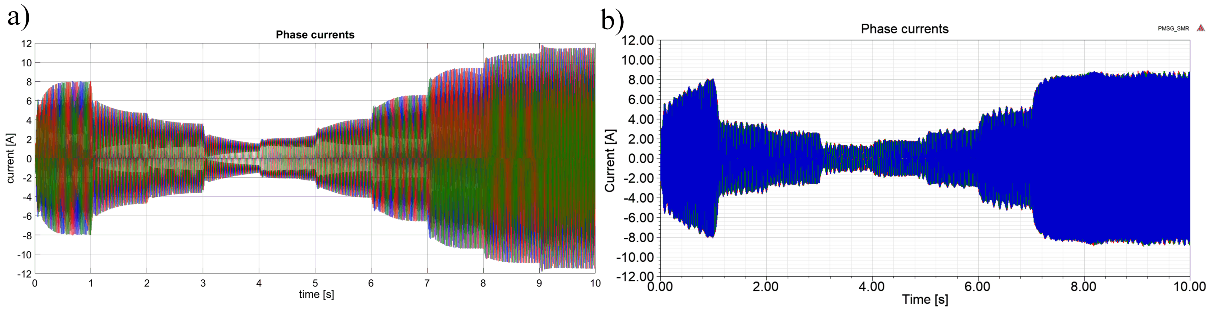

Fig. 6.22. Phase currents for 0.86 m blades, simulation (a), and co-simulation (b)

6.5. Conclusions

In this Chapter some results of the co-simulation were compared against the classical simulation models. From the initial validation and comparison with measurements (section 6.3) it was clear the advantages that the co-simulation deliver over the classical PMSG models. Furthermore, the co-simulation was applied to a complete WECS with MPPT strategy and its results showed that the machine might not work as intended at certain wind speeds.

Here is important to mention that the machine would be operating in overload mode since as stated in the IM used as basis for the PMSG the stator windings are designed for a 3.5 A nominal current and up to 18 A start-up current (short time) according to [62].

7. Full converter with Field Oriented Control

As stated in Chapter 5, a widespread approach to control the WT is the use of a Machine Side Converter (MSC), namely a full converter connected to the generator. In this thesis the MSC is operated with the field oriented control. In this chapter the setup for the MSC under FOC is presented. Then, some initial validation of the co-simulation results compared against laboratory measurements are presented. Finally some results connected with the demagnetization model explained in Chapter 3 are discussed.

7.1. Field Oriented Control

The vector control also called Field Oriented Control in the literature [139, 143, 144], is a control method in which the stator currents and voltages of a multiphase machine (three in this thesis) are represented as two orthogonal components that can be visualized as a vector. In Fig. 7.1 the representation of such a coordinate system is shown.

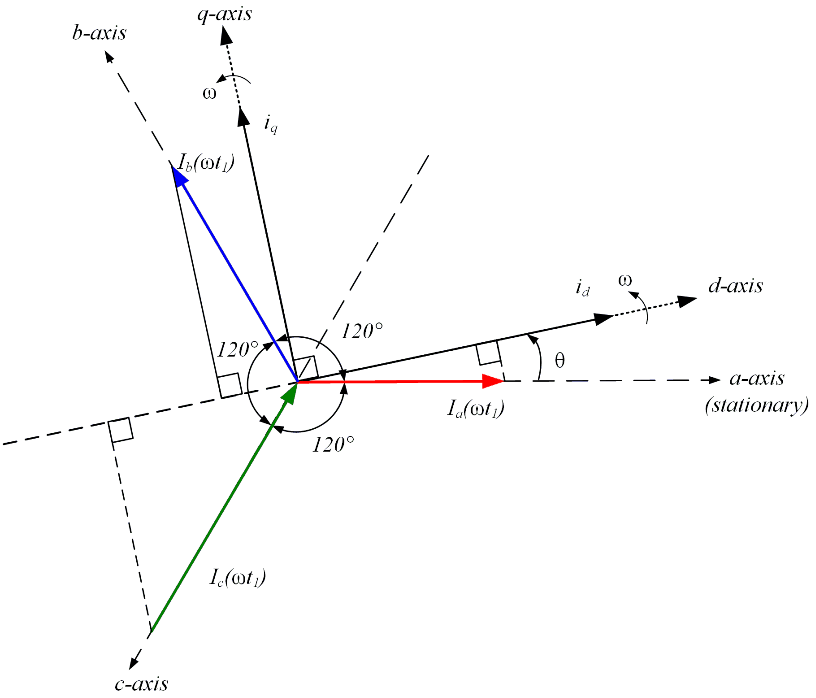

Fig. 7.1. Vector diagram illustrating the principle of FOC

In Fig. 7.1 the representation of the amplitudes of the three phase currents (i_a,i_b and i_c) are decomposed by their projections over the dq rotating reference frame's axis and the sum of their components over each axis conform the vectors d and q.

In Fig. 7.2 the explanation to: *why to do this transformation to a rotating reference frame?* becomes more clear. Notice in the lower right corner the plot with the amplitude of the i_d and i_q vectors. There, the constant value of those currents (almost DC values), contain the information of the three phases to control.

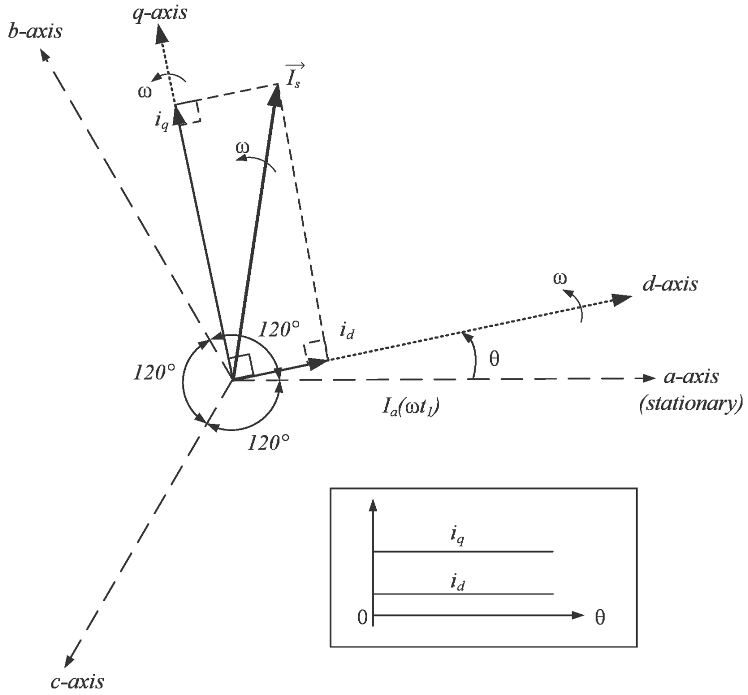

Fig. 7.2. Decomposition of the vector $\overrightarrow{I_s}$ into the dq rotating reference frame

As is well known from the control theory [145], the controllers (e.g. PID) work well when they have to compare to semi-constant values (feedback and reference), therefore the ability to represent the whole electromagnetic behaviour of the machine with two variables is very useful. As shown in the inset of Fig. 7.2 the two values are independent of the rotor angle θ, this means that under steady state conditions (no change in the currents), the variables i_d and i_q are constant through the time.

Paraphrasing the last paragraph, it is easier to control two quasi-stationary variables than to track three amplitudes and three phase angles of time varying signals (sinusoidal signals).

The FOC has also downsides. As it can be seen in both, Fig. 7.1 and Fig. 7.2, the angle θ is of paramount importance when it comes to calculating the vectors i_d and i_q (namely transformations). Furthermore, the angle has to be coincident with the position of the rotor, specifically with the position of the magnets in the rotor. In Fig. 7.3 the position of the d and q vectors in the W shape machine is shown.

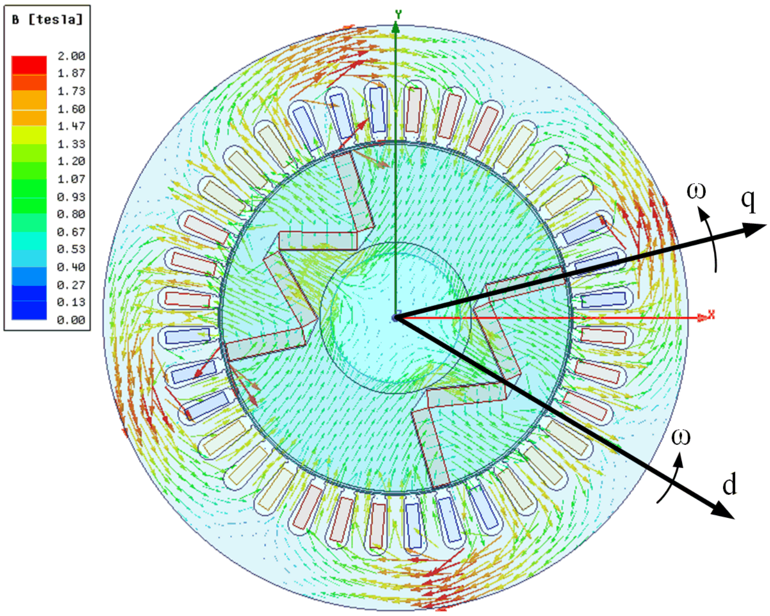

Fig. 7.3. Alignment of the d-axis and q-axis over the actual PMSG rotor

Notice that the alignment of the d axis in Fig. 7.3 is with the magnetic field, namely the magnetic flux density vector $\overrightarrow{B}$ coming out of the permanent magnets. From Fig. 7.3 is also clear why this control method is called "*Field Oriented*". Here, ω is the synchronous speed of the generator and can be calculated as:

$$\omega = \frac{\omega_e}{p} = \frac{2\pi f_s}{p} \tag{7.1}$$

where ω_e is the electrical speed, p is the number of pole pairs (2 in this case), f_s is the stator frequency in Hertz. The angle θ can be found from:

$$\theta(t) = \int_0^t \omega(t)dt + \theta_0 \tag{7.2}$$

where θ_0 is the initial angular position. Because the alignment of the dq axis with the magnetic field from the rotor is important to have a correct θ_0 and/or a correct alignment of the encoder over the shaft.

7.2. Transformations

As explained in the last section the FOC strongly depends on the transformations to achieve its control goal. In this thesis the FOC was realized with the two-step transformation method. First the stator currents are transform to the two-phase variables in a stationary reference frame called the *abc*/$\alpha\beta$ transformation or *Clarke transformation* in honour to its pioneer: professor Edith Clarke.

The Clarke transformation is given by:

$$\begin{bmatrix} i_\alpha \\ i_\beta \end{bmatrix} = \frac{2}{3} \begin{bmatrix} 1 & -1/2 & -1/2 \\ 0 & \sqrt{3}/2 & -\sqrt{3}/2 \end{bmatrix} \cdot \begin{bmatrix} i_a \\ i_b \\ i_c \end{bmatrix} \tag{7.3}$$

where i_α and i_β are the two-phase variables that represent the three-phase current i_a, i_b and i_c in the stationary reference frame. Then a second transformation is done to convert the $\alpha\beta$ signals to DC variables. This transformation to a *rotating reference frame* was pioneered by Robert. H. Park, therefore it is known as $\alpha\beta$*/dq* transformation or *Park transformation*, and is given as:

$$\begin{bmatrix} i_d \\ i_q \end{bmatrix} = \begin{bmatrix} \cos\theta & \sin\theta \\ -\sin\theta & \cos\theta \end{bmatrix} \cdot \begin{bmatrix} i_\alpha \\ i_\beta \end{bmatrix} \tag{7.4}$$

where i_d and i_q are the two quasi-stationary variables (DC variables) that represent all the information of the three-phase *abc* variables. A further step in the FOC used in this thesis is the transformation of these two DC variables back to the alpha-beta reference frame. This transformation is called *Inverse Park* and is given by:

$$\begin{bmatrix} i_\alpha \\ i_\beta \end{bmatrix} = \begin{bmatrix} \cos\theta & -\sin\theta \\ \sin\theta & \cos\theta \end{bmatrix} \cdot \begin{bmatrix} i_d \\ i_q \end{bmatrix} \tag{7.5}$$

Notice again the importance of the angle θ in equations 7.4 and 7.5. Another more general transformation is the *abc/dq* transformation and is given by:

$$\begin{bmatrix} i_d \\ i_q \end{bmatrix} = \frac{2}{3} \begin{bmatrix} \cos\theta & \cos(\theta - 2\pi/3) & \cos(\theta - 4\pi/3) \\ -\sin\theta & -\sin(\theta - 2\pi/3) & -\sin(\theta - 4\pi/3) \end{bmatrix} \cdot \begin{bmatrix} i_a \\ i_b \\ i_c \end{bmatrix} \tag{7.6}$$

Notice that by setting θ to zero in equation 7.6 then the Clarke transformation is obtained (equation 7.3), this happens since the $\alpha\beta$ reference frame does not rotate in the space (θ=0).

The dq variables contain all the information of the three-phase abc variables assumed that the three-phase system is balanced, this means:

$$i_a + i_b + i_c = 0 \tag{7.7}$$

this also means that given two independent variables the third one can be calculated.

For the Clarke transformation the balance assumption is not necessary since the original transformation was composed of three variable $\alpha\beta\gamma$ as shown in [146], but the variables γ is zero when the system is balanced.

7.3. Analysis of the PMSG under Field Oriented Control

In this thesis the interaction of the PMSG with the full converter under DFOC is investigated. In Fig. 7.4 the schematic diagram of the system under test is presented.

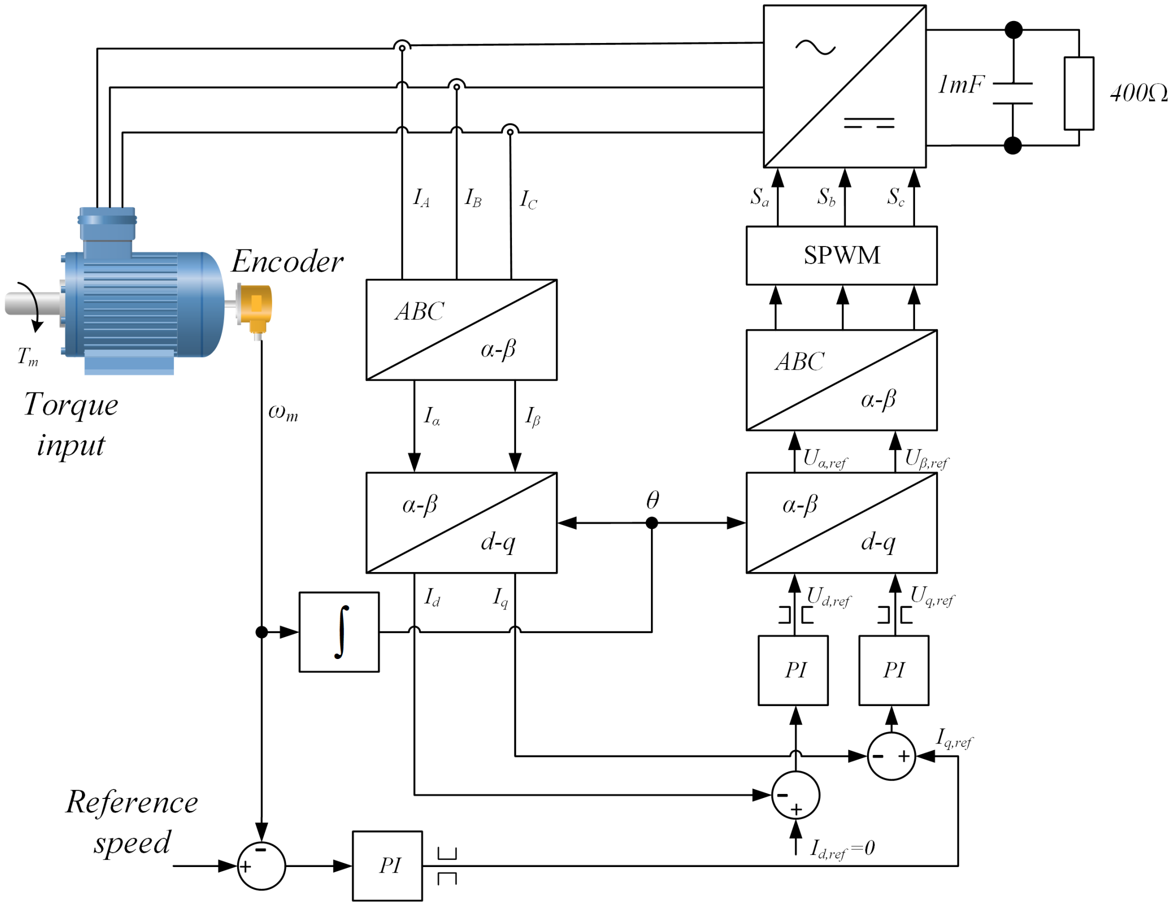

Fig. 7.4. Schematic diagram of the PMSG with full converter under DFOC

In Fig. 7.4 the three currents are measured and converted to $\alpha\beta$ with the Clarke transformation then to dq with the Park transformation compared against the reference values compensated with the currents' proportional and integral (PI) controllers and converted back to $\alpha\beta$ with the inverse Park transformation and to 3 sinusoidal signals with the inverse Clarke transformation. Notice that the reference signal for i_d is equal zero. This control scheme is called as zero d-axis current (ZDC) control in the literature [147]. Finally the three sinusoidal signals are compared against a triangular signal to generate the trigger signals for the two-level voltage source converter (2L-VSC), namely full converter. The angle θ is of very important in order to obtain the currents i_d and i_q.

Notice in Fig. 7.4 that the PI controllers are limited by *saturation*. The limits in the currents' PI controllers are set to 0.9 and -0.9 p.u. in order not to exceed the machine current ratings. Also the speed controller is limited to ± 45 with saturation. All PI controllers have anti-windup with clamping.

7.4. Co-simulation of the PMSG with the full converter

The setup described before is analyzed by means of the co-simulation approach. Here the machine is modeled by the FEM, then the power electronics' circuits are modeled in Simplorer (nowadays Twin Builder) a multidomain systems modeler with compilers of Verilog Hardware Description Language with Analog and Mixed Signal extensions (VHDL-AMS), Simulation Program with Integrated Circuit Emphasis (SPICE), C and C++ code. These and the ability to interconect different software make the Simplorer a very useful tool to design and analyze complex systems. Some early examples can be found in [148] and [149].

In Fig. 7.5 the diagram of the co-simulation is shown. Notice the resistors and the inductors before the PMSG symbol (connection to the FEM) these are the stator phase resistance and the phase leakage inductance (inductance of the end windings).

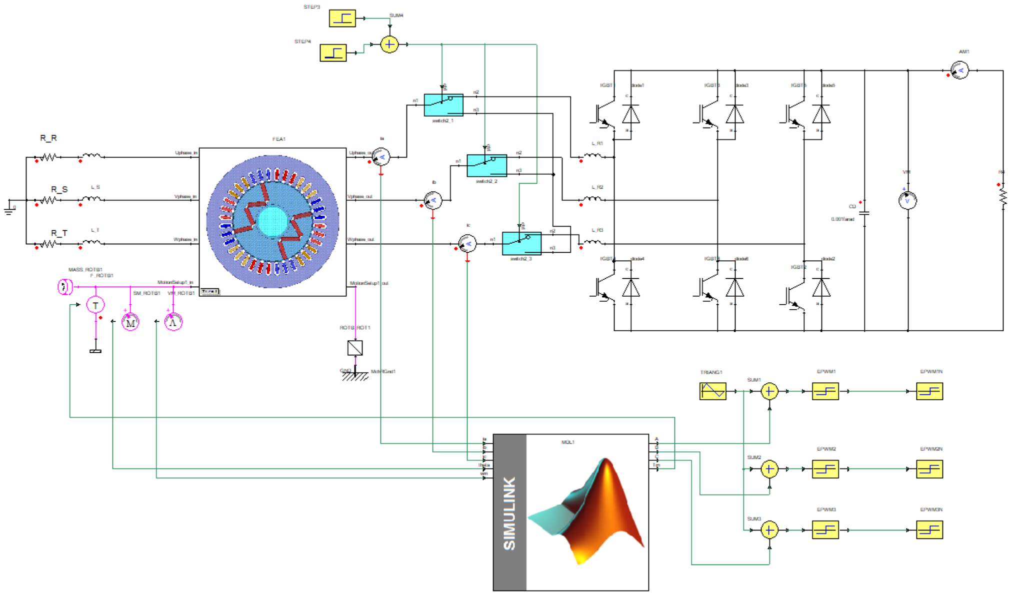

Fig. 7.5. Co-simulation diagram of the PMSG with full converter in the Simplorer software

The signals that come out from the Simulink symbol (link to the program) are the input torque to the PMSG, and the three reference voltages (sinusoidal signals) to compare against the triangular wave and generate the transistors' trigger signals. This comparison and trigger generation are the yellow blocks on the lower right side of Fig. 7.5. An example of this trigger signal generation can be seen in Fig. 7.6 where the three reference signals are compared against a triangular wave of 1kHz (Fig. 7.6a) generating the six trigger signals for the insulated gate bipolar transistors (IGBT) shown in Fig. 7.6b, the end result are the *sinusoidal like* currents presented in 7.6c.

From Fig. 7.6 it is important to mention that the defects clearly visible in the current signals (noise) are a consequence of mainly two sources: first, the very low switching frequency used in the PWM generation (1kHz) and its effect on the PMSG windings, second, the own nature of the PMSG back EMF that, as was shown in Chapter 6, section 6.3, is more *trapezoidal* than sinusoidal.

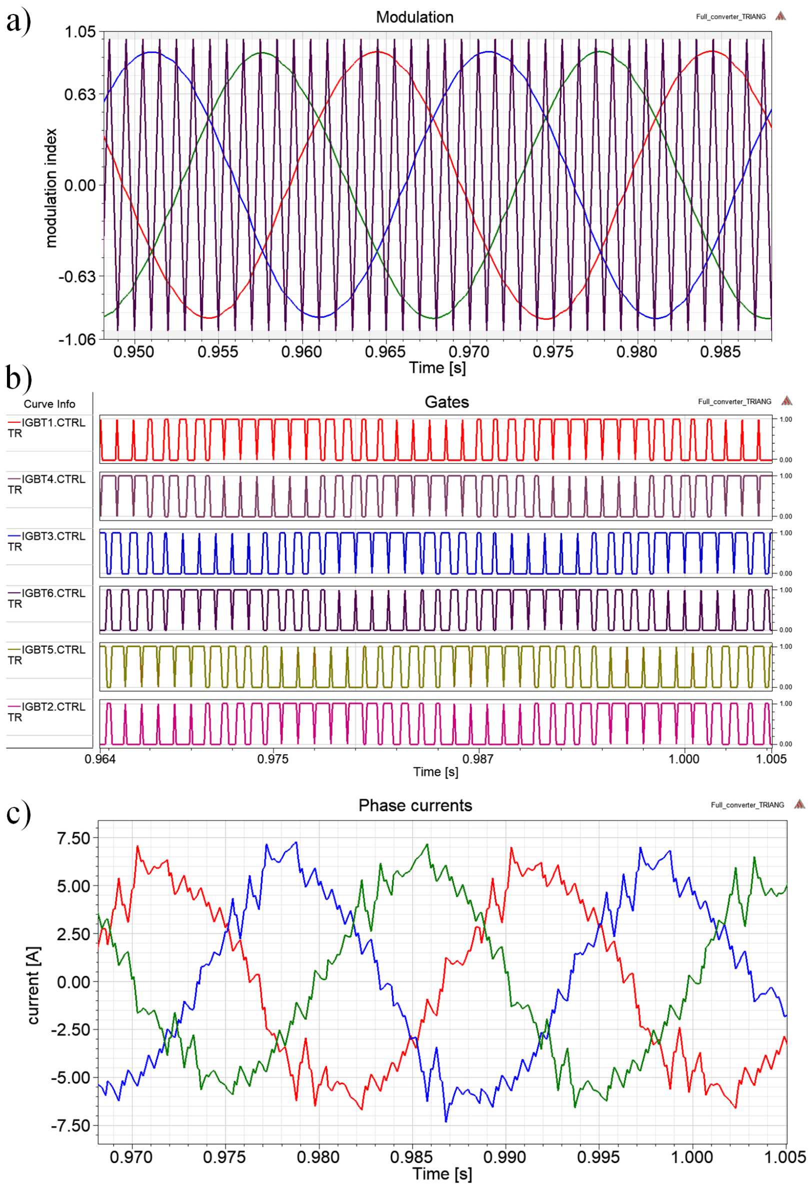

Fig. 7.6. Co-simulation signals (at 1kHz for demonstration purposes), from reference and triangular wave (a), trigger signals (b) and PMSG currents (c)

It is also important to mention that due to the defects in the current signals throughout this thesis a switching frequency of 3kHz was selected in order to obtain more sinusoidal like signals. Also, it is well known in the literature that a higher switching frequency eliminates most of this defects but since in this thesis the analysis of the electromagnetic phenomena in connection with the control is of main interest, and due to the co-simulation approach that calculates the electromagnetic fields at each time step of the co-simulation (as described in Chapter 6, section 6.1). Therefore, a higher switching frequency would make the co-simulation more time consuming due to the necessary smaller time step.

7.5. Validation of the full converter topology

In Fig. 7.7 the laboratory setup with the PMSG prototype is presented. In this setup the IM is applying the torque to the PMSG. The IM is controlled by an industrial drive and the prototype PMSG is controlled by an *in-house made* 2L-VSC (also called Machine Side Converter). The converter is controlled by the DS 1103 hardware in the loop (HIL) interface with the Control Desk terminal (these last two from the company DSpace).

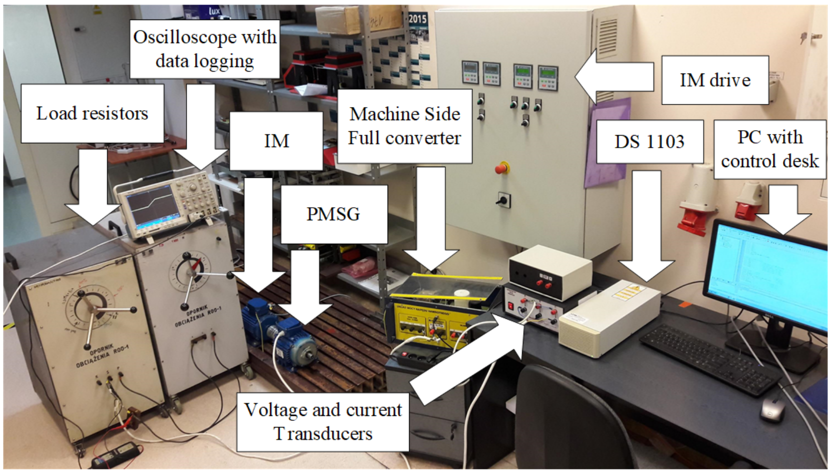

Fig. 7.7. Laboratory setup for the validation of the PMSG with full converter under DFOC

The load is connected to the DC bus of the 2L-VSC. Just as in the co-simulation the DC bus load is a 400 ohm resistance only that in the setup it is made of two resistors in series in order not to exceed each resistor maximum voltage rating of 500 V.

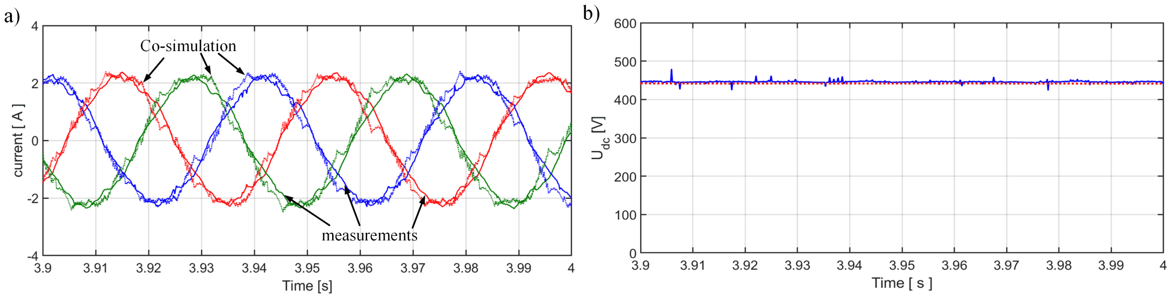

Fig. 7.8. Comparison between co-simulation results (dotted lines) and measurements (solid lines) at 750 rpm and 7 Nm input torque, for phase currents (a), and DC bus voltage(b)

In Fig. 7.8 the comparison between the measurements and the co-simulation of the PMSG under DFOC are presented. There the PMSG has a 750 rpm reference speed (half nominal speed) and the IM is applying 7 Nm of torque. Notice the similarities in the peak values. The difference between the co-simulation currents and the measurements is mostly due to the higher switching frequency (higher than 3 kHz) at which the experiments were done.

In Fig.7.9 the comparison between the measured dq currents (solid line) and the co-simulation dq currents (dotted lines) is shown. In Fig. 7.9a the raw co-simulation dq signals appear very noisy. The measurements are less noisy because the low pass filter nature of the digital system, namely the speed measurements come from an incremental encoder, with a limited number of counts per revolution (which provide a position), therefore, to obtain speed, a derivative operation is needed. As consequence, the rotational speed measure results are rather noisy and a suitable filter is used to reduce the noise as described in [150]. In Fig. 7.9b a smoothed co-simulation dq signals are shown. There a moving average filter was used.

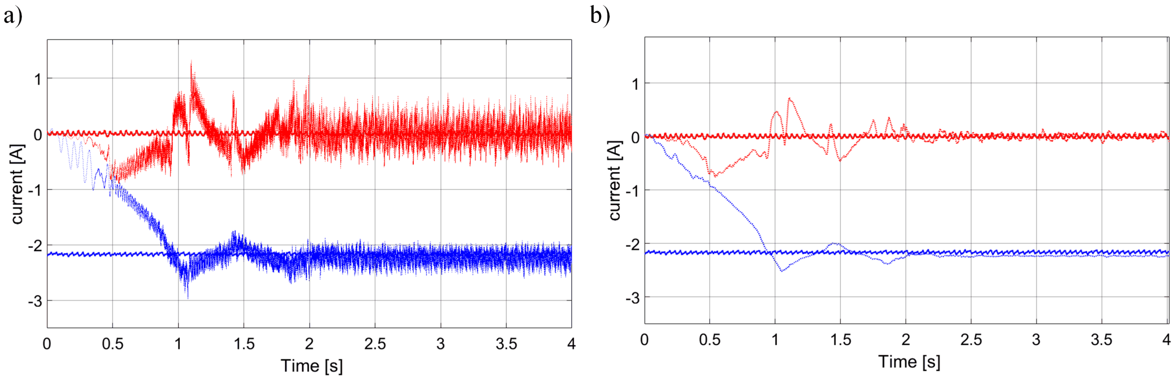

Fig. 7.9. Comparison between co-simulation results (dotted lines) and measurements (solid lines) at 750 rpm and 7 Nm input torque, for dq current, raw signals (a), smoothed co-simulation (b)

7.6. Direct Field Oriented Control of the PMSG through short circuit

Once the interconnection between the PMSG's FEA and the power electronics and control is established, the analysis of certain selected faults is done in order to asses the machine's reliability, specifically its resiliency to demagnetization. In Fig. 7.10 the schematic diagram of the first fault analyzed is presented.

The selected fault and location obey to previous studies about the IPM synchronous motor and their fault responses to different short circuits. In 2003, Prof. Jahns and his group from Madison-Wisconsin [151] analysed the single phase short circuit (asymmetrical short circuit) with analytical model and measurements and proposed to create intentionally the three phase short circuit fault after the asymmetrical fault was detected. Almost 10 years later Prof. Jahns again, retakes the topic with the evolution of the FEA software to include demagnetization properties in the materials (as explained in Chapter 3). In [152] the group from Madison analyse which of the four fault conditions had the biggest potential to demagnetize the rotor magnets:

- Symmetrical three-phase short-circuit fault
- Asymmetrical short-circuit faults (single transistor short circuit, line-to-line short-circuit fault)

— Phase-leg open-circuit fault

— Uncontrolled generator (UCG) mode fault

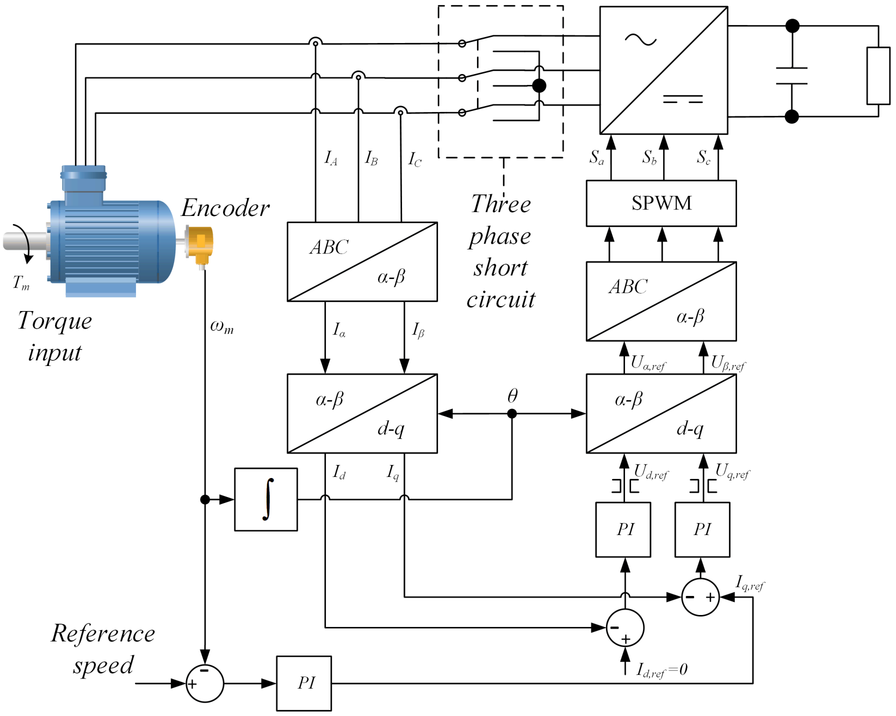

Fig. 7.10. Schematic diagram of the three phase short circuit location

In that paper, [152], they conclude that the asymmetrical short circuit has the highest demagnetization risk. Here is important to note that the analysis done by the Wisconsin group, were done for an IPM in motor operation.

In Fig. 7.11 the input torque and speed reference for the co-simulation done in this thesis, are presented. Notice in Fig. 7.11a the reference speed ramp at 4.5 s from 157 to 78.5 rad/s, this is from nominal to half speed. This was done to show that the system is still responding to the control.

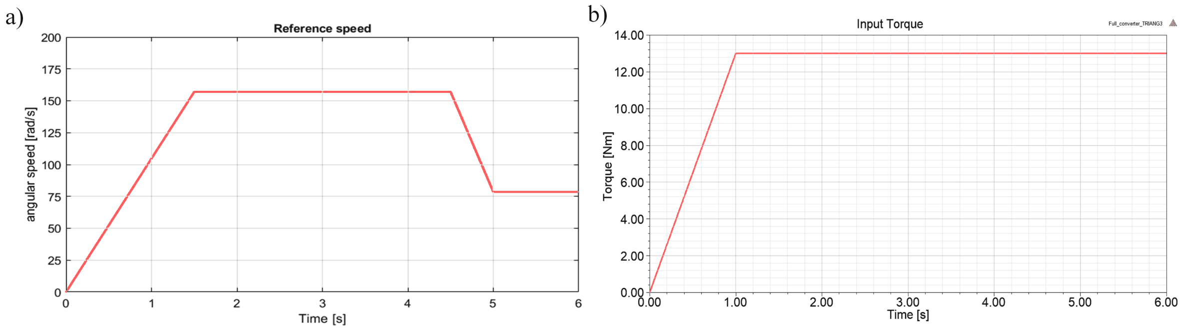

Fig. 7.11. Input signals of the system, reference speed a), and input torque b)

In Fig. 7.12 the results of the three-phase short circuit while operating the PMSG at 80°C and with an input torque of 13 Nm are shown. The short circuit starts at 2.5 s and lasts 100 ms.

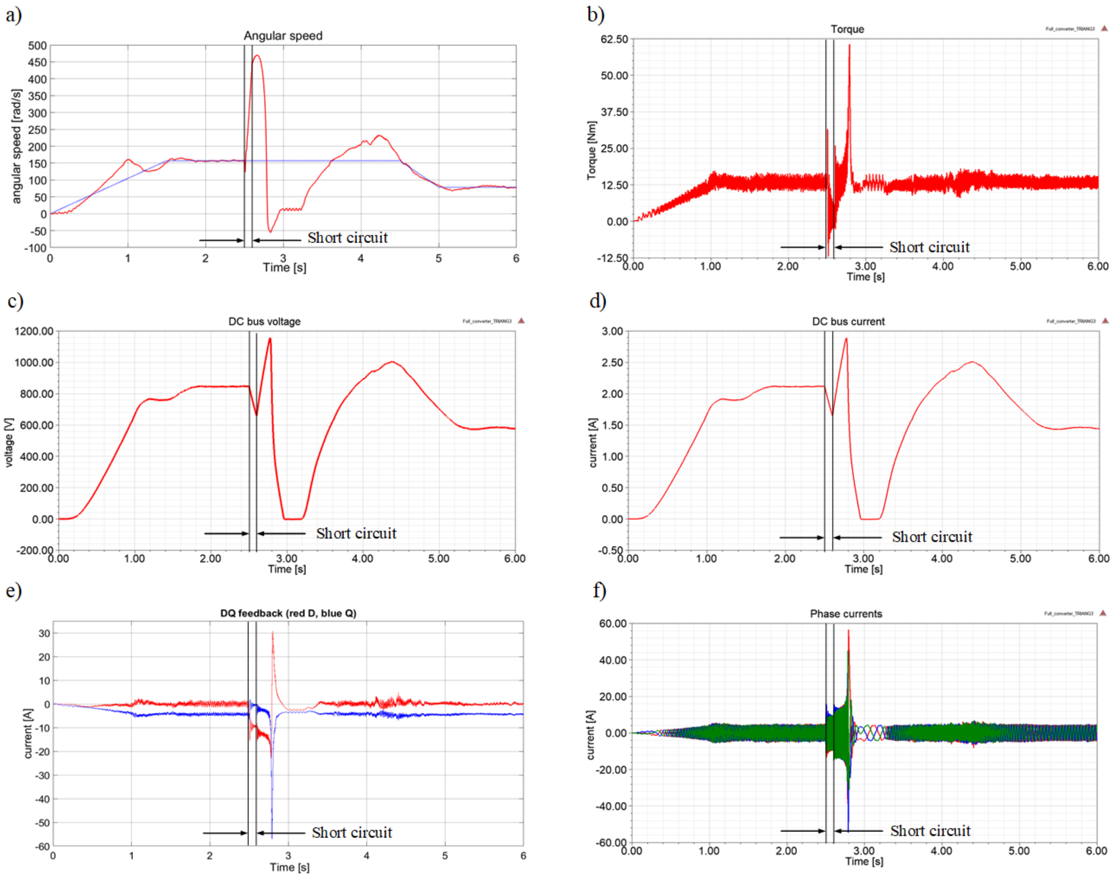

Fig. 7.12. Co-simulation results for 80°C magnets and 13 Nm of input torque: angular speed ω a), torque at the shaft b), DC bus voltage c), DC bus current d), dq currents e), and phase currents f)

Notice in Fig. 7.12e and f that the maximum current (current peak) does not occur during the short circuit but rather after the fault clearance. Also notice in Fig 7.12e that the d current (red) reaches 23 A peak after the short circuit. This is very important for the analysis that will be done at the end of the chapter.

In Fig. 7.13 the results for the same experiment but at higher input torque (15 Nm) are shown. Notice that the co-simulation was stopped at ~3.4 s. This is because the angular speed already exceeded 30000 rpm (3140 rad/s), which means that the system is completely out of control.

Also in Fig. 7.13 the maximum current occurs after the fault clearance. Although, in Fig. 7.13a is visible that the 15 Nm of input torque accelerates the machine to a speed, to which the control is no longer able to break. In Fig. 7.13e and f, a big current peak occurs at ~3.25 s.

From the speed achieved (>30000 rpm) and the duration of the post-fault state, is clear that the machine will be mechanically damaged if it is not stopped before. Is important to notice that these last two co-simulations (Fig. 7.12 and Fig. 7.13) were done at 80°C. As was presented in Chapter 3, the temperature at which the magnets are operating have a big influence on their demagnetization.

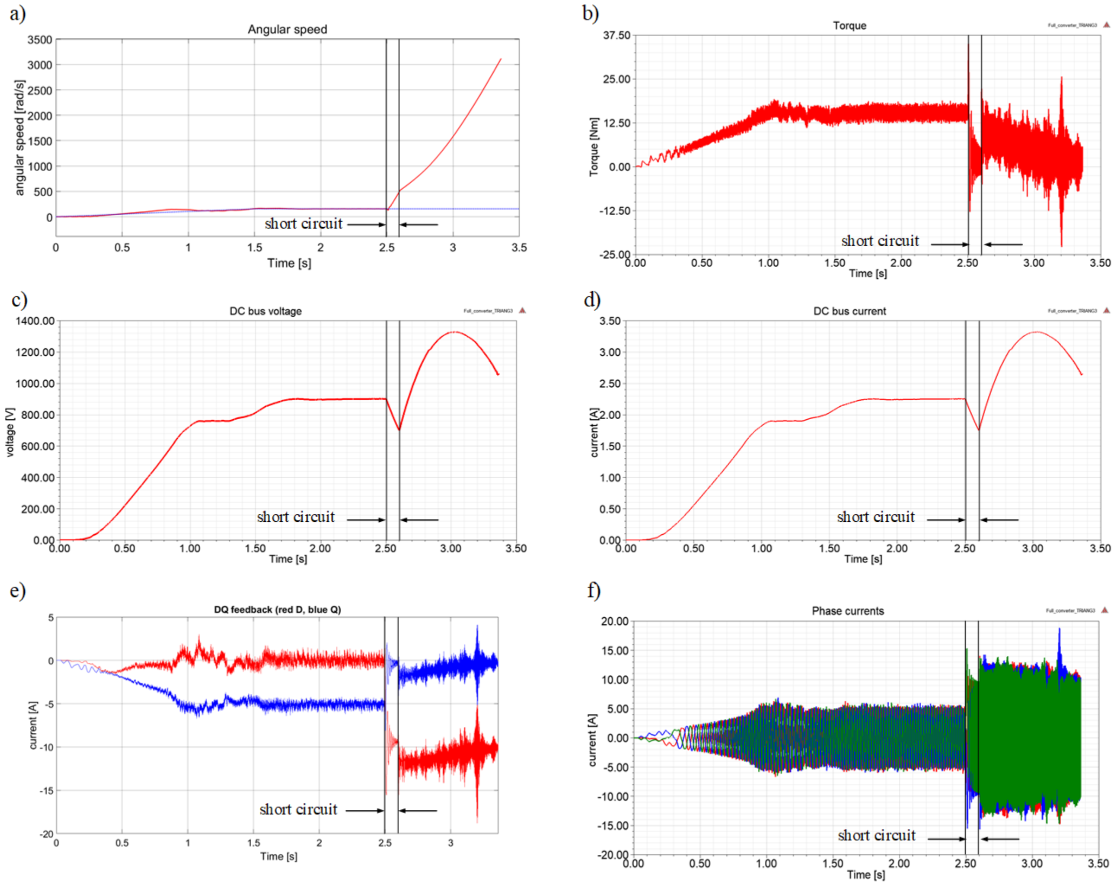

Fig. 7.13. Co-simulation results for 80°C magnets and 15 Nm of input torque: angular speed ω a), torque at the shaft b), DC bus voltage c), DC bus current d), dq currents e), and phase currents f)

In Fig. 7.14 the results for a 13 Nm input torque but with a higher temperature (110°C) are presented. Notice that the co-simulation was stopped at 4.5 s. In comparison with Fig. 7.12 (same input torque but at 80°C magnets) the PMSG does not return to nominal speed (not before 2 s after the fault). From the results shown in Fig. 7.14e and f, and due to the fact that the d-axis current reaches $\sim$33 A, it is clear that the PMSG is deeply demagnetized. Also notice that the angular speed reaches 650 rad/s (6200 rpm) in Fig.7.14a. This is mainly due to the fact that during the short circuit the hotter magnets lose some of their ability to stop the machine opposing the input torque as in Fig. 7.12a. The weakening of the *electromagnetic brake* property with higher temperature was presented in the results of Chapter 3, Section 3.4.

An additional experiment in order to corroborate the findings of Prof. Jahns in [152] was done with a line-to-line short circuit (asymmetrical short circuit). The co-simulation diagram of the system and the location of the fault is presented in Fig. 7.15. The results of the co-simulation are presented in Fig. 7.16.

Notice in Fig. 7.16e and f that again the highest current peak occurs after the fault clearance. Also notice in Fig. 7.16a that the maximum speed was 320 rad/s (3000 rpm) which is inside the normal speed range for the machine.

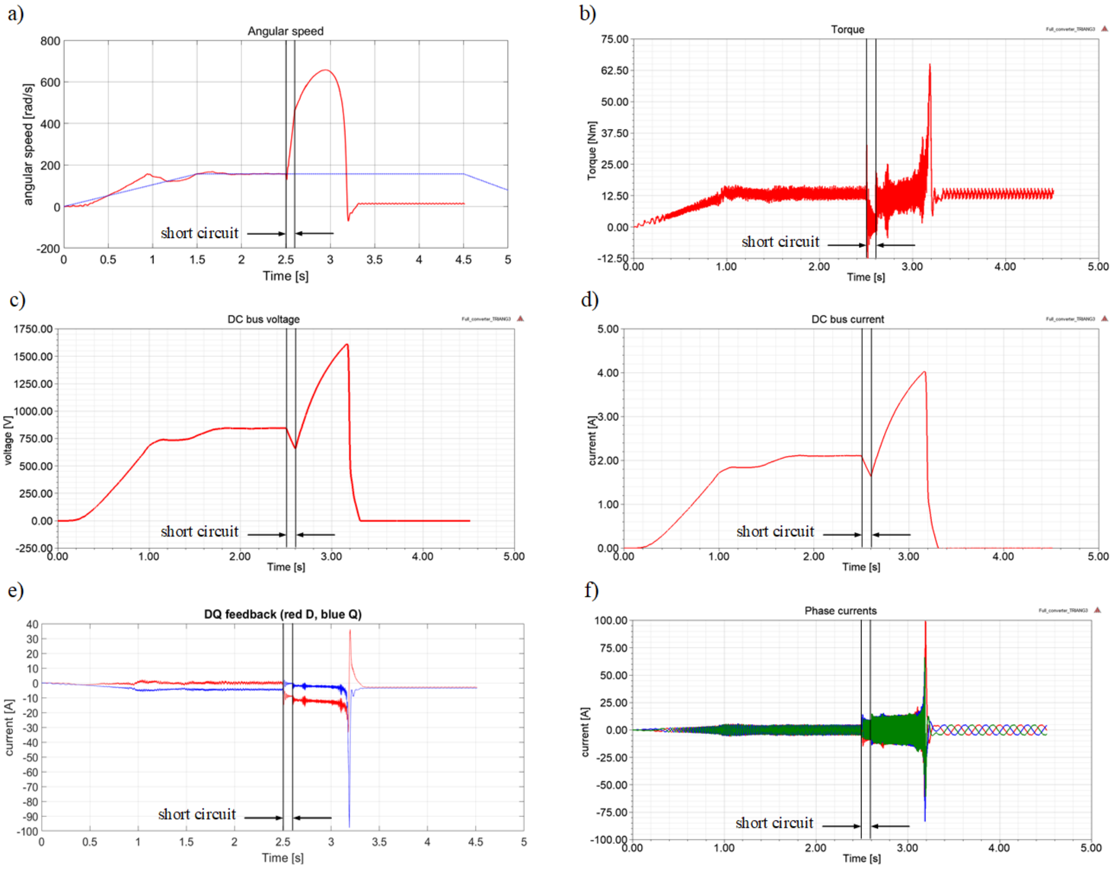

Fig. 7.14. Co-simulation results for 110°C magnets and 13 Nm of input torque: angular speed ω a), torque at the shaft b), DC bus voltage c), DC bus current d), dq currents e), and phase currents f)

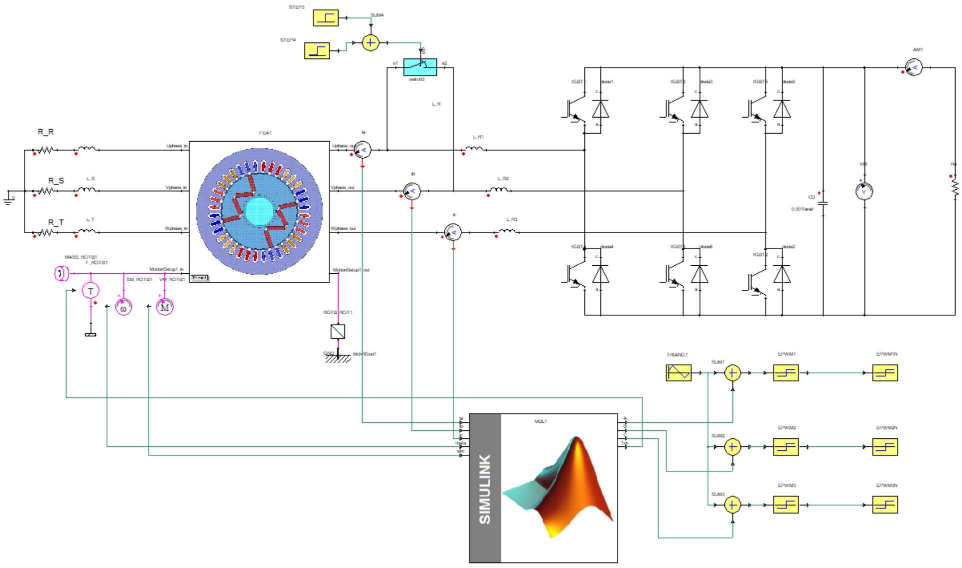

Fig. 7.15. Co-simulation diagram of the line-to-line short circuit

In Fig. 7.17 a close up of the phase current inside the red rectangle of Fig. 7.16f is shown. There, is clearer that the short circuit currents are not as big as the post-fault current peak. Also, in the insets Fig. 7.17 b, c, d and e the magnetic flux density **B** inside the magnets is shown.

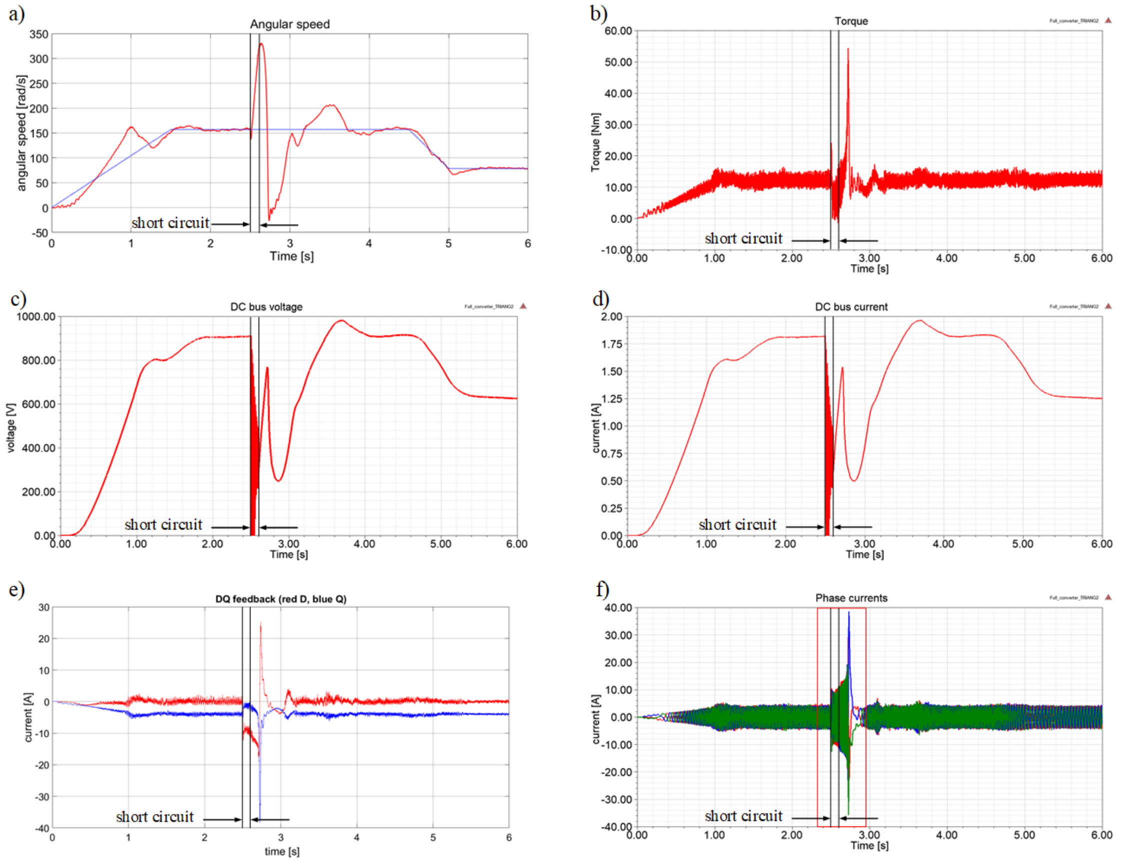

Fig. 7.16. Co-simulation results for 2 phase short circuit, 80°C magnets and 13 Nm of input torque: angular speed a), torque at the shaft b), DC bus voltage c), DC bus current d), dq currents e), and phase currents f)

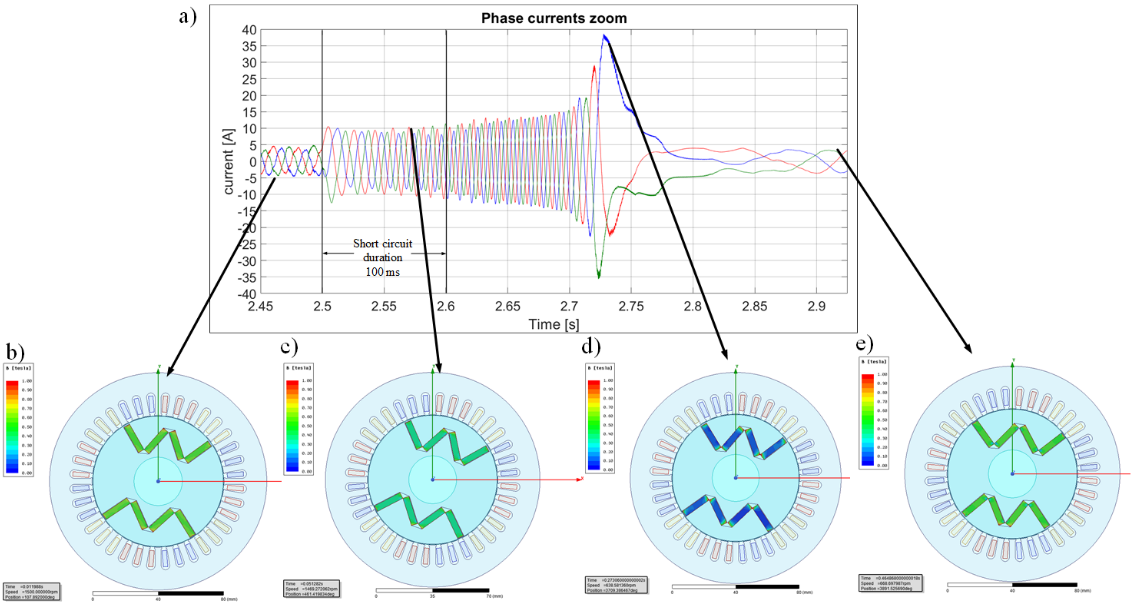

Fig. 7.17. Close up of the phase currents and magnetic flux density **B** during line-to-line short circuit fault: phase current a), **B** before the fault b), **B** during the fault c), **B** at the current peak d) and **B** after the peak e)

For a better comparison of the effects of this peak current reached after the fault clearance in Fig. 7.18 the magnetic flux density **B** inside the magnets for the three phase short circuit fault are shown. This results correspond to the magnets at 110°C and 13 Nm input torque case also shown in Fig. 7.14. Notice that the trailing magnets (inside the red circle) are the ones that have been demagnetized the most. Red arrow indicate rotation direction.

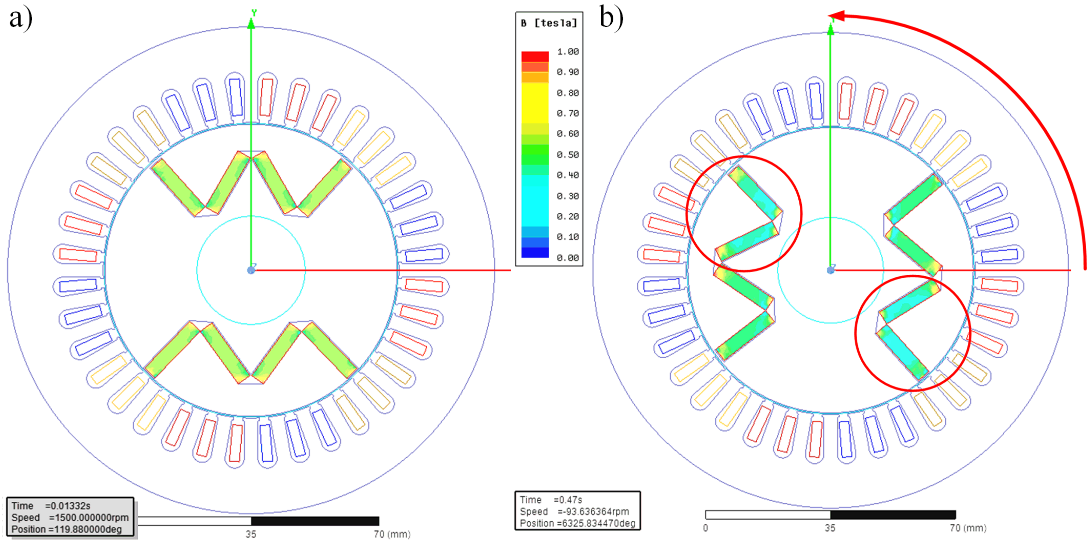

Fig. 7.18. Magnetic flux density distribution **B** inside the magnets at 110°C: before the peak current a) and after the peak current b) shown in Fig. 7.14

Here, it is important to describe the sequence of events that take place before the peak current occurs. First the short circuit (symmetrical or asymmetrical) takes place. Then, the machine momentarily decelerates since the PMSG is working as an electromagnetic brake as shown in Chapter 3 Section 3.4. This small moment is only visible as a small lower speed at the beginning of the short circuit, e.g. Fig. 7.16a. Almost immediately the input torque, namely torque applied by the prime mover (wind, water, steam, etc.), surpasses the breaking torque and accelerates the machine. This acceleration continues during the whole length of the short circuit (so therefore the urgency of clearing the fault as soon as possible). If the fault is cleared quickly and the speed is not too high (<5000 rpm in this case) then the DFOC will try to bring the speed back to the reference (decelerate), for doing that the current in the stator will grow until the current peak, which works as a break of the PMSG, bringing the rotor speed to zero (even negative speed due to inertia). After reaching zero speed, and because the input torque is still constant, the PMSG will accelerate to the reference speed after some overshoot and/or transient.

7.7. Conclusions

The last results are in good agreement with the results presented in [102] and [153]. There the authors reported that for an IPM machine, in *dynamic demagnetization* conditions, the trailing edge of the magnets are the first ones to demagnetize. Even more recently, in [154] those authors presented similar results and compared with results of the *static demagnetization* which they concluded are less severe than the demagnetization that occurs when the machine is rotating (dynamic).

As for the publications of the Wisconsin group, [151, 152] it is important to mention that, as most of the literature available, they are operating the IPM as a motor. Therefore, it is understandable that the conclusions are different than the results presented in this thesis. In other words, Prof. Jahns and his team concluded that the asymmetric line-to-line short circuit fault creates the higher risk for demagnetization of an IPM motor, but, as it was presented in this Chapter, the condition *after the fault clearance* when the DFOC is trying to recover the speed it had before the fault, that is where the peak current against the magnets occurs.

If the input torque is too big (>13 Nm here) or the short circuit too long (>150 ms here) then the machine is at a state where the control will not be able to bring back the speed. This mode is the uncontrolled generator (UCG). This was also described by Prof. Jahns earlier in [155], although there he focused again in the IPM as a motor and described the UCG mode as the absence of trigger signals in the converter, making the inertia of the motor operate the IPM machine as a generator supplying current to the DC bus through the converter freewheeling diodes. In [155] and [152] Prof. Jahns assumes that the IPM shaft experience a breaking torque until the rotor speed is reduced sufficiently to extinguish the current flow. This is an acceptable assumption since the IPM motor was the one providing torque before the UCG fault. In this thesis the prime mover is normally separated from the converter control and therefore it will keep producing torque before, during and after the short circuit. Therefore the urgency in clearing the fault and stopping the shaft before the PMSG suffers a mechanical malfunction due to overspeed or high demagnetization.

8. Operation of the PMSG after partial demagnetization

In this Chapter the effects of the partial demagnetization over the full converter control, are analysed. First the results for healthy machine are compared with 3 scenarios of a partially demagnetized PMSG at 80°C. Then those results are compared with an scenario where the demagnetization occurred by current peak after fault clearance as explained in Chapter 7 Section 7.6. It is relevant to mention that the cases studied in this chapter are extreme demagnetization cases which nevertheless the converter and its DFOC were able to maintain operating.

8.1. Four study cases

Here the results of the analysis of four states of the machine are compared. In Fig. 8.1 the magnetic flux density **B** distribution of the four studied cases is presented.

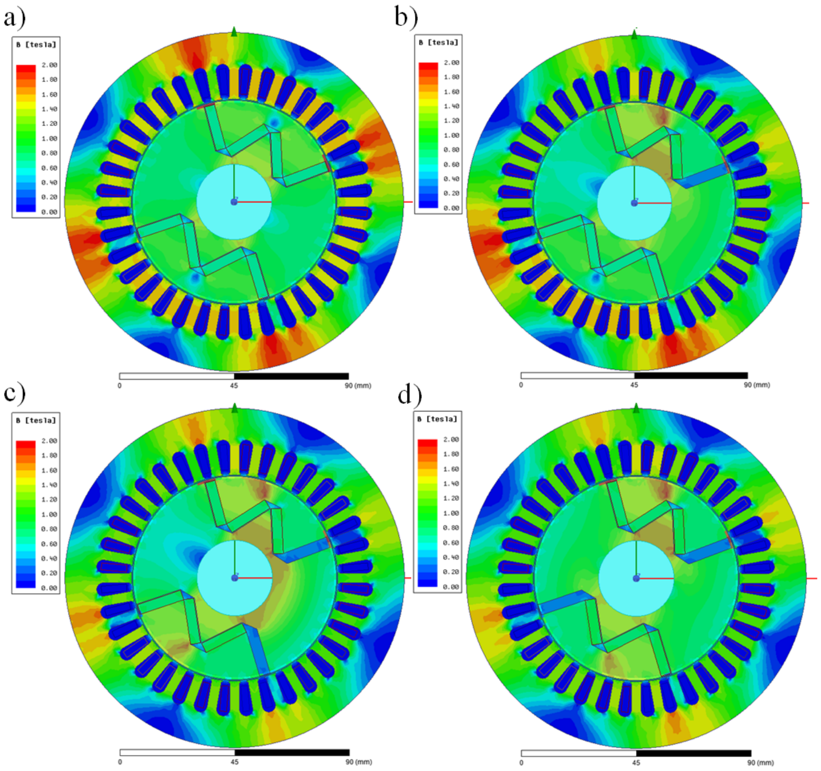

Fig. 8.1. Magnetic flux density **B** distribution over the PMSG for: healthy a), 12.5% demagnetization b), 25% demagnetization c) and 25% demagnetization opposite side d)

The demagnetized cases presented in Fig. 8.1 b, c and d are a valid simplification used in the literature to analyse demagnetization e.g. [156, 157, 158], namely, in those papers the authors break or extracted magnets from the rotor in order to analyse signals (e.g. currents, vibration, etc.) for the detection and assessment of demagnetization.

In Fig. 8.2 the co-simulation diagram of the experiments performed with the four cases is presented. Notice in the diagram that the DC bus load is changed during the co-simulation, i.e. additional resistors are connected in parallel to the initial one. The initial resistor has 1000 Ω. The second resistor, also of 1000 Ω, is connected in parallel at 2 s making 500 Ω total. Finally the third resistor (1000 Ω too) is connected at 4 s making 333.33 Ω total. This was done to assess robustness of the controller which should maintain the reference speed when additional loads are connected.

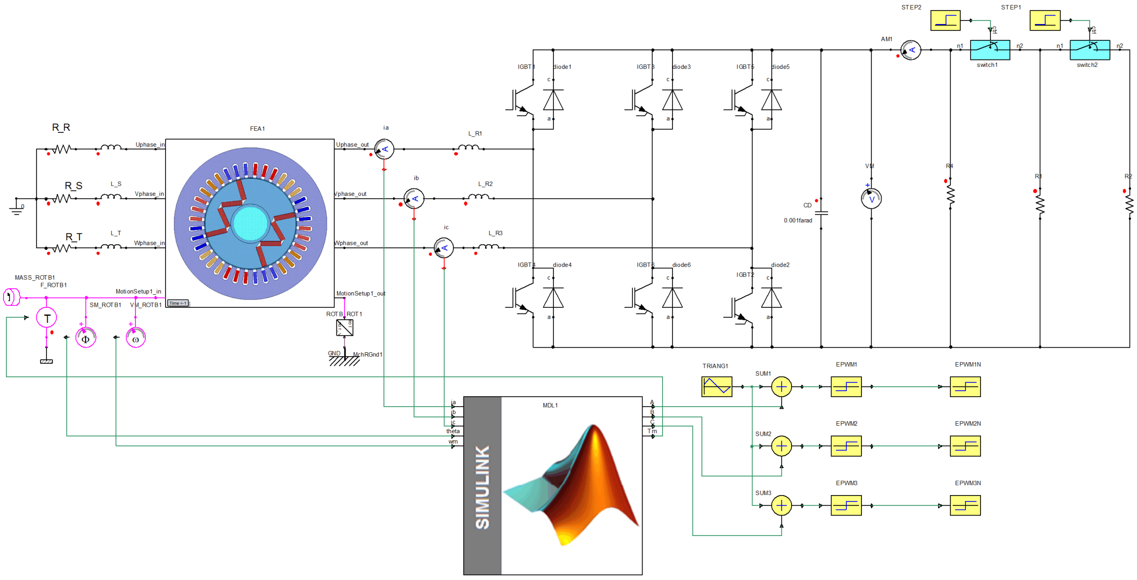

Fig. 8.2. Co-simulation diagram for the analysis of the four cases

It should be mentioned that the input torque was kept constant at 15 Nm, also the magnets temperature is 80°C constant and the PWM frequency is 3 KHz. The reference speed starts at nominal 1500 rpm (157 rad/s) and from 2.5 to 3.5 s a ramp from nominal to half nominal speed (78.5 rad/s) is given. Again this change in the speed reference follows the controller assessment.

In Fig. 8.3 the results speed feedback signal from the co-simulation is presented. It is shown in two different charts (a and b) for clarity purposes. Notice that even in steady state (from 1.5 to 2 s) there are some small oscillations in the speed signal (even in the healthy case). These oscillations are connected with the stator tooth (cogging torque) and the fact that in the co-simulation the speed is not filtered. Normally the speed measurement is obtained from incremental encoders, then a derivative operation is needed to obtain a speed measure. As consequence, the rotational speed measurement results are rather noisy and a suitable filter must be used to reduce the noise. This filter should be designed correctly to not introduce too much lag as explained in [150]. In the co-simulations presented in this thesis no filter was used to avoid introducing any lag and avoid limiting the bandwidth of the control loop.

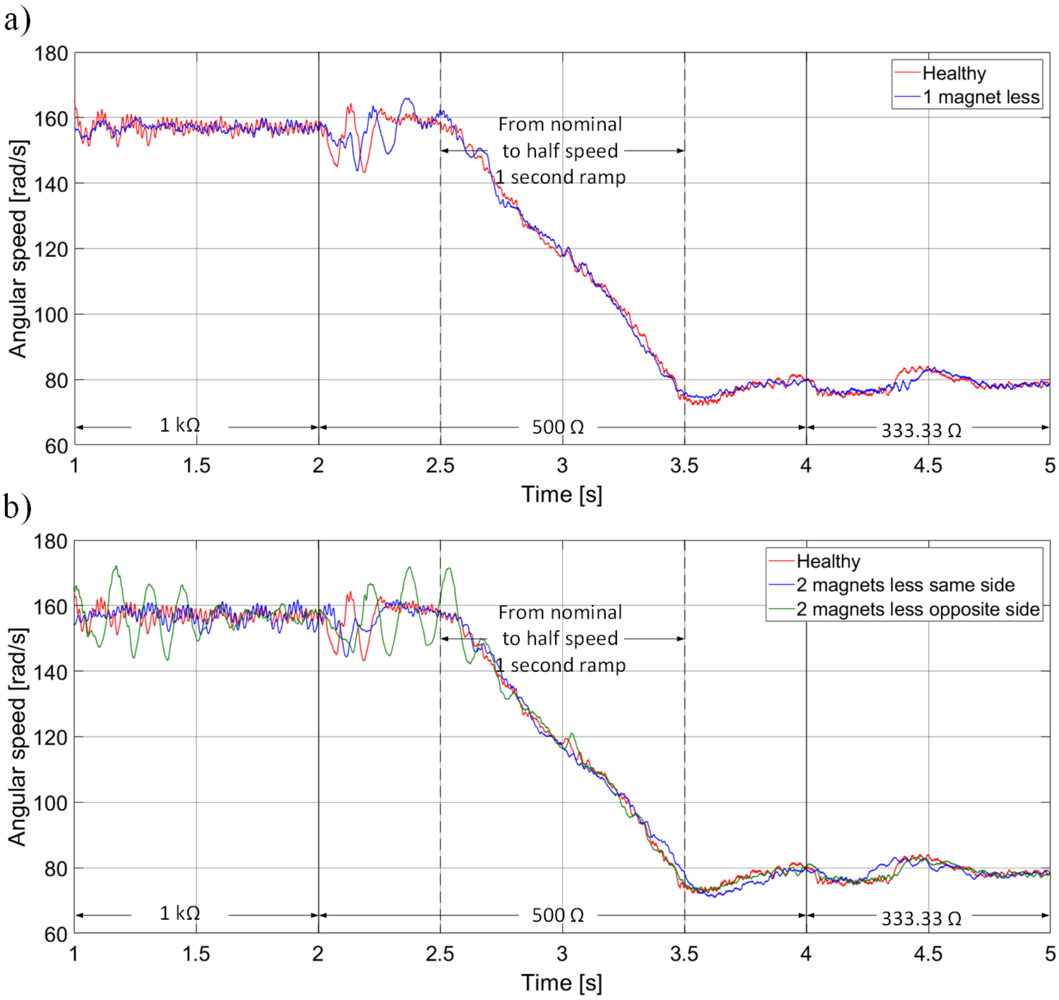

Fig. 8.3. Angular speed from nominal 1500 rpm (157 rad/s) to half speed (78.5 rad/s) comparison for healthy and one magnet less a), and healthy and two magnets less b)

In Fig. 8.3 the big oscillations are connected with the control, namely with the transient response of the system. That is also the reason why we have the oscillations when the DC bus load is changed (between 2 an 2.5 s). Notice that in Fig. 8.3b the biggest oscillations can be seen on the two magnets less opposite side case, although the PMSG remains under control as it follows the reference speed ramp and also achieves steady state at half nominal speed.

It is important to bear in mind that the proportional-integral (PI) controllers were tuned for the healthy case, namely all the gains are the same for the four cases here studied. Despite that fact, the behaviour of the system is quite different for the demagnetized cases. This difference in the behaviour of the system can be seen also in Fig. 8.4. There the DC bus voltage and DC bus current are presented. As it was shown in Chapter 3 Section 3.4, a partially demagnetized PMSG will produce less back EMF therefore less voltage and current.

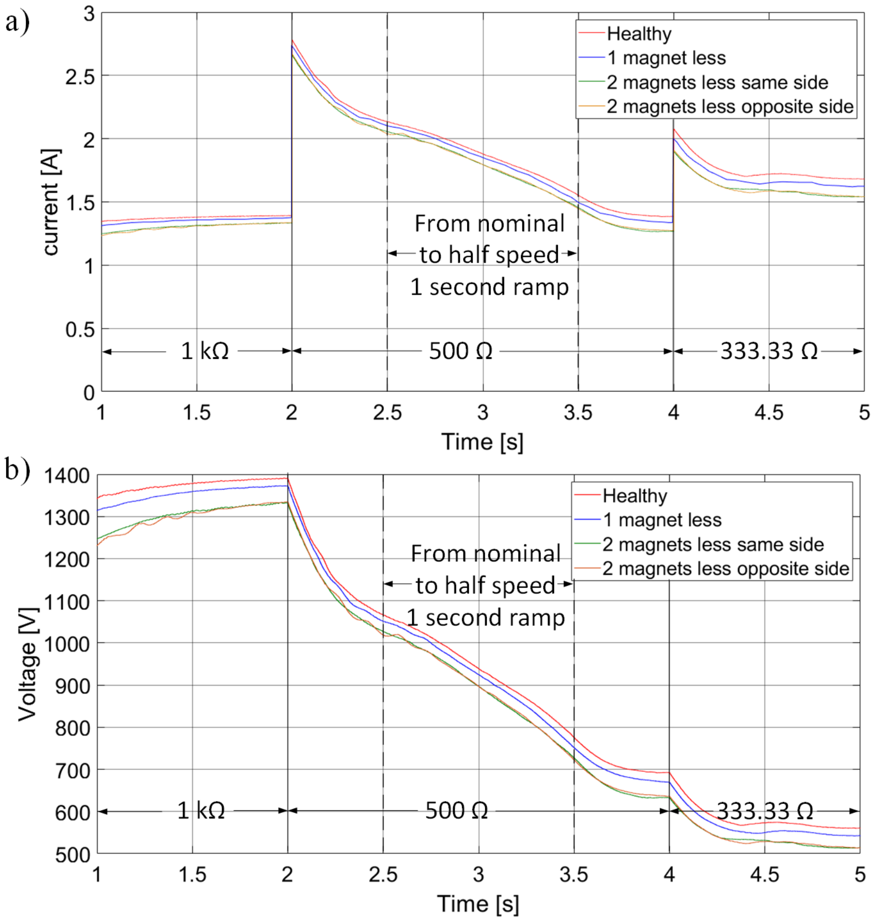

Fig. 8.4. Comparison for the four cases of the DC bus: voltage a), and current b)

In Fig. 8.5 the dq signals for 3 cases are compared, these correspond to Fig. 8.1 a, b and c. Notice the difference in the q current even though all the cases had the same input torque.

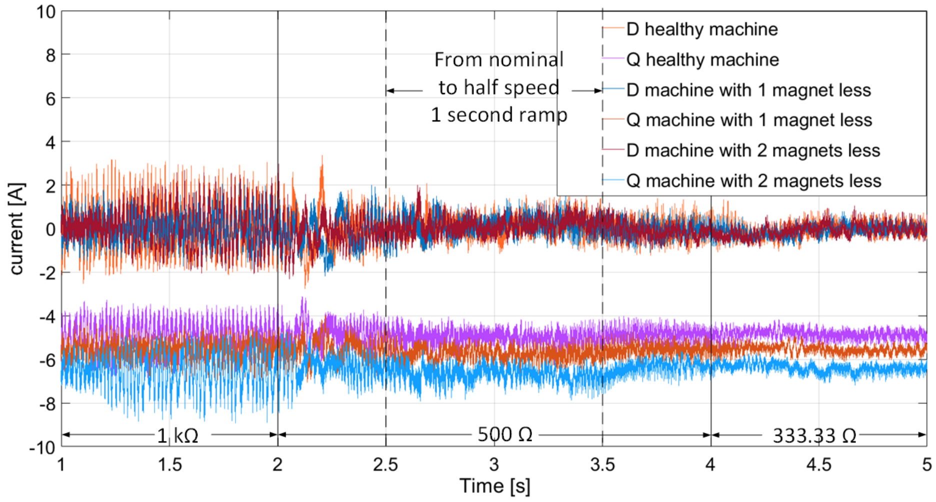

Fig. 8.5. DQ current signal comparison

From the Figures 8.4 and 8.5 is clear the difference between the demagnetized cases and the healthy PMSG. Still the DC bus signals or the q current couldn't be employed as a fault indicator. This is because at higher input torque, the current level (d current) would be the same for the healthy PMSG than for the two magnets less case (blue q current in Fig. 8.5). In other words, the DC bus voltage and currents depend not only on the health status of the PMSG but also on the load, and the q current depends on the input torque of the PMSG, since it is not common to have the input torque measurement then is not feasible to use the q current for demagentization assessment.

It may perhaps be observed without straying too far afield from our primary focus that some literature reports the use of the d current to asses demagnetization. For example, in [159], the authors propose analytically and in simulation the demagnetization detection by analysing the d current harmonics. In Fig.8.6 an additional comparison between the two magnet less cases is shown.

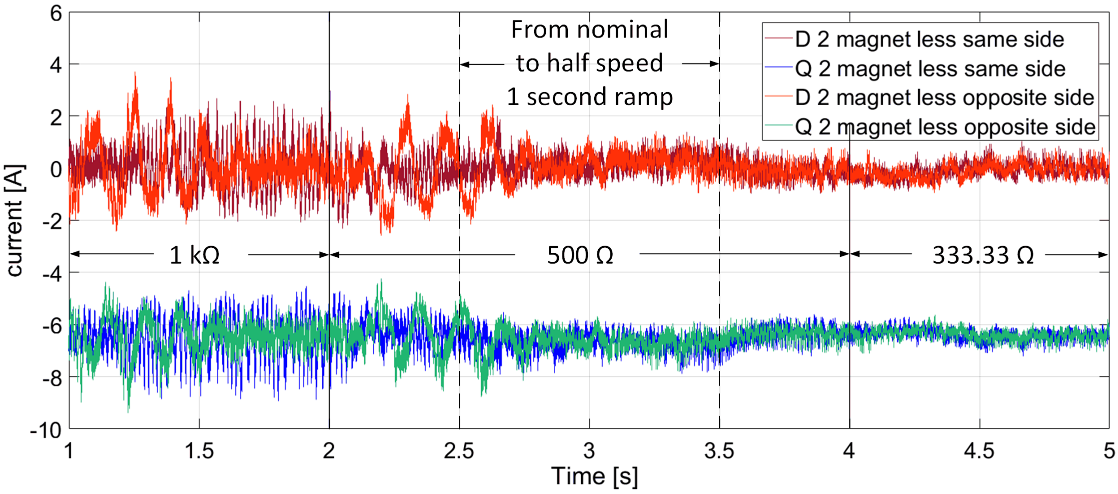

Fig. 8.6. DQ current signals comparison depending on demagnetization position

In Fig. 8.6 the oscillation of the two magnets opposite side case that were visible in the speed are also visible in the dq currents. Still, it must be pointed out that the two magnets same side has bigger ripples in steady state at full speed (1.5 to 2 s).

8.2. Comparison with extremely demagnetized cases

Here some further results from the analysis of extreme demagnetization cases are presented as means for comparison with the results presented in the last Section for two magnets less opposite side case.

In Fig. 8.7 the reference speed and the input torque for the two co-simulations that will be compared in this section are shown.

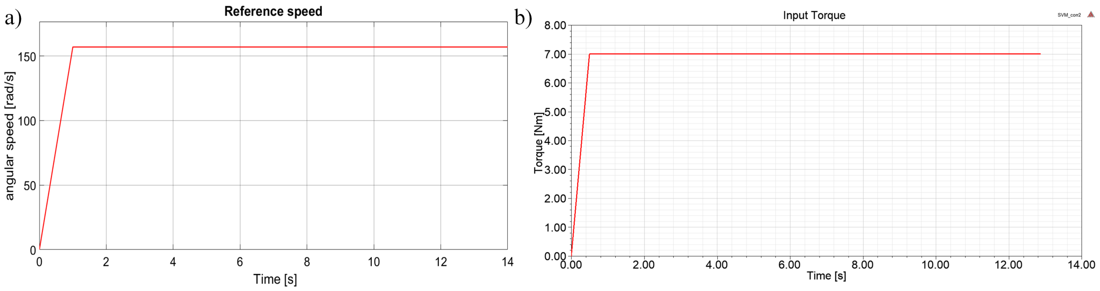

Fig. 8.7. Co-simulation reference speed a) and input torque b)

The results of the co-simulation with two magnets less opposite side with these input signals (1500 rpm and 7 Nm) are presented in Fig. 8.8.

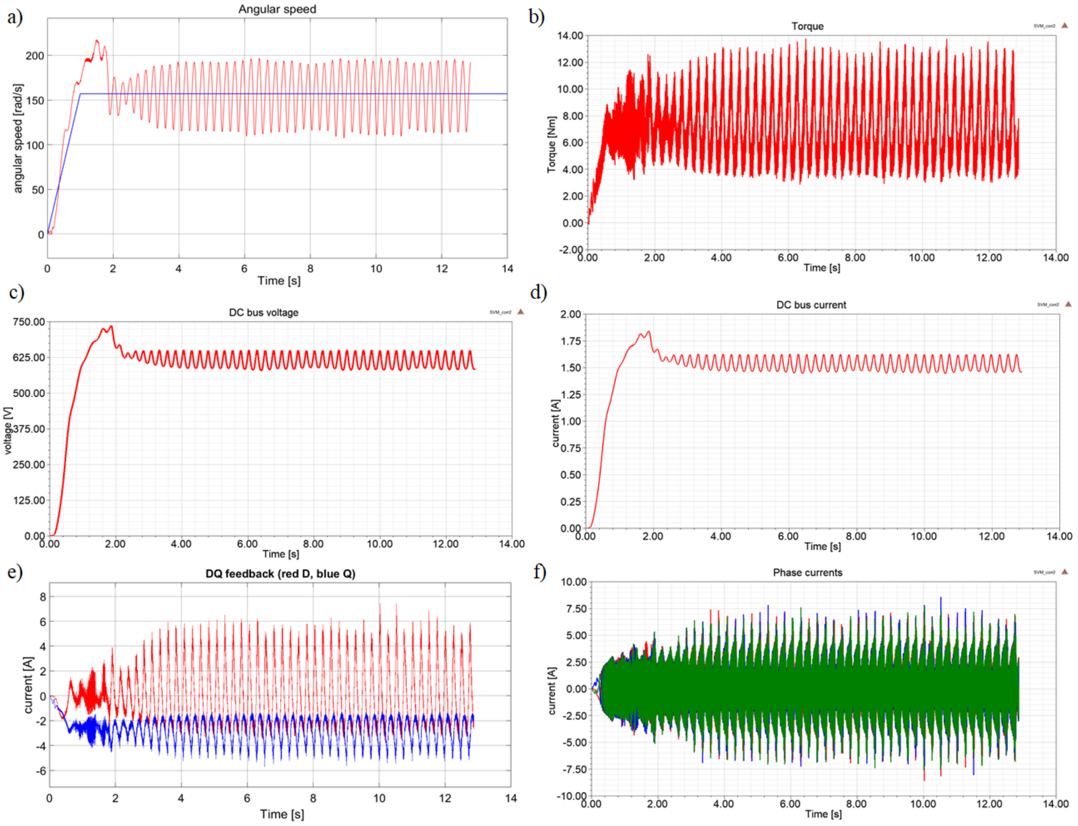

Fig. 8.8. Co-simulation results for two magnets less 7 Nm of input torque: angular speed a), torque at the shaft b), DC bus voltage c), DC bus current d), dq currents e), and phase currents f)

In Fig. 8.8 is clear that the lack of two magnets on the opposite side leads to big oscillations in the system. Still, it is noteworthy the ability of the FOC to maintain the control of the speed. The simulation was stopped at 13 s because it was already clear that the system reached stability (underdamped) and the osccillations were not getting bigger neither smaller. Notice in Fig. 8.8e that the oscillations in the d current are bigger than the ones in the q current.

In Fig. 8.9 the results of the co-simulation of a line-to-line short circuit, when the magnets are at 150°C, are presented. This is a similar co-simulation as the one presented at the end of

Chapter 7 Section 7.6, the differences are that the speed reference is kept constant (no ramp), the input torque is lower (see Fig. 8.7) and magnet temperature is higher (150°C).

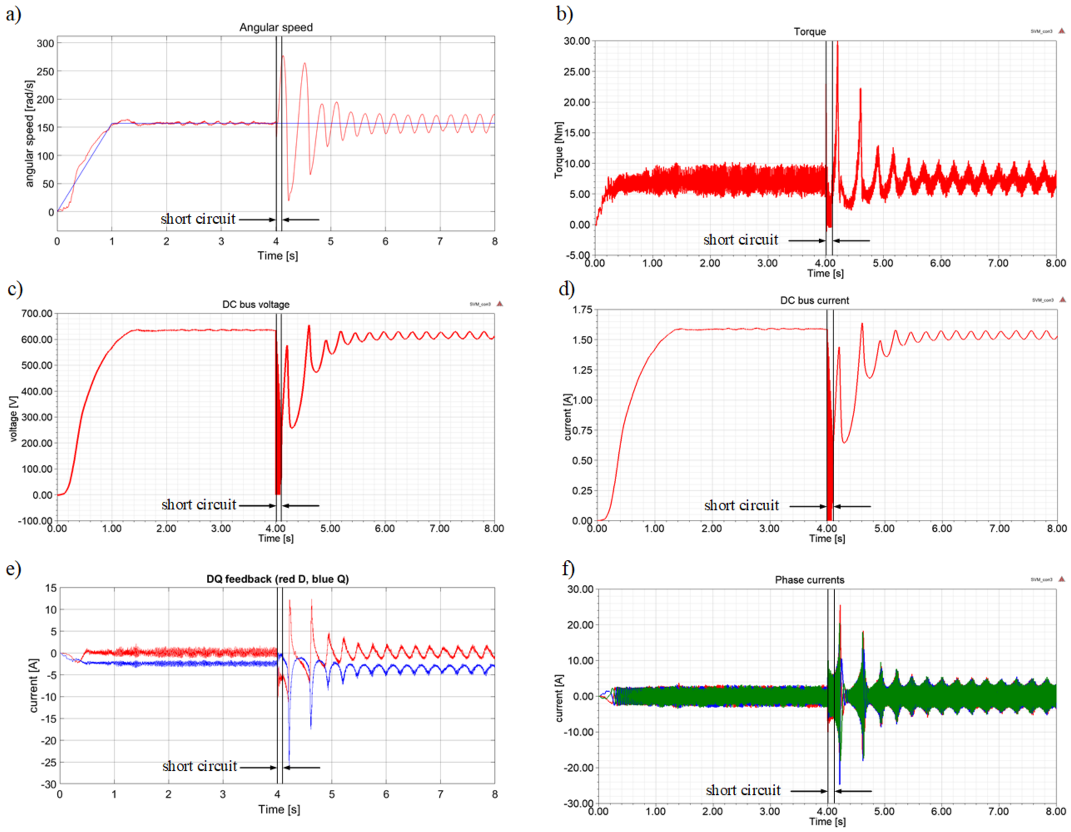

Fig. 8.9. Co-simulation results for line-to-line short circuit with magnets at 150°C: angular speed a), torque at the shaft b), DC bus voltage c), DC bus current d), dq currents e), and phase currents f)

The results shown in Fig. 8.9 are an extreme case of demagnetization, and as mentioned in Chapter 3 Section 3.4, the PMSG should not be operated at those temperatures. Nevertheless, the similarities found between these results and the analysis with two magnets less opposite side confirm that the oscillations appear when the machine is partially demagnetized. Also notice in Fig. 8.9c that that the converter ratings were not surpassed (<1.2kV) and the maximum momentary speed was 2600 rpm (272 rad/s).

In Fig. 8.10 the comparison of the dq currents for the two cases analysed in this section.

From Fig. 8.10 it can be observed that the two magnets less opposite side is an even more extreme case of partial demagnetization than the line-to-line short circuit with 150°C, what is remarkable is the ability of the FOC to maintain stability even with 25% demagnetization (2 magnets less).

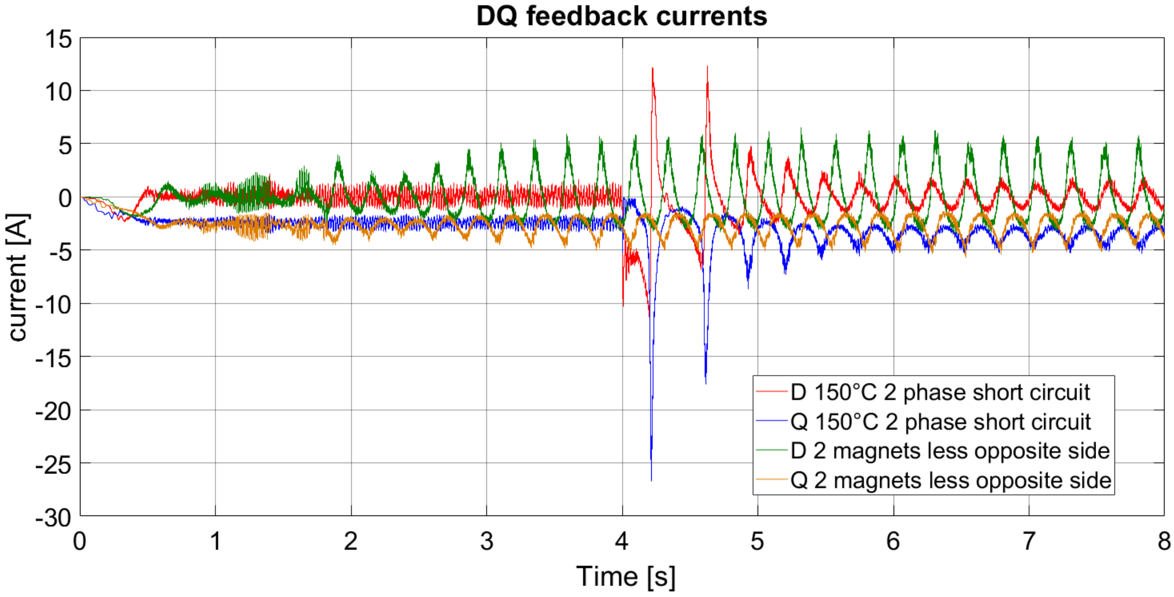

Fig. 8.10. DQ currents comparison for the case with two magnets less opposite side and 2 phase short circuit with magnets at 150°C

8.3. Conclusions

From the cases analysed in this Chapter it is safe to say that: *the PMSG can be operated during permanent magnet faults* as stated in the second hypothesis of this thesis. It is needless to say that this affirmation has some prerogatives, for instance, as it can be seen from the two magnets less opposite side case, the stability of the system is getting compromised by the oscillations. Furthermore, it may not be even acceptable the level of vibrations and torque ripples that the PMSG may produce when operated in such a state. At any rate, the last two cases presented in this Chapter are examples of extreme demagnetization, therefore if the system is able to operate in such circumstances, then it can be assumed that it will also operate at smaller demagnetization rates.

Here is also important to mention that as explained in [15] another possibility of such a state of the PMSG could be by the corrosion of the Nd-Fe-B magnets. This is because the Nd-Fe-B material is more prompt to corrosion than steel and therefore if it is not protected correctly the corrosion could render the sintered magnet back into useless powder. In other words, the absence of magnets in the PMSG rotor could be also due to ambient factors. In the literature similar PMSG have been reported in close contact with water e.g. a PMSG for a Kaplan micro hydro in [160] and the generators of the *Wave Dragon* in [161] and [162] also with Kaplan turbines.

9. Small Wind Turbine with full converter under Direct Field Oriented Control

In this chapter the simulation, co-simulation and demagnetized PMSG co-simulation cases, controlled using Direct Field Oriented control algorithm, are presented. First a comparison of the results between the simulation in Matlab Simulink with the SimPower sytems' toolbox against the results from the co-simulation are compared in a similar manner as was done in Chapter 6 Section 6.4. Then the results between the healthy PMSG and the two magnets less on the opposite side of the rotor (as shown in Chapter 8) are presented and analysed. Finally some conclusions about the interaction of the different components of the WECS are given.

9.1. Full WECS with MPPT under Field Oriented Control

In Fig. 9.1 the schematic of the WECS analysed in this Chapter is presented. Notice that the input of the whole system is wind speed V_{wind} in m/s. The constant K_{opt} is the same as described in equation 5.5 (Chapter 5, Section 5.3).

$$K_{opt} = \frac{0.5\pi\rho C_{p\_max} R^5}{{\lambda_{opt}}^3} \tag{9.1}$$

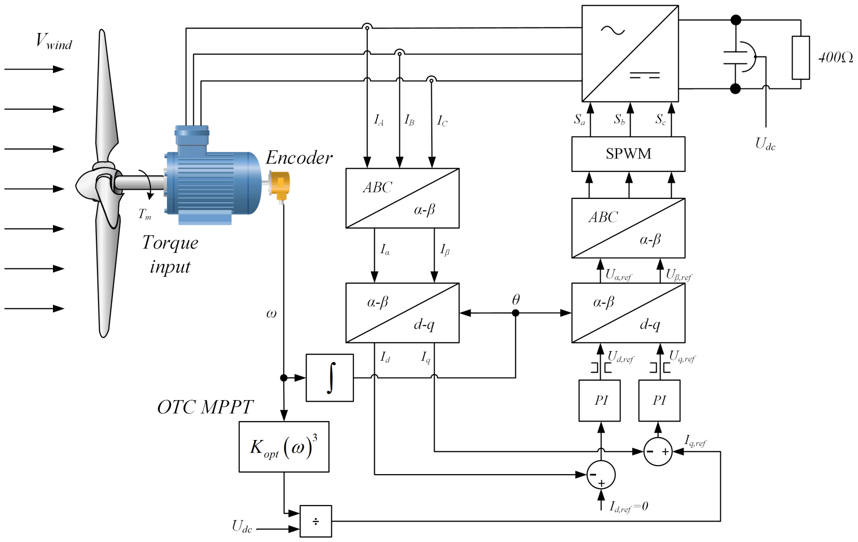

Fig. 9.1. Schematic diagram of the WECS with MPPT under FOC

In Fig. 9.2 the diagram of the Simulink with SimPower Systems' simulation is presented. The red rectangle is the part of the diagram that will be replaced by the co-simulation.

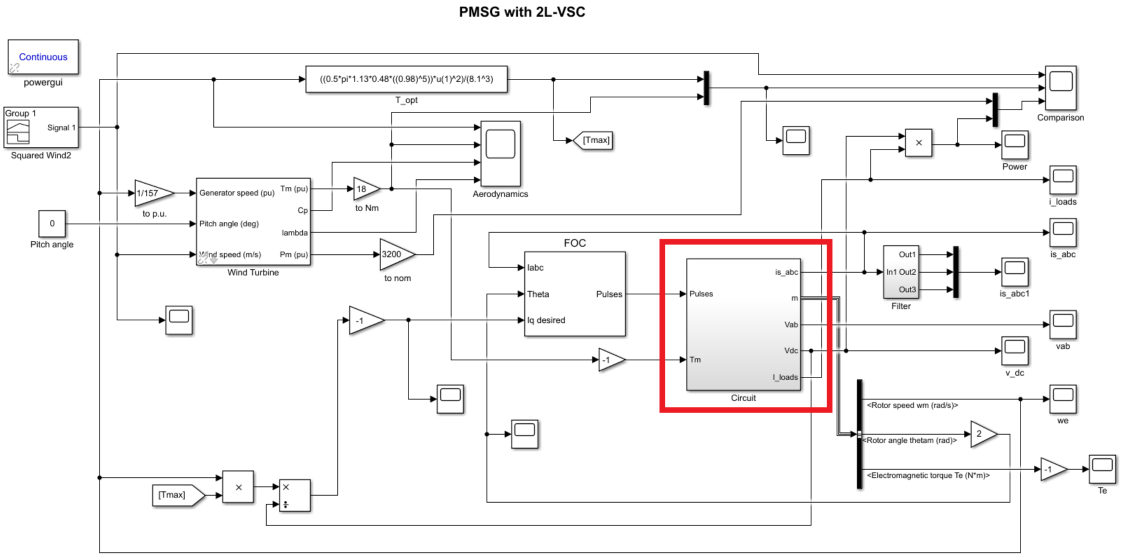

Fig. 9.2. Simulink diagram for the SimPower Systems' toolbox simulation

In Fig. 9.3 the diagram for the control of the SWT (including WT model) for the co-simulation is presented. Notice that the parameters for the simulation and the co-simulation are the same.

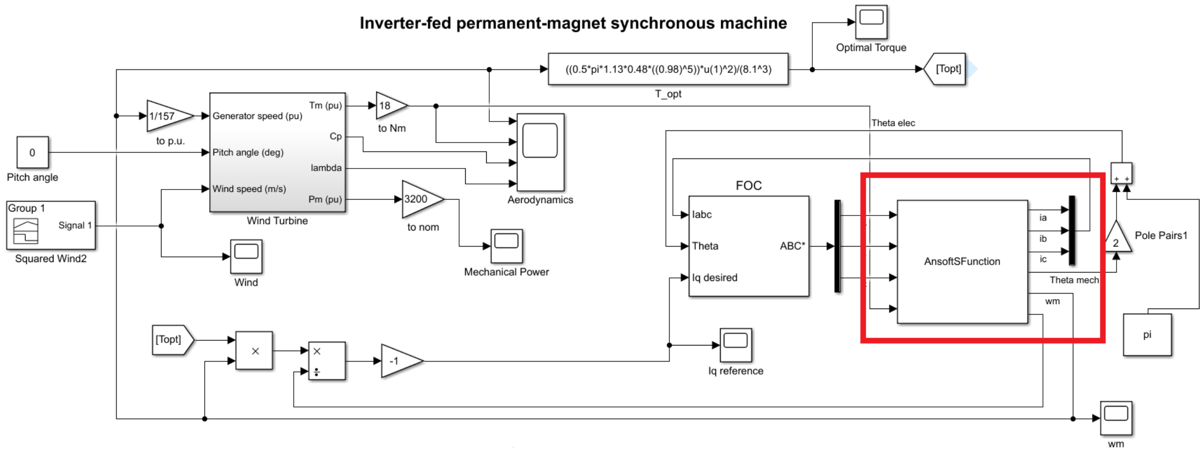

Fig. 9.3. Simulink diagram for the co-simulation. Red rectangle is the link to Simplorer

For both, simulation and co-simulation, the radius of the turbine R is 0.98 m, the C_{p_max} is 0.48 and the optimal tip speed ration λ_{opt} is 8.1, also is expected that the WT is able to generate 3200 W of mechanical power and 18 Nm of torque with a wind spees of 11 m/s.

The aerodynamic behaviour of the WT is given by the equation 5.2 (Chapter 5, Section 5.3) where the pitch angle =0 (because no pitch control is included) and λ_i is calculated as equation A.14 from Appendix A.

9.2. Comparison of simulation to co-simulation

In Fig. 9.4 the transients of the output power, torques, power coefficient Cp and tip speed ratio λ, for the simulation (a, b, c, d) and co-simulation (e, f, g, h) are presented.

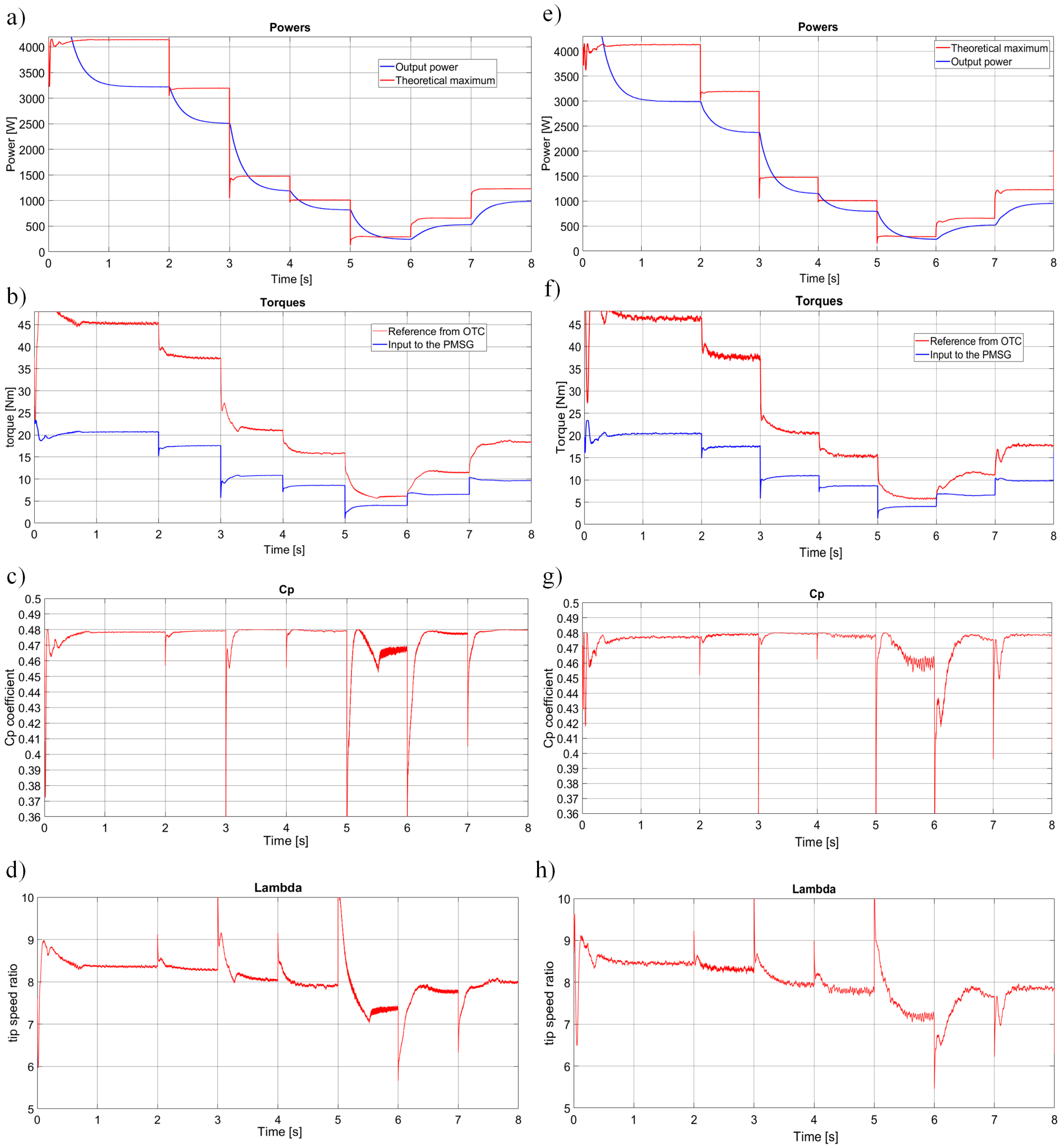

Fig. 9.4. Results from the simulation: powers a), torques b) Cp c) and Lambda d) and for the co-simulation: powers e), torques f) Cp g) and Lambda h)

Notice that in both (simulation and co-simulation) the MPPT strategy keeps the Cp close to C_{p_max}=0.48, this is done by varying the tip speed ratio λ in order to be as close as possible to λ_{opt}=8.1 this is done by controlling the PMSG torque reference. Since λ only depends on the wind speed, the turbine radius R (which is constant) and the shaft's angular speed, then only ω can be modified through the PMSG torque to obtain λ_{opt}.

In Fig. 9.5 the input signal for the simulation and co-simulations presented in this Chapter is shown. As was mentioned in Chapter 6 Section 6.4 the staircase wind speed is used only as an example to asses the control response of the MPPT strategy.

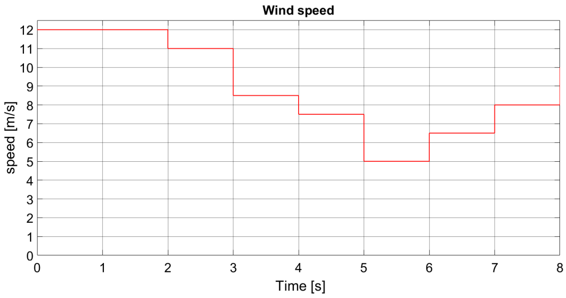

Fig. 9.5. Input signal for the simulation and co-simulations of the WECS

In Fig. 9.6 the angular speed and the input torque to the PMSG are presented. Notice that they are almost the same for simulation and co-simulation.

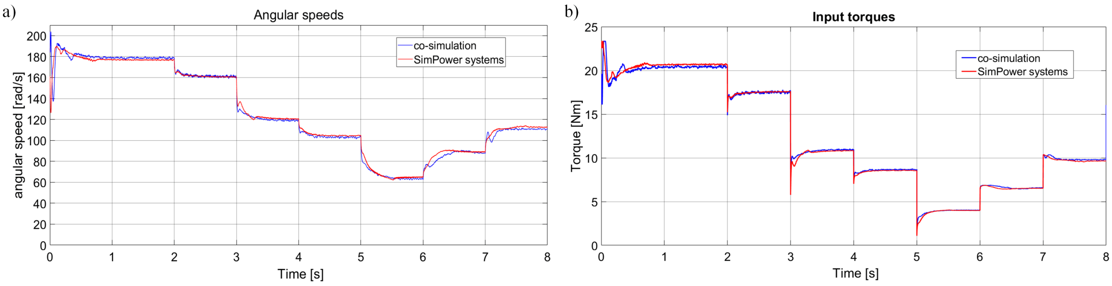

Fig. 9.6. Simulation (red) and co-simulation (blue) angular speed a) and input torque to the PMSG b)

Although the results shown in Fig. 9.6 are similar for both (simulation and co-simulation) the output power for both systems is not so similar, mainly at high wind speeds. This can be observed in Fig. 9.7.

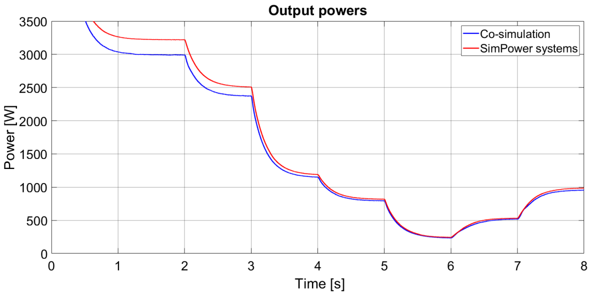

Fig. 9.7. Power output at the DC bus load for simulation (red) and co-simulation (blue)

The differences in Fig. 9.7 can be explained by the results shown in Chapter 6 Section 6.2 also published in [141]. There, it was shown that the co-simulation results are closer to real measurements of the PMSG.

In Fig. 9.8 the electromagnetic torque (torque at the shaft of the PMSG) is presented. Notice that at higher wind speeds (higher power) the torque ripples are bigger for both.

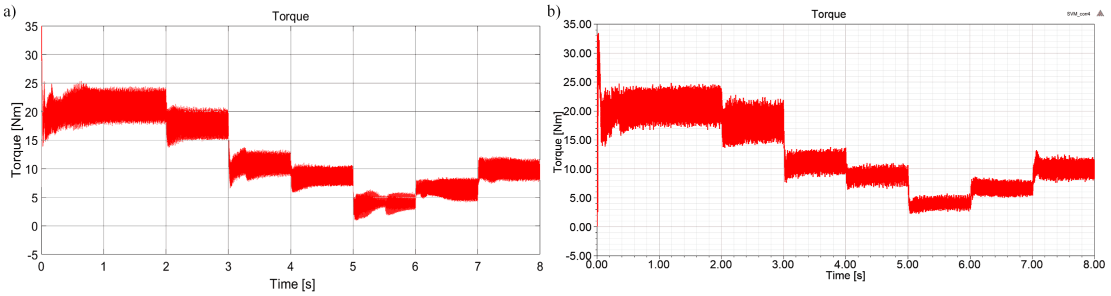

Fig. 9.8. Torque at the shaft for simulation a) and co-simulation b)

In Fig. 9.9 the phase currents for the simulation and co-simulation are presented for the SWT under FOC. Even at 3 kW output power the FOC maintains the currents lower than 10 A.

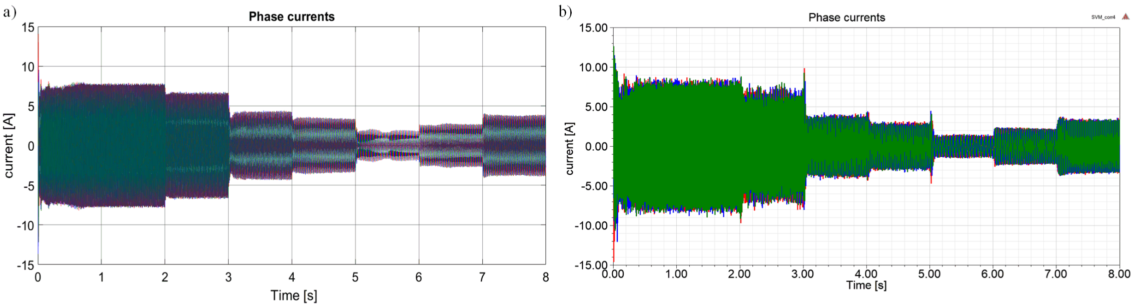

Fig. 9.9. Phase currents for simulation a) and co-simulation b)

In Fig. 9.10 the DQ currents for simulation and co-simulation are shown. Here is visible that the co-simulation feedback signals are more noisy than the simulated ones.

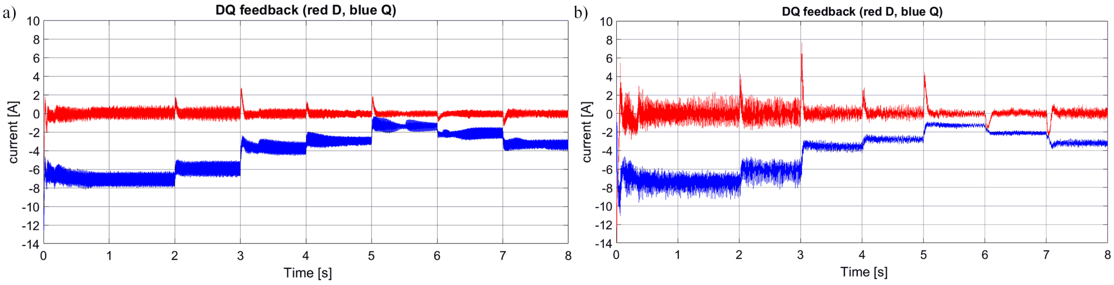

Fig. 9.10. DQ currents for simulation a) and co-simulation b)

It is visible that current D is kept on zero and current Q depends on the torque reference from the OTC algorithm. Also notice that the D and Q current ripples are bigger when the input power (wind speed) is high. Although the D current ripples are are bigger that the ones for Q.

9.3. Demagnetized Small Wind Turbine under Field Oriented Control

In Fig. 9.11 the DC bus output power for two co-simulations is presented. One is the co-simulation presented earlier in this Chapter and the second is the co-simulation made with the PMSG with two magnets less opposite side. All the parameters and input signals are the same for both co-simulations (wind speed as shown in Fig. 9.5).

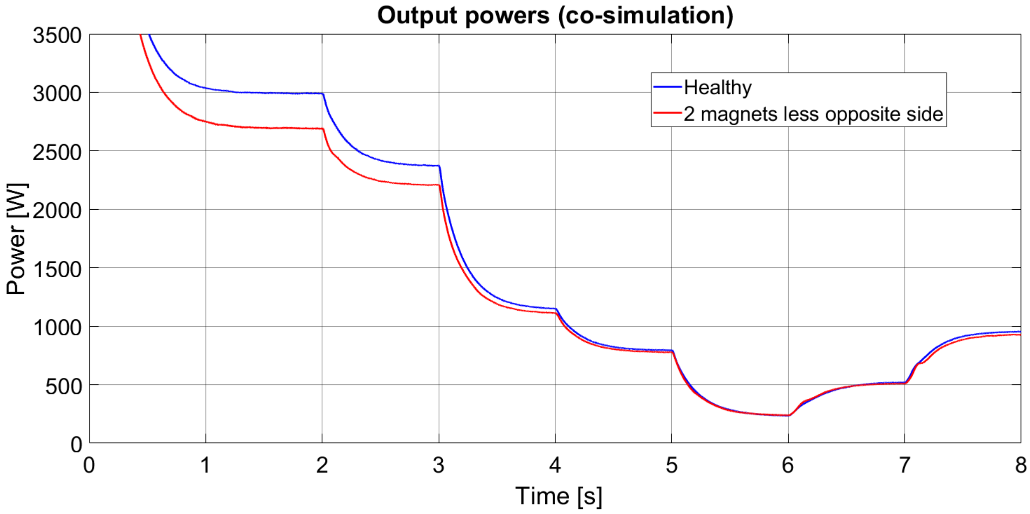

Fig. 9.11. DC bus output power for healthy PMSG (blue) and PMSG with 25% demagnetization (red)

In Fig. 9.11 the difference between the two cases is not connected to the modeling of the machine, this can be observed also in Fig. 9.12, there the torque generated by the SWT as an input to the PMSG, is presented for both cases.

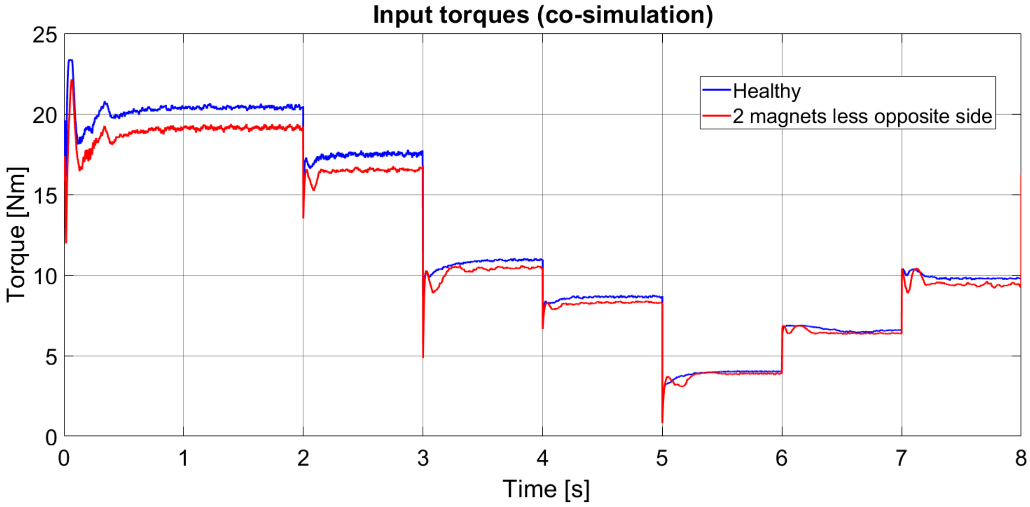

Fig. 9.12. Input torque for healthy PMSG (blue) and PMSG with 25% demagnetization (red)

The lower torque of Fig. 9.12 is linked to the shaft's angular speed presented in Fig. 9.13. There the angular speed of the shaft is has to be higher in the demagnetized case to maintain the voltage.

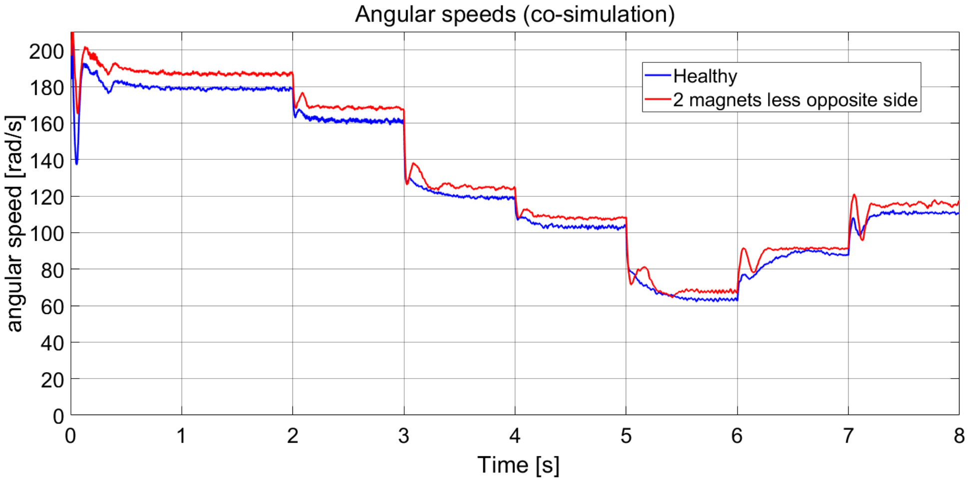

Fig. 9.13. Angular speed for healthy PMSG (blue) and PMSG with 25% demagnetization (red)

From the results presented in Figures 9.11, 9.12 and 9.13 is visible that the demagnetized case loses efficiency due to its inability to follow more closely the optimal torque reference. This is also visible in the MPPT results shown in Fig. 9.14 a and b.

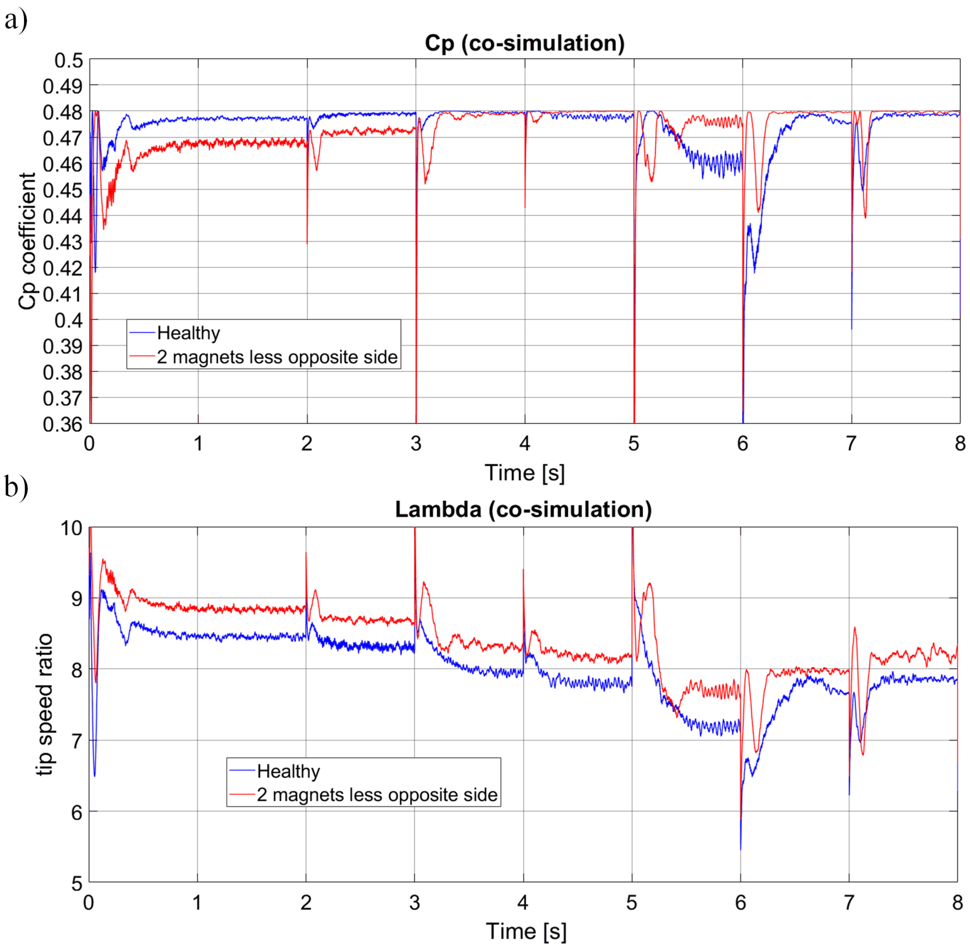

Fig. 9.14. Healthy PMSG (blue) and PMSG with 25% demagnetization (red): Cp a) and Lambda b)

Finally in Fig. 9.15 the phase currents for the 25% demagnetized case is presented. Notice that, although the output power didn't reach the 3 kW (∼2.6 kW in Fig. 9.11) the amplitude of the phase currents in the demagnetized case reaches over 10 A in strong winds (first two seconds with 12 m/s).

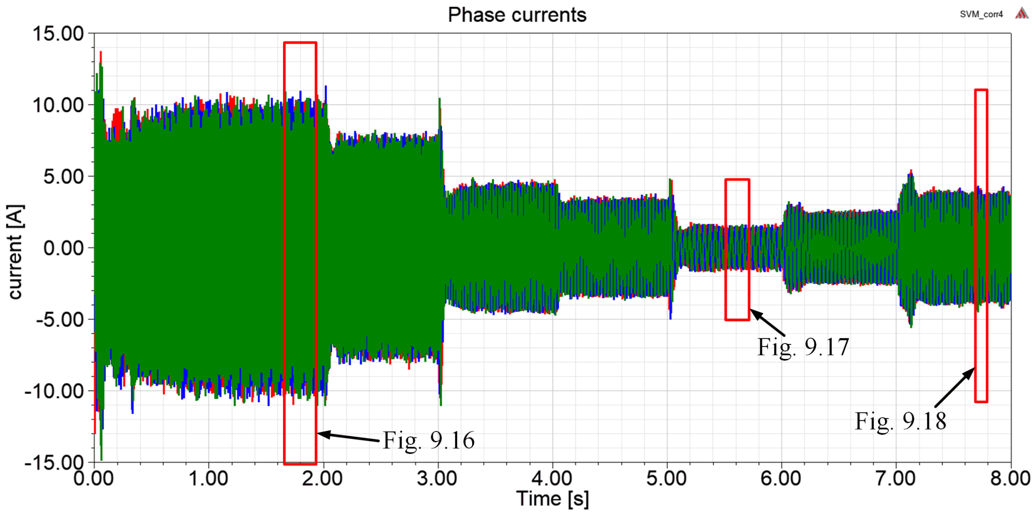

Fig. 9.15. Phase currents for the PMSG with 25% demagnetization

The higher speed and bigger currents at strong wind speeds, show that the control is trying to follow the optimal torque reference, although the demagnetized PMSG is not able to obtain the desired performance. This is an important finding because the operation of an already demagnetized PMSG with such high currents will provoque the machine's temperature to rise putting the rotor in risk of further demagnetization. In Fig. 9.16 a close-up of the phase currents during strong winds (12 m/s) is shown for the demagnetized PMSG.

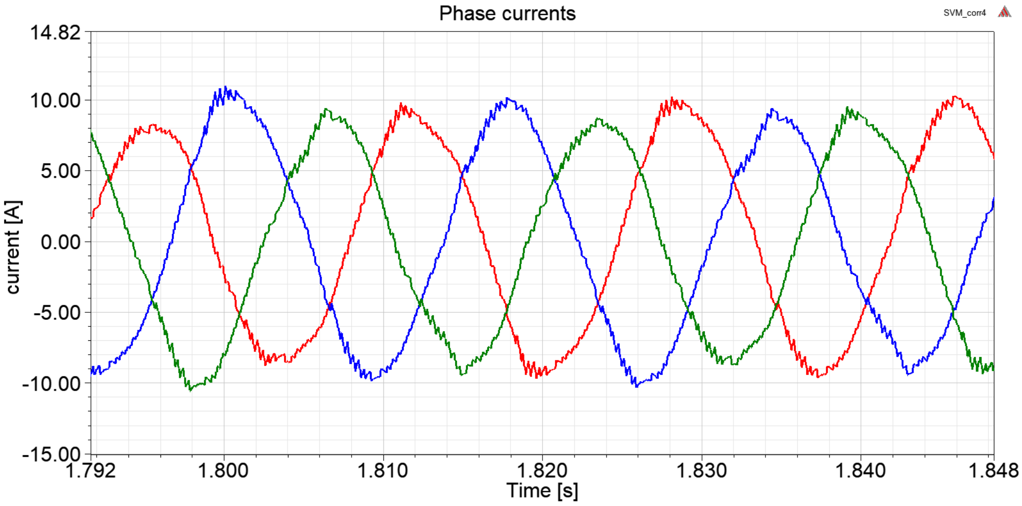

Fig. 9.16. Phase currents for the PMSG with 25% demagnetization at 12 m/s input wind speed

In Fig. 9.17 a close-up of the phase currents at 5 m/s wind speed for the demagnetized PMSG is presented.

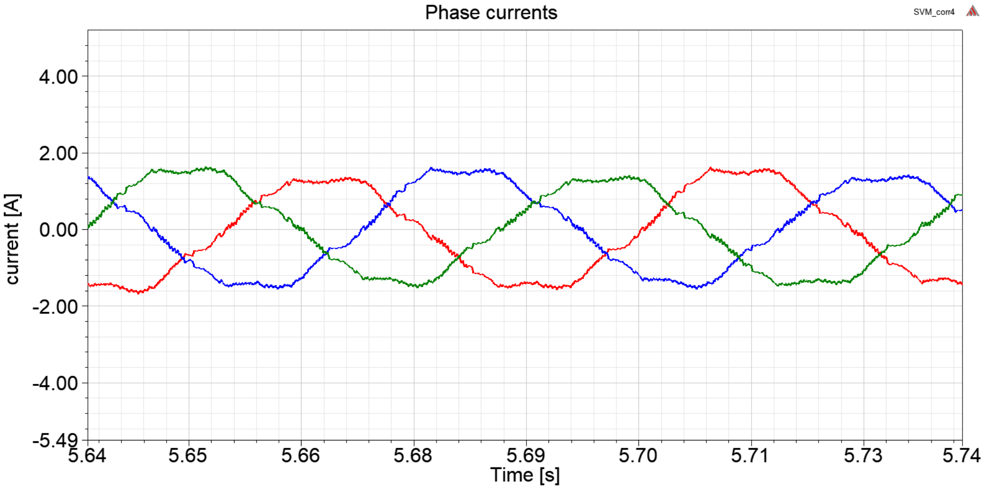

Fig. 9.17. Phase currents for the PMSG with 25% demagnetization at 5 m/s input wind speed

In Fig. 9.18 a close-up of the phase currents at 8 m/s input wind speed for the demagnetized PMSG is shown.

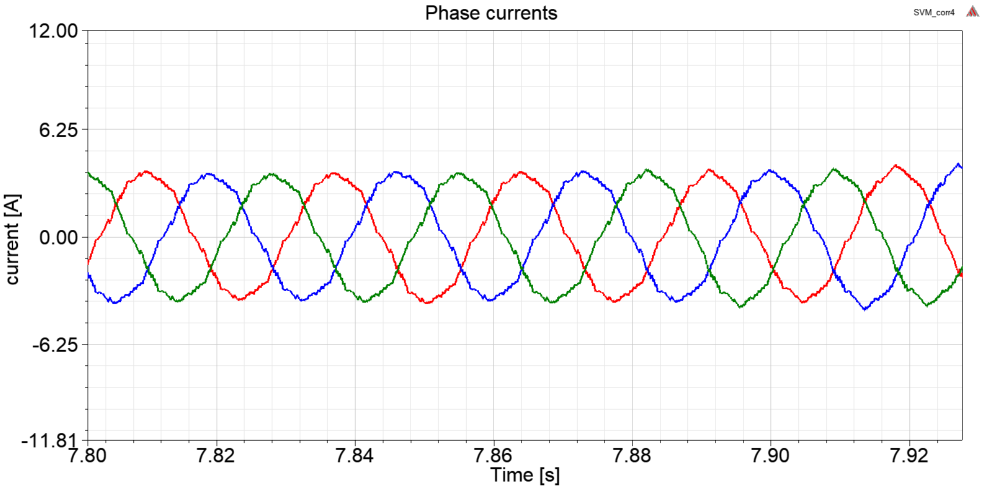

Fig. 9.18. Phase currents for the PMSG with 25% demagnetization at 8 m/s input wind speed

9.4. Conclusions

In this Chapter, the simulation and co-simulations of the complete WECS was presented. Clear differences, which were discussed in previous Chapters, between the simulation and co-simulation machine modelling are visible. Of greater importance, is the co-simulation's ability to model the PMSG faults. Even by changing the parameters of the SimPower systems' toolbox PMSG model wouldn't provide the results obtained by the co-simulation. This is because the flux linkage provided by the magnets in the SimPower systems' model is a machine constant that represents the whole machine (not a localised demagnetization feature).

In general, the currents shown in Figures 9.16, 9.17 and 9.18 are the greatest advantage of the co-simulation approach. There the information about the machine health status is embedded with the 3 kHz PWM switching signal. The currents have a sinusoidal form thanks to the FOC and PWM. Anyhow, some non-sinusoidal shape can be observed in the strong wind case (Fig. 9.16) and in the low wind speed (Fig. 9.17). Still these wave forms are not the same as the currents obtained when only the passive rectifier was connected to the PMSG (Chapter 6).

On the other hand, the co-simulation approach has the inconvenience that the computational time to obtain these results is many times longer than the SimPower Systems' simulation. This is, for the 8 seconds shown in this Chapter the co-simulations took $\sim$57 hours running on a Core i7 with 16 GB of RAM and SSD for the program's memory. This in comparison with the 45 seconds the Simulink SimPower systems' simulation took.

10. General conclusions

In this Chapter a summary of the of the achievements obtained in the development of this thesis is given. First the design of the novel IPM PMSG is discussed and the main advantages and disadvantages are compared. Then some insights into the demagnetization failure mechanisms and modelling for the PMSG are presented. Next, the results obtained with the co-simulation method for the SWT with passive rectifier and boost converter are discussed, and the new findings when using the co-simulation method for such complex systems are summarised. In the third section the implementation of the 2L-VSC with FOC is discussed on the basis of its advantages over the passive rectifier with boost converter. Finally, the operation of the PMSG with a full converter before, during, and after demagnetization is discussed and the importance of those findings are commented.

10.1. About the design of the PMSG

As shown in Chapter 2, the author developed a novel PMSG on the basis of an IM (Sh90-L4). The PMSG was designed as an IPM with the same stator of the IM (overlapping distributed three-phase windings). In order to save costs an approach called in the literature "induced pole" [77, 163] was adopted. Specifically, the usage of both sides of the magnets avoiding to use double the number of magnets. It was latter discovered that previous literature called this approach "*consequent pole*" in [164, 165]. There, professor Lipo and his students were the first ones to use such a configuration in the rotor of a transverse flux machine.

In [166] another author designed and manufactured an IPM with the consequent pole approach. It should be pointed out that in that publication (with a consequent pole IPM) the author warned about the potential disadvantage of the consequent pole approach in the form of an increase in machine noise in comparison to the standard IPM.

Although, in this thesis only the consequent pole PMSG prototype was tested (no standard IPM) it can be confirmed that the built prototype is quite noisy. Nevertheless, it was also confirmed that the built PMSG was very efficient and was able to produce more than 2.3 kW with 15 Nm input torque, in the same form factor where the IM was able to generate 10 Nm output torque with 1.5 kW. In general the PMSG almost double the rated power of the IM (around 73% higher). All these results demonstrate the efficiency of the consequent pole although this approach is not compatible with other approaches like the halbach array (Mallison-Halbach array) [15, 167].

It is important to point out the asymmetric geometry of the rotor which made necessary to use every time the complete geometry of the machine for the FEA. This asymmetry was done in order to obtain a lower THD while having a high back EMF as explained in Chapter 2.

As was shown in the multiple analysis (Chapter 3 and 7) the N38SH Nd-Fe-B magnets are able to operate very well up to temperatures of 100°C, and even in overload conditions. This mainly thanks to their SH rating for high temperatures, namely their relative amount of dysprosium in the magnetic powder.

Despite its high efficiency, the PMSG has some drawbacks, the torque ripple and its associated vibrations and noise could be prevented with some modifications, literature suggests that shaping the magnetic field helps to obtain a sinusoidal like back EMF [16, 168]. Other authors propose shaping the pole shoe and adding some holes in front of the magnets [19]. Also, the torque ripples can be reduced by skewing the magnets inside the rotor as published in [169, 160]. A combination of all these methods for a SWT can be found in [170]. Further work should include some of these methods for the reduction of torque ripples.

10.2. About the SWT co-simulation

In Chapter 5 some results of the co-simulation of the whole WECS are presented. The first results are the validation of the co-simulation with a passive rectifier, namely the comparison with the laboratory measurements where it was found that even the trapezoidal model of the SimPower Systems toolbox in Matlab Simulink was not able to model with accuracy the IPM, not to mention an asymmetric rotor like the one designed.

The co-simulation results with the passive rectifier and boost converter showed that it is useful to use this approach in comparison to the mathematical model of the PMSG in order to obtain more realistic results. In other words, the results obtained with the co-simulation showed some saturation of the PMSG when the currents' amplitude reached 10 A. This was related to the fact that the passive rectifier with boost converter is not able to work as a chopper as with the switched-mode rectifier. Therefore, the boost converter has a maximum input power limit and when the limit is reached the machine is saturated and stalls the turbine as showed in Chapter 5 Section 6.4. So for that converter topology (passive rectifier+boost converter) it is worth to use co-simulation to asses which control parameters (voltages and currents) have the biggest impact in the control loop, namely, when the machine will reach saturation.

Also, as presented in Chapter 9 the operation of the WECS with a 2L-VSC under FOC shows a similar behaviour but the advantage is that the full converter is able to maintain operation at high wind speed by converting the power into higher DC bus voltage. Another important result is the ability of the FOC to maintain operation even when the machine has been severely demagnetized (25% demagnetization).

From the SimPower systems' simulation and the co-simulation, it was observed that for the correct simulation and co-simulation of such complex interconnected systems, it is important to have correct models of the different components, namely, the model of the PMSG clearly is more accurate when using the FEM. On the other hand, the model of the WT is also important. Different models found in the literature had many simplifications that ultimately overestimated or underestimated the WT capacity to provide certain power level (output torque) for a certain wind speed. The model described in Appendix A is one of the most used in power systems' design and simulation. It is important to bear in mind that these models are still some simplified version of the real behaviour of the WT. Some other more complex models which include the aero-elastic simulation of horizontal-axis wind turbines (HAWT) like the FAST software from the National Renewable Energy Laboratory (NREL) in the USA, can be used for more accuracy in the WT model's output torque. However, it is commonly accepted that the results obtained with the WT model described in Appendix A, provide a dynamic behaviour close enough to the three-bladed HAWT for control analysis.

10.3. About the demagnetization

During the development of this thesis it was noticed that the permanent magnet machines have gained popularity as driving force for the different electromobility alternatives e.g. electric-vehicles (EV), personal electromobility (electric scooters, e-bikes) and even some early developments in aircraft (the more electric aircraft). Due to the pervasive use of the PM machines is of great importance to analyse their failure modes in different environments.

From the early design phase it was noticed the strong magnetic field generated by the Nd-Fe-B. Also in the design phase, the magnet thickness was chosen not only to produce the necessary magnetic flux density in the air gap but also to avoid possible demagnetization, by having operating points close to the B-H curve's knee. As was shown in Chapter 3 the selection of the N38SH material for the Nd-Fe-B magnets allowed for a continuous operation with magnet temperatures up to 100°C with almost no risk of demagnetization.

Notwithstanding, in Chapter 7 Section 7.6 some very interesting results are presented. In order to analyse this kind of fault (demagnetization) in the PMSG, the author applied the faults that were reported in the literature to have the biggest impact to drive the IPM to demagnetization, namely, asymmetrical short circuit and symmetrical short circuit. What was found, was that the short circuit currents were not high enough to drive the operating point of the magnets into demagnetization. Nevertheless, the sequence of steps that the short circuit triggers after the fault clearance proved to be more damaging for the PMSG than the short circuit itself.

This was still in good agreement with the theory and some of the results reported earlier that claimed that the state in which the transistors are not switching anymore and the IPM machine accelerates due to inertia was also of relevance to study and avoid an overvoltage on the DC bus due to the power (current) flowing in through the freewheelig diodes of the VSC. This condition called uncontrolled generator actually applies too in the case of the PMSG after fault clearance when the FOC's PI controllers are still in saturation and recovering from the acceleration the machine suffered due to the short circuit and the input torque present during the fault.

In other words, the UCG condition and the FOC trying to decelerate the machine back to the speed reference generate a demagnetizing current bigger (>1.5 times) than the short circuit currents. This currents proved to demagnetize at least partially the PMSG working with magnets at 80°C in nominal speed and 13 Nm input torque. Obviously when the machine was operating at higher temperature or at higher torque (or both) the demagnetization due to the UCG and FOC was bigger. In Fig. 10.1 the speed, voltages and currents for a 2 phase short circuit during nominal operation of the PMSG is shown.

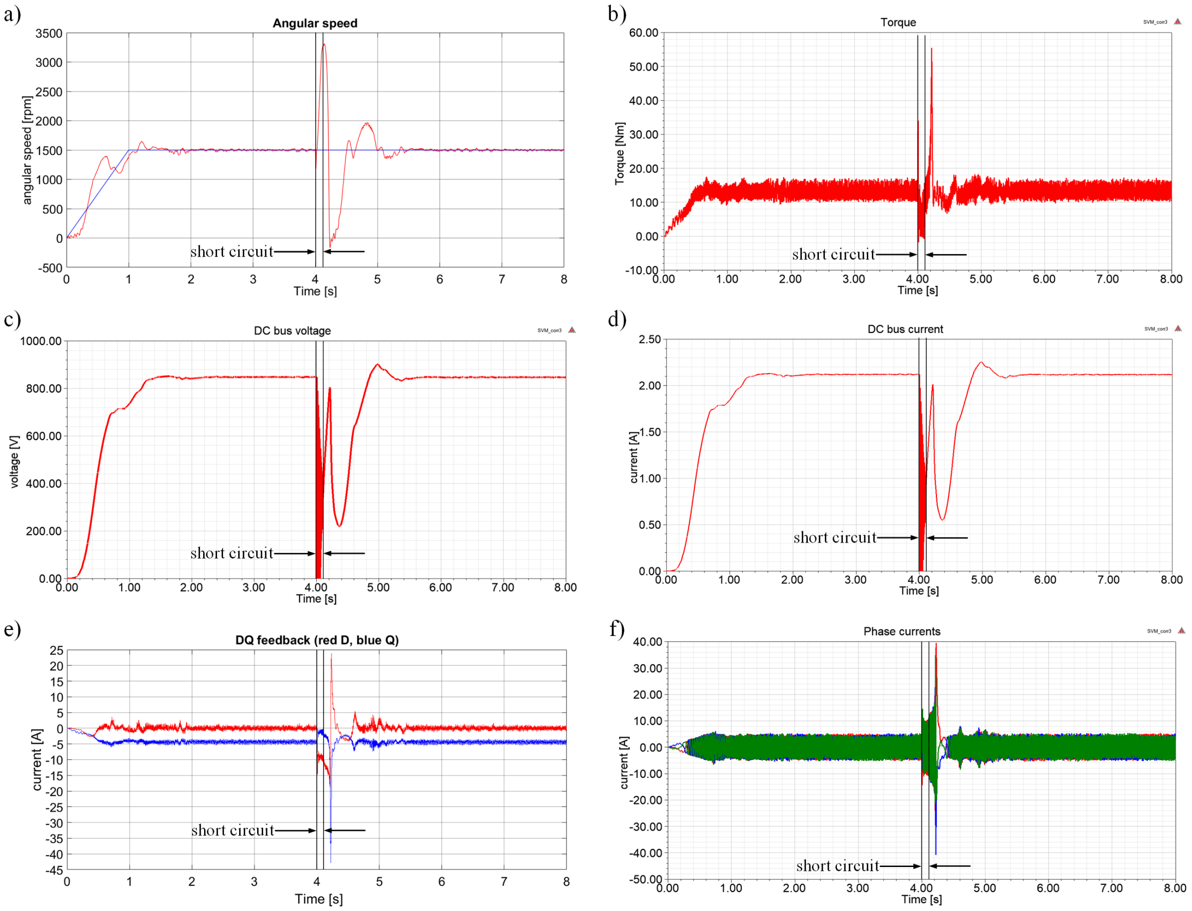

Fig. 10.1. Co-simulation results for 2 phase short circuit, 80°C magnets and 13 Nm of input torque: angular speed a), torque at the shaft b), DC bus voltage c), DC bus current d), dq currents e), and phase currents f)

It is important to mention that the current peak in the PMSG stator winding, due to the UCG and FOC deceleration, is very brief and generally no other parameters exceed the system's ratings, namely the DC bus voltage doesn't reach more than 1.2 kV (normal rating for the IGBTs' module) the DC bus current is also not over 5 A and for the case presented in Fig. 10.1 the speed reaches only to 3500 rpm which is still inside the PMSG operating region.

In Fig. 10.2 the effect of the small partial demagnetization becomes more clear. There, the current control response, namely the output signals for the current PI controllers are presented. Two cases are shown. First the in Fig. 10.2a the output signals for the 80ºC case presented in Fig. 10.1, and then for a similar case (same input torque and reference speed) but for magnets at 100ºC.

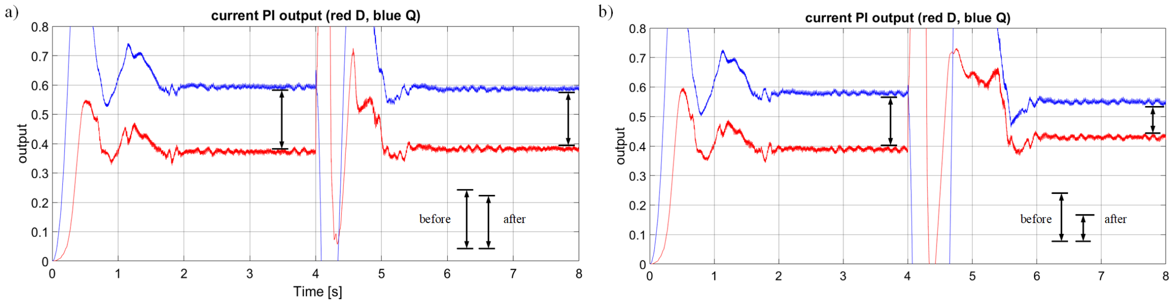

Fig. 10.2. Co-simulation results for 2 phase short circuit with 13 Nm input torque, current control output signals for: 80°C magnets a) and 100°C magnets b)

Although, the output signals of the current controllers seem to have a consistent behaviour with the demagnetization level, they cannot be considered as a fault index because the need of steady state and dependence on the PI parameters and the load (also the DC bus voltage level). For a better fault index the analysis of the D current showed in Chapter 8 and other methods analysed in the literature [171, 172] where most of them are based on current measurements.

10.4. About the operation of a demagnetized PMSG

Throughout the thesis different cases were presented, where the PMSG was operated either, already demagnetized or the dynamic demagnetization occurred during operation. In both cases there is evidence that the PMSG is able to operate even after severe demagnetization. Nevertheless, there are effects that impact on the performance of the machine once it has been demagnetized. These effects have a toll on the operating range of the PMSG. In other words, after demagnetization the FOC is able to operate the PMSG but at high input torque (>10Nm for the PMSG of this thesis) the system is not able to follow the reference because now the output power is lower.

Other authors in the literature have reported the effects that partial demagnetization has on the cogging torque (lower) and when the machine is loaded, in the torque ripples (higher) e.g.

in [173]. Also the study of the change in the back-EMF harmonics due to demagnetization has been done e.g. in [174]. But most of the literature focus on the machine signals after demagnetization with no regards to the effects on the control. In this thesis the combination of the PMSG in FEM with the control algorithm allows to asses the control behaviour before, during and after demagnetization and even analyse more complex phenomena that could drive the machine into demagnetization even without operating at high temperatures or outside the machine rating.

As mentioned in Chapter 1, it is of paramount importance to design wind energy conversion systems that can endure the harsh operating environments with low (or almost no) maintenance and on-site supervision. This *design-for-reliability* calls for the use of more complex simulation tools that can analyse the different faults that the WECS may encounter. In this thesis the use of co-simulation for a direct-driven PMSG SWT has proven to give an insight over the interactions between the control and the electromagnetic fields that could drive the machine to a less reliable operation due to partial demagnetization.

The author has completely achieved the purpose of the work. Theses have been proven. The work was tested in simulation and experiment.

10.5. The most important achievements of the author

As was explained in this Chapter the use of state-of-the-art approaches in the design of a PMSG allowed to obtain a high efficiency (>90%) PMSG from a series production IM.

The use of state-of-the-art simulation approach, referred in early literature as "time stepping field-circuit coupling simulation". Since it involves different software programs, the author prefer the name "co-simulation" (also used in the literature) for this approach. Thanks to the co-simulation some problems of operating the PMSG in high input torque were averted, namely, limit on the saturation of the machine and in the effects of the control when operating a partially demagnetized PMSG.

Finally, some not previously reported consequences of the short circuit fault when operating the PMSG under FOC were discovered. This means, the impact of the FOC after clearing the fault and its influence on demagnetization.

According to the author, the most important achievements include:
- Making the PMSG generator model in the FEM program;
- Preparation of the PMSG generator prototype and its testing;
- Development of a research concept using three programs - co-simulation;
- Development of a wind turbine simulation model and OTC control algorithm;
- Analysis of generator operation in various operating conditions;

— Experimental verification of open and closed system (software development in C language on DS1103 card);

— Analysis of the impact of phase-to-phase short-circuit on demagnetization processes and the effect of partial demagnetization on the operation process of the PMSG generator.

10.6. Author's list of publications

During the development of this Thesis the author published the following per-review scientific papers:

1. Quintal-Palomo, R. E., Figueroa-Espinoza, B. and Lopez-Gonzalez, J., (2016) "Analysis of a direct-drive wind turbine with Axial-Flux Permanent-Magnet Generator operating in close-shore conditions," IECON 2016 - 42nd Annual Conference of the IEEE Industrial Electronics Society, Florence, pp. 5532-5537. doi: 10.1109/IECON.2016.7793756
2. Quintal-Palomo, R. E., Gwoździewicz, M., and Dybkowski, M. (2016). "Parametric analysis for the design of a 4 pole radial permanent magnet generator for small wind turbines". Power Electronics and Drives, 1 (36)(2).
3. Gwozdziewicz M. and Quintal-Palomo, R. E. (2017), "Induced pole permanent magnet synchronous generator," 2017 International Symposium on Electrical Machines (SME), Naleczow, pp. 1-4. doi: 10.1109/ISEM.2017.7993542
4. Quintal-Palomo, R. E., Gwozdziewicz, M. and Dybkowski, M. (2017), "Design and test of an internal permanent magnet generator for small wind turbine applications", 2017 19th European Conference on Power Electronics and Applications (EPE'17 ECCE Europe), IEEE, p. P.1-P.4.
5. Quintal-Palomo, R. E., Gwozdziewicz, M. and Dybkowski, M. (2019), "Modelling and co-simulation of a permanent magnet synchronous generator", COMPEL - The International Journal for Computation and Mathematics in Electrical and Electronic Engineering, Vol. ahead-of-p No. ahead-of-print, available at: https://doi.org/10.1108/COMPEL-12-2018-0501.
6. Quintal-Palomo, R. E. (2019). "Analysis of current signals in a partially demagnetized vector controlled Interior Permanent Magnet generator". Power Electronics and Drives.
7. Quintal-Palomo, R. E. and Dybkowski, M. (2019). "Modelling and Co-Simulation of Small Wind Turbine with Permanent Magnet Synchronous Generator". Przeglad Elektrotechniczny.

Appendix

A. The Power in the Wind

A.1. Betz's limit

The extraction of energy from the wind can be explained from the continuity equation and the rate change of the kinetic energy, in other words, the change in the wind speed before and after the wind turbine. As shown in Fig.A.1 the amount of air that enters the surface A_1 has to be the same that exits through A_2. From the continuity equation we have:

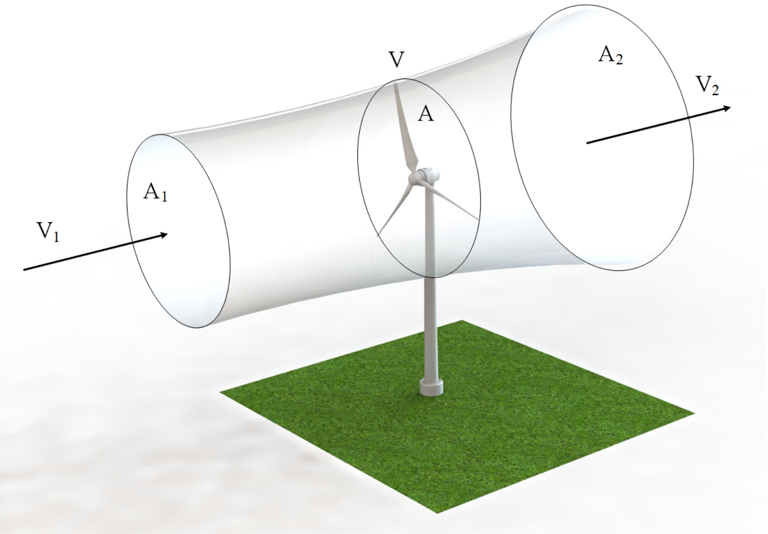

Fig. A.1. Wind vectors and areas for kinetic energy conversion

$$\rho_1 \cdot A_1 \cdot V_1 = \rho \cdot A \cdot V = \rho_2 \cdot A_2 \cdot V_2 \,, \tag{A.1}$$

where ρ_1 is the air density entering the area A_1 with a speed of V_1. Likewise, ρ and ρ_2 are the air densities at area A and A_2 respectively. The momentum flow rate is given by:

$$\rho \cdot A \cdot V^2 \,, \tag{A.2}$$

From equations A.1 and A.2 the force exerted on the wind turbine is:

$$P = F \cdot V = \left(\rho_1 \cdot A_1 \cdot {V_1}^2 - \rho_2 \cdot A_2 \cdot {V_2}^2\right) \cdot V \,, \tag{A.3}$$

The rate of change of the kinetic energy $V_1 - V_2$:

$$P = \frac{1}{2}\left(\rho_1 \cdot A_1 \cdot {V_1}^3 - \rho_2 \cdot A_2 \cdot {V_2}^3\right) \,, \tag{A.4}$$

Now the question arises *How much of this power can be extracted?*. Theoretically:

$$\begin{aligned} P_{theoretical} &= \rho \cdot A \cdot \frac{V_1 + V_2}{2} \cdot \left({V_1}^2 - {V_2}^2\right) && \text{(A.5a)} \\ &= \frac{\rho \cdot A \cdot {V_1}^3}{2} \cdot \left(1 + \frac{V_2}{V_1}\right) \cdot \left(1 - \frac{{V_2}^2}{{V_1}^2}\right) \,, && \text{(A.5b)} \\ &= P_0 \cdot C_{p\_th} && \text{(A.5c)} \end{aligned}$$

where C_{p_th} is the *theoretical* power coefficient and P_0 is the initial power in the wind. Notice that in P_0 the wind speed V_1 is cubic (raised to the power of three). Now analysing C_{p_th}:

$$C_{p\_th} = \frac{1}{2} \cdot \left(1 + \frac{V_2}{V_1}\right) \cdot \left(1 - \frac{{V_2}^2}{{V_1}^2}\right) \,, \tag{A.6}$$

If we make $x = V_2/V_1$ then:

$$C_{p\_th} = \frac{1}{2} \cdot (1 + x) \cdot (1 - x^2) \,, \tag{A.7}$$

So, to find the maximum power coefficient we derive equation A.7 and equal to zero:

$$\frac{dC_{p\_th}}{dx} = \frac{1}{2} \cdot \left(-3x^2 - 2x + 1\right) = 0 \,, \tag{A.8}$$

Solving for x we obtain two possible results, $x = -1$ or $x = 1/3$. So taking the positive result:

$$\left(\frac{V_2}{V_1}\right)_{opt} = \frac{1}{3} \,, \tag{A.9}$$

Now from equation A.6 and equation A.9 we get:

$$C_{p\_th} = \frac{1}{2}\left(1 + \frac{1}{3}\right)\left(1 - \frac{1}{9}\right) = \frac{16}{27} \approx 0.59 \,, \tag{A.10}$$

This means that we can only obtain around 59% of the power from the wind kinetic energy. This was discovered first by the German Physicist Albert Betz in 1919. Obviously this theoretical limit assumes no aerodynamic losses like the turbulence induced by the tower and other blade holding structures (as in the case of Darrieus and Savonius rotor) neither takes into account the blade tip induced turbulence and other losses associated with the surface friction. Notice in equation A.4 that the energy exchange was even assumed adiabatic (no change in the *medium* temperature) this means no change in the air density ρ.

In Fig. A.2 some qualitative analysis from the different rotor topologies is given. Here is clear why the most common configuration for commercial wind turbines is the three-bladed rotor. Notice also that even very aerodynamically advanced blades are only able to achieve around 0.48 C_p, in other words, 48% of the power from the wind.

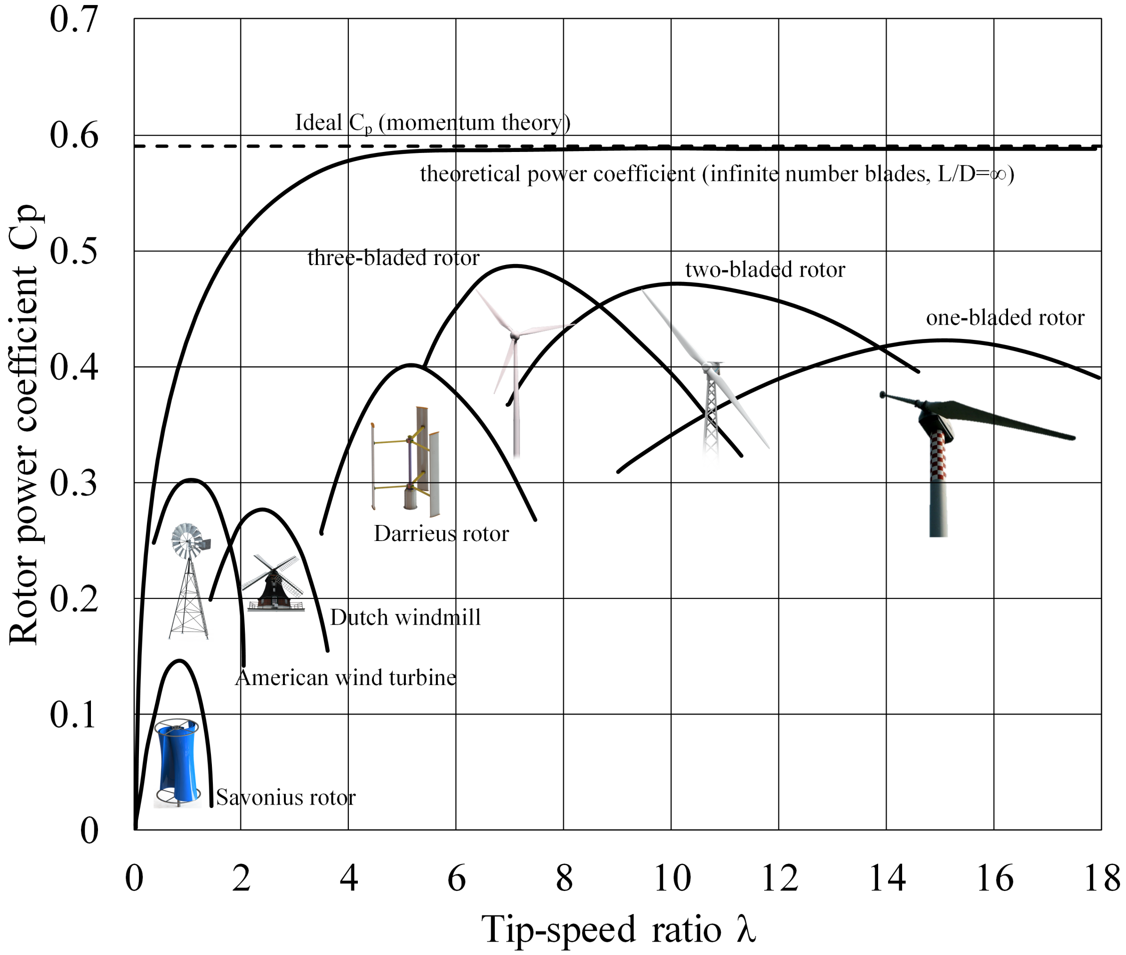

Fig. A.2. Tip speed ratio vs Power Coefficient for different rotor topologies. Data from [8]

As it was demonstrated before, the three-bladed rotor cannot extract more than 59% of the power from the wind, but in reality this coefficient is even lower. In Fig. A.3 three different approximations for the aerodynamic behaviour of the three-bladed rotor are shown. The blue curve is the most accurate since it correctly describes the start-up behaviour of the wind turbine, this means, the tip speed ratio (relation between the tangential speed of the tip of a blade and the actual speed of the wind) is small since the rotational speed ω is small because the turbine does not start to rotate until after a certain cut in wind speed. So, reminding the tip speed ratio equation:

$$\lambda = \frac{Tip\,speed\,of\,the\,blade}{Wind\,speed} = \frac{\omega R}{V}\,, \tag{A.11}$$

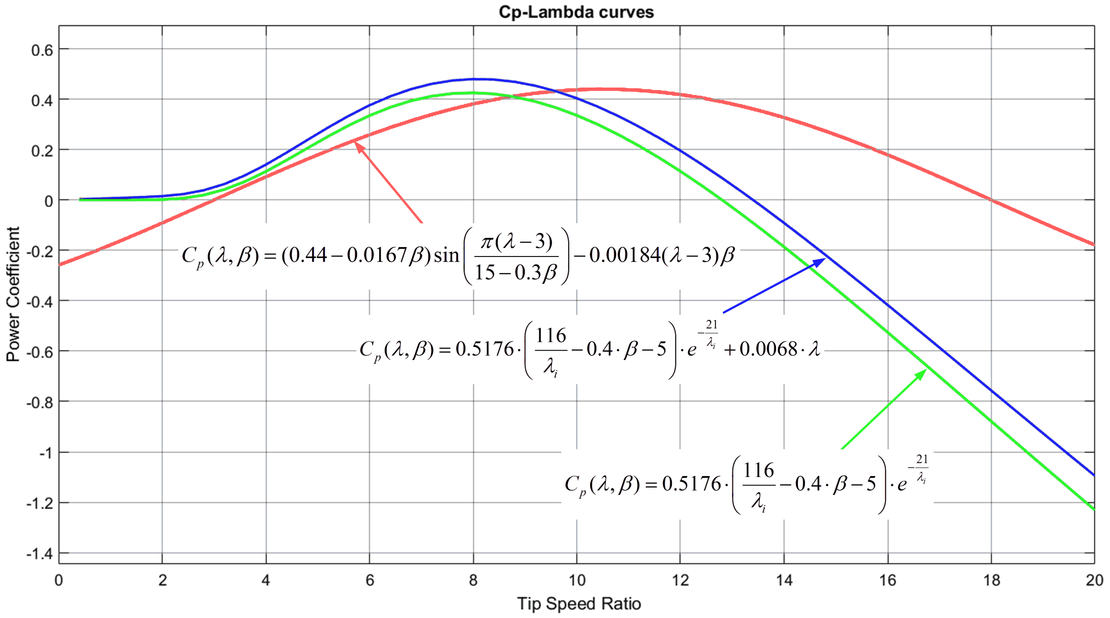

Fig. A.3. Three different approximations for the aerodynamic behaviour of a three-bladed rotor (β=0)

Notice from equation A.11 that since the turbine radius R is in meters, the rotational speed ω is in radians per second and the wind speed V is in meters per second, then lambda is unit-less. In Fig. A.3 the power coefficient C_p is dependent on lambda and the blade's pitch angle β, although the plotted curves are shown only for $\beta = 0$.

As mentioned before the preferred aerodynamic model of the wind turbine is:

$$C_p(\lambda, \beta) = c1 \cdot \left(\frac{c2}{\lambda_i} - c3 \cdot \beta - c4\right) \cdot e^{-\frac{c5}{\lambda_i}} + c6 \cdot \lambda\,, \tag{A.12}$$

where $c1$, $c2$, $c3$, $c4$, $c5$, and $c6$ are coefficients obtained by polynomial regression or curve fitting of experimental measurements or by the Blade Element Theory (BET), also λ_i is defined as:

$$\frac{1}{\lambda_i} = \frac{1}{\lambda + 0.08\beta} - \frac{0.035}{\beta^3 + 1}\,, \tag{A.13}$$

and for β=0:

$$\lambda_i = \frac{\lambda}{1 - 0.035\lambda}\,, \tag{A.14}$$

In Fig. A.3 the green curve is an approximation similar to the model in equation A.12 but with the last term omitted. The red curve is a very rough approximation based on a sinus that has the disadvantage of not being able to provide correct values of C_p for low rotational speeds, and having two or more maximum points due to the sinusoidal periodicity. A deeper analysis of these and other models for the aerodynamic behaviour of a wind turbine can be found in [175], and an analysis of the coefficients in equation A.12 can be found in [176].

B. Machine Parameters

Here a summary of the most important parameters of the designed PMSG are presented. In Table B.1 the measurements of voltage peak values measured line-to-line are shown for four different speeds. In Fig. B.1 the linear regression slope is what is known in the literature as voltage constant or back EMF constant [140], here the constant is 414.2 V_{peak}L-L/krpm.

Table B.1. PMSG peak voltage measured line-to-line for different speeds

speed [rpm]	V_{peak}L-L
1500	620
1000	415.6
500	208
0	0

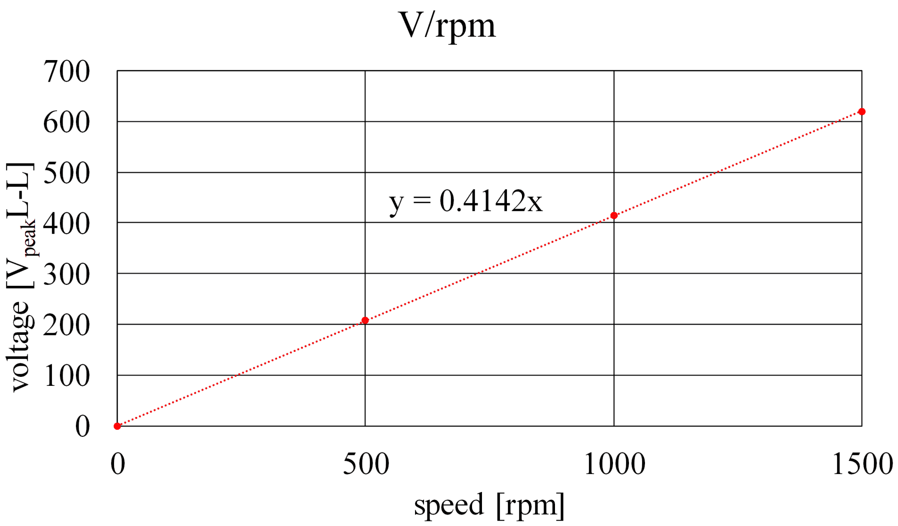

Fig. B.1. Voltage constant for the W shape PMSG

Note that as explained in [141] the voltage constant was tuned to 335.1V_{peak}L-L/krpm which corresponds to 0.8 Wb. In Table B.2 the other parameters of the W shape PMSG are presented. The nominal power is given as 2500 W although is important to mention that the nominal power in this particular machine is closely related to the thermal dissipation, in other words, the PMSG can operate at higher input torque giving higher output power but only for a short time. This is called in the literature a "short overload", e.g. [177], this is shown in Fig. B.2.

Table B.2. W shape consequent pole PMSG parameters

	Value
Pole pairs	2
Nominal power	2500 W
Nominal speed	1500 rpm
Stator phase resistance	5.56 Ω
Stator phase inductance	4.11 mH
Inertia	$0.015 \text{kg}\cdot\text{m}^2$
Viscous damping	0.0004924 N·m·s
Flux linkage established by magnets	0.8 Wb

The lower part of Fig. B.2 is the IPM in generating mode. This means that the PMSG can operate at higher input torque (higher than 15 Nm), producing more than 2500 W (as shown in Fig. 2.21) but for a short amount of time.

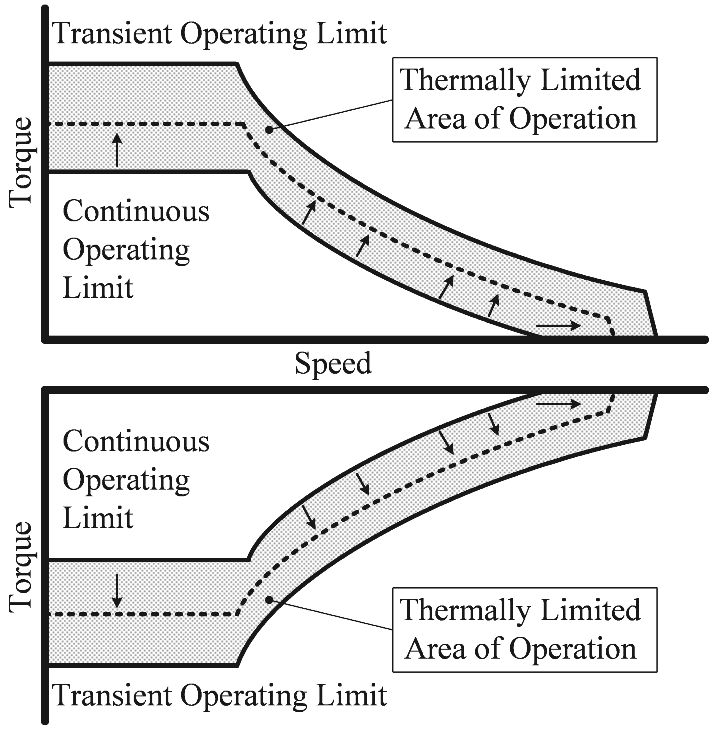

Fig. B.2. Operating regions of an IPM machine

Bibliography

[1] U. Shipurkar, K. Ma, H. Polinder, F. Blaabjerg, and J. A. Ferreira, "A review of failure mechanisms in wind turbine generator systems", in *2015 17th European Conference on Power Electronics and Applications (EPE'15 ECCE-Europe)*. sep 2015, pp. 1–10, IEEE.

[2] S. Lammens, "ZF WPT Market Intelligence OWI-Lab", Tech. Rep. 1, ZF Friedrichshafen AG, Löwentaler Straße 20, 88046 Friedrichshafen, Germany, September 09, 2012.

[3] S. Sheng, "Report on Wind Turbine Subsystem Reliability - A Survey of Various Databases", *NREL/PR-5000-59111,National Renewable Energy Laboratory NREL*, 2013.

[4] P. Tavner and F. Spinato, "Reliability of different wind turbine concepts with relevance to offshore application", *European Wind Energy Conference, Brussels*, January 2008.

[5] P. Tavner, "How are we going to make offshore wind farms more reliable?", *Supergen Wind*, 2011.

[6] DfR-solutions, "Designing reliability in electronics", workshop, 2012.

[7] J. Kang, "General purpose permanent magnet motor drive without speed and position sensor", *Yaskawa Electric Corp., Japan, Yaskawa Application Note WP. AFD*, 2009.

[8] E. Hau, *Windkraftanlagen: Grundlagen. Technik. Einsatz. Wirtschaftlichkeit*, Springer-Verlag, 1988.

[9] O. Gutfleisch, "Controlling the properties of high energy density permanent magnetic materials by different processing routes", *Journal of Physics D: Applied Physics*, vol. 33, no. 17, pp. R157–R172, sep 2000.

[10] A. Quesada, "The permanent magnets challenge", in *Difusion del Instituto de Ceramica y Vidrio CSIC*, September 2014.

[11] E. Spooner and B. J. Chalmers, "TORUS: a slotless, toroidal-stator, permanent-magnet generator", *IEE Proceedings B - Electric Power Applications*, vol. 139, no. 6, pp. 497–506, Nov 1992.

[12] S. Hieke, M. Stamann, D. Lagunov, R. Leidhold, A. Masliennikov, A. Duniev, and A. Yehorov, "Two-phase transverse flux machine with disc rotor for high torque low speed application", in *2017 19th European Conference on Power Electronics and Applications (EPE'17 ECCE Europe)*, Sept 2017, pp. P.1–P.8.

[13] Z. Goryca, "Low speed disk generator for small wind power station, Wolnoobrotowy generator tarczowy do małej elektrowni wiatrowej", *XVI Konferencja „Problemy Eksploatacji Maszyn i Napędów Elektrycznych", Rytro*, vol. 28, pp. 30, 2008.

[14] M. Rolak, R. Kot, M. Malinowski, Z. Goryca, and J. T. Szuster, “Design of small wind turbine with maximum power point tracking algorithm”, in *2011 IEEE International Symposium on Industrial Electronics*, June 2011, pp. 1023–1028.

[15] J. Gieras, *Permanent Magnet Motor Technology*, Electrical and Computer Engineering. CRC Press, 3rd edition, aug 2009.

[16] E. Muljadi and J. Green, “Cogging torque reduction in a permanent magnet wind turbine generator”, in *21st American Society of Mechanical Engineers Wind Energy Symposium*, Reno, Nevada, 2002, number January, pp. 340–342.

[17] A. Jabbari, M. Shakeri, and A. Nabavi, “Shape optimization of permanent magnet motors using the reduced basis technique”, *World Academy of Science, Engineering and Technology*, vol. 37, pp. 592, 2009.

[18] K. Wang, Z. Q. Zhu, and G. Ombach, “Torque improvement of five-phase surface-mounted permanent magnet machine using third-order harmonic”, *IEEE Transactions on Energy Conversion*, vol. 29, no. 3, pp. 735–747, Sept 2014.

[19] S. K. Lee, G. H. Kang, J. Hur, and B. W. Kim, “Stator and Rotor Shape Designs of Interior Permanent Magnet Type Brushless DC Motor for Reducing Torque Fluctuation”, *IEEE Transactions on Magnetics*, vol. 48, no. 11, pp. 4662–4665, nov 2012.

[20] B. C. Yun, K. K. Han, D. Y. Lee, G. H. Kang, K. B. Jang, H. K. Shin, and G. T. Kim, “A study on the improvement of dynamic characteristics in interior permanent magnet motor by rotor shape design”, in *2008 International Conference on Electrical Machines and Systems*, Oct 2008, pp. 3126–3130.

[21] C. S. Koh and J. S. Seol, “New cogging-torque reduction method for brushless permanent-magnet motors”, *IEEE Transactions on Magnetics*, vol. 39, no. 6, pp. 3503–3506, Nov 2003.

[22] J. S. Yu, H. W. Cho, J. Y. Choi, S. M. Jang, and S. H. Lee, “Optimum design of stator and rotor shape for cogging torque reduction in interior permanent magnet synchronous motors”, *Journal of Power Electronics*, vol. 13, no. 4, pp. 546–551, 2013.

[23] M. A. Ghadamyari, M. Moallem, and B. Fahimi, “Improving the torque characteristics of interior pm synchronous motor using an asymmetric on-off method on the rotor surface”, *Progress In Electromagnetics Research*, vol. 54, pp. 55–65, 2017.

[24] M. Malinowski, A. Milczarek, R. Kot, Z. Goryca, and J. T. Szuster, “Optimized energy-conversion systems for small wind turbines: Renewable energy sources in modern distributed power generation systems”, *IEEE Power Electronics Magazine*, vol. 2, no. 3, pp. 16–30, Sept 2015.

[25] Z. Goryca, M. Ziółek, and M. Malinowski, “Cogging torque of the multipolar generator with permanent magnets, Moment zaczepowy wielobiegunowej maszyny z magnesami trwałymi”, *Zeszyty Problemowe-Maszyny Elektryczne*, , no. 88, 2010.

[26] B. S. Umesh and K. Sivakumar, “Generation of multilevel voltage profile for torque ripple reduction of a 15 phase pole-phase modulated induction motor drive using two-level inverter structure”, in *2016 IEEE International Conference on Industrial Technology (ICIT)*, March 2016, pp. 1002–1007.

[27] R. Cuzner, C. Goshaw, T. Nguyen, A. Bendre, and M. Mekhiche, “Evaluation of medium voltage electric propulsion drive for electromagnetic compatibility using multidomain modeling”, in *Conference Record of the 2004 IEEE Industry Applications Conference, 2004. 39th IAS Annual Meeting.*, Oct 2004, vol. 3, pp. 2010–2017 vol.3.

[28] X. Li, S. Kher, S. Huang, V. V. Ambalavanar, and Y. Hu, “Component modeling and system level simulation of aircraft electrical systems.”, *Engineering Letters*, vol. 24, no. 2, 2016.

[29] A. I. Maswood, N. Sarangan, and A. Venkataraman, “Comparison of current control methods for a near unity power factor converter in a wind generator system feeding stand-alone loads”, *Conference Record - IAS Annual Meeting (IEEE Industry Applications Society)*, pp. 1–8, 2011.

[30] A. Antony and M. Khalid, “A modular DC DC converter with medium frequency transformer for power conversion in offshore wind farms”, in *2017 International Conference on Energy, Communication, Data Analytics and Soft Computing, ICECDS 2017*. aug 2018, pp. 1526–1531, IEEE.

[31] N. S. Kumar and S. V. Devi, “Design of power electronic transformer based variable speed wind energy conversion system”, in *2016 International Conference on Circuit, Power and Computing Technologies (ICCPCT)*. mar 2016, pp. 1–7, IEEE.

[32] K. Senthilnathan and K. I. Annapoorani, “Co-simulation and hardware implementation of multi-port rectifier for power system and renewable energy applications”, *Wind Engineering*, p. 0309524X1878038, jun 2018.

[33] A. Zidan, B. Housseini, M. Tarbouchi, D. Bouchard, and A. F. Okou, “Incorporating Saturation in Permanent-Magnetic Synchronous Generator Modeling for All-Electric Ship Applications”, in *2018 6th IEEE International Conference on Smart Energy Grid Engineering, SEGE 2018*. aug 2018, pp. 260–266, IEEE.

[34] S. Yang, *Novel sensorless generator control and grid fault ride-through strategies for variable-speed wind turbines and implementation on a new real-time simulation platform*, PhD thesis, Iowa State University, Digital Repository, Ames, 2010.

[35] Y. Y. Hong, Y. T. Ye, Y. R. Chang, Y. D. Lee, and P. W. Liu, “FPGA-based on-line Neural Network in Energy Storage System for Power Regulation of Wind-turbine Generator”, in *International Conference on Power Systems Transients (IPST2015)*, Cavtat, 2015.

[36] S. Singh and B. Jain, “Real Time Simulation of Power Electronic Converters”, in *2018 International Conference on Control, Power, Communication and Computing Technologies (ICCPCCT)*. mar 2018, pp. 450–454, IEEE.

[37] P. Zhou, D. Lin, W. N. Fu, B. Ionescu, and Z. J. Cendes, “A general cosimulation approach for coupled field-circuit problems”, *IEEE Transactions on Magnetics*, vol. 42, no. 4, pp. 1051–1054, apr 2006.

[38] U. Knorr and R. Juchem, “A complete co-simulation-based design environment for electric and hybrid-electric vehicles, fuel-cell systems, and drive trains”, in *SAE Technical Paper*. 03 2003, SAE International.

[39] S. Kanerva, J. Kaukonen, A. Szucs, and T. Hautamaki, "Coupled fem-control simulation in the analysis of electrical machines and converters", in *2006 12th International Power Electronics and Motion Control Conference*, Aug 2006, pp. 1925–1930.

[40] S. Kanerva, S. Seman, and A. Arkkio, "Inductance model for coupling finite element analysis with circuit simulation", *IEEE Transactions on Magnetics*, vol. 41, no. 5, pp. 1620–1623, May 2005.

[41] A. Arkkio, *Analysis of induction motors based on the numerical solution of the magnetic field and circuit equations*, Phd thesis of the helsinki university of technology, 1987.

[42] S. J. Salon, "Finite element analysis of electric machinery", *IEEE Computer Applications in Power*, vol. 3, no. 2, pp. 29–32, April 1990.

[43] N. Bianchi, *Electrical Machine Analysis Using Finite Elements*, CRC Press, Boston, MA, 1st edition, jun 2005.

[44] T. A. Lipo, *Introduction to AC Machine Design*, IEEE Press Series on Power Engineering. John Wiley & Sons, Inc., Hoboken, NJ, USA, aug 2017.

[45] A. Tessarolo, F. Luise, S. Pieri, A. Benedetti, M. Bortolozzi, and M. De Martin, "Design for Manufacturability of an Off-Shore Direct-Drive Wind Generator: An Insight Into Additional Loss Prediction and Mitigation", *IEEE Transactions on Industry Applications*, vol. 53, no. 5, pp. 4831–4842, sep 2017.

[46] H. Toliyat, S. Nandi, S. Choi, and H. Meshgin-Kelk, *Electric Machines*, CRC Press, oct 2012.

[47] M. Rosu, P. Zhou, D. Lin, D. Ionel, M. Popescu, F. Blaabjerg, V. Rallabandi, and D. Staton, *Multiphysics Simulation by Design for Electrical Machines, Power Electronics, and Drives*, John Wiley & Sons, Inc., Hoboken, NJ, USA, dec 2018.

[48] A. Haniotis, A. Kladas, and J. Tegopoulos, "Coupled field, circuit and mechanical modelling of wind turbine", *COMPEL - The international journal for computation and mathematics in electrical and electronic engineering*, vol. 25, no. 2, pp. 357–367, apr 2006.

[49] S. Schöps, H. De Gersem, and T. Weiland, "Winding functions in transient magnetoquasistatic field-circuit coupled simulations", *COMPEL - The international journal for computation and mathematics in electrical and electronic engineering*, vol. 32, no. 6, pp. 2063–2083, nov 2013.

[50] M. P. Ciurys, "Electromagnetic phenomena analysis in brushless DC motor with speed control using PWM method", *Open Physics*, vol. 15, no. 1, pp. 907–912, dec 2017.

[51] M. P. Ciurys, "Analysis of the influence of inverter PWM speed control methods on the operation of a BLDC motor", *Archives of Electrical Engineering*, vol. 67, no. 4, pp. 939–953, 2018.

[52] Z. Wenxiang, C. Ming, Z. Xiaoyong, H. Wei, and K. Xiangxin, "Analysis of Fault-Tolerant Performance of a Doubly Salient Permanent-Magnet Motor Drive Using Transient Cosimulation Method", *IEEE Transactions on Industrial Electronics*, vol. 55, no. 4, pp. 1739–1748, apr 2008.

[53] J. Zhao, X. Gao, B. Li, X. Liu, and X. Guan, "Open-Phase Fault Tolerance Techniques of Five-Phase Dual-Rotor Permanent Magnet Synchronous Motor", *Energies*, vol. 8, no. 11, pp. 12810–12838, nov 2015.

[54] C. M. Apostoaia, "Multi-domain system models integration for faults detection in induction motor drives", in *IEEE International Conference on Electro/Information Technology*. jun 2014, pp. 388–393, IEEE.

[55] C. M. Apostoaia and M. Cernat, "Fault detection in synchronous motor drives, a co-simulation approach", in *2015 Intl Aegean Conference on Electrical Machines & Power Electronics (ACEMP), 2015 Intl Conference on Optimization of Electrical & Electronic Equipment (OPTIM) & 2015 Intl Symposium on Advanced Electromechanical Motion Systems (ELECTROMOTION)*. sep 2015, pp. 617–622, IEEE.

[56] Y. Cetinceviz, D. Uygun, and H. Demirel, "Multi-criterion design and 2D cosimulation model of 4 kW PM synchronous generator for standalone run-of-the-river stations", in *2015 International Conference on Renewable Energy Research and Applications (ICRERA)*. nov 2015, vol. 5, pp. 1470–1476, IEEE.

[57] C. Ocak, D. Uygun, and I. Tarimer, "FEM based multi-criterion design and implementation of a PM synchronous wind generator by fully coupled co-simulation", *Advances in Electrical and Computer Engineering*, vol. 18, no. 1, pp. 37–42, 2018.

[58] J. Gonzalez, C. Hernandez, E. Melgoza, C. Espinoza, J. L. Hernandez, M. A. Arjona, and F. J. Martinez, "Analysis of a PMSG and its power electronic converter in isolated operation", in *2016 XXII International Conference on Electrical Machines (ICEM)*. sep 2016, pp. 126–131, IEEE.

[59] M. Irfan, E. Azizul-Hakim, D. Suhardi, N. Kasan, M. Effendy, I. Pakaya, and A. Faruq, "A Design of Electrical Permanent Magnet Generator for Rural Area Wind Power Plant", *International Journal of Power Electronics and Drive Systems (IJPEDS)*, vol. 9, no. 1, pp. 269, mar 2018.

[60] G. Persarvet, *Evaluation of Finite Element Method Based Software for Simulation of Hydropower Generator - Power Grid Interaction*, PhD thesis, Uppsala Universitet, 2011.

[61] P. Makolo, *Wind Generator Co-Simulation with Fault Case Analysis Master of Science Thesis*, PhD thesis, Chalmers University of Technology, Göteborg, 2013.

[62] Celma Indukta, "Sh 90L4", `https://www.cantonigroup.com/celma/en/page/offer/details/1/146/Sh90L-4`, 2019, Accessed: 01.06.2019.

[63] A. El-Refaie, "Fractional-slot concentrated-windings: A paradigm shift in electrical machines", in *2013 IEEE Workshop on Electrical Machines Design, Control and Diagnosis (WEMDCD)*, March 2013, pp. 24–32.

[64] J. Bernatt, T. Glinka, M. Jakubiec, E. Krol, and R. Rossa, "Electric motors with permanent magnets with two-zone rotational speed control", in *2007 International Aegean Conference on Electrical Machines and Power Electronics*, Sept 2007, pp. 653–658.

[65] E. Spooner, P. Gordon, J. R. Bumby, and C. D. French, "Lightweight ironless-stator pm generators for direct-drive wind turbines", *IEE Proceedings - Electric Power Applications*, vol. 152, no. 1, pp. 17–26, Jan 2005.

[66] K. Tuttelberg, T. Vaimann, and A. Kallaste, "Analysis of a slow-speed slotless permanent magnet synchronous generator", in *2013 4th International Youth Conference on Energy (IYCE)*, June 2013, pp. 1–5.

[67] M. Valavi, A. Nysveen, R. Nilssen, R. D. Lorenz, and T. Rølvåg, "Influence of pole and slot combinations on magnetic forces and vibration in low-speed pm wind generators", *IEEE Transactions on Magnetics*, vol. 50, no. 5, pp. 1–11, May 2014.

[68] M. Godoy Simões, F. A. Farret, and F. Blaabjerg, "Small wind energy systems", *Electric Power Components and Systems*, vol. 43, no. 12, pp. 1388–1405, 2015.

[69] W. Deng, S. Zuo, F. Lin, and S. Wu, "Influence of pole and slot combinations on vibration and noise in external rotor axial flux in-wheel motors", *IET Electric Power Applications*, vol. 11, no. 4, pp. 586–594, 2017.

[70] C. Rossi, P. Corbelli, and G. Grandi, "W-cvt continuously variable transmission for wind energy conversion system", in *2009 IEEE Power Electronics and Machines in Wind Applications*, June 2009, pp. 1–10.

[71] "Testing cheap wind power", `https://www.technologyreview.com/s/416038/testing-cheap-wind-power/`, Accessed: 05.03.2019.

[72] F. T. Jorgensen, T. O. Andersen, and P. O. Rasmussen, "The cycloid permanent magnetic gear", *IEEE Transactions on Industry Applications*, vol. 44, no. 6, pp. 1659–1665, November 2008.

[73] K. Atallah, J. Wang, S. D. Calverley, and S. Duggan, "Design and operation of a magnetic continuously variable transmission", *IEEE Transactions on Industry Applications*, vol. 48, no. 4, pp. 1288–1295, July 2012.

[74] S. Gerber and R. J. Wang, "Design and evaluation of a magnetically geared pm machine", *IEEE Transactions on Magnetics*, vol. 51, no. 8, pp. 1–10, Aug 2015.

[75] F. Spinato, P. J. Tavner, G. J. W. V. Bussel, and E. Koutoulakos, "Reliability of wind turbine subassemblies", *IET Renewable Power Generation*, vol. 3, no. 4, pp. 387–401, December 2009.

[76] A. Kallaste, T. Vaimann, and A. Belahcen, "Possible manufacturing tolerance faults in design and construction of low speed slotless permanent magnet generator", in *2014 16th European Conference on Power Electronics and Applications*, Aug 2014, pp. 1–10.

[77] R. T. Ugale, B. N. Chaudhari, S. Baka, S. S. Dambhare, and A. Pramanik, "Induced pole rotor structure for line start permanent magnet synchronous motors", *IET Electric Power Applications*, vol. 8, no. 4, pp. 131–140, April 2014.

[78] M. Gwoździewicz and J. Zawilak, "Single-phase line start permanent magnet synchronous motor. rotor construction and stator winding optimization", *Archives of Electrical Engineering*, vol. 62, no. 2, pp. 227–236, 2013.

[79] T. Zawilak, "Patent: Two-speed synchronous motor with permanent magnets (Dwubiegowy silnik synchroniczny z magnesami trwałymi)", , no. PL 207671 B1, Int. Cl. H02K 1/27, H02K 21/14, 2007.

[80] M. Gwozdziewicz and J. Zawilak, "Limitation of torque ripple in medium power line start permanent magnet synchronous motor", in *XXIV Symposium Electromagnetic Phenomena in Nonlinear Circuits*. Helsinki, Finland, 2016, pp. 7–8.

[81] H. R. Kirchmayr, "Permanent magnets and hard magnetic materials", *Journal of Physics D: Applied Physics*, vol. 29, no. 11, pp. 2763, 1996.

[82] B. Bochenkov and S. Lutz, "A review of modern materials of permanent magnets", in *Proceedings. The 8th Russian-Korean International Symposium on Science and Technology, 2004. KORUS 2004.*, June 2004, vol. 1, pp. 201–203 vol. 1.

[83] M. H. Walmer, J. F. Liu, and P. C. Dent, "Current status of permanent magnet industry in the united states", in *20th International Workshop on Rare Earth Permanent Magnets and their Applications*, September 2008.

[84] S. Dong, W. Li, H. Chen, and R. Han, "The status of chinese permanent magnet industry and r&d activities", *AIP Advances*, vol. 7, no. 5, pp. 056237, 2017.

[85] V. B. Honsinger, "The fields and parameters of interior type ac permanent magnet machines", *IEEE Transactions on Power Apparatus and Systems*, vol. PAS-101, no. 4, pp. 867–876, April 1982.

[86] "Typical data for SURA M400-50A from Cogent", `http://cogent-power.com/cms-data/downloads/m400-50a.pdf`, Accessed: 2017-12-18.

[87] S. Lipiński and J. Zawilak, "Transient Heat Transfer During the Starting Process of a Line Start Permanent Magnet Synchronous Motor", in *2018 International Symposium on Electrical Machines (SME).* jun 2018, pp. 1–4, IEEE.

[88] J. M. D. Coey, *Magnetism and Magnetic Materials*, Cambridge University Press, Cambridge, 2010.

[89] O. Gutfleisch, M. A. Willard, E. Brück, C. H. Chen, S. G. Sankar, and J. P. Liu, "Magnetic Materials and Devices for the 21st Century: Stronger, Lighter, and More Energy Efficient", *Advanced Materials*, vol. 23, no. 7, pp. 821–842, feb 2011.

[90] G. H. Kang, J. P. Hong, G. T. Kim, and J. W. Park, "Improved parameter modeling of interior permanent magnet synchronous motor based on finite element analysis", *IEEE Transactions on Magnetics*, vol. 36, no. 4, pp. 1867–1870, jul 2000.

[91] G. H. Kang, J. Hur, H. Nam, J. P. Hong, and G. T. Kim, "Analysis of irreversible magnet demagnetization in line-start motors based on the finite-element method", *IEEE Transactions on Magnetics*, vol. 39, no. 3, pp. 1488–1491, may 2003.

[92] S. Ruoho, E. Dlala, and A. Arkkio, "Comparison of Demagnetization Models for Finite-Element Analysis of Permanent-Magnet Synchronous Machines", *IEEE Transactions on Magnetics*, vol. 43, no. 11, pp. 3964–3968, nov 2007.

[93] S. Ruoho, J. Kolehmainen, J. Ikaheimo, and A. Arkkio, "Interdependence of Demagnetization, Loading, and Temperature Rise in a Permanent-Magnet Synchronous Motor", *IEEE Transactions on Magnetics*, vol. 46, no. 3, pp. 949–953, mar 2010.

[94] W. N. Fu and S. L. Ho, "Dynamic Demagnetization Computation of Permanent Magnet Motors Using Finite Element Method With Normal Magnetization Curves", *IEEE Transactions on Applied Superconductivity*, vol. 20, no. 3, pp. 851–855, jun 2010.

[95] P. Zhou, D. Lin, Y. Xiao, N. Lambert, and M. A. Rahman, "Temperature-Dependent Demagnetization Model of Permanent Magnets for Finite Element Analysis", *IEEE Transactions on Magnetics*, vol. 48, no. 2, pp. 1031–1034, feb 2012.

[96] K. C. Kim, K. Kim, H. J. Kim, and J. Lee, "Demagnetization Analysis of Permanent Magnets According to Rotor Types of Interior Permanent Magnet Synchronous Motor", *IEEE Transactions on Magnetics*, vol. 45, no. 6, pp. 2799–2802, jun 2009.

[97] C. Kral, R. Sprangers, J. Waarma, A. Haumer, O. Winter, and E. Lomonova, "Modeling demagnetization effects in permanent magnet synchronous machines", in *The XIX International Conference on Electrical Machines - ICEM 2010*. sep 2010, pp. 1–6, IEEE.

[98] R. Fratila, A. Benabou, A. Tounzi, and J. C. Mipo, "Nonlinear Modeling of Magnetization Loss in Permanent Magnets", *IEEE Transactions on Magnetics*, vol. 48, no. 11, pp. 2957–2960, nov 2012.

[99] K&J Magnetics Inc, "Demagnetization (BH) Curves for Neodymium Magnets", `https://www.kjmagnetics.com/bhcurves.asp`, 2019, Accessed: 27.05.2019.

[100] S. Sjokvist and S. Eriksson, "Experimental Verification of a Simulation Model for Partial Demagnetization of Permanent Magnets", *IEEE Transactions on Magnetics*, vol. 50, no. 12, pp. 1–5, dec 2014.

[101] H. Xiong, J. Zhang, M. W. Degner, C. Rong, F. Liang, and W. Li, "Permanet magnet demagnetization test fixture design and validation", in *2015 IEEE Energy Conversion Congress and Exposition (ECCE)*. sep 2015, pp. 3914–3921, IEEE.

[102] Y. S. Lee, K. T. Kim, and J. Hur, "Finite-Element Analysis of the Demagnetization of IPM-Type BLDC Motor With Stator Turn Fault", *IEEE Transactions on Magnetics*, vol. 50, no. 2, pp. 889–892, feb 2014.

[103] G. Choi and T. M. Jahns, "Demagnetization characteristics of permanent magnet synchronous machines", in *IECON 2014 - 40th Annual Conference of the IEEE Industrial Electronics Society*. oct 2014, pp. 469–475, IEEE.

[104] V. I. Patel, J. Wang, and S. S. Nair, "Demagnetization Assessment of Fractional-Slot and Distributed Wound 6-Phase Permanent Magnet Machines", *IEEE Transactions on Magnetics*, vol. 51, no. 6, pp. 1–11, jun 2015.

[105] S. Zhang and T. G. Habetler, "Transient Demagnetization Characteristics of Interior Permanent Magnet Synchronous Machines with Stator Inter-Turn Short Circuit Faults for Automotive Applications", in *2018 IEEE Energy Conversion Congress and Exposition (ECCE)*. sep 2018, pp. 1661–1667, IEEE.

[106] S. Hamidizadeh, N. Alatawneh, R. R. Chromik, and D. A. Lowther, "Comparison of Different Demagnetization Models of Permanent Magnet in Machines for Electric Vehicle Application", *IEEE Transactions on Magnetics*, vol. 52, no. 5, pp. 1–4, may 2016.

[107] Arnold Magnetic Technologies Corp., "Neodymium Iron Boron N38 magnets", `https://www.arnoldmagnetics.com/wp-content/uploads/2017/11/N38-151021.pdf`, 2019, Accessed: 01.06.2019.

[108] S. Lipiński, "2D steady-state thermal analysis of a line-start, permanent magnet synchronous motor", *Przegląd Elektrotechniczny*, vol. 1, no. 3, pp. 183–186, 2017.

[109] S. Lipiński, "Three-Dimensional Thermal Model of a Line-Start Permanent Magnet Synchronous Motor Using Computational Fluid Dynamics", *Przegląd Elektrotechniczny*, vol. 1, no. 2, pp. 179–182, 2017.

[110] G. Iwanski and W. Koczara, "PLL Grid Synchronization of the Standalone DFIG based Wind Turbine or Rotary UPS", in *EUROCON 2007 - The International Conference on "Computer as a Tool"*. 2007, pp. 2550–2555, IEEE.

[111] D. Ban, D. Žarko, M. Mađerčić, Z. Čulig, M. Petrinić, B. Tomičić, and J. Študir, "Generator technology for wind turbines, trend in application and production in croatia", in *Sovetuvanje MAKO CIGRE (5; 2007)*, 2007.

[112] D. Snieckus (RECHARGE), "GE unveils market-changing 12MW offshore wind turbine", `https://www.rechargenews.com/wind/1443296/ge-unveils-market-changing-12mw-offshore-wind-turbine`, 2018, Accessed: 04.03.2019.

[113] Novawind, "Novawind WT 2.5 MW", `http://novawind.ru/eng/production/wey25/`, 2018, Accessed: 04.03.2019.

[114] S. Heier, *Grid Integration of Wind Energy*, John Wiley & Sons, Ltd, Chichester, UK, 3rd edition, apr 2014.

[115] K. P. Skokov and O. Gutfleisch, "Heavy rare earth free, free rare earth and rare earth free magnets - Vision and reality", *Scripta Materialia*, vol. 154, pp. 289–294, 2018.

[116] Siemens-Gamesa, "G132-5.0 MW Technical specifications", 2018.

[117] J. Lloberas, A. Sumper, M. Sanmarti, and X. Granados, "A review of high temperature superconductors for offshore wind power synchronous generators", *Renewable and Sustainable Energy Reviews*, vol. 38, pp. 404–414, 2014.

[118] J. E. Rodríguez, "Siemens, Gamesa to form world's largest wind farm business", `https://www.reuters.com/article/us-gamesa-m-a-siemens/siemens-gamesa-to-form-worlds-largest-wind-farm-business-idUSKCN0Z22JC`, 2019, Accessed: 18.07.2019.

[119] S. Chatterjee and S. Chatterjee, "Review on the techno-commercial aspects of wind energy conversion system", *IET Renewable Power Generation*, vol. 12, no. 14, pp. 1581–1608, 2018.

[120] M. Doppelbauer and P. Winzer, "A lighter motor for tomorrow's electric car", *IEEE Spectrum*, vol. 54, no. 7, pp. 26–31, July 2017.

[121] D. A. Torrey, "Switched reluctance generators and their control", *IEEE Transactions on Industrial Electronics*, vol. 49, no. 1, pp. 3–14, Feb 2002.

[122] B. Ge and D. C. Ludois, "Design Concepts for a Fluid-Filled Three-Phase Axial-Peg-Style Electrostatic Rotating Machine Utilizing Variable Elastance", *IEEE Transactions on Industry Applications*, vol. 52, no. 3, pp. 2156–2166, may 2016.

[123] C. Jiang, K. T. Chau, C. Liu, and W. Han, "Design and Analysis of Wireless Switched Reluctance Motor Drives", *IEEE Transactions on Industrial Electronics*, vol. 66, no. 1, pp. 245–254, jan 2019.

[124] C. Liu, "Emerging Electric Machines and Drives — An Overview", *IEEE Transactions on Energy Conversion*, vol. 33, no. 4, pp. 2270–2280, dec 2018.

[125] GE Renewable Energy, "HALIADE 150-6MW OFFSHORE WIND TURBINE", `https://www.ge.com/renewableenergy/wind-energy/turbines/offshore-turbine-haliade`, 2016, Accessed: 04.03.2019.

[126] R. M. Pacella, "How It Works: The Next-Gen Wind Turbine", `https://www.popsci.com/technology/article/2010-03/next-gen-wind-turbine`, 2010, Accessed: 30.06.2019.

[127] D. J. Mayer, "Wind Energy for Remote Telecommunications Sites-A Case History", in *INTELEC '82 - International Telecommunications Energy Conference*. 1982, pp. 434–436, IEEE.

[128] A. D. Tipney-Hicks and R. Attwood, "Hybrid Schemes for Remote Power Systems", in *INTELEC '84 - International Telecommunications Energy Conference*. 1984, pp. 166–169, IEEE.

[129] AWEA-American Wind Energy Association, "The wind energy applications guide", *Washington, DC: AWEA*, 2001.

[130] P. Gipe, "Photos of Northern Power HR3 Wind Turbines", `http://www.wind-works.org/cms/index.php?id=533`, 2013, Accessed: 20.05.2019.

[131] D. M. Whaley, W. L. Soong, and N. Ertugrul, "Investigation of switched-mode rectifier for control of small-scale wind turbines", *Fourtieth IAS Annual Meeting. Conference Record of the 2005 Industry Applications Conference, 2005.*, vol. 4, no. 4, pp. 2849–2856, 2005.

[132] K. Buchert and F. W. Fuchs, "Comparison of three phase rectifier topologies in small wind turbines", in *2014 16th European Conference on Power Electronics and Applications, EPE-ECCE Europe 2014*. aug 2014, pp. 1–10, IEEE.

[133] Z. Zhang, Y. Zhao, W. Qiao, and L. Qu, "A Space-Vector-Modulated Sensorless Direct-Torque Control for Direct-Drive PMSG Wind Turbines", *IEEE Transactions on Industry Applications*, vol. 50, no. 4, pp. 2331–2341, jul 2014.

[134] P. Gajewski and K. Pieńkowski, "Application of direct torque and power control to the wind turbine system with pmsg", *Czasopismo Techniczne*, vol. 2016, no. Elektrotechnika Zeszyt 2-E 2016, pp. 173–190, 2016.

[135] H. A. Young, M. A. Perez, J. Rodriguez, and H. Abu-Rub, "Assessing Finite-Control-Set Model Predictive Control: A Comparison with a Linear Current Controller in Two-Level Voltage Source Inverters", *IEEE Industrial Electronics Magazine*, vol. 8, no. 1, pp. 44–52, mar 2014.

[136] L. Bigarelli, A. Lidozzi, M. Di Benedetto, L. Solero, S. Odhano, and P. Zanchetta, "Modulated Optimal Model Predictive Control for Variable Speed Gen-Sets", in *2018 IEEE Energy Conversion Congress and Exposition (ECCE)*. sep 2018, pp. 6859–6865, IEEE.

[137] N. Freire, J. Estima, and A. Cardoso, "A comparative analysis of pmsg drives based on vector control and direct control techniques for wind turbine applications", *Przegląd Elektrotechniczny*, vol. 88, no. 1, pp. 184–187, 2012.

[138] M. Heydari and K. Smedley, "Comparison of maximum power point tracking methods for medium to high power wind energy systems", in *2015 20th Conference on Electrical Power Distribution Networks Conference (EPDC)*. apr 2015, number April, pp. 184–189, IEEE.

[139] B. Wilamowski and D. Irwin, *The industrial electronics handbook*, CRC press, 2nd edition, 2011.

[140] MathWorks, “SimPower Systems PMSG Model”, `https://www.mathworks.com/help/physmod/sps/powersys/ref/permanentmagnetsynchronousmachine.html`, 2018, Accessed: 29.05.2019.

[141] R. E. Quintal-Palomo, M. Gwozdziewicz, and M. Dybkowski, “Modelling and co-simulation of a permanent magnet synchronous generator”, *COMPEL - The international journal for computation and mathematics in electrical and electronic engineering*, July 2019.

[142] R. Quintal-Palomo and M. Dybkowski, “Modelling and Co-Simulation of Small Wind Turbine with Permanent Magnet Synchronous Generator”, *Przeglad Elektrotechniczny*, vol. "in press", no. 9, 2019.

[143] M. P. Kaźmierkowski and H. Tunia, *Automatic control of converter-fed drives*, Studies in electrical and electronic engineering. Elsevier, 1994.

[144] B. K. Bose, *Modern Power Electronics and AC Drives*, Eastern Economy Edition. Prentice Hall PTR, 2002.

[145] K. Ogata, *Modern Control Engineering*, Instrumentation and controls series. Prentice Hall, 2010.

[146] W. C. Duesterhoeft, M. W. Schulz, and E. Clarke, “Determination of Instantaneous Currents and Voltages by Means of Alpha, Beta, and Zero Components”, *Transactions of the American Institute of Electrical Engineers*, vol. 70, no. 2, pp. 1248–1255, jul 1951.

[147] B. Wu, Y. Lang, N. Zargari, and S. Kouro, *Power Conversion and Control of Wind Energy Systems*, John Wiley & Sons, Inc., Hoboken, NJ, USA, jul 2011.

[148] C. Schulte and J. Böcker, “Co-simulation of an electric traction drive”, in *2013 International Electric Machines Drives Conference*, May 2013, pp. 974–978.

[149] Z. Peng, L. Chai, and Y. Sheng, “Co-simulation modeling and fault diagnosis of closed-loop squirrel-cage motor systems”, in *2017 12th IEEE Conference on Industrial Electronics and Applications (ICIEA)*, June 2017, pp. 718–722.

[150] A. Bellini, S. Bifaretti, and S. Costantini, “A Digital Speed Filter for Motion Control Drives with a Low Resolution Position Encoder”, *Automatika : časopis za automatiku, mjerenje, elektroniku, računarstvo i komunikacije*, vol. 44, no. 1-2, pp. 67–74, 2003.

[151] B. A. Welchko, T. M. Jahns, W. L. Soong, and J. M. Nagashima, “IPM synchronous machine drive response to symmetrical and asymmetrical short circuit faults”, *IEEE Transactions on Energy Conversion*, vol. 18, no. 2, pp. 291–298, jun 2003.

[152] G. Choi and T. M. Jahns, “Interior permanent magnet synchronous machine rotor demagnetization characteristics under fault conditions”, in *2013 IEEE Energy Conversion Congress and Exposition*. sep 2013, pp. 2500–2507, IEEE.

[153] K. T. Kim, Y. S. Lee, and J. Hur, “Transient analysis of irreversible demagnetization of permanent-magnet brushless DC motor with interturn fault under the operating state”, *IEEE Transactions on Industry Applications*, vol. 50, no. 5, pp. 3357–3364, 2014.

[154] H. K. Kim and J. Hur, “Dynamic Characteristic Analysis of Irreversible Demagnetization in SPM-and IPM-Type BLDC Motors”, *IEEE Transactions on Industry Applications*, vol. 53, no. 2, pp. 982–990, 2017.

[155] T. M. Jahns and V. Caliskan, "Uncontrolled generator operation of interior PM synchronous machines following high-speed inverter shutdown", *IEEE Transactions on Industry Applications*, vol. 35, no. 6, pp. 1347–1357, 1999.

[156] W. Le Roux, R. G. Harley, and T. G. Habetler, "Detecting Rotor Faults in Low Power Permanent Magnet Synchronous Machines", *IEEE Transactions on Power Electronics*, vol. 22, no. 1, pp. 322–328, jan 2007.

[157] Z. Yang, X. Shi, and M. Krishnamurthy, "Vibration monitoring of PM synchronous machine with partial demagnetization and inter-turn short circuit faults", in *2014 IEEE Transportation Electrification Conference and Expo (ITEC)*. jun 2014, pp. 1–6, IEEE.

[158] Y. Park, C. Yang, S. B. Lee, D. M. Lee, D. Fernandez, D. Reigosa, and F. Briz, "Online Detection and Classification of Rotor and Load Defects in PMSMs Based on Hall Sensor Measurements", *IEEE Transactions on Industry Applications*, vol. 55, no. 4, pp. 3803–3812, jul 2019.

[159] D. Casadei, F. Filippetti, M. Mengoni, Y. Gritli, G. Serra, A. Tani, and L. Zarri, "Detection of magnet demagnetization in five-phase surface-mounted permanent magnet generators", in *2012 3rd IEEE International Symposium on Power Electronics for Distributed Generation Systems (PEDG)*. jun 2012, pp. 841–848, IEEE.

[160] Z. Goryca, S. Rozowicz, K. Dabala, and Z. Krzemien, "Design and tests of generators for micro hydro plants", in *2017 International Symposium on Electrical Machines (SME)*. jun 2017, pp. 1–4, IEEE.

[161] J. Tedd, J. P. Kofoed, M. Jasinski, A. Morris, E. Friis-Madsen, R. Wisniewski, and J. D. Bendtsen, "Advanced control techniques for WEC wave dragon", in *7th European Wave and Tidal Energy Conference EWTEC*, Porto, Portugal, 2007, European Ocean Energy Association.

[162] Marian P. Kazmierkowski and Marek Jasinski, "Power electronics for renewable sea wave energy", in *2010 12th International Conference on Optimization of Electrical and Electronic Equipment*. may 2010, pp. 4–9, IEEE.

[163] D. Mingardi, N. Bianchi, and M. D. Pre, "Geometry of Line Start Synchronous Motors Suitable for Various Pole Combinations", *IEEE Transactions on Industry Applications*, vol. 53, no. 5, pp. 4360–4367, sep 2017.

[164] J. A. Tapia, F. Leonardi, and T. A. Lipo, "Consequent pole permanent magnet machine with field weakening capability", in *IEMDC 2001. IEEE International Electric Machines and Drives Conference (Cat. No.01EX485)*. 2001, pp. 126–131, IEEE.

[165] J. A. Tapia, F. Leonardi, and T. A. Lipo, "Consequent-pole permanent-magnet machine with extended field-weakening capability", *IEEE Transactions on Industry Applications*, vol. 39, no. 6, pp. 1704–1709, nov 2003.

[166] S. A. Evans, "Novel rotor design for interior permanent magnet brushless machines: Initial investigation", in *2008 18th International Conference on Electrical Machines*. 2008, IEEE.

[167] F. Luise, A. Tessarolo, F. Agnolet, S. Pieri, M. Scalabrin, M. Di Chiara, and M. De Martin, "Design Optimization and Testing of High-Performance Motors: Evaluating a Compromise Between Quality Design Development and Production Costs of a Halbach-Array PM Slotless Motor", *IEEE Industry Applications Magazine*, vol. 22, no. 6, pp. 19–32, nov 2016.

[168] S. A. Evans, “Salient pole shoe shapes of interior permanent magnet synchronous machines”, in *The XIX International Conference on Electrical Machines - ICEM 2010*. sep 2010, number 1, pp. 1–6, IEEE.

[169] W. Zhao, T. A. Lipo, and B. I. Kwon, “Torque Pulsation Minimization in Spoke-type Interior Permanent Magnet Motors With Skewing and Sinusoidal Permanent Magnet Configurations”, *IEEE Transactions on Magnetics*, vol. 51, no. 11, pp. 1–4, nov 2015.

[170] M. García-Gracia, A. Jiménez-Romero, J. Herrero-Ciudad, and S. Martín-Arroyo, “Cogging Torque Reduction Based on a New Pre-Slot Technique for a Small Wind Generator”, *Energies*, vol. 11, no. 11, pp. 3219, nov 2018.

[171] Z. Ullah and J. Hur, “A Comprehensive Review of Winding Short Circuit Fault and Irreversible Demagnetization Fault Detection in PM Type Machines”, *Energies*, vol. 11, no. 12, 2018.

[172] J. Faiz and H. Nejadi-Koti, “Demagnetization Fault Indexes in Permanent Magnet Synchronous Motors—An Overview”, *IEEE Transactions on Magnetics*, vol. 52, no. 4, pp. 1–11, apr 2016.

[173] S. Zarate, G. Almandoz, G. Ugalde, J. Poza, and A. J. Escalada, “Effects of Demagnetization on Torque Ripples in Permanent Magnet Synchronous Machines With Manufacturing Tolerances”, in *2018 XIII International Conference on Electrical Machines (ICEM)*. sep 2018, IEEE.

[174] A. C. Barmpatza and J. C. Kappatou, “Demagnetization faults detection in an axial flux permanent magnet synchronous generator”, in *Proceedings of the 2017 IEEE 11th International Symposium on Diagnostics for Electrical Machines, Power Electronics and Drives, SDEMPED 2017*. aug 2017, vol. 2017-Janua, pp. 153–159, IEEE.

[175] D. Rekioua, *Wind Power Electric Systems*, Green Energy and Technology. Springer London, London, 1 edition, 2014.

[176] D. Wood, *Small Wind Turbines*, Green Energy and Technology. Springer London, London, 1 edition, 2011.

[177] J. Bernatt, T. Glinka, M. Jakubiec, E. Krol, and R. Rossa, “Electric motors with permanent magnets with two-zone rotational speed control”, in *2007 International Aegean Conference on Electrical Machines and Power Electronics*. sep 2007, pp. 653–658, IEEE.

[178] P. C. Krause, O. Wasynczuk, S. D. Sudhoff, and S. Pekarek, *Analysis of Electric Machinery and Drive Systems*, Wiley-IEEE Press, 2013.

[179] P. Zalas, T. Zawilak, and J. Zawilak, “Synchronization process of permanent magnet synchronous motor from over synchronous speed”, in *2015 Selected Problems of Electrical Engineering and Electronics (WZEE)*, Sept 2015, pp. 1–4.

[180] M. Malinowski, *Sensorless control strategies for PWM rectifier*, PhD thesis, Warsaw University of Technology, 2001.

[181] T. Zawilak, L. Antal, and J. Zawilak, “The influence of load level on current deformation in ac permanent magnet motor (Wpływ obciążenia na odkształcenie prądu w silniku)”, *Zeszyty Problemowe – Maszyny Elektryczne*, , no. 75, pp. 1–4, 2006.